TECHNISCHE UNIVERSITÄT WIEN
Vienna University of Technology

DISSERTATION

3D Structure of Human Auditory Nerve Fibers and its Impact on Excitation with Cochlear Implants

Ausgeführt zum Zwecke der Erlangung des akademischen Grades eines Doktors der technischen Wissenschaften

unter der Leitung von
Prof. DDDr. Frank Rattay
Institut für Analysis und Scientific Computing (E101)

eingereicht an der Technischen Universität Wien
Fakultät für Mathematik und Geoinformation

von
Amirreza Heshmat
Matrikelnummer: 01225217
[redacted]

Wien, am 7. Dezember 2021

Die approbierte gedruckte Originalversion dieser Dissertation ist an der TU Wien Bibliothek verfügbar.
The approved original version of this doctoral thesis is available in print at TU Wien Bibliothek.
TU Bibliothek Your knowledge hub WIEN

Acknowledgments

Foremost, I would like to express my sincere gratitude to my advisor Prof. Frank Rattay for the invaluable mentorship and the continuous support of my Ph.D. study and related research, for his patience, inspiration, motivation, and immense knowledge. His guidance helped me in all the time of research and writing of this dissertation. Words are not enough to express my thanks and gratitude to you, and I am honored to work with you and learn so much from you.

I would also like to thank Prof. Anneliese Schrott-Fischer for her patience, guidance and for giving me the opportunity to develop my knowledge under her supervision in the Laboratory for Inner Ear Biology of the Clinic of Ear Nose and Throat Medicine, Medical University of Innsbruck.

I would like to express my gratefulness to Prof. Werner Hemmert for his support, sharing of constructive comments and suggestions, as well as guidance.

I genuinely express my thanks to Prof. Eugenijus Kaniusas for accepting to be a member of the defense committee of my dissertation and for his academic support.

My sincere thanks also go to Dr. Rudolf Glueckert and Dr. Stephan Handschuh, who helped me learn and discover valuable techniques to obtain data. Further, my special appreciation goes to Dr. Andreas Fellner for his help, support, and sharing of his experience.

I would also like to express my appreciation to the Austrian Science Fund (FWF) for the financial support of this project.

My heartfelt gratitude goes to my colleague, who is also my beloved wife, Sogand Sajedi. I thank her wholeheartedly for her love, encouragement, and precious support.

Last but not least, I am so grateful to my parents, who raised me with love and for their valuable support throughout my life as well as for believing in me.

Die approbierte gedruckte Originalversion dieser Dissertation ist an der TU Wien Bibliothek verfügbar.
The approved original version of this doctoral thesis is available in print at TU Wien Bibliothek.
TU Bibliothek Your knowledge hub WIEN

Abstract

The cochlea in the inner ear has a sophisticated three-dimensional bony spiral shape consisting of three fluid-filled chambers in the bony labyrinth. The cochlea is responsible for sound perception and hearing process, and in humans, it is coiled about two and three-fourth to three turns and varies in length. Sound is converted to electrical signals by sensory hair cells. The signals are transferred to the cochlear nuclei through type I myelinated spiral ganglion neurons, consisting of 95% of the auditory nerve fibers (ANFs).

A perfect hearing perception is possible with a healthy auditory system. People who have problems in their auditory system suffer from hearing deficits. Extraction of the auditory information is only possible by decoding the firing pattern of cochlear neurons in the central nervous system. Consequently, any disruption in this spiking pattern causes problems in speech understanding, particularly in hearing deficit cases. Sensory hair cells and ANFs can be damaged by over-exposure to noise, toxic, or inherent. These damages are irreversible and cause permanent hearing loss. Moreover, the majority of the ANFs degenerate by the loss of hair cells. However, in the human cochlea, some of these fibers survive for years, for instance, people with sensorineural hearing loss or partially intact ANFs, which the survived fibers are possible to be excited by a cochlear implant (CI).

CI is a surgically implanted device that stimulates survived auditory nerves extracellularly by bypassing the damaged or dead region of the neurons. The CI is usually inserted into the scala tympani and can restore the hearing sense in people with severe to profound hearing loss levels. Although, the number of surviving auditory fibers, neural health status, and electrode position of the CI array are crucial and impact the excitability of the auditory neurons.

On the other hand, the CI has critical limitations, leading to some dissatisfaction of CI users to understand speech in a noisy environment and having poor music perception. Hence, computational modeling studies have been used to investigate aspects that are not feasible on live human users to overcome the limitations and improve the functionality of CIs. Moreover, human cochlear geometry and cochlear neurons arrangement have a considerable impact on the outcome of CIs. Hence, other benefits of using computer simulation to investigate these effects and analyze the resulting excitation profiles that lead to reduced animal experiments, improve the CI outcomes, and increase the satisfaction of CI recipients. In this matter, the excitation behavior of auditory nerves by a CI can be studied with computational models. Electrical field distribution along ANFs elicited by a CI can be modeled using the finite element

Die approbierte gedruckte Originalversion dieser Dissertation ist an der TU Wien Bibliothek verfügbar.
The approved original version of this doctoral thesis is available in print at TU Wien Bibliothek.
TU Bibliothek Your knowledge hub WIEN

method, which is used as input for neuron models to simulate the reaction of ANFs to micro-stimulation.

However, a detailed three-dimensional finite element model of human cochlea, three-dimensional helical structure and the spiral ANF pathways, and a realistic CI model are essential for a reliable computational investigation and to study the temporal fine structure of the transmitted neural code as well as tonotopic behavior of the electrically stimulated cochlear.

In this dissertation, the computational model uses an accurate three-dimensional anatomically detailed finite element model of a human cochlea and thirty reconstructed tonotopically organized auditory pathways of type I ANFs. In addition, two different CI arrays, a lateral and a perimodiolar system, were modeled and added to the finite element of the cochlea model to evaluate the excitation profiles of the ANFs. Both CI models are designed according to manufacturer data. Furthermore, for more accurate results in computational investigations related to CI research, it is needed to have realistic information as much as possible from the cochlea and adapted to models. For this purpose, four human cochleae were used to quantify and analyze impact hearing loss levels on peripheral axon changes in diameter and myelination thickness from type I of the ANFs to determine a degeneration pattern based on hearing loss levels, and the obtained data related to degeneration human ANFs were applied for further investigations as follows:

In the first examination, degeneration patterns of the peripheral part of human ANFs investigations were accomplished based on hearing loss levels of several human cochleae. In addition, synaptic excitation and the excitation properties of electrical potential distributions induced by two CI were analyzed. The main findings indicated: (i) the unimodal distribution of control peripheral axon diameters becomes multimodal for hearing loss cases; a group of thin peripheral axon fibers with diameters between 0.3 and 1 µm with a peak at 0.5 µm appeared. (ii) Postsynaptic currents from inner hair cells excite such thin peripheral axon fibers easier and earlier in comparison with healthy conditions. However, this advantage is lost as their conduction velocity decreases proportionally with the diameter and causes increased spike latency and jitter in the soma and central axon. Firing probability reduces through the soma passage due to the low intracellular current flow in thin peripheral axon fibers during spiking. (iii) Compared with peripheral axon diameter, variations in myelin thickness have a small impact on spiking performance. (iv) Contrary to synaptic excitation, CIs cause several spike initiation sites in the peripheral axon, soma region, and central axon; moreover, fiber excitability reduces with fiber diameter. In a few cases where weak stimuli elicit spikes of a target neuron in the central axon, peripheral axon diameter reduction has no effect. However, in many cases, a spike in a target neuron is first initiated in the peripheral axon, and

Die approbierte gedruckte Originalversion dieser Dissertation ist an der TU Wien Bibliothek verfügbar.
The approved original version of this doctoral thesis is available in print at TU Wien Bibliothek.
TU Bibliothek Your knowledge hub WIEN

consequently, peripheral axon degeneration demands an increase in threshold currents. (v) Threshold currents of a target neuron and co-stimulation of degenerated ANFs in other frequency regions depend on the electrode position, including its distance to the outer wall of the scala tympani, the cochlear turn, and the three-dimensional pathway of the target neuron.

Among all different techniques, polarity sensitivity is a promising way to evaluate the neural status of ANFs in CI users. The second part of the dissertation was investigated polarity behavior under the application of symmetric and asymmetric pulse shapes, monopolar and multipolar CI stimulation strategies, and perimodiolar and lateral CI array systems. Our main findings are as follows: (i) action potential (AP) initiation sites occurred mainly in the peripheral site in the lateral system regardless of stimulation strategies, pulse polarities, pulse shapes, cochlear turns, and ANF degeneration levels. However, in the perimodiolar system, AP initiation sites varied between peripheral and central processes, depending on stimulation strategies, pulse shapes, and pulse polarities. (ii) In the perimodiolar array, clusters formed in threshold values based on cochlear turns and degeneration levels for multipolar strategies only when asymmetric pulses were applied. (iii) In the perimodiolar array, a declining trend in polarity (anodic threshold/cathodic threshold) with multipolar strategies was observed between intact or slight degenerated cases and more severe degenerated cases, whereas in the lateral array, cathodic sensitivity was noticed for intact and less degenerated cases and anodic sensitivity for cases with high degrees of degeneration. The results suggest that a combination of asymmetric pulse shapes, focusing more on multipolar stimulation strategies, as well as considering the distances to the modiolus wall, allows us to distinguish the degeneration patterns of ANFs across the cochlea.

The last section of investigation in this dissertation tried to analyze the excitation of ANFs based on different CI insertions, scala tympani versus scala vestibuli. Due to some circumstances, such as ossification and obstruction of scala tympani, the CI insertion can be done in the scala vestibuli, which is a valuable alternative. Therefore, a computational study was performed to analyze ANF excitation features as well as AP initiation sites in both scalae and demonstrate similarity and dissimilarity between scala tympani and scala vestibuli implantations.

For this part of the investigation, several ANFs with similar distances to the center of electrodes were selected in both scala tympani and scala vestibuli by considering the different levels of ANF degeneration. The main results demonstrate that the excitation thresholds of stimulating electrodes in both scalae were cathodic sensitive in the intact case and the AP initiation sites occur in the peripheral process regardless of the electrode position. In contrast, in the degenerated cases, the excitation behavior of ANFs changed, and AP initiation sites differ

Die approbierte gedruckte Originalversion dieser Dissertation ist an der TU Wien Bibliothek verfügbar.
The approved original version of this doctoral thesis is available in print at TU Wien Bibliothek.
TU Bibliothek WIEN Your knowledge hub

depending on polarity and electrode position. Furthermore, the three-dimensional ANF pathways significantly impact the excitation threshold and AP initiation sites. The other outcome displays that polarity sensitivity depends on the array system, pulse shape, and ANF health status for the scala tympani case; however, in the scala vestibuli case, the polarity effect disappears regardless of pulse shape, CI array system, cochlear turn, and ANF health status. Although it is needed, more investigations will be done to analyze the ANF excitation behavior and polarity sensitivity under different conditions between scala tympani and scala vestibuli.

Die approbierte gedruckte Originalversion dieser Dissertation ist an der TU Wien Bibliothek verfügbar.
The approved original version of this doctoral thesis is available in print at TU Wien Bibliothek.
TU Bibliothek Your knowledge hub WIEN

Zusammenfassung

Die Cochlea im Innenohr hat eine ausgeklügelte dreidimensionale knöcherne Spiralform, die aus drei flüssigkeitsgefüllten Kammern im knöchernen Labyrinth besteht. Die Cochlea ist für die Klangwahrnehmung und den Hörprozess verantwortlich. Beim Menschen hat sie meist zwei und drei Viertel bis drei Windungen und variiert in der Länge. Schall wird von sensorischen Haarzellen in elektrische Signale umgewandelt. Die Signale werden über myelinisierte Spiral Ganglion Neuronen vom Typ I, die zu 95% aus den Hörnervenfasern (ANF) bestehen, an die Cochlea-Kerne übertragen.

Eine perfekte Hörwahrnehmung ist mit einem gesunden Hörsystem möglich. Menschen, die Probleme in ihrem Hörsystem haben, leiden unter Hördefiziten. Die Extraktion der auditiven Informationen ist nur möglich, indem das Feuermuster von Cochlea-Neuronen im zentralen Nervensystem entschlüsselt wird. Folglich verursacht jede Störung in diesem Spiking-Muster Probleme beim Sprachverständnis, insbesondere in Fällen von Hördefiziten. Sensorische Haarzellen und ANFs können durch übermäßige Exposition gegenüber Lärm inhärent geschädigt werden. Diese Schäden sind irreversibel und verursachen einen dauerhaften Hörverlust. Darüber hinaus degeneriert die Mehrheit der ANF durch den Verlust von Haarzellen. In der menschlichen Cochlea überleben jedoch einige dieser Fasern jahrelang, zum Beispiel Menschen mit sensorineuralem Hörverlust oder teilweise intakten ANF. Die überlebenden Fasern können durch ein Cochlea-Implantat (CI) angeregt werden.

CI ist ein chirurgisch implantiertes Gerät, das überlebende Hörnerven extrazellulär stimuliert indem es die beschädigte oder abgestorbene Region der Neuronen umgeht. Das CI wird normalerweise in die scala tympani eingeführt und kann den Hörsinn bei Menschen mit schwerem bis hochgradigem Hörverlust wiederherstellen. Die Anzahl der überlebenden Hörfasern, der neuronale Gesundheitszustand und die Elektrodenposition des CI-Arrays sind jedoch entscheidend und beeinflussen die Erregbarkeit der auditiven Neuronen.

Auf der anderen Seite hat das CI kritische Einschränkungen, was zu einer gewissen Unzufriedenheit der CI-Benutzer führt, Sprache in einer lauten Umgebung zu verstehen und eine schlechte Musikwahrnehmung zu haben. Daher wurden computergestützte Modellierungsstudien verwendet, um Aspekte zu untersuchen, die bei lebenden menschlichen Benutzern nicht durchführbar sind, um die Einschränkungen zu überwinden und die Funktionalität von CIs zu verbessern. Darüber hinaus haben die menschliche Cochlea-Geometrie und die Anordnung der Cochlea-Neuronen einen erheblichen Einfluss auf das

Die approbierte gedruckte Originalversion dieser Dissertation ist an der TU Wien Bibliothek verfügbar.
The approved original version of this doctoral thesis is available in print at TU Wien Bibliothek.
TU WIEN Bibliothek Your knowledge hub

Ergebnis von CIs. Vorteile der Verwendung von Computersimulationen, um diese Effekte zu untersuchen und die resultierenden Anregungsprofile zu analysieren sind, die Tierversuche zu reduzieren , die CI-Ergebnisse verbessern und damit die Zufriedenheit der CI-Empfänger erhöhen. In dieser Hinsicht kann das Erregungsverhalten von Hörnerven durch ein CI mit Computermodellen untersucht werden. Die elektrische Feldverteilung entlang der von einem CI ausgelösten ANF kann mit der Finite-Elemente-Methode modelliert werden, die als Input für Neuronenmodelle verwendet wird, um die Reaktion von ANF auf Mikrostimulation zu simulieren.

Ein detailliertes dreidimensionales Finite-Elemente-Modell der menschlichen Cochlea, der dreidimensionalen spiralförmigen Struktur und der spiralförmigen ANF-Pfade sowie ein realistisches CI-Modell sind jedoch für eine zuverlässige computergestützte Untersuchung und die Untersuchung der zeitlichen Feinstruktur des übertragenen neuronalen Codes sowie des tonotkopischen Verhaltens der elektrisch stimulierten Cochlea unerlässlich.

In dieser Dissertation profitiert das Berechnungsmodell von einem genauen dreidimensionalen anatomisch detaillierten Finite-Elemente-Modell einer menschlichen Cochlea, und dreißig rekonstruierte tonotopisch organisierte Hörbahnen vom Typ I ANF wurden verwendet. Darüber hinaus wurden zwei verschiedene CI-Arrays, ein laterales und ein perimodiolares System, modelliert und dem Cochlea-Modell hinzugefügt, um die Anregungsprofile der ANF zu bewerten. Beide CI-Modelle sind nach Herstellerangaben konzipiert. Darüber hinaus ist es für genauere Ergebnisse in computergestützten Untersuchungen im Zusammenhang mit der CI-Forschung erforderlich, so viele realistische Informationen wie möglich aus der Cochlea zu haben und an Modelle anzupassen. Zu diesem Zweck wurden vier menschliche Cochleae verwendet, um die Auswirkungen des Hörverlusts auf periphere Axonänderungen des Durchmessers und der Myelinisierungsdicke zu quantifizieren und zu analysieren, um ein Degenerationsmuster basierend auf den Hörverlustwerten zu bestimmen, und die erhaltenen Daten im Zusammenhang mit der Degeneration menschlicher ANF wurden für weitere Untersuchungen wie folgt verwendet:

In der ersten Untersuchung wurden Degenerationsmuster des peripheren Teils menschlicher ANF-Untersuchungen basierend auf Hörverlustwerten mehrerer menschlicher Cochleae durchgeführt. Zusätzlich wurden die synaptische Anregung und die Anregungseigenschaften elektrischer Potentialverteilungen, die durch zwei CI induziert werden, analysiert. Die wichtigsten Ergebnisse waren: (i) Die unimodale Verteilung der peripheren Axondurchmesser der Kontrolle wird multimodal für Fälle von Hörverlust; wo eine neue Gruppe dünner peripherer Axonfasern mit Durchmessern zwischen 0.3 und 1 µm mit einem Peak bei 0.5 µm erschien. (ii) Postynaptische Ströme aus inneren Haarzellen regen solche dünnen peripheren

Die approbierte gedruckte Originalversion dieser Dissertation ist an der TU Wien Bibliothek verfügbar.
The approved original version of this doctoral thesis is available in print at TU Wien Bibliothek.
TU Bibliothek Your knowledge hub WIEN

Axonfasern leichter und früher an als unter Kontrollbedingungen. Dieser Vorteil geht jedoch verloren, da ihre Leitungsgeschwindigkeit proportional mit dem Durchmesser abnimmt und eine erhöhte Spike-Latenz und Jitter im Soma und im zentralen Axon verursacht. Die Feuerwahrscheinlichkeit verringert sich durch die Soma-Passage aufgrund des geringen intrazellulären Stromflusses in dünnen peripheren Axonfasern während des Spikings. (iii) Im Vergleich zum peripheren Axondurchmesser haben Schwankungen der Myelindicke einen geringen Einfluss auf die Spiking-Leistung. (iv) Im Gegensatz zur synaptischen Erregung verursachen CIs mehrere Spike-Initiationsstellen im peripheren Axon, in der Soma-Region und im zentralen Axon. Darüber hinaus nimmt die Fasererregbarkeit mit dem Faserdurchmesser ab. In einigen wenigen Fällen, in denen schwache Reize spikes eines Zielneurons im zentralen Axon hervorrufen, hat die periphere Axondurchmesserreduktion keine Wirkung. In vielen Fällen wird jedoch zuerst ein spike in einem Zielneuron im peripheren Axon eingeleitet, und folglich erfordert die Degeneration des peripheren Axons eine Erhöhung der Schwellenströme. (v) Schwellenströme eines Zielneurons und die Kostimulation degenerierter ANF in anderen Frequenzbereichen hängen von der Elektrodenposition ab, einschließlich ihres Abstands zur Außenwand, der Cochlea-Windung und des dreidimensionalen Weges des Zielneurons.

Die Polaritätsempfindlichkeit unter allen verschiedenen Techniken ist ein vielversprechender Weg, um den neuronalen Status von ANFs bei CI-Anwendern zu bewerten. In diesem Teil der Dissertation wurde das Polaritätsverhalten unter Anwendung symmetrischer und asymmetrischer Pulsformen, monopolarer und multipolarer CI-Stimulationsstrategien sowie perimodiolarer und lateraler CI-Array-Systeme untersucht. Unsere Hauptergebnisse sind wie folgt: (i) Aktionspotential (AP) Initiationsstellen traten hauptsächlich an der peripheren Stelle im lateralen System auf, unabhängig von Stimulationsstrategien, Pulspolaritäten, Pulsformen, Cochlea-Drehungen und ANF-Degenerationsgrad. Im perimodiolären System variierten die AP-Initiationsstellen jedoch zwischen peripheren und zentralen Prozessen, abhängig von Stimulationsstrategien, Pulsformen und Pulspolaritäten. (ii) Im perimodiolären Array bildeten sich Cluster in Schwellenwerten basierend auf Cochlea-Windungen und Degenerationsgraden für multipolare Strategien nur dann, wenn asymmetrische Impulse angewendet wurden. (iii) Im perimodiolären Array wurde ein abnehmender Trend in der Polarität (anodische Schwelle/kathodische Schwelle) mit multipolaren Strategien zwischen intakten oder leicht degenerierten Fällen und schwereren degenerierten Fällen beobachtet, während im lateralen Array eine kathodische Empfindlichkeit für intakte und weniger degenerierte Fälle und eine anodische Sensitivität für Fälle mit hohem Degenerationsgrad festgestellt wurde. Die Ergebnisse deuten darauf hin, dass eine Kombination aus asymmetrischen Pulsformen, die sich mehr auf multipolare Stimulationsstrategien konzentrieren, sowie die Berücksichtigung der

Die approbierte gedruckte Originalversion dieser Dissertation ist an der TU Wien Bibliothek verfügbar.
The approved original version of this doctoral thesis is available in print at TU Wien Bibliothek.
TU Bibliothek WIEN Your knowledge hub

Abstände zur Modioluswand es uns ermöglicht, die Degenerationsmuster von ANF in der Cochlea zu unterscheiden.

Der letzte Untersuchungsabschnitt in dieser Dissertation versuchte, die Anregung von ANF basierend auf verschiedenen CI-Insertionen, scala tympani versus scala vestibuli, zu analysieren. Aufgrund einiger Umstände, wie Verknöcherung und Obstruktion von scala tympani, kann die CI-Insertion in der scala vestibuli erfolgen, was eine wertvolle Alternative darstellt. Daher wurde eine Computerstudie durchgeführt, um ANF-Anregungsmerkmale sowie AP-Initiationsstellen in beiden scalae zu analysieren und Ähnlichkeit und Unähnlichkeit zwischen scala tympani- und scala vestibuli-Implantationen zu demonstrieren.

Für diesen Teil der Untersuchung wurden mehrere ANF mit ähnlichen Abständen zum Zentrum der Elektroden sowohl in scala tympani als auch in scala vestibuli ausgewählt, indem die verschiedenen Ebenen der ANF-Degeneration berücksichtigt wurden. Die Hauptergebnisse zeigen, dass die Anregungsschwellen der stimulierenden Elektroden in beiden Scalae im intakten Fall kathodisch empfindlich waren und die AP-Initiationsstellen im peripheren Prozess unabhängig von der Elektrodenposition auftreten. Im Gegensatz dazu änderte sich in den degenerierten Fällen das Anregungsverhalten von ANFs, und die AP-Initiationsstellen unterscheiden sich je nach Polarität und Elektrodenposition. Darüber hinaus beeinflussen die dreidimensionalen ANF-Pfade signifikant die Anregungsschwelle und die AP-Stellen. Die Simulationen zeigen, dass die Polaritätsempfindlichkeit von den Array-Typen, der Pulsform und dem ANF-Gesundheitsstatus für den scala tympani-Fall abhängt. Im Fall von scala vestibuli verschwindet der Polaritätseffekt jedoch unabhängig von Pulsform, CI-Array-System, Cochlea-Turn und ANF-Gesundheitszustand. Da es notwendig ist, werden weitere Untersuchungen durchgeführt, um das ANF-Anregungsverhalten und die Polaritätsempfindlichkeit unter verschiedenen Bedingungen zwischen scala tympani und scala vestibuli zu analysieren.

Die approbierte gedruckte Originalversion dieser Dissertation ist an der TU Wien Bibliothek verfügbar.
The approved original version of this doctoral thesis is available in print at TU Wien Bibliothek.
TU Bibliothek Your knowledge hub WIEN

Contents

Acknowledgments ii
Abstract iii
Zusammenfassung vii
List of Figures xv
List of Tables xxiv
Abbreviations xxv
Chapter 1 1
1.1 Anatomy and physiology of the human auditory system 1
1.1.1 The Outer Ear 2
1.1.2 The Middle Ear 3
1.1.3 The Inner Ear 3
1.2 Human auditory nerve 8
1.2.1 Human hearing spectrum 9
1.2.2 Types, causes, and degrees of hearing loss 15
1.2.3 Degree of hearing loss and evaluation of hearing 18
1.2.4 How is hearing loss restored? 20
1.3 Cochlear implant overview 20
1.3.1 Structure, function, and design of cochlear implant 22
1.4 Scala tympani versus scala vestibuli implantations 25
1.5 Limitations & Objectives 28
1.6 Outlines 32
Chapter 2 33
2.1 General Methods 34
2.1.1 Cell membrane 34
2.1.2 Membrane electrical properties 36
2.1.3 Hodgkin and Huxley model 37
2.1.4 Compartment models 41
2.1.5 Multi-compartment model of human spiral ganglion neuron 43
2.1.6 Extracellular stimulation 45
2.1.7 Activating function 46

Die approbierte gedruckte Originalversion dieser Dissertation ist an der TU Wien Bibliothek verfügbar.
The approved original version of this doctoral thesis is available in print at TU Wien Bibliothek.
TU WIEN Bibliothek Your knowledge hub

2.1.8 Numerical solution 47
2.1.9 Finite Element Method 49
2.1.10 FE Model Configurations 50
2.1.11 Modeling cochlear implant array in COMSOL 54
2.1.12 Image processing 59
2.2 Distinctive Methods 63
2.2.1 Degeneration pattern of human cochlear nerves 63
2.2.2 Impact pulse shapes, CI stimulation strategies, and array types on polarity behavior of human auditory nerve fibers 68
2.2.3 Scala tympani vs. scala vestibuli implantations 73
Chapter 3 78
3.1 Degeneration pattern of peripheral axon of human ANFs based on hearing loss levels 78
3.1.1 Variations in peripheral axon diameter and myelination thickness 79
3.1.2 Correlation between peripheral axon diameter, myelination thickness, and G-ratio 83
3.1.3 Impact of peripheral axon diameter and myelination thickness on synaptic threshold current and action potential arrival time in the axon 91
3.1.4 Extracellular stimulation 98
3.2 Impact different parameters on threshold current and polarity sensitivity 105
3.2.1 Impact of type of array, pulse shape, stimulus strategy, and degeneration level on threshold current 105
3.2.2 Impact of type of array, pulse shape, stimulus strategy, and degeneration level on polarity ratios and polarity sensitivity 111
3.2.3 Impact of type of array, pulse shape, pulse polarity, stimulus strategy, and degeneration level on action potential initiation sites 116
3.2.4 Impact of distance between channels and distance to modiolus wall on polarity sensitivity 119
3.3 Scala tympani versus scala vestibuli electrodes 126
3.3.1 Stimulation at threshold 126
3.3.2 Stimulation of intact auditory nerve fibers 132
3.3.3 Stimulation of intermediate vs. progressive degenerated auditory nerve fibers 135
3.3.4 Strong versus weak stimulation 138
3.3.5 Scala tympani versus scala vestibuli cochlear implant arrays 140

Die approbierte gedruckte Originalversion dieser Dissertation ist an der TU Wien Bibliothek verfügbar.
The approved original version of this doctoral thesis is available in print at TU Wien Bibliothek.
TU Bibliothek Your knowledge hub WIEN

Chapter 4 155
4.1 Degeneration pattern of human cochlear nerves 155
4.1.1 Variation in peripheral axon diameter 155
4.1.2 Appearance of small fibers in hearing loss specimens and consequences 156
4.1.3 Degeneration level affects cochlear implant outcomes 156
4.1.4 Clinical implications 157
4.1.5 Modeling details and limitations 157
4.1.6 Conclusion 158
4.2 Impact different parameters on threshold current and polarity sensitivity 160
4.2.1 Effect of pulse shape 160
4.2.2 Effect of cochlear implant stimulation strategy 162
4.2.3 Effect of cochlear implant array 163
4.2.4 Perceptual efficacy 164
4.2.5 Conclusion 165
4.3 Scala tympani versus scala vestibuli implantations 166
References 170
Curriculum Vitae 189

Die approbierte gedruckte Originalversion dieser Dissertation ist an der TU Wien Bibliothek verfügbar.
The approved original version of this doctoral thesis is available in print at TU Wien Bibliothek.
TU Bibliothek Your knowledge hub WIEN

List of Figures

Figure 1.1. The anatomy of the human ear. It consists of three main parts: the outer ear, the middle ear, and the inner ear. The Figure is taken (Lumen Learning, 2021)..... 2

Figure 1.2. Anatomy of the human cochlea. **(A)** Snail shape of the cochlea. **(B)** Cross-section of the cochlea consists of three chambers and cochlear nerves. **(C)** Schematic representation of organ of Corti structure including hair cells. The stereocilia lengths are not in scale; only the longest stereocilia of the outer hair cells are in contact with the tectorial membrane. The Figure is taken (Lumen Learning, 2021). 4

Figure 1.3. Illustration of inner hair cells. **(A)** Schematic of mechanoelectrical transduction operated by inner hair cells. **(B)** Representation of hair bundle (stereocilia) and afferent nerve fiber (left) and more detail in the right part shows synaptic vesicles (small green circles) are gathered in ribbon (blue ellipse) synapses in several release zones at the lower part and the voltage-gated calcium channels (light blue cylinders). The Figure adapted from (Parsons, 2006; BIO 264, BYU IDAHO)..... 7

Figure 1.4. Configurations of auditory nerve fibers innervation with spiral ganglion neurons type I (blue) and II (green). There are three rows of the outer hair cells vs. one row of the inner hair cells performing the innervation system. The figure is taken from (Liberman, 2017)..... 8

Figure 1.5. Illustration of spiral ganglion neurons (SGN) in humans. Myelinating Schwann cells (dark blue, 1) cover and myelinate both peripheral and central processes of the type I SGNs (red) that innervate the inner hair cells (IHC). Satellite glial cells (green, 2) surround all SGN cell bodies (somata). Non-myelinating Schwann cells (light blue, 3) cover both the central and peripheral processes of the type II SGNs (yellow) that innervate the outer hair cells (OHC). In the organ of Corti, beyond the habenula perforata, the peripheral processes of type I and type II are non-myelinated. The figure and caption are adapted from (Locher *et al.*, 2014)..... 9

Figure 1.6. Representation of a sound wave. **(A)** Demonstrating different terms such as amplitude and pressure in the frequency diagram. **(B)** Comparison of high and low frequencies..... 10

Figure 1.7. Schematic depiction of the uncoiled cochlea and basilar membrane structure. **(A)** The uncoiled cochlea and basilar membrane show arriving vibrations from the tympanic membrane into the cochlea. **(B)** Traveling sound waves along the basilar membrane and frequency mapping appear due to the physical properties of the basilar membrane. Figure adapted from (Lumen Learning, 2021)..... 11

Figure 1.8. Neural tuning curves of five auditory nerve fibers with CF from 1.3 to 16.6 kHz. The lowest curves correspond to a firing rate of 25 spikes per second above their spontaneous rate. Minima mark the frequencies (CF) where the fibers are most sensitive. Note that stimulus frequency intervals rise with increased sound pressure level, as seen from the dashed line, which denotes a comfortable speech sound pressure level (60 dB). Figure and caption adapted from (Rattay and Lutter, 1997). 12

Figure 1.9. Basilar membrane displacements of the Peterson Bogert model were computed with the numerical method. **(A-C)** Basilar membrane movements along the cochlea for particular times. **(D)** Stimulus with a sinusoidal signal. **(E)** Basilar membrane movements are plotted against time. Figure and caption adapted from (Rattay and Lutter, 1997). 13

Die approbierte gedruckte Originalversion dieser Dissertation ist an der TU Wien Bibliothek verfügbar.
The approved original version of this doctoral thesis is available in print at TU Wien Bibliothek.
TU WIEN Bibliothek Your knowledge hub

Figure 1.10. Illustration of the tonotopic organization of the human hearing organ, cochlea. The figure is taken from (Lahav and Skoe, 2014). 14

Figure 1.11. The Volley principle. A periodic acoustic stimulus will cause firing patterns in different axons of one hair cell as marked with a - e. The combined signal contains all the minima of sound even when no single fiber is able to fire with this high frequency. Figure and caption adapted from (Rattay, 1990). 15

Figure 1.12. Schematic representation of different degeneration SGN type I in humans. **(A)** Indicating the normal status of SGN with IHC connection to peripheral and projected to soma and reach the brainstem with central axons. **(B)** Presenting the first level of degeneration in patients with SNHL causes loss of hair cells. **(C)** Demonstrating the second level of SGN type I degeneration in people with SNHL difficulties resulting in losing supporting cells as well as peripheral axons. The figure is adapted from (Liu *et al.*, 2015)..... 17

Figure 1.13. Audiogram graphs with different hearing loss levels. **(A-D)** demonstrate people with mild, moderate, severe, and profound hearing loss levels, respectively. The air conduction for the right and left ear showed the red circle and blue cross in all graphs. Noted gray area indicates normal hearing for children. The figure is adapted (Happy Ears Hearing Center). 19

Figure 1.14. Frictional electrical machine with a glass globe (Wikimedia Commons, 2020). 21

Figure 1.15. Illustration of a cochlear implant with key components of cochlear. The external part consists of a microphone, processor, and transmitter. The internal part includes a receiver located under the skin and an array with electrode contacts, which is inserted in the scala tympani. The figure is taken from (Reiss, 2020). 23

Figure 1.16. Representation of lateral CI array versus perimodiolar CI array. **(A)** Lateral array, dark green, with 12 electrode contacts depicting in red located of the lateral wall of the array, far away from the modiolus. **(B)** perimodiolar array, light green, with 22 electrode contacts showing in orange located on the inner (medial) wall of the array, close to the modiolus and scala tympani wall. 25

Figure 1.17. Ossification degrees of scala tympani. **(A)** Degree I ossification happens at the round window. **(B)** Degree II ossification appears up to 180° of the basal turn. **(C)** Degree III ossification occurs above 180° of the ST. **(D)** A tunnel drilled the beginning part of the basal turn from the round window for partial CI insertion. **(E)** Scala vestibuli implantation in the fully basal obstruction. The Figure is taken from (Smullen and Balkany, 2005). 27

Figure 2.1. Differential distribution of ions in intra- and extracellular medium of the cell membrane. The gradient of concentration and voltage influence the equilibrium potential. The Figure is adapted from (Wikimedia Commons, 2021). 35

Figure 2.2. Comparison of gating variables in Hodgkin and Huxley (HH model) experiment, m, n, and h indicated in solid lines with red, blue, and green, respectively, and Rattay model of the human auditory nerve with the same gating variable represents with the dashed line in same color code manner..... 39

Figure 2.3. A schematic of an action potential during a stimulus is applied. The action potential is generated due to the activation of sodium channels leading to the rise in membrane potential; through the depolarization, sodium channels inactivate, and potassium channels activate, causing a decrease in the membrane potential. Finally, all channels are closed and membrane reaches the resting state. 41

Figure 2.4. Schematic drawing of single- and multi-compartment models. **(A)** Single compartment model includes capacitance and ion currents across the cell membrane. **(B)** Multi-compartment model of soma and its processes. Note that due to potential changes from one subunit to the other, a multi-compartment model consists of an axial current that flows between neighboring compartments. The Figure is adapted from (Rattay, Lutter and Felix, 2001)..... 42

Die approbierte gedruckte Originalversion dieser Dissertation ist an der TU Wien Bibliothek verfügbar.
The approved original version of this doctoral thesis is available in print at TU Wien Bibliothek.
TU Bibliothek Your knowledge hub WIEN

Figure 2.5. Representation of the compartment model of a human SGN. Geometric parameters are indicated in the top part; the colors describe the electrical parameters. The electrical network model of the soma area in the green box is displayed at the right, including the corresponding differential equation in the nth compartment. The currents are defined by extracellular potential Ve, intracellular potential Vi, membrane capacitance Cm, membrane conductance Gm, and intracellular resistance R (Potrusil *et al.*, 2020). 44

Figure 2.6. Activating function generated by extracellular stimulation of a straight non-myelinated axon with a spherical electrode. **(A)** Geometry and isopotentials for a point source 50 µm above a fiber positioned at the x-axis. **(B)** Calculating activating function by using extracellular potential. **(C)** A fiber with d = 1 µm and compartment length Δx = 10 µm results in a peak activating function value of 740 mV/ms. Figure and caption are slightly adapted from (Rattay et al., 2012). 47

Figure 2.7. 3D visualization of 30 differently colored fibers from the basal (black), middle (green), and apical (red) cochlea turns together with the scala tympani. An electrode array (gray circles) of a 12 channels CI (light blue) is inserted in the scala tympani of the model (Heshmat et al., 2020). 51

Figure 2.8. A micro-CT image of a human cochlea **(A)** provided the raw data for the COMSOL model **(B)**. **(A)** Scala tympani (ST) is the cave where electrodes are inserted. Scala vestibuli (SV), and scala media (SM) coil up the bony modiolus (M). Rosenthal's canal (RC) within M houses somata of auditory nerve fibers. 51

Figure 2.9. The segmented components of the human cochlea model. **(A)** The three scalae presented with blue, light green, and red for scala tympani (ST), scala vestibuli (SV), and scala media (SM), respectively. In addition, the whole cochlear nerves (CN) are indicated by dark green. **(B-D)** The surrounded bone structure of the cochlea is shown gradually with light pink for better visualization. 52

Figure 2.10. Representation of creating a cochlear implant array in COMSOL. **(A)** Using Interpolation Curve for generating a curvature based on a series of coordinates. **(B)** Applying Partition Edges module to model the position of electrode contacts on the curve. **(C)** Converting the curve to the spiral cylinder. **(D)** Adding the sphere shape of electrode contacts to the cylinder model. **(E)** The cochlear implant array separates and deletes the overlapping section. The coordinate system in panel (E) applies to all panels. 55

Figure 2.11. 3D model of two investigated cochlear implant electrode arrays were modeled into scala tympani. **(A)** The lateral array includes 12 electrodes shown in green that are close to the lateral wall of the scala tympani and a larger array length that covers the upper-middle and apical turn of the cochlea. **(B)** The perimodiolar array consists of 22 electrodes shown in orange that are close to the medial wall of the scala tympani and near to the cell bodies of the cochlear nerves. 56

Figure 2.12. Investigating the effect of the ground boundary on extracellular voltage. **(A)** Representation of two ground boundaries, cuboid vs. sphere. **(B)** Showing the external voltage profile along a target neuron with different boundary sizes: cuboid and sphere displayed old and new boundary, respectively. 57

Figure 2.13. The outer boundary of the FE model that was modeled with a sphere and cochlea was placed in the center. 58

Figure 2.14. High-resolution micro-CT scan with an isotropic voxel size of 2.4 µm of a human cochlear nerve. 61

Figure 2.15. Segmentation of human cochlea from high-resolution micro-CT scans with an isotropic voxel size of 15 µm in Amira. Segmented **(A)** scala tympani, **(B)** scala media, and **(C)** scala vestibuli. **(D)** Combined all segmented scalae. (E-F) Segmented the whole cochlear nerves projecting to internal acoustic meatus in two different views. **(G)** segmented three scalae and cochlear nerves. 62

Die approbierte gedruckte Originalversion dieser Dissertation ist an der TU Wien Bibliothek verfügbar.
The approved original version of this doctoral thesis is available in print at TU Wien Bibliothek.
TU Bibliothek WIEN Your knowledge hub

Figure 2.16. Light microscopy image of the peripheral part of ANFs in the healthy human specimen, taken in the Inner Ear Biology lab at the Medical University of Innsbruck. The corresponding segmentation of myelination thickness, peripheral diameter, and fiber diameter was performed in MATLAB using the axon segmentation toolbox. 65

Figure 2.17. A schematic cross-section of a peripheral axon of the cochlear nerve demonstrates myelinated and non-myelinated parts of the fiber. G-ratio can be determined by the ratio of the peripheral axon diameter to the myelinated peripheral fiber diameter (the inner to the outer diameter of a myelinated fiber). 66

Figure 2.18. 3D model of scala tympani includes 12 electrodes of a lateral CI (left) and 22 electrodes of a perimodiolar CI (that is close to the center, right) and the 14 pathways of ANFs in the basal turn. The peripheral axons, soma positions, and central axons of the nerve pathways are represented with colored solid lines, yellow spheres, and colored dashed lines, respectively. For the sake of clarity, all electrode positions are shown as blue spheres, although in calculations, each active electrode is a hemisphere. The axis of modiolus is marked as a red sphere. The Figure and caption are taken from (Heshmat *et al.*, 2020). 67

Figure 2.19. The 3D model of scala tympani including 12 electrodes of the lateral CI (left) and 22 electrodes of the perimodiolar CI (electrodes are close to the center, right) and the three investigated pathways ANFs. The peripheral part, soma position, and central part of the nerve pathways are represented with colored solid lines, yellow spheres, and colored dashed lines, respectively. For the sake of clarity, all electrode positions are shown by dark blue circles. In calculations, however, each active electrode is considered a hemisphere. The axis of the modiolus is marked with a red circle. ... 68

Figure 2.20. Illustration of symmetric and asymmetric pulse shapes in both anodic and cathodic polarity. **(A-C)** represent the asymmetric pulse shapes: monophasic, pseudo-monophasic, and triphasic. **(D)** demonstrates symmetric pulse shape, biphasic commonly used in cochlear implants. .. 71

Figure 2.21. Forced current flow (I) from the stimulating CI channel for monopolar, bipolar, tripolar, and partial tripolar configuration. **(A)** Monopolar and multipolar strategies by considering the adjacent basal channel. **(B)** Multipolar strategies by considering the second basal adjacent channel in perimodiolar CI. **(C)** Multipolar strategies by considering a shorter inter-channel distance in the lateral CI. 72

Figure 2.22. 3D view of the FEM of the human cochlea model with one ANF (in cyan), the electrodes inside the scala vestibuli and scala tympani are shown in blue spheres and the soma in red. 74

Figure 2.23. Cochlear implants inserted in scala tympani (ST) and scala vestibuli (SV). **(A)** Insert a lateral array with 12 electrode contacts in the ST (green) and SV (dark pink). **(B)** Insertion of perimodiolar array with 22 electrode contacts in the ST (green) and SV (dark pink). Noted that each CI array insertion (ST vs. SV) is used separately in calculations. 77

Figure 3.1. Histograms and fit kernel distributions (dashed lines) for peripheral axon diameter of the ANFs in the basal turn for control vs. specimens with determined hearing loss level. **(A)** Profound impairment case (S1). **(B-C)** Moderate impairment specimens (S2 and S3). 80

Figure 3.2. Histograms and fit kernel distributions (dashed lines) for myelination thickness (MT) of the ANFs in the basal turn for control vs. specimens with determined hearing loss level. **(A)** Profound impairment case (S1). **(B-C)** Moderate impairment specimens (S2 & S3). 81

Figure 3.3. Histograms and fit kernel distributions (dashed lines) for PD and MT of the ANFs in the middle turn for control vs. specimens with determined hearing loss level. **(A)** Showing PD distribution of severe impairment case (S1). **(B)** Representing PD distribution of slight impairment case (S2). **(C)** Showing MT distribution of S1 case. **(D)** Indicating MT distribution of S2 case. 82

Die approbierte gedruckte Originalversion dieser Dissertation ist an der TU Wien Bibliothek verfügbar.
The approved original version of this doctoral thesis is available in print at TU Wien Bibliothek.
TU Bibliothek WIEN Your knowledge hub

Figure 3.4. Histograms and fit kernel distributions (dashed lines) for PD and MT of the ANFs in the apical turn for control vs. specimen with determined hearing loss level. **(A)** Showing PD distribution of moderate impairment case (S1). **(B)** Representing MT distribution of mild impairment case (S1). 83

Figure 3.5. Scatter plot for the MT against PD of the ANFs in the basal turn for control and three specimens with determined hearing loss level **(A)** Profound case. **(B-C)** Moderate cases. The best-fit linear regression to each scatterplot is included. 84

Figure 3.6. Scatter plot for the G-ratio against PD of the ANFs in the basal turn for control and three specimens with determined hearing loss level **(A)** Profound case. **(B-C)** Moderate cases. The best-fit linear regression to each scatterplot is included. 85

Figure 3.7. Scatter plot for the G-ratio and MT against PD of the ANFs in the middle turn for control and two specimens with determined hearing loss level **(A-B)** Showing scatter plot for the G-ratio against PD for S1 and S2 cases. **(C-D)** representing scatter plot for the MT against PD for S1 and S2 cases. The best-fit linear regression to each scatterplot is included. 86

Figure 3.8. Scatter plot for the G-ratio and MT against PD of the ANFs in the apical turn for control and a specimen with determined hearing loss level. **(A)** Illustrating scatter plot for the G-ratio against PD. **(B)** Demonstrating scatter plot for the MT against PD. The best-fit linear regression to each scatterplot is included. 87

Figure 3.9. Boxplot of peripheral axon diameter **(A)**, myelination thickness **(B)**, and G-ratio **(C)** for the control and three hearing loss cases (S1, S2, and S3) in the basal turn. The red horizontal line represents the median of the data, the box includes 50 % of the data, and the whiskers reach the highest and lowest values within 95 % of the distribution. Open gray circles represent single values outside 95 % of the distribution. 88

Figure 3.10. Boxplot of peripheral axon diameter **(A)**, myelination thickness **(B)**, and G-ratio **(C)** for the control and two hearing loss cases (S1, S2) in the middle turn. Same configuration as Figure 3.9. 89

Figure 3.11. Boxplot of peripheral axon diameter **(A)**, myelination thickness **(B)**, and G-ratio **(C)** for the control and a hearing loss case (S1) in the apical turn. Same configuration as Figure 3.9. 90

Figure 3.12. Intracellular ANF stimulation simulating synaptic excitation. **(A)** Excitation and AP conduction along the ANF (300 pA, 100 µs). AP is initiated in the first compartment (blue; note the quicker excitation when PD is reduced marked by dashed vertical line; pre-somatic compartments are marked with arrowhead for PD = 0.5 µm and show slow conduction velocity for thin fibers). Conducted APs are shown for all active compartments with a vertical shift indicating the compartment's location. The arrival time of the AP in the soma (orange) increases when PD decreases. Axon's conduction velocity (marked by red line at AP peaks) outmatches all dendritic cases as a consequence of the larger axon diameter (4 µm). **(B)** Membrane voltage in the soma for varied PD demonstrates increased latency when PD is reduced; no AP for PD = 0.3 µm. **(C)** Synaptic threshold current for AP conduction as a function of PD (red) and linear fit (black dashed line). **(D)** Probability of spike conduction across the soma as a function of G-ratio for various PD. In panels A–C, G-ratio = 0.625 (mean value of the control). **(A-B)** were calculated without noise, **(C-D)** with the stochastic model that included current fluctuations in the active membrane. 92

Figure 3.13. ANF responses at dendrite (first compartment), soma, and axon (last compartment) are marked with D, S, and A, respectively. (A) Later APs and larger jitters for synaptic stimuli at threshold (Ith) versus (B) more synchronized responses for synaptic stimuli at $I0$ = 1.2 × threshold are represented for G-ratios = 0.625 and 0.5. While the arrows start at the stimuli onset, the delays represent the time when the membrane voltage reaches 0 mV (shown with gray dashed horizontal lines). Recording point A of simulations corresponds with the axonal terminal from the micro-CT sample (Potrusil et al., 2020). 95

Die approbierte gedruckte Originalversion dieser Dissertation ist an der TU Wien Bibliothek verfügbar.
The approved original version of this doctoral thesis is available in print at TU Wien Bibliothek.
TU Bibliothek Your knowledge hub WIEN

Figure 3.14. Spike pattern comparison between control and hearing loss cases in three cochlear regions. **(A)** Delay (mean values) as a function of PD (20 runs per PD). **(B–E)** Spiking patterns of the investigated specimens (S1 vs. control) based on the number of counted fibers in different cochlear regions, the basal, middle, and apical, stimulated with 300 pA. The horizontal and vertical green lines in panel B represent the membrane voltage value at 0 mV and the corresponding time (delay) at soma after the stimulus onset, respectively. The color code in panel **(B)** applies to **(C–E)**. Recording point at axonal terminal. The x-axis of the right panel in panel E applies to all spike pattern graphs. 97

Figure 3.15. Membrane voltage along ANF basal7 (137°, G-ratio = 0.625) as a response of intra- and extracellular stimulation. **(A)** Membrane voltage for PD = 2 vs. 0.5 µm at pulse offset (0.1 ms) and 1 ms after intracellular stimulus onset with a pulse amplitude at threshold (Ith) and 1.2 × threshold. Right panel: AP propagation along the ANF with PD = 2 µm at threshold. Each line shows the membrane voltage at a fixed time. The green and red lines represent the times corresponding to stimulus offset and the first achievement of the AP peak, respectively. **(B)** Same configuration for extracellular stimulation of lateral electrode EL5 and **(C)** perimodiolar electrode CA11. Vertical dashed pink, cyan, and green lines represent the positions of the peripheral terminal, soma, and axonal terminal, respectively. Arrowheads indicate that the firing starts at presoma. 99

Figure 3.16. Demonstrates the electrode distances (upper panel) and the inverse relationship of extracellular voltage (lower panel) along the fiber of five target neurons in blue and red, which were stimulated with perimodiolar and lateral CI systems, respectively. 100

Figure 3.17. Excitation thresholds of TNs and co-stimulated ANFs along the fiber angles calculated for ten electrodes. The electrode thresholds for three PD of 2, 0.5, and 0 µm (without peripheral axon) is demonstrated in the upper, middle, and lower panel, respectively. Note that all investigated ANFs are considered with the same peripheral axon, soma, and central axon diameters at each level of calculation. Vertical dashed lines indicate the angle of electrodes, filled symbols TN, unfilled co-stimulated neurons (blue for perimodiolar, red for lateral CI system). 101

Figure 3.18. Threshold profiles of three TNs for perimodiolar CI. Thresholds are shown for four stimulation configurations: MP, BP, TP, and PTP with **(A)** monophasic, **(B)** pseudo-monophasic, **(C)** triphasic, and **(D)** biphasic pulse. Blue, green, and red colors represent B11, B7, and M9, respectively, in all panels. ANFs status based on degeneration levels are indicated with circle, rectangle, triangle, cross, diamond, and plus shapes for AS1, AS2, AS3, AS4, AS5, and AS6, respectively. Black dotted lines represent the ANO/CAT = 1. Legend from top-left panel A applies to all panels. 107

Figure 3.19. Comparison of the transmembrane voltage just above the threshold. **(A)** Comparison between excitation of the initiation sites for both pulse shapes. During the first cathodic phase, the strongest deviations from the resting voltage appear in a central process region close to the soma. Hyperpolarization of the monophasic pulse (55mV) is almost three times larger than for the pseudo-monophasic pulse (20mV). In monophasic stimulation, the central process compartment with the strongest hyperpolarization elicits the spike by break excitation (thick black line), and this spike is conducted in both directions (thin black lines). Break excitation is an overshoot of membrane voltage in the direction of the resting potential after a strong hyperpolarization. This overshooting trend is strongly supported by the weak second phase of the pseudo-monophasic pulse (gray lines). Consequently, the pseudo-monophasic stimulation needs less hyperpolarization during the first phase. **(B)** Degeneration status AS6, without peripheral process, when monophasic pulse is applied. **(C)** Excitation of fiber with healthy status for monophasic pulse. 108

Figure 3.20. Threshold profiles of three TNs for lateral CI. Layout as in Figure 3.18. 110

Figure 3.21. Polarity ratios for different degeneration levels stimulated with the monophasic pulse. Threshold ratios are shown for the TNs B11, B7, and M9 with color-coded degeneration levels **(A)** monopolar (MP), **(B)** bipolar (BP), **(C)** tripolar (TP), **(D)** partial tripolar (PTP) stimulation strategies. The horizontal dotted lines indicate the polarity ratio ANO/CAT = 1. 112

Die approbierte gedruckte Originalversion dieser Dissertation ist an der TU Wien Bibliothek verfügbar.
The approved original version of this doctoral thesis is available in print at TU Wien Bibliothek.
TU Bibliothek Your knowledge hub WIEN

Figure 3.22. Polarity ratios for different degeneration levels stimulated with the pseudo-monophasic pulse. Layout as in Figure 3.21. 113

Figure 3.23. Polarity ratios for different degeneration levels stimulated with the triphasic pulse. Layout as in Figure 3.21. 114

Figure 3.24. Polarity ratios for different degeneration levels stimulated with the biphasic pulse. Layout as in Figure 3.21. 115

Figure 3.25. AP initiation sites at ANO and CAT thresholds for monophasic pulse in four stimulation strategies **(A)** MP, **(B)** BP, **(C)** TP, **(D)** PTP. The TNs: B11, B7, and M9 are demonstrated with star, rectangle, and circle, respectively. In addition, the lateral and perimodiolar CI systems are indicated with red and blue colors. Pulse polarity is identified by filled (ANO) and unfilled shapes (CAT). Gray dashed lines show the soma positions. 116

Figure 3.26. AP initiation sites at ANO and CAT thresholds for pseudo-monophasic pulse in four stimulation strategies **(A)** MP, **(B)** BP, **(C)** TP, **(D)** PTP. Layout as in Figure 3.25. 117

Figure 3.27. AP initiation sites at ANO and CAT thresholds for triphasic pulse in four stimulation strategies **(A)** MP, **(B)** BP, **(C)** TP, **(D)** PTP. Layout as in Figure 3.25. 118

Figure 3.28. AP initiation sites at ANO and CAT thresholds for biphasic pulse in four stimulation strategies **(A)** MP, **(B)** BP, **(C)** TP, **(D)** PTP. Layout as in Figure 3.25. 118

Figure 3.29. Threshold of three TNs for perimodiolar CI for four different pulse types and three multipolar strategies (BP+1, TP+1, and PTP+1) by changing the distance between channels of both CI systems. **(A)** Monophasic, **(B)** pseudo-monophasic, **(C)** triphasic, and **(D)** biphasic pulse. Layout as in Figure 3.18. 120

Figure 3.30. Threshold of three TNs for lateral CI for four different pulse types and three multipolar strategies (BP-V1, TP-V1, and PTP-V1) by changing the distance between channels of both CI systems. **(A)** Monophasic, **(B)** pseudo-monophasic, **(C)** triphasic, and **(D)** biphasic pulse. Layout as in Figure 3.18. 121

Figure 3.31. Polarity ratios for different degeneration levels stimulated with the monophasic pulse by changing the distance between channels of both CI systems. **(A)** bipolar (BP), **(B)** tripolar (TP), and **(C)** partial tripolar (PTP) stimulation strategies. The horizontal dotted lines show the polarity ratio is equal to one (ANO/CAT = 1). 122

Figure 3.32. Polarity ratios for different degeneration levels stimulated with the pseudo-monophasic pulse by changing the distance between channels of both CI systems. Layout as in Figure 3.31. 123

Figure 3.33. Polarity ratios for different degeneration levels stimulated with the triphasic pulse by changing the distance between channels of both CI systems. Layout as in Figure 3.31. 124

Figure 3.34. Polarity ratios for different degeneration levels stimulated with the biphasic pulse by changing the distance between channels of both CI systems. Layout as in Figure 3.31. 125

Figure 3.35. Threshold stimulation of TN B12 for intact **(A)**, intermediate **(B)**, and progressive case **(C)** for the scala tympani electrode (left) and the scala vestibuli electrodes (right). In each panel, traces represent the membrane voltage over time in selected compartments for ANO (left) and CAT (right) pulses. The green, blue, red, and violet lines represent peripheral nodes, pre-somatic compartments, soma, and central nodes, respectively. Corresponding threshold values are displayed on the top of each panel. The bottom part in panel **(A)** of CAT pulse shows the extracellular potential Ve for CAT along the first part of the TN (blue line), the soma positions (black spheres), the largest (negative) Ve and Ve of soma (horizontal black dashed lines); the vertical black dashed lines indicate the positions of nodes of Ranvier and the blue curves show the distances of the compartment centers to the electrodes. The golden curves indicate the spike initiation compartments. 127

Die approbierte gedruckte Originalversion dieser Dissertation ist an der TU Wien Bibliothek verfügbar.
The approved original version of this doctoral thesis is available in print at TU Wien Bibliothek.
TU Bibliothek Your knowledge hub WIEN

Figure 3.36. Threshold stimulation of TN=B7 for intact **(A)**, intermediate **(B)**, and progressive **(C)** for the scala tympani electrode (left) and the scala vestibuli electrodes (right). Layout as in Figure 3.34. 128

Figure 3.37. Threshold stimulation of TN=B2 for intact **(A)**, intermediate **(B)**, and progressive **(C)** for the scala tympani electrode (left) and the scala vestibuli electrodes (right). Layout as in Figure 3.34. 129

Figure 3.38. Threshold stimulation of TN=M7 for intact **(A)**, intermediate **(B)**, and progressive **(C)** for the scala tympani electrode (left) and the scala vestibuli electrodes (right). Layout as in Figure 3.34. 130

Figure 3.39. Threshold stimulation of TN=M4 for intact **(A)**, intermediate **(B)**, and progressive **(C)** for the scala tympani electrode (left) and the scala vestibuli electrodes (right). Layout as in Figure 3.34. 131

Figure 3.40. Threshold stimulation of TN=M1 for intact **(A)**, intermediate **(B)**, and progressive **(C)** for the scala tympani electrode (left) and the scala vestibuli electrodes (right). Layout as in Figure 3.31. 132

Figure 3.41. Threshold stimulation of intact target fibers, B12 (top), B2(middle), and M1(bottom) for the scala tympani electrodes (left) and scala vestibuli electrodes (right). In each panel, upper traces represent the membrane voltage over time in selected compartments for CAT pulse. The green, blue, red, violet, black (only in A), and orange lines represent peripheral nodes, pre-somatic compartments, soma, central nodes, internodes, and AP initiation sites, respectively. Corresponding threshold values are displayed on the top. The lower part in each panel shows the extracellular potential (Ve) distribution for CAT along the peripheral process of the ANFs (blue line) and the soma position (black spheres), the soma and largest (negative) Ve (horizontal grey dashed lines); the vertical grey dashed lines indicate the positions of nodes of Ranvier; a schematic illustration between the blue and the green curves shows the compartments with internodes in grey, nodes in black and soma in red circle. The green curves show the distance to the electrode center along the peripheral process; the corresponding AF (light blue curve, $Iext/C$) is reproduced with its zero line (horizontal grey dashed line); the stars in color coded manner represent the AP starting node in orange, the possible winner in the right and left neighborhoods in purple and light blue, respectively; the last colored traces show the corresponding AF (solid line) and the axial voltage changes, $dVmdt$, (dashed line) of the same compartments during the stimulus time with the same color code as in the stars: AP initiation compartment in orange, right and left possible winners in purple and light blue, respectively. 135

Figure 3.42. Threshold stimulation of intermediate and progressive degeneration target fibers top and bottom of each panels, respectively, for B12 **(A)**, B2 **(B)**, and M1 **(C)** for the scala tympani electrodes (left) and scala vestibuli electrodes (right). In each panel, traces represent the membrane voltage over time in selected compartments for ANO and CAT pulses. The green, blue, red, violet, and orange lines represent peripheral nodes (intermediate degeneration), pre-somatic compartments (intermediate degeneration), soma, central nodes, and AP initiation sites, respectively. Corresponding threshold values are displayed on the top for both polarity. The middle traces represent the corresponding AF (light blue curve, $Iext/C$) with its zero line (horizontal grey dashed line); the stars in color coded manner represent the AP starting node in orange and the first AP initiation site in green. 137

Figure 3.43. (A) ANO/CAT threshold values for six color coded target fibers **(B)** The AP initiation sites for the strong amplitudes (progressive degeneration thresholds) of both ANO and CAT pulses on the intact, intermediate, and progressive degenerated ANFs are displayed for the six target fibers for scala tympani electrodes (blue) vs. scala vestibuli (red). 139

Figure 3.44. Excitation profile of B14. **(A)** Fiber distance to the stimulating electrodes. **(B)** the extracellular voltage Ve versus length of the fiber in ST and SV are shown with blue and green curves,

Die approbierte gedruckte Originalversion dieser Dissertation ist an der TU Wien Bibliothek verfügbar.
The approved original version of this doctoral thesis is available in print at TU Wien Bibliothek.
TU Bibliothek Your knowledge hub WIEN

respectively. **(C)** Threshold profiles of B14. The intact (healthy) ANF is displayed as circles, and the degenerated ANF is indicated with diamonds and triangles for severe and progressive cases. The blue and green-filled symbols show thresholds for ST and SV CIs. The black and red unfilled symbols represent biphasic and pseudo-monophasic pulse shapes. Black dashed lines represent the ANO/CAT=1. 142

Figure 3.45. Polarity ratios for the perimodiolar (left) and lateral (right) CI arrays for intact and two degeneration levels for ST and SV active electrodes. **(A)** Biphasic pulse and **(B)** pseudo-monophasic pulses stimulated both CI arrays within ST and SV. Threshold ratios are shown for B14. The horizontal dotted lines indicate the polarity ratio ANO/CAT = 1. 143

Figure 3.46. Excitation profile of B5 for perimodiolar CI (left) and lateral CI (right). Layout as in Figure 3.44. 145

Figure 3.47. Polarity ratios are demonstrated for B5. Layout as in Figure 3.45. 146

Figure 3.48. Threshold profiles of B3 for perimodiolar CI (left) and lateral CI (right). Layout as in Figure 3.44. 147

Figure 3.49. Polarity ratios are shown for B3. Layout as in Figure 3.45. 149

Figure 3.50. Threshold profiles of M9 for perimodiolar CI (left) and lateral CI (right). Layout as in Figure 3.44. 150

Figure 3.51. Polarity ratios are shown for M9. Layout as in Figure 3.45. 152

Die approbierte gedruckte Originalversion dieser Dissertation ist an der TU Wien Bibliothek verfügbar.
The approved original version of this doctoral thesis is available in print at TU Wien Bibliothek.
TU Bibliothek Your knowledge hub WIEN

List of Tables

Table 1.1. The degree and classification of hearing loss 18

Table 2.1. Electrical key parameters of the HH model. 38

Table 2.2. Summary of all nerve fiber bundles along the cochlea in respect to their angle and frequency (Potrusil et al., 2020). All angles are measured from the round window concerning the modiolus axis to the terminal of ANFs. 53

Table 2.3. Electrical conductivities of the human inner ear components were used in the FEM..... 58

Table 2.4. Specimen details on hearing deficits as provided by the Innsbruck Medical University, Department of Otorhinolaryngology, Laboratory for Inner Ear Biology..... 64

Table 2.5. Angles of the investigated electrodes and the corresponding target neurons (TN) were measured from the round window with respect to the modiolus axis. 66

Table 2.6. Angles of the investigated electrodes and the corresponding target neurons (TN) measured from the round window with respect to the modiolus axis; compare Figure 2.19. 69

Table 2.7. Six ANFs statuses based on degeneration levels of peripheral diameter. 69

Table 2.8. Names and angles of the investigated auditory nerve fibers as target neurons (TN) were measured from the round window with respect to the modiolus axis. 73

Table 2.9. Standard parameters for human cochlear neurons. 75

Table 2.10. Names, frequencies, and angles of the investigated auditory nerve fibers as target neurons (TN) were measured from the round window concerning the modiolus axis. 76

Table 2.11. Three ANFs statuses based on degeneration levels of peripheral axon diameter. 77

Table 3.1. Mean delay $\pm$ STD (jitter) for the counted fibers in each specimen. For the calculation an intracellular stimulus of 300 pA and a various run number, based on each fiber group quantity, are chosen. 96

Table 3.2. Thresholds of TNs and the co-stimulated neurons for ten investigated electrodes for the lateral and perimodiolar electrode array systems. 104

Table 3.3. Excitation currents of TNs in both polarities for different degeneration levels for investigated scala tympani (ST) and scala vestibuli (SV) electrodes for perimodiolar array system with biphasic and pseudo-monophasic pulses. 153

Table 3.4. Excitation currents of TNs in both polarities for different degeneration levels for investigated scala tympani (ST) and scala vestibuli (SV) electrodes for lateral array system with biphasic and pseudo-monophasic pulses. 154

Die approbierte gedruckte Originalversion dieser Dissertation ist an der TU Wien Bibliothek verfügbar.
The approved original version of this doctoral thesis is available in print at TU Wien Bibliothek.
TU Bibliothek Your knowledge hub WIEN

Abbreviations

AP	Action Potential
ANO	Anodic
ANF	Auditory Nerve Fiber
BP	Bipolar
CAT	Cathodic
CF	Characteristic Frequency
CI	Cochlear Implant
CN	Cochlear Nerve
dB	Decibel
EABR	Evoked Auditory Brainstem Response
ECAP	Evoked Compound Action Potential
FEM	Finite Element Method
GR	G-ratio
HH	Hodgkin and Huxley
IHC	Inner Hair Cell
LW	Lateral Wall
MP	Monopolar
MT	Myelination Thickness
ODE	Ordinary Differential Equation
OHC	Outer Hair Cell
PTP	Partial Tripolar
PM	Perimodiolar
PD	Peripheral axon Diameter
PPS	Pulse number Per Second
SM	Scala Media
ST	Scala Tympani
SV	Scala Vestibuli
SNHL	Sensorineural Hearing Loss
SPL	Sound Pressure Level
SGN	Spiral Ganglion Neuron
SD	Standard Deviation
TN	Target Neuron
3D	Three Dimensional
TP	Tripolar

Die approbierte gedruckte Originalversion dieser Dissertation ist an der TU Wien Bibliothek verfügbar.
The approved original version of this doctoral thesis is available in print at TU Wien Bibliothek.
TU WIEN Bibliothek Your knowledge hub

Die approbierte gedruckte Originalversion dieser Dissertation ist an der TU Wien Bibliothek verfügbar.
The approved original version of this doctoral thesis is available in print at TU Wien Bibliothek.
TU Bibliothek Your knowledge hub WIEN

Chapter 1

Introduction

This chapter provides the basic knowledge required for a better understanding of this study. The first section (1.1) provides comprehension of the anatomical and physiological features of the human ear. The structure, function, innervation of the human auditory system and human hearing spectrum, as well as types, degrees, and causes of hearing loss, are described in section 1.2. In addition, the most typical and usually hearing loss type in humans is explained. The following section (1.3) presents how hearing restoration happens with cochlear implants (CIs).

Additionally, CI structure, function, and types are described. Moreover, section 1.4 gives some background on two different implantations, scala tympani vs. scala vestibuli. In addition, an important question arises that when and why scala vestibuli implantation is needed. Finally, in section 1.5, the limitation of recent clinical and computational studies in the CI community is discussed, consequently addressing the aims of this study.

1.1 Anatomy and physiology of the human auditory system

Hearing is one of the sixth senses that has a profound impact on people's daily life. Hearing allows humans to communicate, learn and discover new aspects of their lives and plays an essential role in their life. The ears are paired hearing organs that begin to form in the sixth week of pregnancy. Despite the tiny size of the ear, it performs a significant role in human beings. The sophisticated structure of the ear provides a sense of hearing by collecting and transferring the sound waves and converting mechanical vibrations into neural impulses, electric signals.

The human auditory system has an individual development chain. Firstly, the development of structural components occurs, such as cochlea development perfectly form by 15 weeks of pregnancy; however, it becomes functional by 20 weeks. Also, the hearing system becomes complete and functional when the cell bodies of auditory neurons connect hair cells to the brainstem, which happens around 25 to 29 weeks of pregnancy (Graven and Browne, 2008).

The human auditory system is divided into three main sections: external ear, middle ear, and inner ear (Figure 1.1). The sound transmission is performed with external and middle ears, and the inner ear is composed of two organs: the cochlea and the vestibular systems. The cochlea is responsible for hearing, and balance is achieved with the vestibular system.

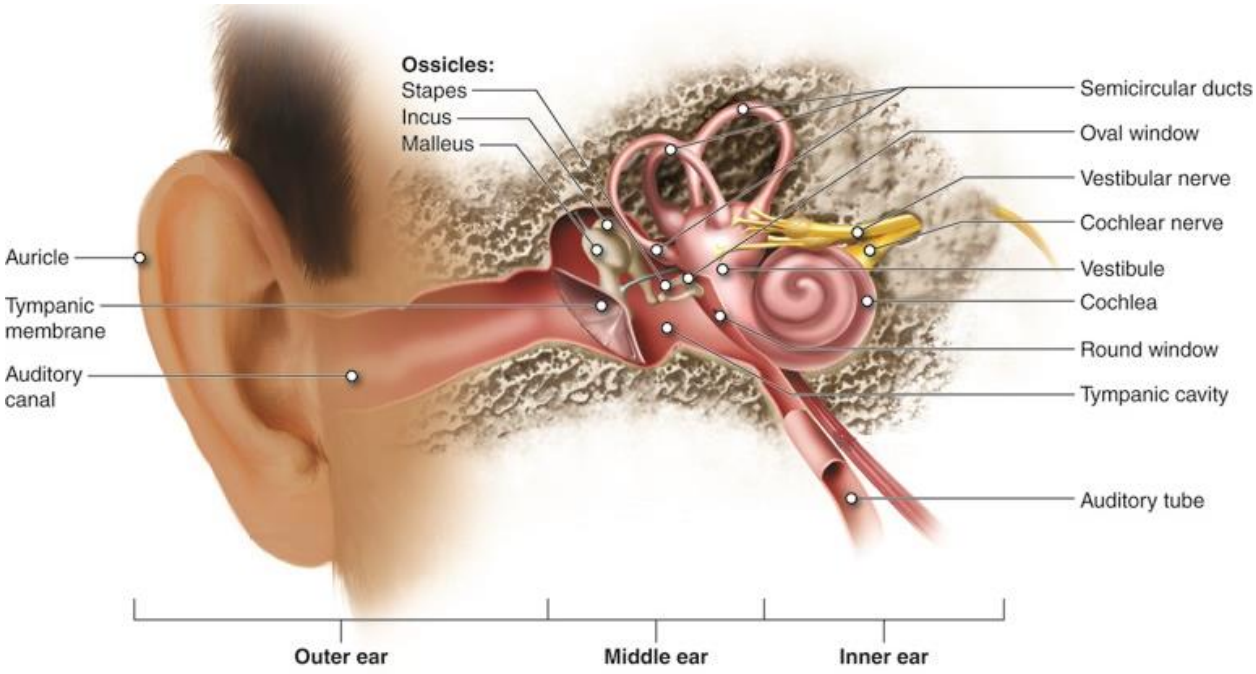

Figure 1.1. The anatomy of the human ear. It consists of three main parts: the outer ear, the middle ear, and the inner ear. The Figure is taken (Lumen Learning, 2021).

1.1.1 The Outer Ear

The external ear involves the pinna, auricle, and external auditory canal. The pinna is the visible part of the ear made of cartilage that collects sound waves from the environment and helps localize the sound waves by funneling them towards the external canal. The external auditory canal, the ear canal, provides a pathway about 3 cm in length and 7 mm in diameter from the external ear to the middle ear. The external auditory canal directs sound waves to the end of the canal, where the tympanic membrane, the eardrum, is located. The ear canal structure provides suitable humidity and temperature levels to preserve the elasticity features of the tympanic membrane. In addition, earwax and hairs of the ear canal protect the inner parts against small foreign particles, insects, and infections that may damage the tympanic membrane.

When the sound waves arrive at the end of the ear canal, they hit the tympanic membrane. The tympanic membrane separates the outer and middle ear and has an oval shape of about 10 mm

Die approbierte gedruckte Originalversion dieser Dissertation ist an der TU Wien Bibliothek verfügbar.
The approved original version of this doctoral thesis is available in print at TU Wien Bibliothek.
TU Bibliothek Your knowledge hub WIEN

in height and 8 mm in width. The function of the tympanic membrane is to convert sound waves into mechanical energy, vibrations.

1.1.2 The Middle Ear

The middle ear is a small-scale air-filled chamber. The sound transmission happens appropriately when the air pressure is equalized between the middle and external ears; hence, the eustachian tube joins the middle ear to the back of the nose and throat to equalize the air pressure in the middle ear.

The lateral wall of the middle ear is attached to the tympanic membrane, and the medial wall adjoins to the inner ear that conducts and transmits the sound to the inner ear by the ossicular chain, which includes three tiny bones, malleus, incus, and stapes (also known as the hammer, anvil, and stirrup, respectively). These three tiny bones act as an amplifier of force to transfer vibrations to the inner ear. Since the middle ear is the air-filled chamber, it enables the sophisticated mechanism of transferring sound and transmitting vibration to the fluid-filled chamber of the cochlea. Another role of the middle ear is protecting the cochlea against loud sounds or noises that may be detrimental to inner ear structures. It reduces, however, with some delay, the magnitude of the vibrations in the fluid system by an involuntary contraction of the tensor tympani and the stapedius muscles.

1.1.3 The Inner Ear

Two essential systems, the cochlear and the vestibular, are housed in the inner ear that provides the sense of hearing and balance. The cochlea has a sophisticated three-dimensional bony spiral-shaped fluid-filled cavity in the bony labyrinth and is responsible for sound perception. In humans, the cochlea is coiled about two and three-fourth (Hardy, 1938) to three turns (Tian, Linthicum and Fayad, 2006) around a spongy bone pillar called the modiolus and enclosed by compact bone called the otic capsule that is rich in the mineral increasing the stiffness of the bony labyrinth (Bast, 1942). Hence, this stiff bony structure reflects received vibrations into the cochlear fluids and prevents absorption by the temporal bone. Due to the dissimilarity of the cochlea shapes and sizes, the human cochlea is individual. A study on 73 human inner ears reported that the length of the outer cochlear wall varied from 38.6 to 45.6 mm, with a mean length of 42.0 mm, while the basal turn represented 53% of the entire cochlea length and ranged from 20.3 to 24.3 mm (Erixon et al., 2009).

The cochlea consists of three fluid-filled chambers, scalae that differ in volume size (Figure 1.2). The largest and most inferior one is called scala tympani (ST), placed below the osseous

Die approbierte gedruckte Originalversion dieser Dissertation ist an der TU Wien Bibliothek verfügbar.
The approved original version of this doctoral thesis is available in print at TU Wien Bibliothek.
TU Bibliothek Your knowledge hub WIEN

spiral lamina that makes the lowest scala. The second-largest and superior scala is named scala vestibuli (SV), which is located above the osseous spiral lamina. Lastly, the smallest chamber is the scala media (SM), also called the cochlear duct, located between ST and SV and houses the organ of Corti (Figure 1.2).

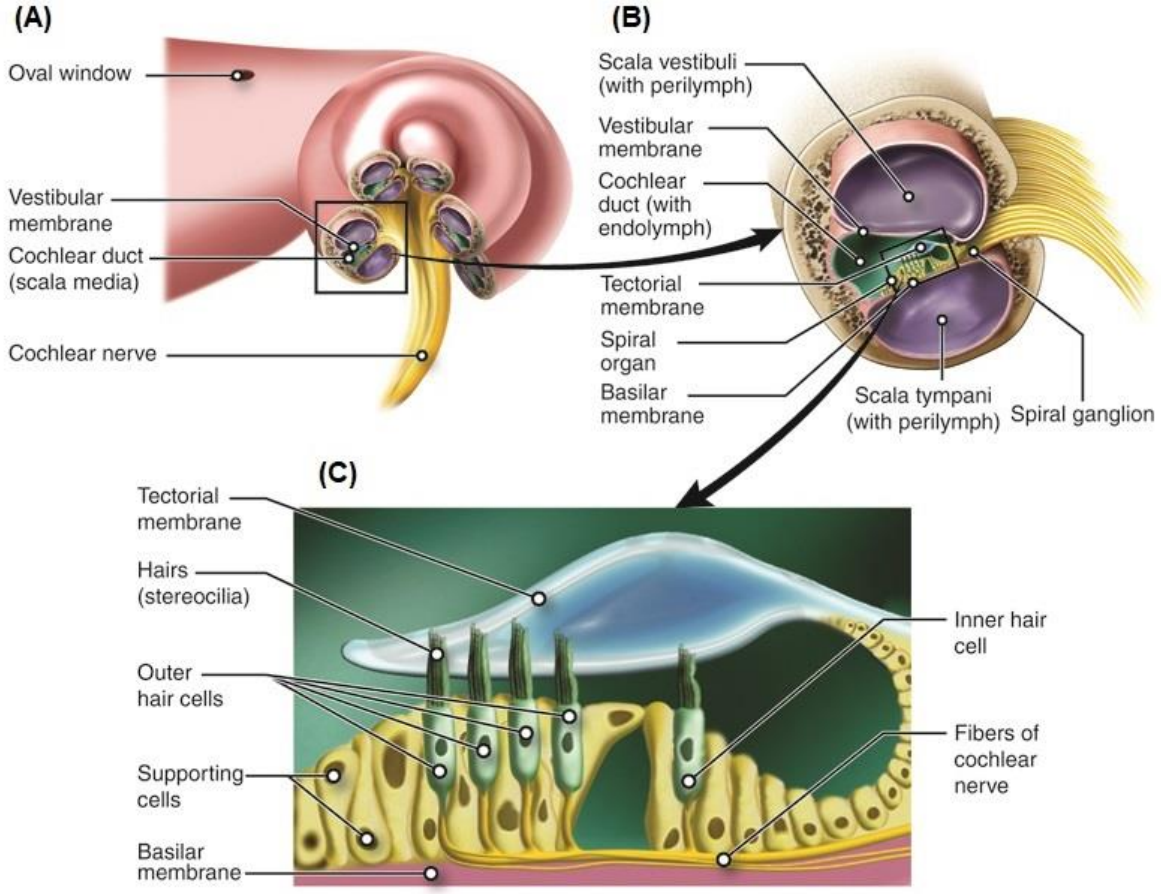

Figure 1.2. Anatomy of the human cochlea. **(A)** Snail shape of the cochlea. **(B)** Cross-section of the cochlea consists of three chambers and cochlear nerves. **(C)** Schematic representation of organ of Corti structure including hair cells. The stereocilia lengths are not in scale; only the longest stereocilia of the outer hair cells are in contact with the tectorial membrane. The Figure is taken (Lumen Learning, 2021).

The ST and SV begin from the initial part of the basal turn distinguished by the round and oval windows, respectively, and continue up to the apex of the cochlea called helicotrema, where they join together and allow fluid to flow between both scalae. The ST and SV are filled with the same fluid called perilymph, possessing low potassium and high sodium concentrations.

On the other hand, SM is filled with endolymph with inversed ion concentrations compared to the ST and SV (low sodium and high potassium). These ions distributions are required for auditory transduction by generating an electrochemical gradient in the cochlea (Wangemann, 2006). These three scalae are separated by membranes. The vestibular membrane, also known

Die approbierte gedruckte Originalversion dieser Dissertation ist an der TU Wien Bibliothek verfügbar.
The approved original version of this doctoral thesis is available in print at TU Wien Bibliothek.
TU Bibliothek Your knowledge hub WIEN

as Reissner's membrane, detaches the SV from the SM (Figure 1.2B). (Wangemann and Schacht, 1996; Davis and Liu, 2011). The Reissner's membrane comprises two different cells. First, an epithelial-cell sheet in the SM side confronts the endolymph, and second, a mesothelial cell encounters the perilymph of the SV. The Reissner's membrane structure acts as a barrier between two different fluids with different ion concentrations of SM and SV, and the membrane is crucial for hearing to keep the endocochlear potential (+80 mV) in the cochlear duct (Rask-Andersen et al., 2012).

The basilar membrane separates ST from SM. Superior of the basilar membrane, the organ of Corti is located. The organ of Corti comprises sensory cells known as several supporting cells, the inner and outer hair cells (Figure 1.2C) (Spoendlin and Schrott, 1990). The hair cells react to the mechanical movements of the basilar membrane because of their mechanosensing structure. Two types of mechanotransduction sensory cells in the organ of Corti are found and organized in one row of inner hair cells (IHCs) and usually three-row of outer hair cells (OHCs). Humans have nearly 12000 OHC and 3400 IHCs (Rask-Andersen et al., 2012).

The IHCs and OHCs play different roles in the human hearing system. IHCs are known as the primary afferent sensory cells of hearing, and each IHC holds about 50-70 stereocilia at the basal end and 100 in the apical turn (Wright, 1984; Glueckert et al., 2005). Peripheral auditory nerve fibers (ANFs) are connected to IHCs to deliver signals to the brainstem called afferent fibers. IHCs transform mechanical impulses into electrical signals by generating action potentials (APs) in the cochlear neurons that ultimately cause sound perception (Dallos, 1992).

On the other hand, OHCs are connected to the fibers that do not send information to the brainstem but bring feedback from the brain to the peripheral of ANFs known as efferent fibers. The efferent fibers that influence OHCs are presynaptic, possibly affecting motility (Dallos, 1992). OHCs play an amplifying role and have their own characteristics to adjust the mechanical properties of the basilar membrane, such as varying stiffness and length. Due to the connection of OHCs to the tectorial membrane, OHCs amplify small movements in the basilar membrane that allow IHCs to detect and convert this movement to electrical signals (Dallos, 1992).

Hair cells are operative components of the basilar membrane and consist of a cell body (nucleus) and stereocilia, protein filament located on top of the hair cells (Figure 1.3A). The stereocilia of each hair cell are connected through tip links and lateral links. Due to the potassium concentration gradient between the cell body and cortilymph, the transmembrane voltages of IHC and OHC are about -40 mV and -70 mV, respectively (Rattay et al., 1998).

Die approbierte gedruckte Originalversion dieser Dissertation ist an der TU Wien Bibliothek verfügbar.
The approved original version of this doctoral thesis is available in print at TU Wien Bibliothek.
TU WIEN Bibliothek Your knowledge hub

The apical part of the hair cell with the stereocilia enters the endolymphatic fluid, identified by its high electrical potential (+85 mV) and high potassium concentration. When sound waves arrive, that causes deflection of stereocilia of IHCs, resulting in potassium ions flowing from the endolymph into the IHCs. Displacement of stereocilia toward the lateral side of the cochlea leads to an enhancement of transduction channel open probability, inducing depolarization of the receptor potential. In contrast, the movement of stereocilia to the medial side decreases the transduction channel open probability and causes hyperpolarization (Figure 1.3A). Potassium currents of depolarization lead to open voltage-gated calcium channels and flow calcium into the cell, inducing releasing vesicles containing neurotransmitters (glutamate) at the hair cell synapse. Diffusion of neurotransmitters from the presynaptic terminal to the postsynaptic terminal, the initial section part of the peripheral part of ANFs, generating an AP (Rattay et al., 1998; Fettiplace and Kim, 2014).

Deflection of the stereocilia changes the probability of the cell's transduction channels opening and closing and is responsible for the voltage fluctuations observed within IHCs. In the active zones at the base of the IHC (Figure 1.3B), sufficient depolarization of the receptor potential results in calcium provoked neurotransmitter release. Changing membrane potential as low as 0.1 mV may cause neurotransmitter release and elicit a spike in ANF. In addition, if releasing neurotransmitter happen adequately, it depolarizes proximal ANFs, resulting in the generation of APs and propagating toward the auditory brainstem (Gebeshuber and Rattay, 2001).

Die approbierte gedruckte Originalversion dieser Dissertation ist an der TU Wien Bibliothek verfügbar.
The approved original version of this doctoral thesis is available in print at TU Wien Bibliothek.
TU Bibliothek Your knowledge hub WIEN

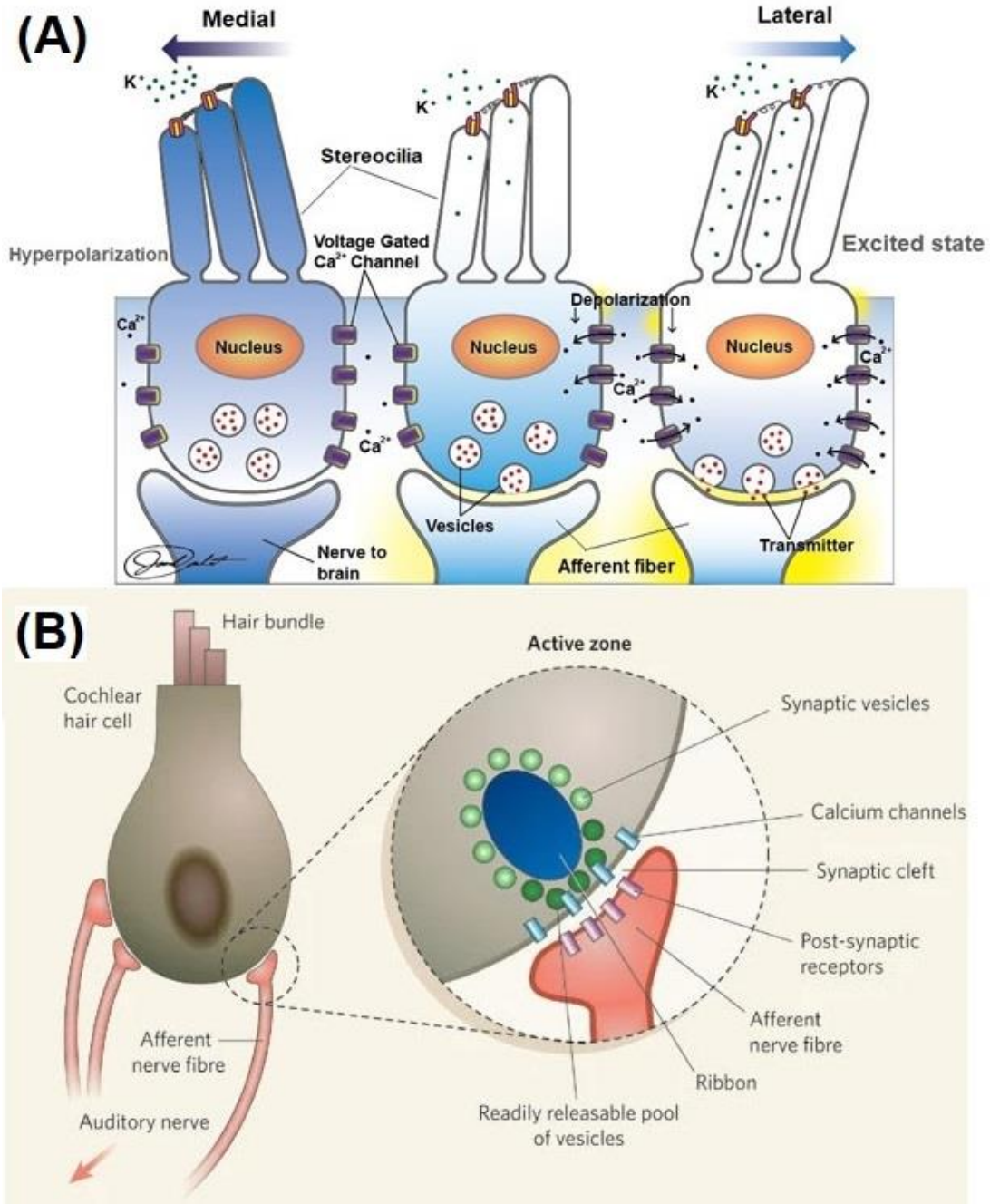

Figure 1.3. Illustration of inner hair cells. **(A)** Schematic of mechanoelectrical transduction operated by inner hair cells. **(B)** Representation of hair bundle (stereocilia) and afferent nerve fiber (left) and more detail in the right part shows synaptic vesicles (small green circles) are gathered in ribbon (blue ellipse) synapses in several release zones at the lower part and the voltage-gated calcium channels (light blue cylinders). The Figure adapted from (Parsons, 2006; BIO 264, BYU IDAHO).

Die approbierte gedruckte Originalversion dieser Dissertation ist an der TU Wien Bibliothek verfügbar.
The approved original version of this doctoral thesis is available in print at TU Wien Bibliothek.
TU Bibliothek Your knowledge hub WIEN

1.2 Human auditory nerve

The vestibulocochlear nerve, known as the eighth cranial nerve (CN VIII), contributes unique sensory innervation to the inner ear and provides a hearing and equilibrium sense for humans and other mammals. The vestibulocochlear nerve instantly separates into two cochlear and vestibular nerves in the internal acoustic meatus, which is a bony canal in the petrous part of the temporal bone. The cochlear (auditory) nerves are sensory nerves that transfer auditory information from the inner ear, the cochlea, to the cochlear nuclei, within the brainstem. Sensory hair cells in the cochlea convert sound into neural signals conducted along the ANFs by two types of spiral ganglion neurons (SGNs), type I and II, located in Rosenthal's canal.

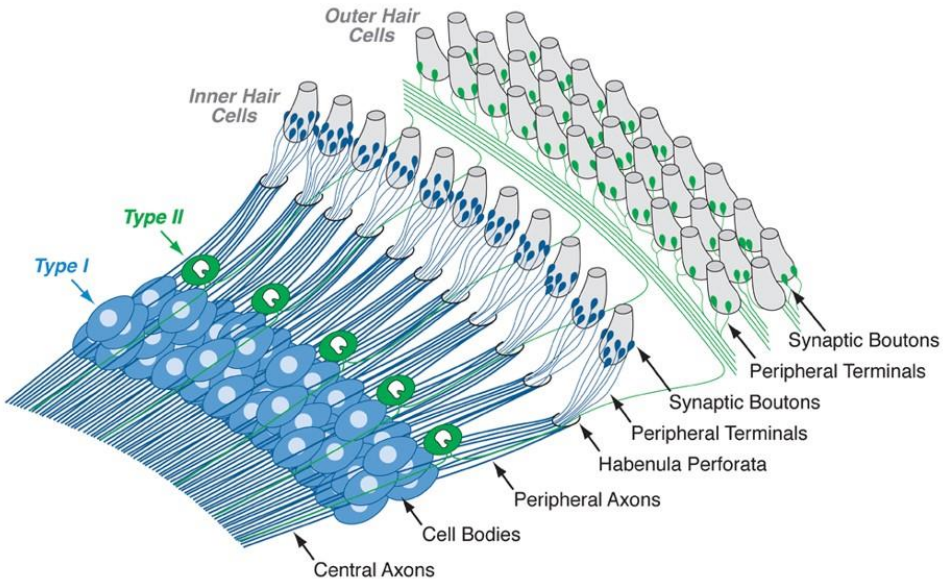

Figure 1.4. Configurations of auditory nerve fibers innervation with spiral ganglion neurons type I (blue) and II (green). There are three rows of the outer hair cells vs. one row of the inner hair cells performing the innervation system. The Figure taken from (Liberman, 2017).

The vast majority, about 95% of SGNs, are bipolar type I cells that connect IHCs via myelinated peripheral axons to large somata (cell bodies) and extend via myelinated central axons to the cochlear nuclei in the brainstem (Figure 1.4) (Ota and Kimura, 1980). In addition, humans with normal hearing status have about 35000 to 40000 ANFs, which means 10-15 ANFs connect each IHC (Nadol, 1983; Viana et al., 2015; Liberman, 2020).

On the other hand, type II includes around 5% of SGNs and innervates various OHCs (Figure 1.4) (Ota and Kimura, 1980; Marrs and Spirou, 2012). The ANFs of type II cells are non-myelinated, and their somata are frequently detected in the periphery of Rosenthal's canal close to the osseous spiral lamina. These smaller non-myelinated type II cells transmit APs from the

Die approbierte gedruckte Originalversion dieser Dissertation ist an der TU Wien Bibliothek verfügbar.
The approved original version of this doctoral thesis is available in print at TU Wien Bibliothek.
TU Bibliothek Your knowledge hub WIEN

OHCs (Spoendlin, 1985). In addition, the function of type II cells is not entirely discovered; however, it is assumed that they act as a cochlear amplifier to increase sound transduction (Jagger and Housley, 2003; Ashmore et al., 2010).

Furthermore, the somata of type I cells include pre- and post-somatic regions that are non-myelinated in humans, whereas in non-primate mammals, they are densely myelinated (Thomsen, 1967; Spoendlin, 1972; Ota and Kimura, 1980; Arnold, 1987; Spoendlin and Schrott, 1989; Xing et al., 2012); In contrast, the peripheral and central axons of ANFs of type I are myelinated by Schwann cells (Figure 1.5) (Locher et al., 2014).

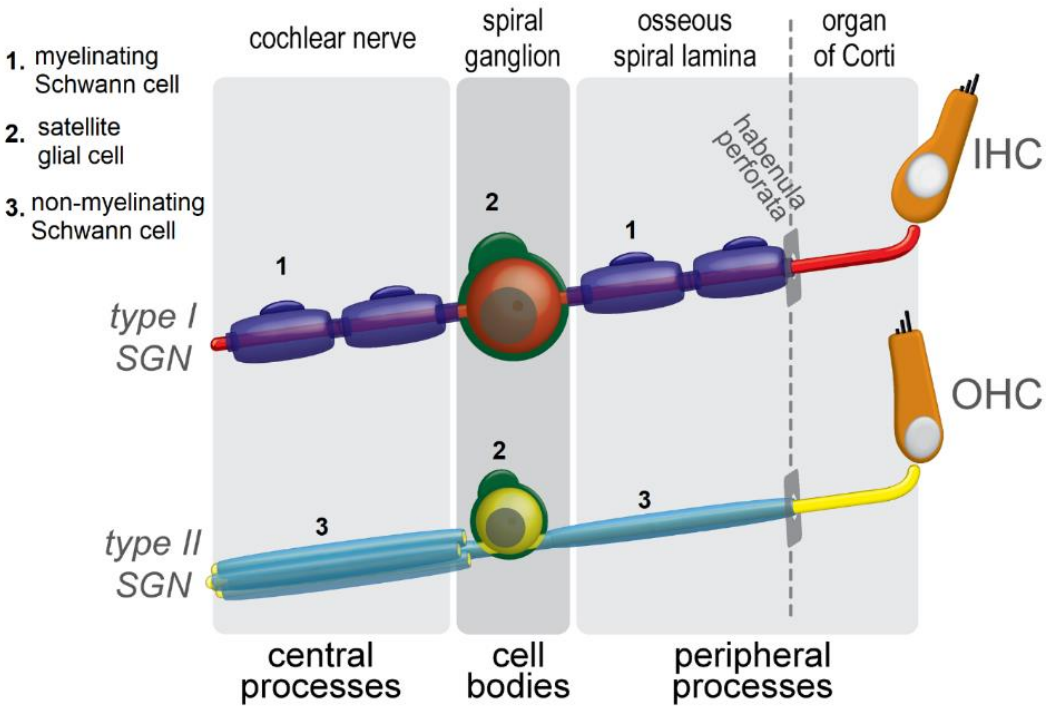

Figure 1.5. Illustration of spiral ganglion neurons (SGN) in humans. Myelinating Schwann cells (dark blue, 1) cover and myelinate both peripheral and central processes of the type I SGNs (red) that innervate the inner hair cells (IHC). Satellite glial cells (green, 2) surround all SGN cell bodies (somata). Non-myelinating Schwann cells (light blue, 3) cover both the central and peripheral processes of the type II SGNs (yellow) that innervate the outer hair cells (OHC). In the organ of Corti, beyond the habenula perforata, the peripheral processes of type I and type II are non-myelinated. The Figure and caption are adapted from (Locher et al., 2014).

1.2.1 Human hearing spectrum

Sound or pressure waves are produced by vibrations transmitted through a medium such as air or liquid that involves high and low-pressure areas, known as compression and rarefaction

Die approbierte gedruckte Originalversion dieser Dissertation ist an der TU Wien Bibliothek verfügbar.
The approved original version of this doctoral thesis is available in print at TU Wien Bibliothek.
TU Bibliothek Your knowledge hub WIEN

(Figure 1.6A). Sounds have frequency (pitch) and intensity (loudness). In general, hertz (Hz) is used for frequency range, and intensity is estimated in decibels (dB), which is the magnitude of a sound on a logarithmic scale. Frequency determines how many cycles can occur in a specific range of time; hence, frequency and period are the precise inverses of each other.

The sound intensity [W/m^2] is determined as the amount of energy transmitting through a unit area per unit time. The product of the pressure (p), and particle velocity ($\vec{v}$) with a magnitude and direction, gives us the intensity ($\vec{I}$):

$$\vec{I} = p\,\vec{v} \tag{1.1}$$

In mathematical terms, for a determined sound pressure (p) in pascals [Pa], the decibels sound pressure level (dB SPL) value is given by:

$$dB\ SPL = 20\log_{10}\left(\frac{p}{p_{ref}}\right) \tag{1.2}$$

where the audiological consider 20 [μPa] as the reference pressure (p_{ref}).

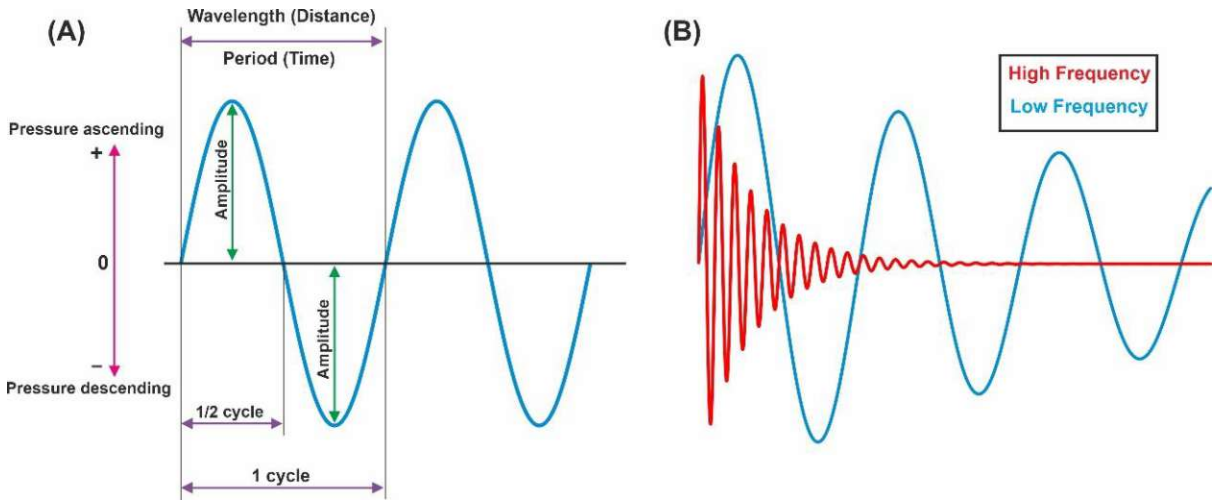

Figure 1.6. Representation of a sound wave. **(A)** Demonstrating different terms such as amplitude and pressure in the frequency diagram. **(B)** Comparison of high and low frequencies.

The human ear has the ability to distinguish both characters, frequency and intensity, from catching sounds. Humans have an incredible hearing system that can detect sounds in a frequency range from 20 to 20000 Hz; however, frequencies for speech are between 250 and 8000 Hz, which is the critical range. In addition, the human hears from 0 dB to about 130 dB, and after maximum hearing level, sound becomes painful and difficult to endure.

Die approbierte gedruckte Originalversion dieser Dissertation ist an der TU Wien Bibliothek verfügbar.
The approved original version of this doctoral thesis is available in print at TU Wien Bibliothek.
TU Bibliothek Your knowledge hub WIEN

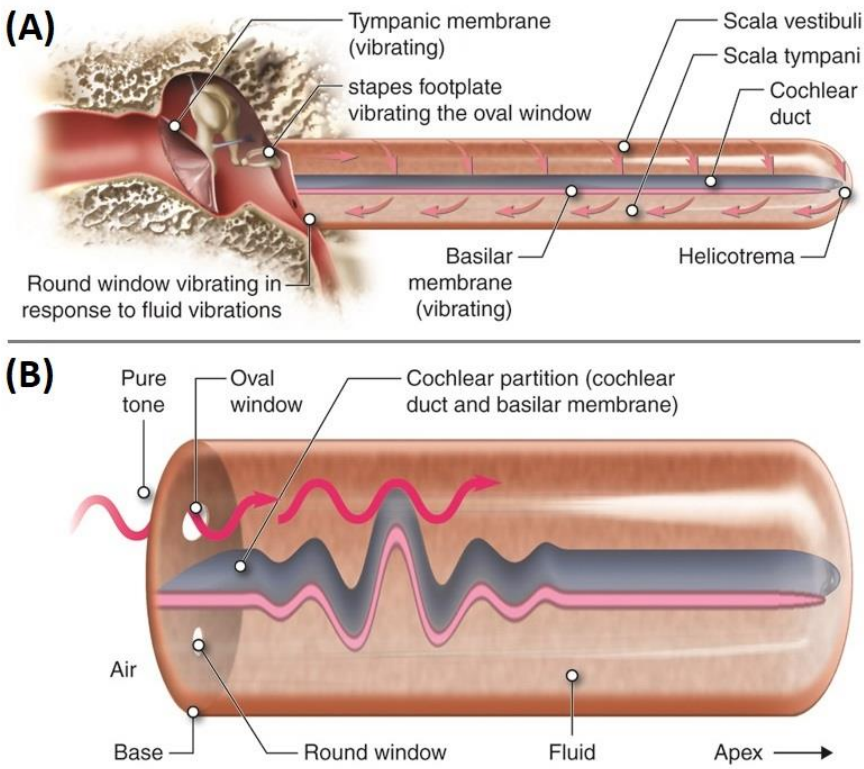

Figure 1.7. Schematic depiction of the uncoiled cochlea and basilar membrane structure. **(A)** The uncoiled cochlea and basilar membrane show arriving vibrations from the tympanic membrane into the cochlea. **(B)** Traveling sound waves along the basilar membrane and frequency mapping appear due to the physical properties of the basilar membrane. Figure adapted from (Lumen Learning, 2021).

The cochlear structure provides a fascinating hearing ability for humans and acts as a spectrum analyzer or a Fourier analyzer of the sound stimulus. There are two theories regarding coding frequency in the cochlea to convey auditory information into the brainstem.

The first theory is called place theory and was introduced by Helmholtz in 1863. The theory conception is based on the structural properties of the basilar membrane. Considering an uncoiled cochlea (Figure 1.7), the basilar membrane is narrow and stiff at the basal turn, whereas it is broader and more elastic at the apical turn. Therefore, the basilar membrane response depends on a particular frequency cause activating individual parts of the basilar membrane; low frequencies create lower vibrations that cause the apical turn to provoke; in contrast, higher frequencies generate more vibrations at the basal turn of the cochlea. This dissimilarity of basilar membrane structure hinders simultaneous movements of the entire basilar membrane when vibrations arrive (Von Békésy and Wever, 1960; Rhode, 1971; Evans and Wilson, 1975; Khanna and Leonard, 1982; Davis and Liu, 2011).

The Neural tuning of five ANFs is displayed in Figure 1.8. Isospiking lines are shown for different firing rates, with the lowest curve representing 25 spikes per second. The minimum

Die approbierte gedruckte Originalversion dieser Dissertation ist an der TU Wien Bibliothek verfügbar.
The approved original version of this doctoral thesis is available in print at TU Wien Bibliothek.
TU Bibliothek Your knowledge hub WIEN

of each curve represents the characteristic frequency (CF) where the fibers are most sensitive. Figure 1.8 shows that as the sound pressure level increases, the sharpness of the neural tuning decreases. In addition, as the stimulus strengthens, firing rates increases and occur in different frequencies other than CF. The highest firing rate in the natural state is less than 300 spikes per second, and ANFs with similar CF respond with different sensitivity (Rattay and Lutter, 1997).

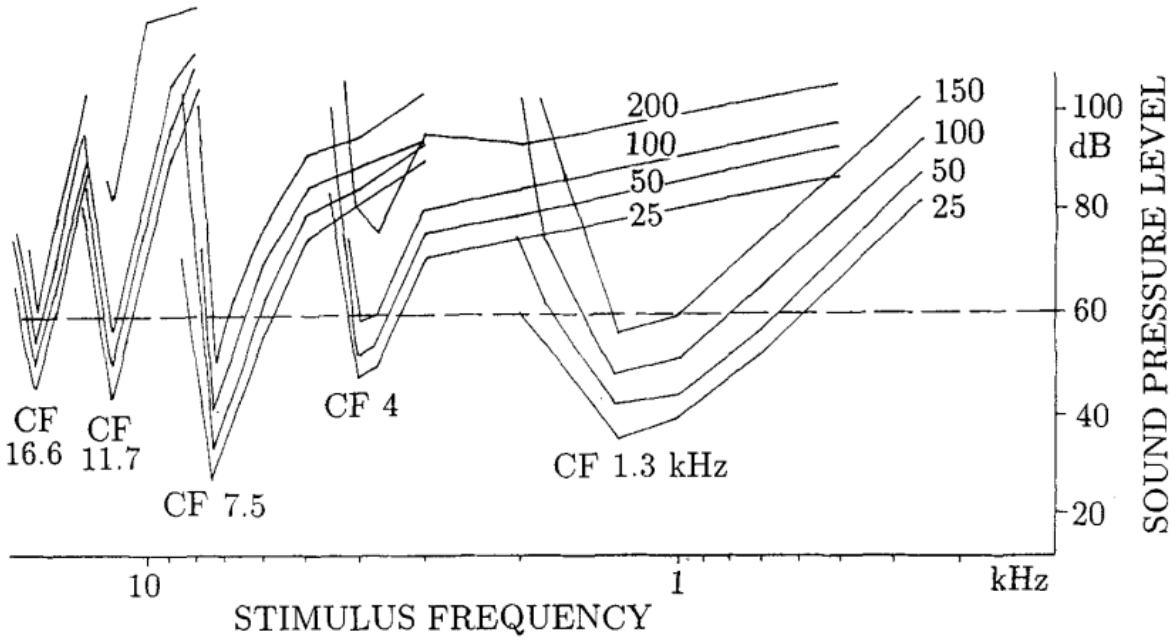

Figure 1.8. Neural tuning curves of five auditory nerve fibers with CF from 1.3 to 16.6 kHz. The lowest curves correspond to a firing rate of 25 spikes per second above their spontaneous rate. Minima mark the frequencies (CF) where the fibers are most sensitive. Note that stimulus frequency intervals rise with increased sound pressure level, as seen from the dashed line, which denotes a comfortable speech sound pressure level (60 dB). Figure and caption adapted from (Rattay and Lutter, 1997).

Figure 1.9 demonstrates basilar membrane displacement of a computer simulation based on the Peterson Bogert model. A sinusoidal signal with 1000 Hz (500 µPa) corresponding to a 28 dB sound pressure level was applied to the model. Basilar membrane movements along the cochlea at specific times were shown in Figure 1.9A for systematic increases of amplitudes. For a better comparison, three snapshots for t = 1, 2, and 20 ms were selected and demonstrated (Figure 1.9B). By considering the first 20 ms of the basilar membrane movements, the exponential increase is observed until the length of the basilar membrane reaches 23 mm (resonance place), and after that, decreases (Figure 1.9C). At places other than resonance, basilar membrane movements reach the maximum displacement only after a few cycles, whereas a longer time is needed to reach the maximum movement at the resonance place (x = 21 vs. x = 23 mm, Figure 1.9E) (Rattay and Lutter, 1997).

Die approbierte gedruckte Originalversion dieser Dissertation ist an der TU Wien Bibliothek verfügbar.
The approved original version of this doctoral thesis is available in print at TU Wien Bibliothek.
TU Bibliothek Your knowledge hub WIEN

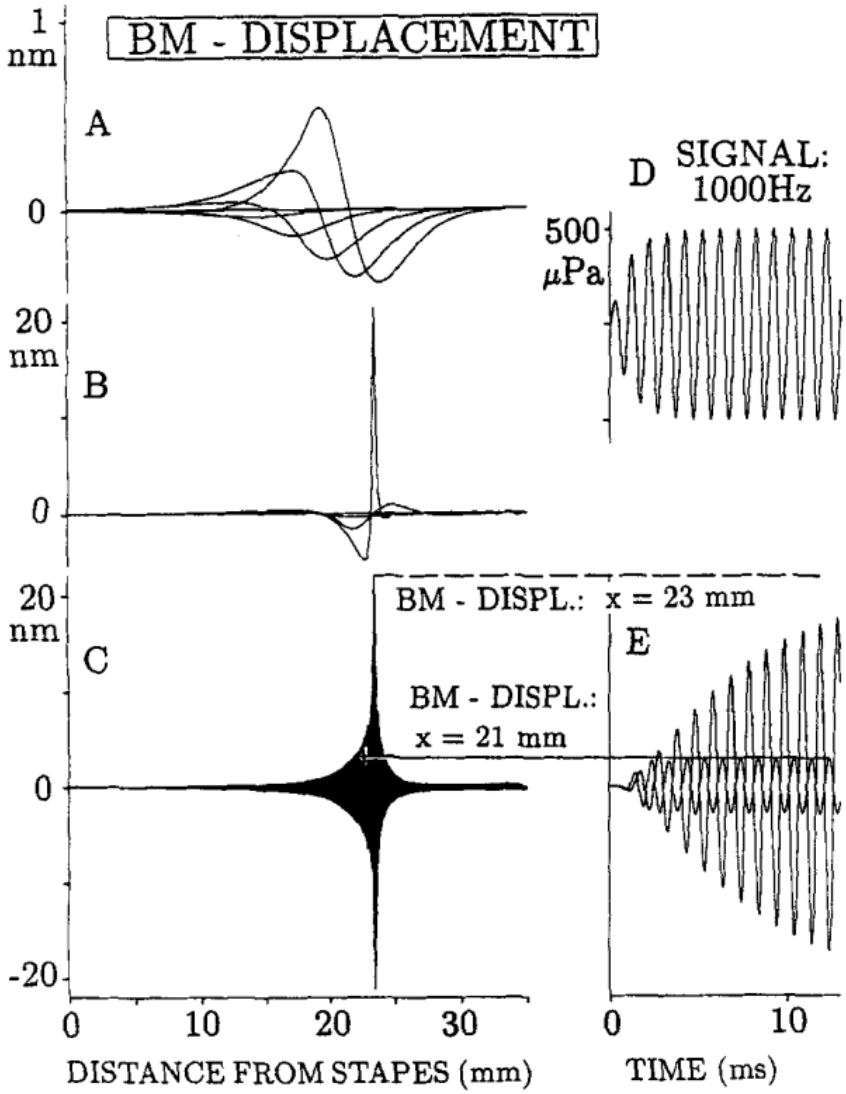

Figure 1.9. Basilar membrane displacements of the Peterson Bogert model were computed with the numerical method. **(A-C)** Basilar membrane movements along the cochlea for particular times. **(D)** Stimulus with a sinusoidal signal. **(E)** Basilar membrane movements are plotted against time. Figure and caption adapted from (Rattay and Lutter, 1997).

This mechanism, displacement of the basilar membrane, is called the tonotopic organization that describes spatial frequency. In addition, the tonotopic organization indicates which SGNs and their corresponding IHCs are responsible for specific frequency ranges in different locations along the cochlea (Figure 1.10).

Die approbierte gedruckte Originalversion dieser Dissertation ist an der TU Wien Bibliothek verfügbar.
The approved original version of this doctoral thesis is available in print at TU Wien Bibliothek.

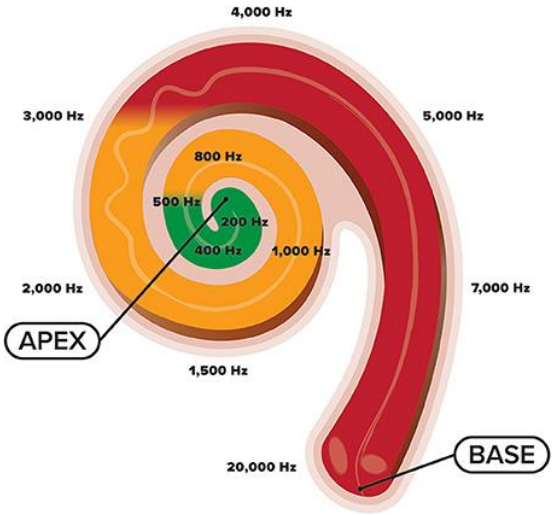

Figure 1.10. Illustration of the tonotopic organization of the human hearing organ, cochlea. The figure is taken from (Lahav and Skoe, 2014).

The second theory is the temporal theory that describes each hair cell responds to every entering tone in the cochlea (Rattay and Lutter, 1997). The temporal theory describes sound perception as dependent on timing or temporal pattern related to ANFs responsible for the sound. Each ANFs generates AP or spike if the cell membrane reaches a particular threshold value. The firing rate, spikes per second, depends on the depolarizing current value, which means higher frequencies induce a higher firing rate and lower frequencies cause lower firing rates.

The resting membrane potential of some hair cells causes generating spike continuously without external stimulus, which is known as spontaneous firing rate (Moore, 2007). It was reported that the ANFs have a spontaneous firing rate of 0.5-120 spikes per second without stimulation (Rattay and Lutter, 1997). Considering the maximum firing rate of human ANFs, about 300 spikes per second, a single SGN can only encode a sound below 300 Hz. More fibers of a group are involved for encoding sound with higher frequencies based on the Volley principle (Figure 1.11). The theory explains that when the frequency is above 500 Hz, how information is transferred to the brainstem since SGN can only fire at a maximum rate of about 500 Hz.

Die approbierte gedruckte Originalversion dieser Dissertation ist an der TU Wien Bibliothek verfügbar.
The approved original version of this doctoral thesis is available in print at TU Wien Bibliothek.
TU Bibliothek Your knowledge hub WIEN

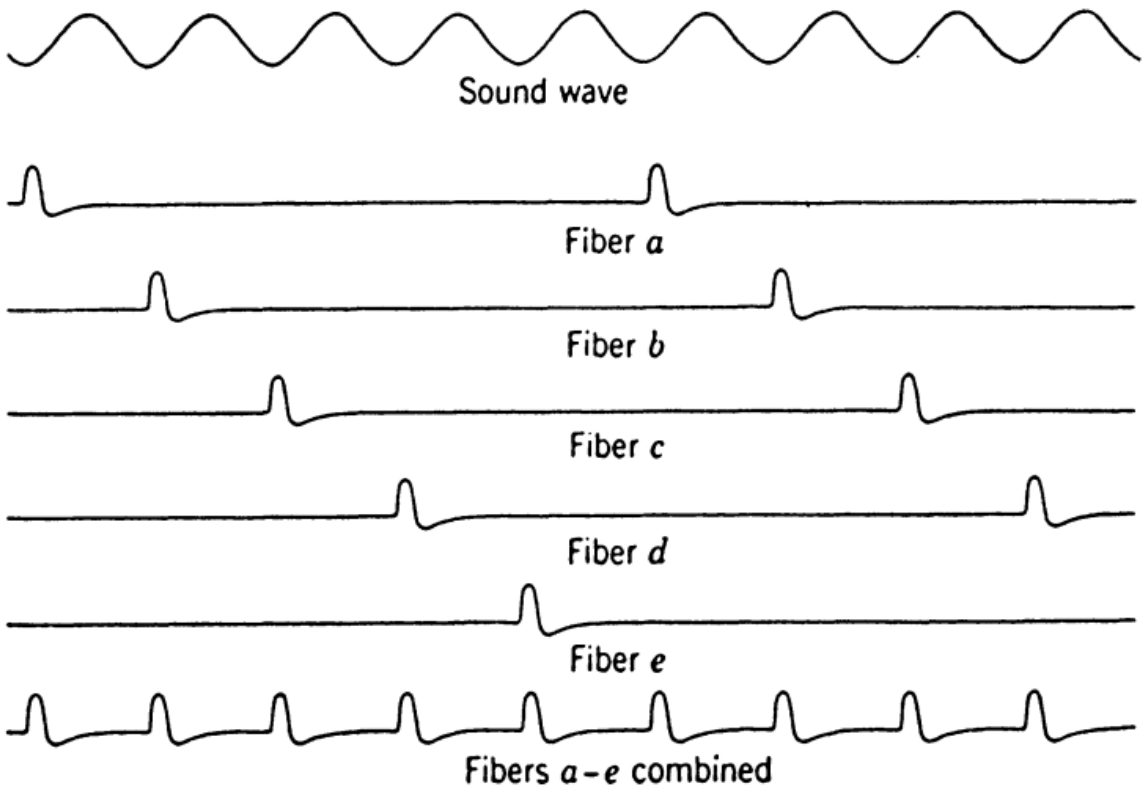

Figure 1.11. The Volley principle. A periodic acoustic stimulus will cause firing patterns in different axons of one hair cell as marked with a - e. The combined signal contains all the minima of sound even when no single fiber is able to fire with this high frequency. Figure and caption adapted from (Rattay, 1990).

1.2.2 Types, causes, and degrees of hearing loss

The damage or dysfunction of ANFs affects hearing sense in humans that can have several reasons to trigger losing hearing sense, such as exposure to noise, hereditary, disease. Hearing loss negatively affects communication, education, and social behavior. Nowadays, nearly 500 million people worldwide have hearing deficits induced by hereditary, aging, disease, medication, and injury. In addition, 1.1 billion young people between 12-35 years are at risk of hearing loss due to exposure to noise in a recreational environment, and by 2050 over 900 million people are expected to have hearing loss difficulties, reported by the World Health Organization (WHO) in 2020 (WHO, 2020).

Currently, three primary forms of hearing loss are known. First, sensorineural hearing loss (SNHL) is the typical type of hearing loss that occurs when cochlear nerves and hair cells are damaged under different circumstances, such as age, exposure to loud noise, drugs, toxic,

Die approbierte gedruckte Originalversion dieser Dissertation ist an der TU Wien Bibliothek verfügbar.
The approved original version of this doctoral thesis is available in print at TU Wien Bibliothek.
TU Bibliothek Your knowledge hub WIEN

hereditary, malformation of the inner ear. SNHL affects the ANFs pathway from hair cells to the brainstem. In addition, the ability to instinctively regenerate hair cells is lacking in humans (Feghali et al., 1998; Edge and Chen, 2008); hence, degeneration of hair cells is permanent and gradually becomes more severe. Although SNHL is not treatable with medications or surgically, using hearing aids or cochlear implants (CIs) can help people with hearing difficulties to restore at least part of their hearing sense.

Furthermore, SNHL affects the organ of Corti and induces degeneration of the organ of Corti (Hinojosa and Marion, 1983). Spoendlin reported that the degeneration of the organ of Corti and sensory hair cells causes some alterations in the peripheral parts of ANFs and cell bodies (Spoendlin, 1984). Over past decades, parameters such as demyelination, reduction in peripheral diameter of ANFs, and gradual degeneration of the cell bodies were reported (Leake and Hradek, 1988; Nadol et al., 1989; Hardie and Shepherd, 1999; Versnel et al., 2007; Heshmat et al., 2020).

Overall, the degeneration schema of the human type I SGNs based on cell anatomies in patients with SNHL can be categorized into two degeneration levels (Figure 1.12). In the first level of degeneration, the loss of hair cells transpires. At this level, the connection of hair cells to the peripheral parts of ANFs is detached (loss of hair cells); however, supporting cells, peripheral and central axons, as well as cell bodies, remain intact (Figure 1.12B). In the second level of degeneration, loss of supporting cells and peripheral parts of ANFs degeneration occurs, resulting in gradually or suddenly loss of peripheral parts up to the non-myelinated region of soma, pre-somatic region (Figure 1.12C). Still, central axons and most cell bodies remain unimpaired, and CIs bypass the degenerated regions resulting in restoring hearing loss (Liu et al., 2015).

Die approbierte gedruckte Originalversion dieser Dissertation ist an der TU Wien Bibliothek verfügbar.
The approved original version of this doctoral thesis is available in print at TU Wien Bibliothek.
TU Bibliothek Your knowledge hub WIEN

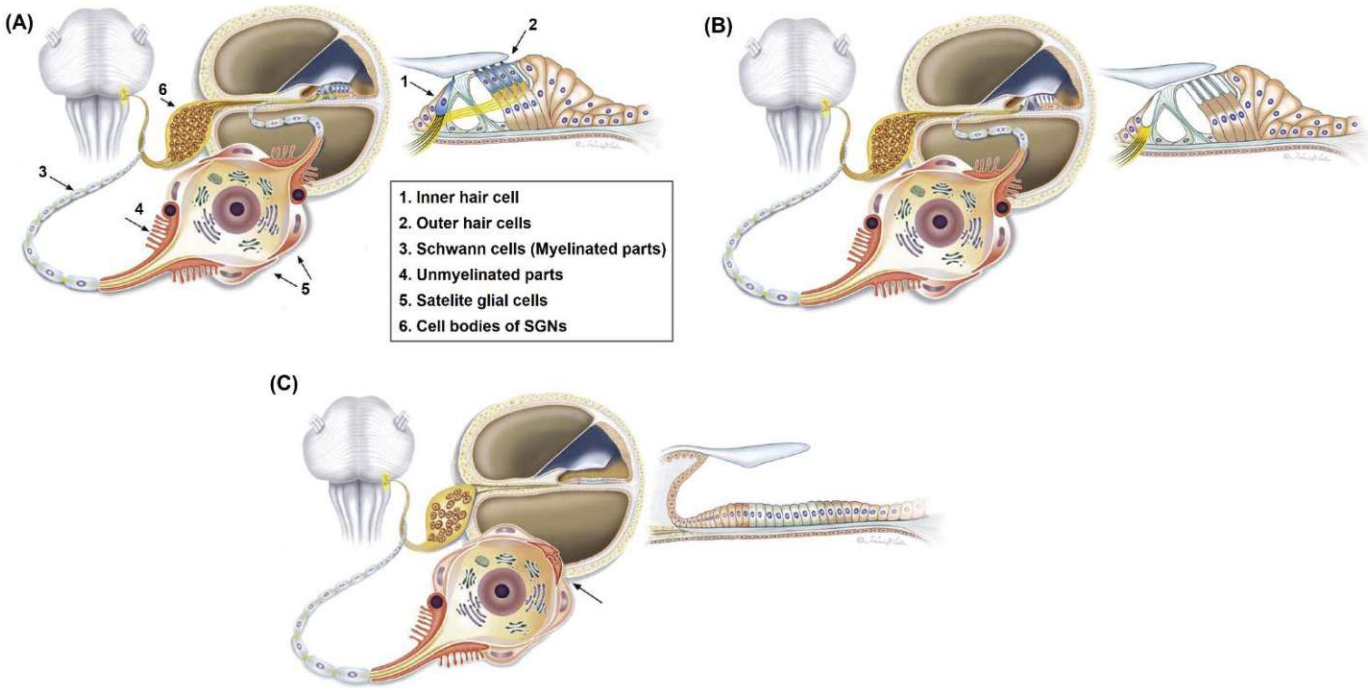

Figure 1.12. Schematic representation of different degeneration SGN type I in humans. **(A)** Indicating the normal status of SGN with IHC connection to peripheral and projected to soma and reach the brainstem with central axons. **(B)** Presenting the first level of degeneration in patients with SNHL causes loss of hair cells. **(C)** Demonstrating the second level of SGN type I degeneration in people with SNHL difficulties resulting in losing supporting cells as well as peripheral axons. The Figure adapted from (Liu et al., 2015).

The second kind of hearing loss is conductive hearing loss that appears when the external or middle ear or both are obstructed due to issues such as tumors, excessive earwax, malformations, infections. When the sound pathway from the external auditory canal to the eardrum as well as the tiny bones in the middle ear is blocked, the sound cannot easily and efficiently reach the inner ear, which results in hearing complications. Medications or, in some cases, surgery can be used to treat conductive hearing loss.

The third type of hearing loss is mixed hearing loss. As the name implies, this hearing loss type is a combination of sensorineural and conductive hearing loss that means all ear parts: the external, the middle, and the inner ear sections can be damaged or obstructed.

Furthermore, hearing loss can occur in one side of the ear, which means only one ear has hearing difficulties; still, the other ear is normal, called unilateral hearing loss, and when hearing loss appears in both ears, named bilateral hearing loss. In addition, the hearing loss level in bilateral cases is either similar or different in both ears, which is called symmetrical and asymmetrical hearing loss, respectively.

Die approbierte gedruckte Originalversion dieser Dissertation ist an der TU Wien Bibliothek verfügbar.
The approved original version of this doctoral thesis is available in print at TU Wien Bibliothek.
TU Bibliothek Your knowledge hub WIEN

Moreover, different classifications are known and applied for describing hearing loss. Progressive hearing loss is used for explaining that hearing becomes worse gradually; however, when hearing loss happens suddenly and quickly, it is called sudden hearing loss. Fluctuating hearing loss indicates hearing getting either better or worse over time; conversely, hearing loss level residing similar with time named stable hearing loss.

1.2.3 Degree of hearing loss and evaluation of hearing

The degree of hearing loss and hearing thresholds has been evaluated using standard criteria as shown in Table 1.1 (WHO, 1991). The hearing loss degrees and pattern of hearing loss across the cochlear nerve, which is covered in various frequencies, referred to hearing loss configuration.

Degree of hearing loss	Hearing loss range (dB)
Normal	0-25
Mild impairment	26-40
Moderate impairment	41-60
Moderately severe impairment	61-80
Severe impairment	81-90
Profound impairment	91+

Table 1.1. The degree and classification of hearing loss.

It is feasible to measure the hearing loss levels of a person and demonstrate it in a graph called an audiogram (Figure 1.13). The understanding of the audiogram delivers information not only for the condition of any presence of hearing loss but also for hearing loss levels. An audiogram demonstrates how loud sounds are for the person to hear it at a particular frequency and reveals a hearing range that varies from normal to the presence of hearing loss level. If the lowest required thresholds are not met, hearing loss is detected.

The audiogram can be helpful to detect the location and level of hearing loss. The audiogram is plotted based on frequency (pitch) on the horizontal axis in Hertz (Hz) versus loudness (hearing level) on the vertical axis in decibel (dB). The human ear detects sounds between 20 Hz up to 20 kHz. The speech frequency range is 400-5000 Hz, and the audiogram usually evaluates frequencies between 20 Hz and 8 kHz.

Die approbierte gedruckte Originalversion dieser Dissertation ist an der TU Wien Bibliothek verfügbar.
The approved original version of this doctoral thesis is available in print at TU Wien Bibliothek.
TU Bibliothek Your knowledge hub WIEN

Pure-tone audiograms were accomplished with a standard audiometer in a sound-attenuated room. Thresholds were measured between 0.125 and 8 kHz. Pure-tone averages are calculated for the low (0.125–0.5 kHz), mid (1–2 kHz), and high (4–8 kHz) frequencies. The frequency ranges of 0.125–0.5, 1–2, and 4–8 kHz are assigned to the cochlea's apical, middle, and basal turns, respectively.

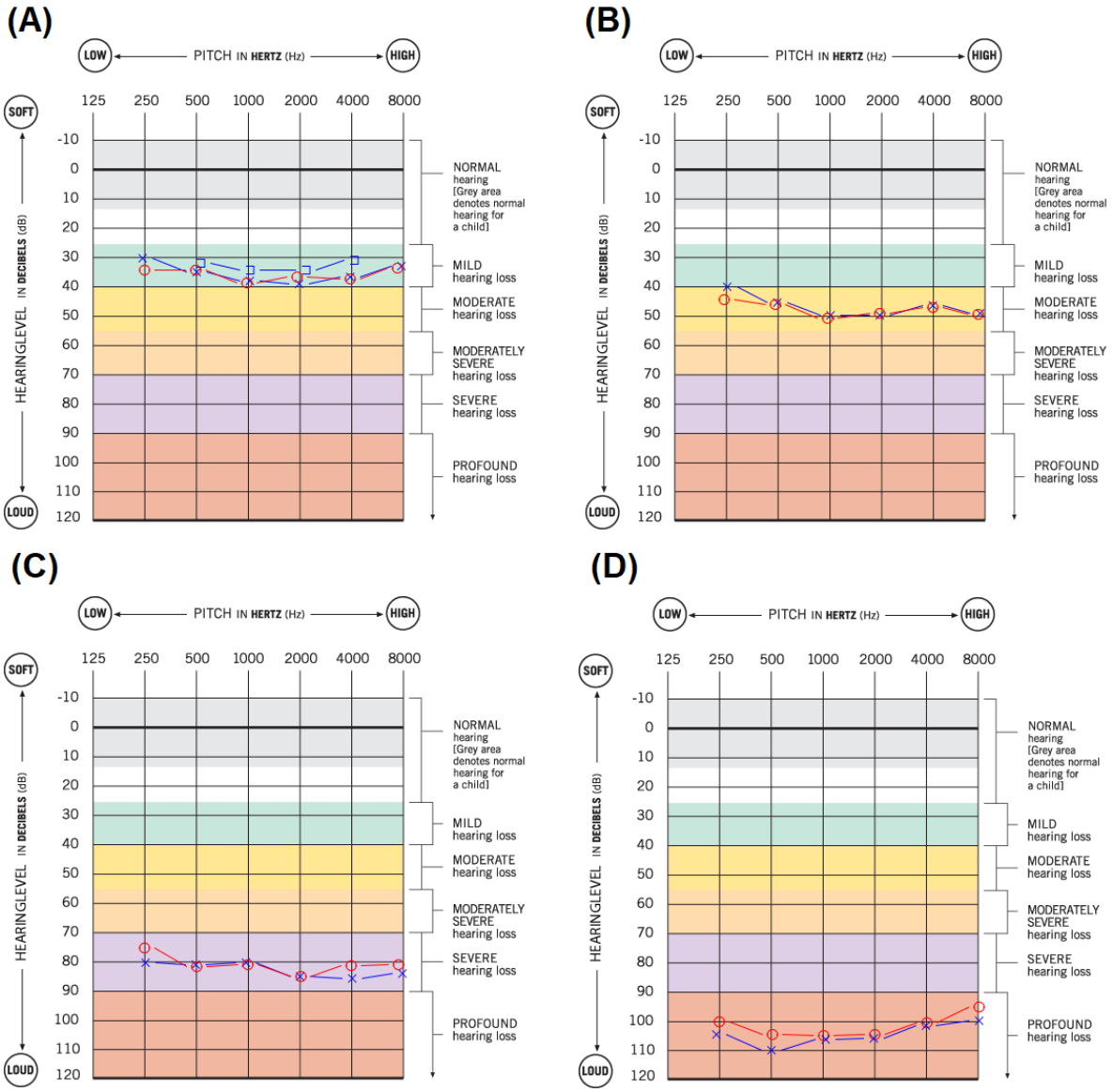

Figure 1.13. Audiogram graphs with different hearing loss levels. **(A-D)** demonstrate people with mild, moderate, severe, and profound hearing loss levels, respectively. The air conduction for the right and left ear showed the red circle and blue cross in all graphs. Noted gray area indicates normal hearing for children. The Figure adapted (Happy Ears Hearing Center).

Die approbierte gedruckte Originalversion dieser Dissertation ist an der TU Wien Bibliothek verfügbar.
The approved original version of this doctoral thesis is available in print at TU Wien Bibliothek.
TU Bibliothek Your knowledge hub WIEN

1.2.4 How is hearing loss restored?

Hearing loss depends on the types and degrees that can be treated with surgery, pharmaceutical drugs, hearing aids, CIs. Yet, the SNHL is more frequent and causes permanent hearing loss. Therefore, hearing aids and CIs can be a possible alternative way to restore hearing loss. Over past decades, several implants and devices have been designed to help impaired people depend on hearing loss types, such as middle ear implants, bone-conduction hearing aids, electric acoustic stimulation, and the most famous and functional device is CI. Concerning the content of this dissertation, only the CI in detail is described in the following sections.

CIs have been being used in both adults and children suffering from SNHL, single side or bilateral hearing. CI candidacy is individual and depends on the different conditions and circumstances that need to be considered; however, people with severe to profound SNHL have hearing loss larger than 75 dB at a frequency above 1 kHz, or deaf-born children can benefit from CIs. Some investigations reported that CI helped treat people suffering from tinnitus, ringing in the ears, and sometimes happens with SNHL. They informed significant reduction in tinnitus by using CI (Van de Heyning et al., 2008; Punte et al., 2013; Távora-Vieira et al., 2015; Servais et al., 2017).

Several studies reported that using CI in people with single-sided deafness improved speech perception in a noisy environment and sound localization (Vlastarakos et al., 2014; Kitterick et al., 2015; Rahne and Plontke, 2016; Sladen et al., 2017). Moreover, several studies demonstrated that bilateral CI has more advantages than unilateral CI, particularly in sound localization and speech perception in noise (Laszig et al., 2004; Nopp et al., 2004; Dunn et al., 2010; Smulders et al., 2016).

1.3 Cochlear implant overview

CI is one of the most successful neuroprostheses on the globe. CI is an electric surgical device with a flexible silicon array containing electrical contacts and wires that spreads electrical current to the survived ANFs. CI improves the hearing perception in deaf or severe to profound hearing loss in adults and children and is used over decades in more than 800000 people with impaired-hearing sense worldwide as well as about 220000, in Europe including 60% adults and 40% children reported by the European Association of Cochlear Implant Users (Boisvert et al., 2020; EURO-CIU, 2020). Regarding the content of this dissertation, CI is addressed in more detail in the following section.

Die approbierte gedruckte Originalversion dieser Dissertation ist an der TU Wien Bibliothek verfügbar.
The approved original version of this doctoral thesis is available in print at TU Wien Bibliothek.
TU Bibliothek Your knowledge hub WIEN

The belief of restoring hearing by using electrical stimulation instead of acoustic stimulation goes back to 1747. The earliest electrical stimulation of the ear was accomplished in 1747 by Giuseppe Veratti, who treated a 70-year-old woman suffering from tinnitus and severe hearing loss. Veratti used glass to transmit electricity, by a frictional electrical machine (Figure 1.14), for about five minutes each session, and after three sessions, the tinnitus issue of the woman disappeared, and she experienced an improvement in her hearing (Marchese-Ragona et al., 2019).

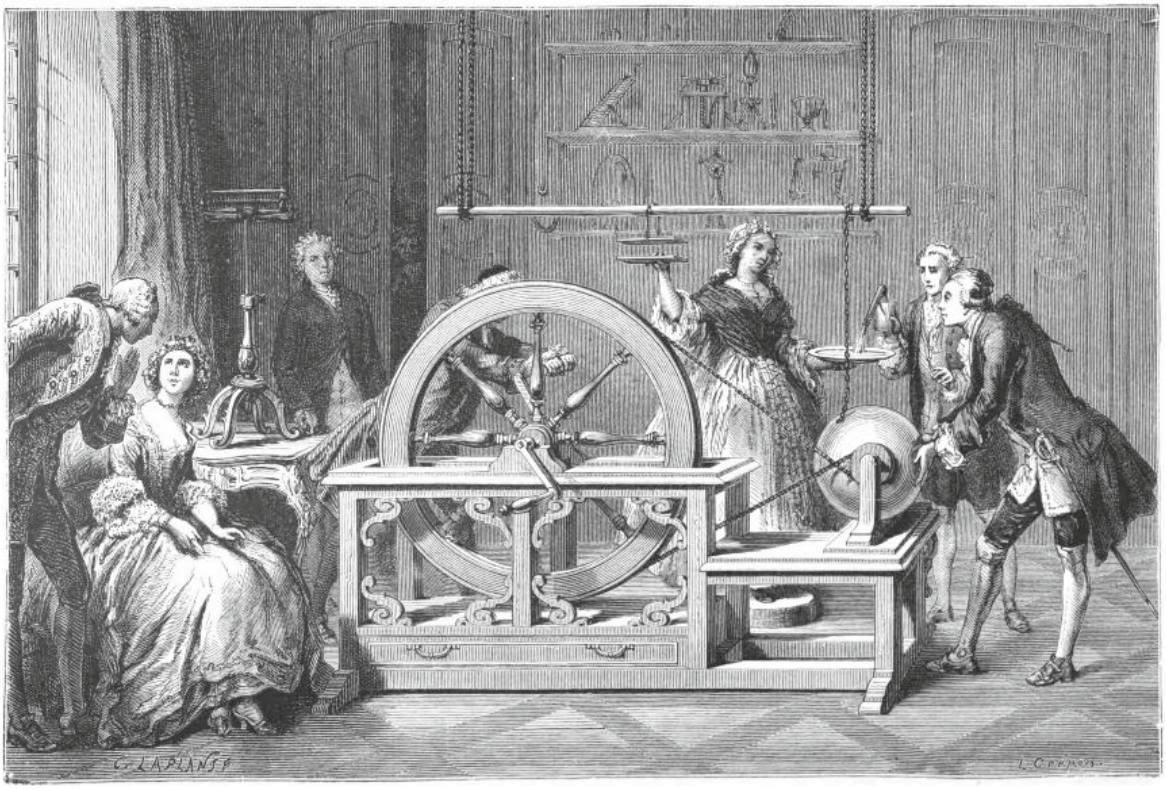

Figure 1.14. Frictional electrical machine with a glass globe (Wikimedia Commons, 2020).

In the following year, in 1748, English scientist Benjamin Wilson applied electrical stimulation in several days on a deaf woman and succeeded in improving the woman's hearing; however, he failed in other six deaf patients with the same method (Wilson, 1752). In the same year, Johan Lindhult reported that he treated five patients suffering from mild to profound hearing loss and tinnitus by applying powerful electrical stimulation (Lindhult, 1752). Ten years later, in 1757, Brydone remedied a woman who was deaf for six months successfully with electricity (Brydone, 1757).

In 1800, Alessandro Volta, who invented the electric battery, used his ears to test electrical stimulation; he put metal rods in his ears and connected them to a circuit of 50 Volts (Volta, 1800). In 1950 a Swedish neurosurgeon, Lundberg, used sinusoidal electric current to stimulate

Die approbierte gedruckte Originalversion dieser Dissertation ist an der TU Wien Bibliothek verfügbar.
The approved original version of this doctoral thesis is available in print at TU Wien Bibliothek.
TU Bibliothek Your knowledge hub WIEN

auditory nerves during surgery (Gisselson, 1950). Seven years later, Djourno and Eyries, in 1957, applied electrical current to stimulate the cochlear nerves directly with a contact laid on the cochlear nerves of a patient through an operation (Djourno et al., 1957).

In 1961, William House and John Doyle studied electrical stimulation of cochlear nerves in two patients with profound-dead hearing by a single-channel electrode located into their ST through the round window (House, 1987). Hence, it was announced as the first CI implantation. Furthermore, another research group, Simmons and White, from Stanford University Medical School, implanted a CI with six electrodes as known as multichannel CI (Simmons, 1966). In late the 70s in Melbourne, Australia, Graeme Clark developed the multichannel CI, significantly, which enhanced spectral perception and speech recognition. The device was surgically implanted in a 48-year-old in Vienna, Austria (Clark, 1978; Clark and Furness, 2013; Mudry and Mills, 2013), and in 1984 the company Cochlear Ltd. made it available in the market by the name of "Nucleus 22".

1.3.1 Structure, function, and design of cochlear implant

A standard CI system is divided into two sections, external and internal components (Figure 1.15). The external component consists of a microphone, speech processor, and transmitter. On the other hand, the internal component involves a receiver-stimulator and electrode array.

The speech processor converts detected sounds (acoustic signals) into electric signals, transforms them into several frequency bands with a filter. In addition, a transmitting coil, attached externally with a magnet, transmits the digital signals (codes) via radiofrequency to the receiver-stimulator. Finally, the internal receiver-stimulator decodes these signals into electrical stimuli and transfer them to different electrodes inside the array, based on frequency ranges.

Die approbierte gedruckte Originalversion dieser Dissertation ist an der TU Wien Bibliothek verfügbar.
The approved original version of this doctoral thesis is available in print at TU Wien Bibliothek.
TU Bibliothek Your knowledge hub WIEN

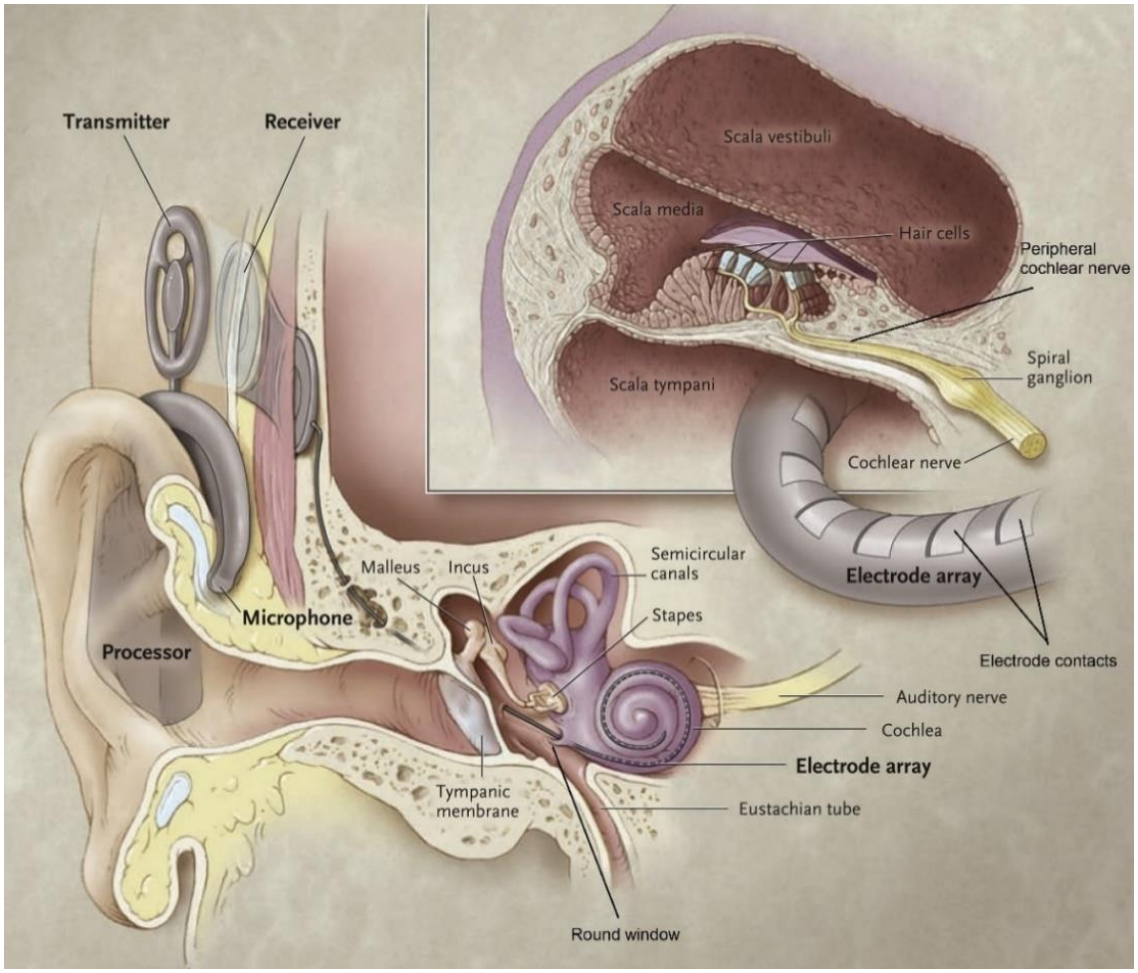

Figure 1.15. Illustration of a cochlear implant with key components of cochlear. The external part consists of a microphone, processor, and transmitter. The internal part includes a receiver located under the skin and an array with electrode contacts, which is inserted in the scala tympani. The Figure taken from (Reiss, 2020).

The electrode array is generally inserted into the ST through the round window of the cochlea, where electrode contacts lie near the auditory nerves. CI bypasses the hair cells and peripheral axon parts, which are damaged or degenerated, and electrically stimulates survived ANFs.

CIs commonly apply the monopolar (MP) strategy as the default stimulation configuration. Since in this strategy less currents are needed to stimulate ANFs, the device, consequently, consumes less battery power, causing increased battery life (Pfingst et al., 2004). The MP strategy is performed by an active electrode from the array and a ground electrode, which is usually located outside the cochlea, inside the internal receiver/stimulator behind the ear. CIs use charge-balanced pulses, often symmetric (cathodic first) biphasic pulses, to avoid any harm to the cochlear tissue due to charge accumulation (Leob and McHardy, 1995; Cunningham and Glade, 2019).

Die approbierte gedruckte Originalversion dieser Dissertation ist an der TU Wien Bibliothek verfügbar.
The approved original version of this doctoral thesis is available in print at TU Wien Bibliothek.
TU Bibliothek Your knowledge hub WIEN

The pulses are delivered to each electrode contact at a rate defined by pulse numbers per second (PPS). Older CIs had low stimulation rates of about 250 PPS or less; however, contemporary CIs increase the rates to 5000 PPS since rates above 2000 PPS enhance the temporal information (Cunningham and Glade, 2019)

It has been trying to improve speech perception and increase CI performance, and one way to achieve this outcome is to increase the number of CI electrodes. However, depending on the CI models and types, the electrode contact numbers of CIs are limited; hence, the only potential method seems to be employing virtual channels.

The concept of virtual channels was introduced by Wilson (Wilson et al., 1993) for the first time. The virtual channel is produced by stimulating two neighboring electrodes that cause creating an individual pitch in between two electrodes, which differs from the two perceived pitches from the two electrodes that are stimulated individually. In addition, the virtual channel pitch can be altered by changing either the amplitude ratio of the electrode current or the ratio of stimulation rates in a chosen electrode (Wilson et al., 1993; Vondrášek et al., 2008; Landsberger and Srinivasan, 2009).s

The three most successful and well-known CI companies are:

i. Cochlear company from Australia was established in 1981 and held the highest market share, about 55% of the CI market. The Cochlear company fabricates seven electrodes array in several lengths with 22 electrodes and channels.
ii. Advanced Bionics from the USA was established in 1993, and before the early 1940s, the company was known by Sonova. Advanced Bionics has about 20% of the CI market and produces four types of the electrode array in different lengths with 16 electrodes and up to 120 virtual channels.
iii. MED-EL company was established in 1990, Austria and keeps 20% of the CI market. The MED-EL company produces three models of the electrode array in various lengths with 12 channels and up to 24 electrodes.

The insertion depth of the CI electrode array depends on the cochlea anatomy (cross-section and length of ST) that varies between CI recipients. The insertion depth usually varies from 15 to 32 mm (270° to 720°) (Dhanasingh and Jolly, 2017); consequently, the full array length is not always achievable.

Die approbierte gedruckte Originalversion dieser Dissertation ist an der TU Wien Bibliothek verfügbar.
The approved original version of this doctoral thesis is available in print at TU Wien Bibliothek.
TU Bibliothek Your knowledge hub WIEN

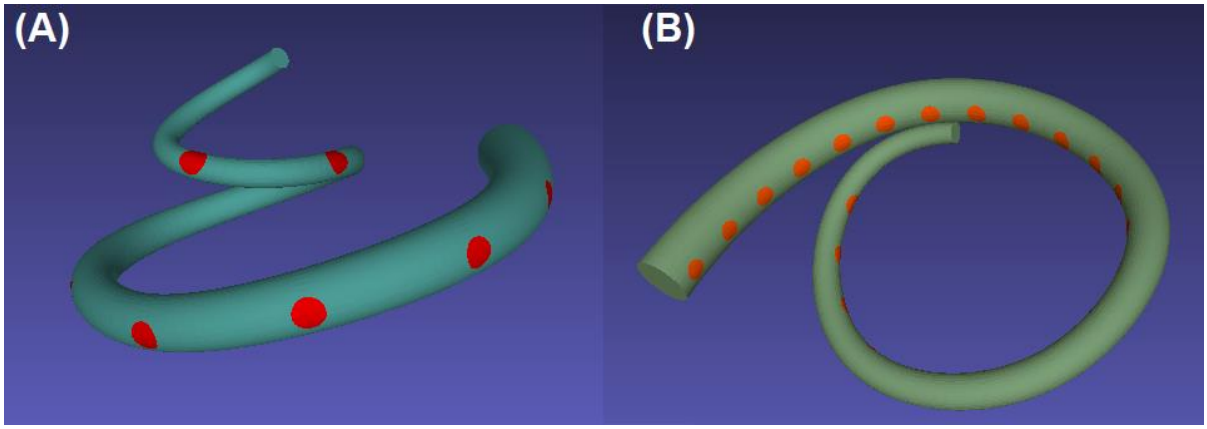

Figure 1.16. Representation of lateral CI array versus perimodiolar CI array. **(A)** Lateral array, dark green, with 12 electrode contacts depicting in red located of the lateral wall of the array, far away from the modiolus. **(B)** perimodiolar array, light green, with 22 electrode contacts showing in orange located on the inner (medial) wall of the array, close to the modiolus and scala tympani wall.

Commonly based on array position in the ST, CIs can be identified and categorized into two groups. First, the lateral wall (LW), and second the perimodiolar (PM) arrays (Figure 1.16). The LW array is positioned close to the lateral wall of ST, far away from the modiolus. On the other hand, the PM array is situated on the medial wall of the ST, close to the cell bodies of SGNs as well as ANFs. As a result of the shorter electrode distance to the modiolus in PM arrays, they have an advantage for ANFs stimulation compared to the LW array.

Several investigations performed on humans reported advantageous such as lower threshold, better localization of the nerve stimulations, broader dynamic range, lower battery consumption, and less channel interactions for PM electrode arrays compared with the LW arrays; however, the risk of intracochlear trauma is higher in the PM arrays (Cohen et al., 2001; Donaldson et al., 2001; Tykocinski et al., 2001; Saunders et al., 2002; Hughes and Abbas, 2006; Lee et al., 2019; Jwair et al., 2021).

1.4 Scala tympani versus scala vestibuli implantations

ST is considered as an initial and approachable way for CI array insertion. However, in the case of cochlear obstruction, the CI array insertion into the ST becomes challenging. The partial or total cochlear obstruction happens when the ST has some impediments due to ossification, fracture and tumor of the temporal bone, otosclerosis, post-meningitis fibrosis, chronic otitis media, as well as autoimmune inner ear diseases (Balkany et al., 1996; Kiefer et al., 2000; Bacciu et al., 2002; Rinia et al., 2006; Coelho and Roland, 2012). In addition, the cochlear ossification degree is divided into three main categories (Figure 1.17). When the ossification

Die approbierte gedruckte Originalversion dieser Dissertation ist an der TU Wien Bibliothek verfügbar.
The approved original version of this doctoral thesis is available in print at TU Wien Bibliothek.
TU Bibliothek Your knowledge hub WIEN

happens at the round window, it is called grade I. If ossification appears at the inferior portion of basal turn up to 180°, it becomes grade II. Finally, when ossification continues, more than 180° of the cochlea turn, it is known as grade III, which profoundly impacts hearing outcomes. (Bird et al., 1999; Zaghis et al., 2003; Smullen and Balkany, 2005).

Ossification and fibrosis in the cochlea can be detected through perioperative imaging procedures of the temporal bone by utilizing magnetic resonance imaging (MRI) and computed tomography (CT). Balkany group (Balkany et al., 1987) reported that the CT imaging was able to predict ossification about 73%; however, another study stated 46% false detection because of fibrous or slight osseous that is not possible to identify by CT (Jackler et al., 1987). In addition, Lin group reported that three patients with normal CT were unable to receive ST implantation (Lin et al., 2006). Although considering both MRI and CI imaging increase the possibility for detecting an obstruction in the cochlea up to about 94%, using only CT decreases the chance to 50% (Isaacson et al., 2009).

Various clinical studies reported that up to 15% of all CI candidates and 80% of CI candidates, who become deaf because of meningitis, suffer from cochlear obstruction (Berrettini et al., 2002; Adunka et al., 2005; Rinia et al., 2006). Therefore, some methods are used to allow CI insertion into the blocked ST, such as removing or drilling ossification and making a tunnel through the basal turn of the cochlea for a full or partial CI array insertion (Figure 1.17D) (Gantz et al., 1988; Gulya and Steenerson, 1996; Balkany et al., 1996; Rinia et al., 2006). Although, some clinical studies reported a full CI array insertion in normal ST cases might cause better speech perception because more channels are involved (Kileny et al., 1992; Geier and Norton, 1992; Fishman et al., 1997; Kiefer et al., 2000; Skinner et al., 2002; Yukawa et al., 2004; O'Connell et al., 2017).

On the other hand, Rinia reported that the benefit of the number of active electrodes in full CI insertion reduced remarkably with increasing the degree of ST obstruction (Rinia et al., 2006). Reducing the active electrode number is done by postoperatively turning off electrodes that may eventually cause device failure (Zeitler et al., 2009).

Based on the clinical and histopathologic findings, the basal turn of ST is a well-known area of obstruction (Green et al., 1991; Berrettini et al., 2002; Barker et al., 2009; Lin, 2009). Due to the anatomical structure of ST, total drilling or removing the obstruction is not feasible. Therefore, instead of the full CI insertion, partial insertion can be alternatively applied. (Cohen and Waltzman, 1993; Gulya and Steenerson, 1996; Kiefer et al., 2000; Bacciu et al., 2002; Rinia et al., 2006; Lee et al., 2011). Several disadvantages, such as poor performance in speech understanding, high voltage requirement, and less optimal CI function, are reported in clinical studies when a partial CI array is used (Gulya and Steenerson, 1996; Riniaet al., 2006). Finally,

Die approbierte gedruckte Originalversion dieser Dissertation ist an der TU Wien Bibliothek verfügbar.
The approved original version of this doctoral thesis is available in print at TU Wien Bibliothek.
TU Bibliothek Your knowledge hub WIEN

despite all CI insertion drawbacks when ST is either partially or fully obstructed, SV insertion is a valuable and reliable possibility.

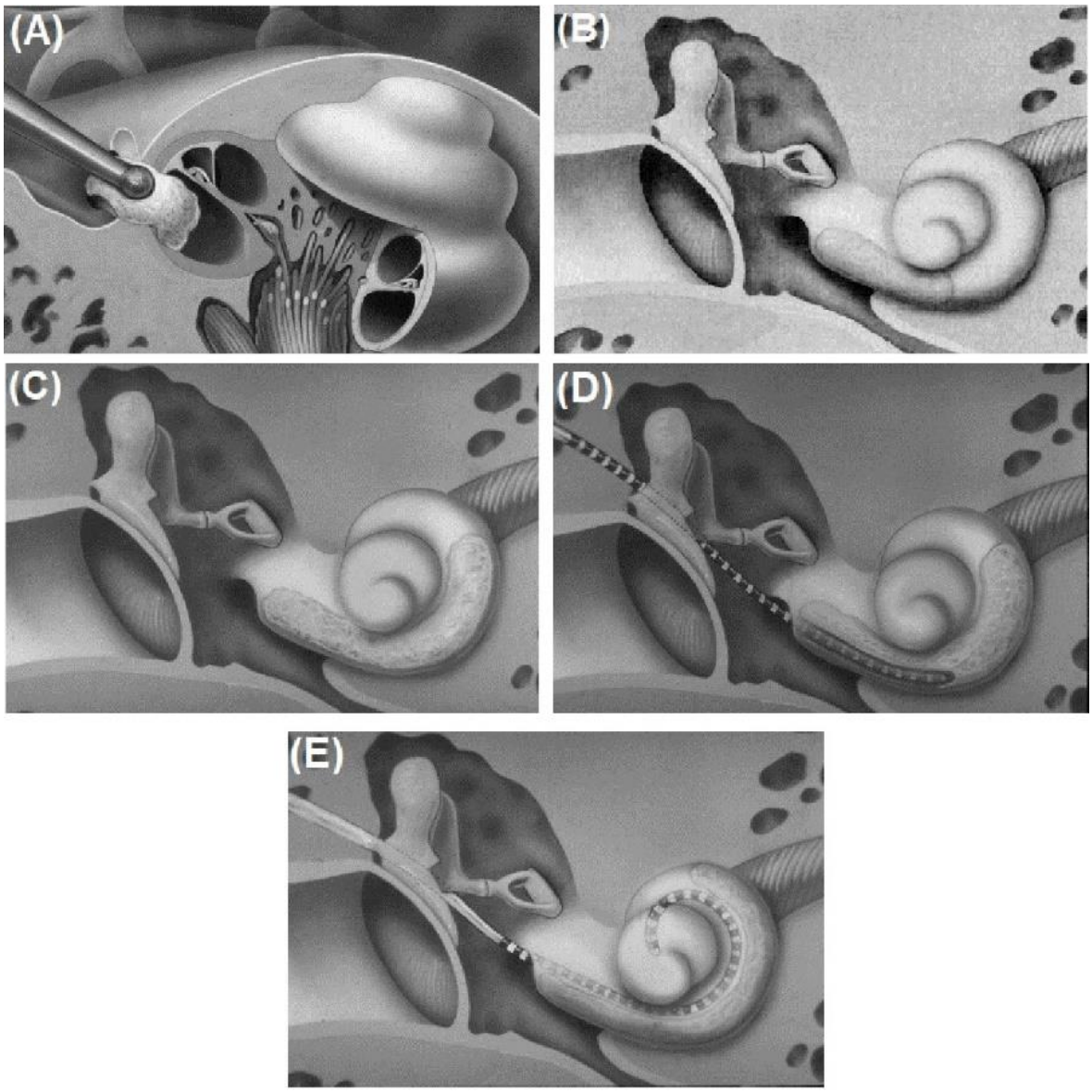

Figure 1.17. Ossification degrees of scala tympani. **(A)** Degree I ossification happens at the round window. **(B)** Degree II ossification appears up to 180° of the basal turn. **(C)** Degree III ossification occurs above 180° of the ST. **(D)** A tunnel drilled the beginning part of the basal turn from the round window for partial CI insertion. **(E)** Scala vestibuli implantation in the fully basal obstruction. The figure is taken from (Smullen and Balkany, 2005).

Steenerson group reported successful SV implantation in 1990 for the first time (Steenerson et al., 1990). They inserted a CI array in the SV for two patients who suffered from post-meningitis ST obstruction by ossification and fibrosis. The results demonstrated comparable outcomes as expected in ST CI users. Two years later, Pijl and Noel (Pijl and Noel, 1992)

Die approbierte gedruckte Originalversion dieser Dissertation ist an der TU Wien Bibliothek verfügbar.
The approved original version of this doctoral thesis is available in print at TU Wien Bibliothek.
TU Bibliothek Your knowledge hub WIEN

studied SV implantation on one patient who first received CI array in ST; however, after a while, the CI array was removed due to subsequent infections from ST and inserted in SV. They reported equivalent results between former ST and later SV implantation.

Various clinical studies that investigated SV implantations reported comparable performance between SV and ST users. Remarkably, some of them published even slightly better performance in SV users. (Deguine et al., 1993; Balkany et al., 1996; Gulya and Steenerson, 1996; Bird et al., 1999; Kiefer et al., 2000; Bacciu et al., 2002; Leonor and Santiago Luis, 2004; Lin et al., 2006, 2009; Nichani et al., 2011; Suzuki et al., 2011; Lee et al., 2019; Stock et al., 2020).

Trudel group (Trudel et al., 2018) published that not only was the outcome equivalent between ST and SV CI users but also, interestingly, the sentence recognition in a noisy environment was better in patients who received CI in SV. Also, a bilateral CI user had better discrimination in noise with the SV implant (Leonor and Santiago Luis, 2004). According to these clinical studies, the SV users displayed even more communication improvements through postoperative tests, control sessions, and during their life. As a result, CI insertion in SV seems to be a worthy alternative that should be considered for patients when the ST is inaccessible.

1.5 Limitations & Objectives

CI recipients are increasing, and CI is one of the most influential medical devices worldwide to help hearing-impaired people having a more pleasant life. CI outcomes depend on individual experiences, and dissatisfactions arise when using CI in a noisy environment or listening to music (Gfeller and Lansing, 1991; Leal et al., 2003; Kong et al., 2004; Stickney et al., 2004; McDermott, 2004; Turner et al., 2004; Caldwell and Nittrouer, 2013; Zirn et al., 2016). Several studies reported considerable variability in outcomes and performances between CI users even by the same audiogram and appropriate listening conditions (Blamey et al., 2012; Holden et al., 2013; Goehring et al., 2017).

Overall, there is no reliable technique to estimate the outcomes of the CI in recipients before surgery because of many unknown factors involved. However, various clinical studies investigated the cause of the variability of the outcomes through CI users. They reported factors such as etiology, using hearing aids, age at implantation, ANFs degeneration and survival status, surgical trauma, residual hearing measures, electrode displacement in the cochlea, duration, and age at onset of moderate to profound hearing loss have impacts on CI performances that can be the reason for significant variations in hearing performance (Gantz

Die approbierte gedruckte Originalversion dieser Dissertation ist an der TU Wien Bibliothek verfügbar.
The approved original version of this doctoral thesis is available in print at TU Wien Bibliothek.
TU Bibliothek Your knowledge hub WIEN

et al., 1993; Summerfield and Marshall, 1995; Waltzman et al., 1995; Albu and Babighian, 1997; Shepherd and Javel, 1997; Gomaa et al., 2003; Friedland et al., 2003; Sly et al., 2007; Finley and Skinner, 2008; Friedland et al., 2010; Blamey et al., 2012; Lazard et al., 2012; Holden et al., 2013; Frisch et al., 2015; Cosentino et al., 2016).

One of the important parameters which influence the CI performance is auditory nerve condition, known as neural health status. Shepherd and coworkers (Shepherd and Javel, 1997; Sly et al., 2007) reported a significant decrease in neural responses for degenerated ANFs compared with healthy cases suggesting that the condition of the auditory nerves could be a factor influencing extracellular stimulation outcomes.

The SGNs of the type I entity are responsible for decoding the auditory information and quality of the firing pattern (Miller and Sachs, 1983; Shamma, 1985; Rattay and Lutter, 1997). In addition, their comprehensive innervation of all tonotopically organized cochlear regions is needed for perfect hearing. Moreover, small variations in fiber diameters of type I with a natural degree of myelination are perfect for accurate spike arrival times in the subsequent neural processing unit. Spoendlin published a narrow range of auditory fiber diameters in children against a broader spectrum in adults. The group reported an enormous increase of percentage for the auditory fibers smaller than 1 µm in hearing deficit specimens, suggesting that in terms of neural health, not only the number of auditory fibers but also a normal range of fiber diameters is one of the critical elements for excellent hearing performance (Spoendlin and Schrott, 1989).

Although the degeneration pattern of IHCs and ANFs is not entirely understood yet, it is related to the nature of the cochlear insult, the duration, and the level of hearing loss. For instance, Nadol reported more auditory fibers in the proximity of Rosenthal's canal than in the habenula perforate in the human cochlea with severe degeneration that proposes the shortening of the peripheral parts of ANFs in case of severe and profound degenerations. In addition, the number of central axons was essentially higher than peripheral axons, and the number of somata was reduced to 10% of the normal range (Nadol, 1977). In the case of age-related degenerations, some clinical studies of human temporal bones reported about 1000 to 1800 somata loss per decade that may reduce hearing-in-noise performance (Otte et al., 1978; Makary et al., 2011).

In cases of cochlear damage as a result of noise or drug exposure, some studies showed that while the loss of IHCs occurred within a few days, the loss of peripheral axons and somata occurred within a few weeks and years, respectively (Liberman and Kiang, 1978; Hinojosa et al., 2001; Wu et al., 2019). A recent investigation reported up to 80% loss of connections between IHCs and ANFs for over 60-year-old human temporal bones, whereas only 10% of

Die approbierte gedruckte Originalversion dieser Dissertation ist an der TU Wien Bibliothek verfügbar.
The approved original version of this doctoral thesis is available in print at TU Wien Bibliothek.
TU Bibliothek Your knowledge hub WIEN

IHC degenerated (Wu et al., 2019). Many histological data of humans demonstrate that ANF degeneration mainly affects the peripheral axons (Nadol, 1990; Schuknecht, 1993).

However, at the beginning of this investigation, no histological data were available on the degeneration of the peripheral axons in terms of diameter and myelination thickness based on the audiogram evaluations in humans. Therefore, the first aim of this study is to investigate ANF conditions in terms of the three degeneration parameters: peripheral axon diameter, myelination thickness, and the inner to the outer diameter of a myelinated fiber, known as g-ratio. This study used four human cochleae at different ages with different hearing levels to estimate all three mentioned terms in different cochlea regions to answer how the degree and type of ANF degeneration occur and consequently disturb the hearing efficiency with or without a CI.

The second goal of this study is to investigate various factors that influence neural health estimation based on the polarity effect phenomenon. However, before going into details, some limitations are addressed, and some influential critical parameters for detecting neural health are described.

Most present-day CIs stimulate survival ANFs with symmetric charge-balanced biphasic pulse, consisting of cathodic (CAT) and anodic (ANO) polarities, in the monopolar strategy (MP) since the charge-balanced pulses reduce tissue damage, power consumption, limit channel interactions, and increase dynamic range (Macherey et al., 2006). However, recent clinical studies suggested that pulse configurations and CI stimulation strategies have an impact on the excitation of ANFs (Bierer, 2007; Undurraga et al., 2010; Bierer and Faulkner, 2010; Bahmer and Baumann, 2012a, 2012b, 2013; Carlyon et al., 2013; Macherey et al., 2006, 2008, 2017; Guérit et al., 2018; Hughes et al., 2018; Mesnildrey et al., 2019; X. Luo et al., 2020).

Moreover, various studies demonstrate that the neural status is closely related to speech perception in CI users (Khan et al., 2005; Nadol and Eddington, 2006; Fayad and Linthicum, 2006; Kamakura and Nadol, 2016). Therefore, CI performance depends not only on the number of survived ANFs but also on neural health status (Hughes et al., 2018). In recent decades, numerous studies tried to estimate neural health individually in CI users and find a relationship between implantation outcomes and survival ANFs. Many techniques have been introduced to examine the neural status in CI users, such as pulse rate, pulse polarity, stimulation mode, interphase gap, and phase duration. These techniques revealed substantial outcome variations between subjects and electrodes during psychophysical and electrophysiological measures (Pfingst and Xu, 2004; Bierer, 2007; Bierer and Faulkner, 2010; Bierer et al., 2015a, 2015b; Cosentino et al., 2016; Schvartz-Leyzac and Pfingst, 2016; Zhou, 2016; Carlyon et al., 2018; DeVries and Arenberg, 2018; Guérit et al., 2018; Mesnildrey et al., 2017, 2019).

Die approbierte gedruckte Originalversion dieser Dissertation ist an der TU Wien Bibliothek verfügbar.
The approved original version of this doctoral thesis is available in print at TU Wien Bibliothek.
TU Bibliothek WIEN Your knowledge hub

Among all the aforementioned techniques, polarity sensitivity is a promising way to estimate neural health based on the difference between negative (cathodic) and positive (anodic) pulse. The concept of polarity sensitivity came from animal studies that reported ANFs are stimulated better by CAT compared to ANO pulses, named CAT sensitivity (Hartmann et al., 1984; Miller et al., 1998, 1999). In addition, computational studies by Rattay (Rattay, 1999, Rattay et al., 2001a, 2001b) investigated the behavior of ANFs for both polarities and reported inversed sensitivity behavior in humans compared to what is reported in animals.

Similar observations in clinical studies demonstrated that the polarity sensitivity of ANFs is a potential approach to identify neural health in CI users to improve CI performance and enhance speech perception (Van Wieringen et al., 2008; Macherey et al., 2008; Undurraga et al., 2010; Carlyon et al., 2013, 2018; Pfingst et al., 2015a, 2015b; DeVries et al., 2016; Schvartz-Leyzac and Pfingst, 2018; Goehring et al., 2019; Jahn and Arenberg, 2019b; Mesnildrey et al., 2020).

On the other hand, several studies on human CI recipients reported different and contradictory outcomes by employing polarity sensitivity (Bahmer and Baumann, 2013; Karg et al., 2013; Undurraga et al., 2013; Macherey et al., 2006, 2017; Mesnildrey et al., 2017; Hughes et al., 2017, 2018; Luo et al., 2020 Xu et al., 2020). As a consequence of conflicting results from recent investigations, polarity behavior depends on several factors and parameters that might differ in individual CI users. Consequently, the polarity sensitivity of human ANFs still remains unknown and raises some questions about the reliability of this technique and how it can be used to estimate neural health. Various studies published that the polarity sensitivity could be better investigated with asymmetric pulse shapes (Van Wieringen et al., 2005, 2008; Bahmer and Baumann, 2013, 2016; Karg et al., 2013; Carlyon et al., 2013; Macherey et al., 2006, 2008, 2017; Bahmer et al., 2017; Guérit et al., 2018; Jahn and Arenberg, 2019b) as well as multipolar stimulation strategies (Carlyon et al., 2005; Bierer et al., 2011; Bierer and Nye, 2014; Long et al., 2014; Bierer et al., 2015; DeVries et al., 2016; DeVries and Arenberg, 2018; Jahn and Arenberg, 2019b; Mesnildrey et al., 2019).

In conclusion, based on the latest mentioned investigations, it has been suggested that various parameters such as symmetric vs. asymmetric pulse shapes and MP strategy vs. multipolar strategies may affect the polarity sensitivity of ANFs in CI users. Therefore, the second aim of this study is to investigate the impact of these parameters on the polarity behavior of ANFs by considering different degeneration levels of peripheral parts of ANFs from the outcomes of the previous investigation. In addition, the effect of the distance to the modiolus axis on polarity sensitivity with two different CI arrays is studied.

The third objective of this dissertation is a comparison of SV vs. ST implantation. Various factors such as electrode extrusion, device failures, postoperative infection at the operative

Die approbierte gedruckte Originalversion dieser Dissertation ist an der TU Wien Bibliothek verfügbar.
The approved original version of this doctoral thesis is available in print at TU Wien Bibliothek.
TU Bibliothek Your knowledge hub WIEN

place, replacement CI as advances in technology development, displacement of the electrode array, replacement due to CI, and receiver electrode failure cause increased necessitating of CI reimplantation (Jackler et al., 1987; Balkany et al., 1998; Lin et al., 2006). In addition, not only due to bone growth around the inserted electrode, perielectrode fibrosis, neoosteogenesis, ossification resulting from the first implantation, and intracochlear breakage but also even without fibrosis and ossification, the reimplantation in ST may not be feasible and induces some complications (Balkany et al., 1996; Alexiades et al., 2001; Battmer et al., 2009, 2006).

Noteworthy, SV provides a mean insertion depth of about 23 mm extending up to 30 mm (Kiefer et al., 2000) that can be beneficial not only for a standard array but also for a deep insertion electrode array. Clinical studies reported that SV implantation outcomes are comparable to ST implantation, and the lateral semicircular canal remains intact, resulting in no detrimental influence on vestibular function (Lin, 2009; Suzuki et al., 2011). Therefore, SV implantation is a valuable alternative when there is a difficulty for CI insertion in ST.

To our knowledge, up to now, there is no computational study to investigate and compare the CI in SV with ST. Thus, the third aim of this study is to investigate the behavior of CI electrodes in both scalae, ST and SV, in a comparable way in which the electrodes are located at an equivalent distance to a specific point of the peripheral process of the closest ANF. The main goal of this part is to analyze ANF excitation features in both scalae and demonstrate similarity and dissimilarity between SV and ST implantations.

1.6 Outlines

Chapter 2 Methods describes all information and fundamental methods used in this study in two sections, one general method and the second distinctive method.

Chapter 3 Results present all outcomes of this study based on the three aims. The first part shows the degeneration pattern of the peripheral section of human auditory neurons and consequently the impact of reduction of peripheral axon and myelination thickness on the intra- and extracellular stimulations. Part two displays the polarity sensitivity of the human auditory system under different circumstances such as pulse shape, CI stimulation strategy, array type, and degeneration level of ANFs. The last part demonstrates that the excitation behavior of ANFs depends on the electrode and CI array insertion between scala tympani and scala vestibuli.

Chapter 4 Discussion represents all findings of this dissertation based on the aims individually and compared with literature regarding the study's findings.

Die approbierte gedruckte Originalversion dieser Dissertation ist an der TU Wien Bibliothek verfügbar.
The approved original version of this doctoral thesis is available in print at TU Wien Bibliothek.
TU Bibliothek Your knowledge hub WIEN

Chapter 2

Methods

The methods chapter is divided into two main parts, the first part is the general method, and the second part is the distinctive method.

The general method outlines characteristics and electrical properties of the cell membrane, mathematical models, computational methods, and image processing required for computing neuron behavior during extracellular electrical stimulation. In section 2.1.1, the cell membrane with its electrical properties is explained. Second, passive and active cell membrane models (2.1.2) and the Hodgkin Huxley model (2.1.3) are presented. In section 2.1.4, compartment models are described; In addition, the multi-compartment model of auditory nerves used in this study is explained in detail (2.1.5). In the two subsequent sections, activating function and numerical solutions are addressed. The finite element models of the human cochlea, electrode arrays, and reconstructed auditory nerve bundles are introduced in sections 2.1.9 to 2.1.11. The following section (2.1.12) explains image processing based on micro-CT data segmentation and data preparation to generate a three-dimensional human cochlea.

The distinctive method describes individually and more specifically all materials, methods, and data preparation used in this dissertation to investigate all aims of the study. The first section (2.2.1) explains data preparation and gathering concerning the degeneration pattern of human cochlear nerves investigation. The specific methods for the particular investigation are described. The second part addresses all performed methods to investigate the impact of pulse shapes, CI stimulation strategies, and arrays on polarity behavior of human ANFs study in section 2.2.2. The third and last section (2.2.3) introduces all methodology for a computational study of scala tympani versus scala vestibuli implantations with electrodes and array insertion in detail.

Die approbierte gedruckte Originalversion dieser Dissertation ist an der TU Wien Bibliothek verfügbar.
The approved original version of this doctoral thesis is available in print at TU Wien Bibliothek.
TU WIEN Bibliothek Your knowledge hub

2.1 General Methods

2.1.1 Cell membrane

A cell membrane is a thin tissue that separates inside the cell from the outside environment and acts as a barrier between the cell and its surroundings to preserve cell configuration. The cell membrane is made of a bilayer of phospholipids and proteins. The phospholipid structure of the membrane carries both hydrophilic (polar) and hydrophobic (nonpolar) regions. In addition, the phospholipid heads are hydrophilic that have attraction features to water; in contrast, the tails are hydrophobic with repellent characteristics by water.

Polar molecules and ions fill the intra- and extracellular mediums of a cell. Cell naturally is in a resting state, which means there is no input current to provoke replacing ions. The intracellular fluid includes a high concentration of potassium (K^+) and organic (A^-) ions that create a negative charge inside the cell and a low small concentration of sodium (Na^+) and chloride (Cl^-) ions. In contrast, the extracellular fluid has a positive charge since the sodium concentration is high and the potassium concentration is low (Figure 2.1). In addition, the cell membrane has an ion permeability feature that makes it more permeable to potassium than sodium and not to organic ions. Furthermore, the distribution of the ions is regulated by ion pumps, ion channels, and the permeability of the membrane. Membrane permeability occurs due to diffusion force (F_D) and electrostatic pressure (F_E), which affects the ion movements between intra- and extracellular spaces.

The electrophysiological features of the cell membrane allow us to study the electrical properties of living cells by measuring the electric current and activity of neurons. Due to the specific cell membrane structure, the electrical properties of the membrane are divided into passive and active properties. The passive membrane facilitates keeping a stable state of the transmembrane voltage, also known as the membrane resting potential. This equilibrium state occurs by gradient and electric forces that can be described by the Nernst and Goldman equations.

Die approbierte gedruckte Originalversion dieser Dissertation ist an der TU Wien Bibliothek verfügbar.
The approved original version of this doctoral thesis is available in print at TU Wien Bibliothek.
TU Bibliothek Your knowledge hub WIEN

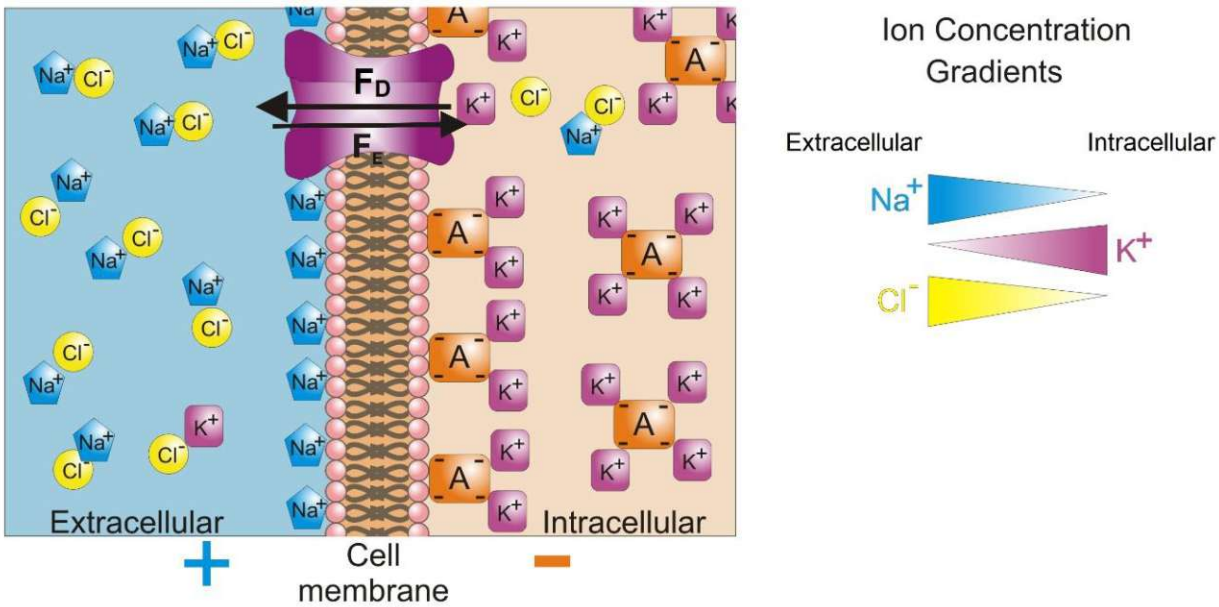

Figure 2.1. Differential distribution of ions in intra- and extracellular medium of the cell membrane. The gradient of concentration and voltage influence the equilibrium potential. The Figure is adapted from (Wikimedia Commons, 2021).

The most crucial ions in humans are sodium (Na^+), potassium (K^+), calcium (Ca^{2+}), and chloride (Cl^-). In addition, the membrane is penetrable to potassium and chloride in the resting state and almost not penetrable to calcium and sodium. The variety of ion concentrations in intra- and extracellular such as high potassium and high sodium concentrations in intracellular and extracellular, respectively, results in a different intra- and extracellular potential.

The ions move freely through the cell membrane through specific channels and structures, which causes an electric field. The equilibrium potential for any concentration gradient of a particular ion crossing the membrane can be measured by the Nernst equation (Nernst, 1888):

$$E = \frac{RT}{zF} \cdot ln \frac{IC_e}{IC_i} \tag{2.1}$$

where E is the Nernst potential for a particular ion in [mV], R is the gas constant (8.314 J/Kmol), T is the temperature in Kelvin, z is the valence of ion, F is the Faraday's constant (96485.33 C/mol), IC_i and IC_e Indicate particular ion concentrations in intra- and extracellular, respectively.

Membrane potential at resting state ($V_{m_{rest}}$) is defined with different intra- and extracellular potentials that can be measured by the Goldman-Hodgkin-Katz equation (Goldman, 1943), in which several ions channels that influence the membrane potential at rest are included:

Die approbierte gedruckte Originalversion dieser Dissertation ist an der TU Wien Bibliothek verfügbar.
The approved original version of this doctoral thesis is available in print at TU Wien Bibliothek.
TU Bibliothek Your knowledge hub WIEN

$$V_{m_{rest}} = \frac{RT}{zF} . ln \frac{p_K[K]_e + p_{Na}[Na]_e + p_{Cl}[Cl]_i}{p_K[K]_i + p_{Na}[Na]_i + p_{Cl}[Cl]_e} \tag{2.2}$$

where K, Na, and Cl represent potassium, sodium, and chloride concentration, respectively. The suffixes i and e stand for intracellular and extracellular medium, p denotes the permeability of the ions mentioned above and measured in [cm/s].

The resting membrane potential ranges from −40 mV to −90 mV depending on neuron types and locations as well as the involved ion channels.

2.1.2 Membrane electrical properties

A patch of a membrane is described either with a passive model if it shows passive properties or with an active model if ion channel dynamics are included. Because of the bilipid nature of the membrane and the appearance of ions with opposite charges, the membrane acts as a capacitor. In a passive approach, however, no voltage-gated ion channels are involved; hence, the membrane is assumed as RC circuit with constant resistance. Ion current flow across the membrane follows Ohm's law

$$V_m = R_m . I_R \tag{2.3}$$

with V_m, R_m, and I_R representing the voltage changes between intra- and extracellular, membrane potential [mV], membrane resistance [kΩ.cm^2], and current density [μA/cm^2].

The capacitance current (I_C) can be calculated as

$$I_C = \frac{dQ}{dt} = C_m . \frac{dV_m}{dt} \tag{2.4}$$

where C_m indicates the membrane capacitance per unit area [μF/cm^2] and Q is the charge. Now, the membrane current density (I_m) in [μA/cm^2] can be determined as

$$I_m = I_C(t) + I_R = C_m . \frac{dV_m}{dt} + \frac{V_m}{R_m} \tag{2.5}$$

If a stimulus current (I_{Stim}) is injected into the cell, the membrane potential is changed, and by considering the first Kirchhoff's law, it is calculated as

$$I_m(t) + I_{Stim}(t) = I_C(t) + I_R + I_{Stim}(t) = 0 \tag{2.6}$$

Die approbierte gedruckte Originalversion dieser Dissertation ist an der TU Wien Bibliothek verfügbar.
The approved original version of this doctoral thesis is available in print at TU Wien Bibliothek.
TU Bibliothek Your knowledge hub WIEN

$$\frac{dV_m(t)}{dt} = -(I_{Stim}(t) + \frac{V_m(t)}{R_m})/C_m \tag{2.7}$$

$$\frac{d(V_i - V_e)(t)}{dt} = -(I_{Stim}(t) + \frac{(V_i(t) - V_e(t)}{R_m})/C_m \tag{2.8}$$

where membrane potential at $t = 0$ is equal to the membrane potential at rest ($V_{m_{rest}}$). V_i and V_e indicate intra- and extracellular voltage membranes, respectively.

In the active model, R_m is not constant. For simplicity, it is described by the sum of the conductances of the involved ion types; the ionic voltage-depending conductances (G_{ion}) are measured in [mS/cm^2].

$$I_{ion} = I_{Na} + I_K + I_L \tag{2.9}$$

$$I_{ion} = G_{Na}(V_m - V_{Na}) + G_K(V_m - V_K) + G_L(V_m - V_L) \tag{2.10}$$

Ion channels types respond differently to changes in the membrane potential. The voltage-gated ion channels were modeled based on voltage-clamp experiments by Hodgkin and Huxley, described in the following section.

2.1.3 Hodgkin and Huxley model

The famous Hodgkin and Huxley (Hodgkin and Huxley, 1952a-c) model, known as the HH model, gives ion kinetic channels information measured from a squid axon. They investigated the influence of ionic movements and membrane potential based on injected current with the insertion of an electrode into the cell; hence, they measured how the movement of ions influences shifts of membrane potential through the injected current. The HH model allows determining membrane potential by applying differential equations.

The HH model includes sodium, potassium, and leakage current flow at an original temperature of about 6.3 °C and -70 mV as the rest membrane potential.

$$V_{ion} = E_{ion} - V_{res} \tag{2.11}$$

Die approbierte gedruckte Originalversion dieser Dissertation ist an der TU Wien Bibliothek verfügbar.
The approved original version of this doctoral thesis is available in print at TU Wien Bibliothek.
TU Bibliothek Your knowledge hub WIEN

$$\frac{dV_m}{dt} = \frac{-[\ g_{Na}m^3h(\ V_m - V_{Na}) +\ \ g_K n^4(\ V_m - V_K) + g_L(\ V_m - V_L\ )] +\ I_{Stim}}{C_m} \tag{2.12}$$

where $C_m = 1$ [μF/cm^2], and g_{Na}, g_K, g_L are the maximum ion conductivities. These maximum conductivities, as well as the Nernst potentials of the involved ions (V_{Na}, V_K, V_L) are listed in Table 2.1.

Ion	g_{ion} [mS/cm^2]	V_{ion} [mV]
Na	120	50
k	36	-77
Leakage (*L*)	0.3	-54.4

Table 2.1. Electrical key parameters of the HH model.

The parameters m, n, and h are voltage-dependent gating probabilities in the HH model quantifying the open states. The parameters m and h are the probability of the sodium channel's activation and inactivation gates, respectively. The n denotes the activation gate probability of the potassium channel. In response to an excitatory stimulus, the probabilities of activation (m, n) enhance, which increases the inflow of sodium inside the cell, resulting in depolarization of membrane potential. In addition, the probability of inactivation gates (h) decrease that resulting in the repolarization of membrane potential. To establish the equilibrium, the probability of potassium channels being open becomes higher, leading to potassium outflow, which repolarizes the membrane voltage and returns it to the resting state.

$$\frac{dm}{dt} = [-(\alpha_m + \beta_m).m +\ \alpha_m].k \tag{2.13}$$

$$\frac{dn}{dt} = [-(\alpha_n + \beta_n).n +\ \alpha_n].k \tag{2.14}$$

$$\frac{dh}{dt} = [-(\alpha_h + \beta_h).h +\ \alpha_h].k \tag{2.15}$$

where k depicting the temperature coefficient for T in $°C$:

$$k =\ 3^{(0.1T-0.63)} \tag{2.16}$$

Die approbierte gedruckte Originalversion dieser Dissertation ist an der TU Wien Bibliothek verfügbar.
The approved original version of this doctoral thesis is available in print at TU Wien Bibliothek.
TU Bibliothek Your knowledge hub WIEN

α and β are gating rates used to fit the calculated and experimental data and can be written as follows:

$$\alpha_m = \frac{2.5 - 0.1V_m}{e^{(2.5-0.1V_m)} - 1} \qquad \beta_m = 4.e^{(-\frac{V_m}{18})} \tag{2.17}$$

$$\alpha_n = \frac{1 - 0.1V_m}{10\,(e^{(1-0.1V_m)} - 1)} \qquad \beta_n = 0.125.e^{(-\frac{V_m}{80})} \tag{2.18}$$

$$\alpha_h = 0.07.e^{(-\frac{V_m}{20})} \qquad \beta_h = \frac{1}{e^{(3-0.1V_m)} + 1} \tag{2.19}$$

where at resting state $t = 0$, V_m, m, n, and h values are equal to 0, 0.05, 0.32, and 0.6, respectively.

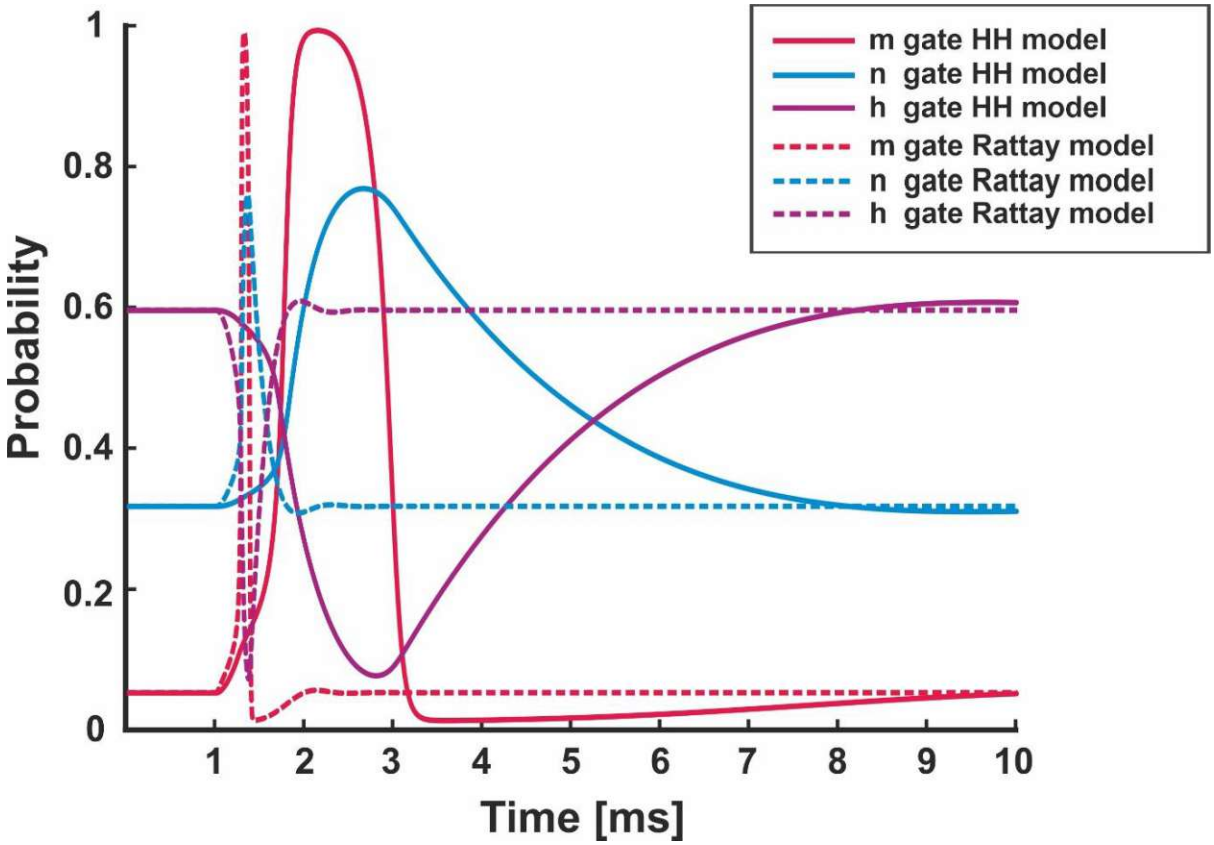

Figure 2.2. Comparison of gating variables in Hodgkin and Huxley (HH model) experiment, m, n, and h indicated in solid lines with red, blue, and green, respectively, and Rattay model of the human auditory nerve with the same gating variable represents with the dashed line in same color code manner.

Die approbierte gedruckte Originalversion dieser Dissertation ist an der TU Wien Bibliothek verfügbar.
The approved original version of this doctoral thesis is available in print at TU Wien Bibliothek.
TU Bibliothek Your knowledge hub WIEN

The gating variable of human auditory neurons in the Rattay model (Rattay et al., 2001b) was based on the HH model but modified. Rattay's model was recommended that all gating variables be sped up by factor k = 12. Figure 2.2 shows the comparison of the probability of all three gating between HH and Rattay models. In addition, Figure 2.3 demonstrates AP based on HH and Rattay models where the AP of Rattay model is faster and sharper than the HH model and similar to the real one based on experiments.

An AP happens through the membrane potential rising (depolarization) and falling (repolarization) under some circumstances and plays a critical role in neurons communication (Figure 2.3). The movements of ions affect the membrane potential by opening and closing the ions channels, and the fast movement of ions due to stimulus (injected current) alters the membrane potential that causes increased membrane potential and generates an AP.

The equations mentioned above can easily describe an AP. Nevertheless, the neuron is not activated if the stimulus is not strong enough to increase the membrane potential to a certain level, called the excitation threshold level or threshold. In contrast, when the stimulus causes the membrane potential to increase to a particular threshold level, Na^+ ion channels open, and Na^+ flows to the intracellular that causes a sharp increase in the membrane potential.

During the rapid increase of membrane potential and before reaching the maximum potential, Na^+ channels start to inactivate, and spontaneously the K^+ ion channels open and leave the intracellular and flow into the extracellular. In addition, diffusion force and electrostatic pressure cause the K^+ leaving to be slower than entering Na^+, and membrane potential raises until the peak where the influx of Na^+ stops.

However, K^+ channels are still active and leaving the cell resulting in decreasing the membrane potential (depolarization) until the membrane potential reaches the resting state and K^+ channels are closed. In addition, the Na^+ and K^+ ions are still not stable and need time to balance the concentration in both intra- and extracellular fluids that takes place in the refractory time, which is called the hyperpolarization phase, where the membrane potential is becoming more negative than the resting membrane potential.

Die approbierte gedruckte Originalversion dieser Dissertation ist an der TU Wien Bibliothek verfügbar.
The approved original version of this doctoral thesis is available in print at TU Wien Bibliothek.
TU Bibliothek Your knowledge hub WIEN

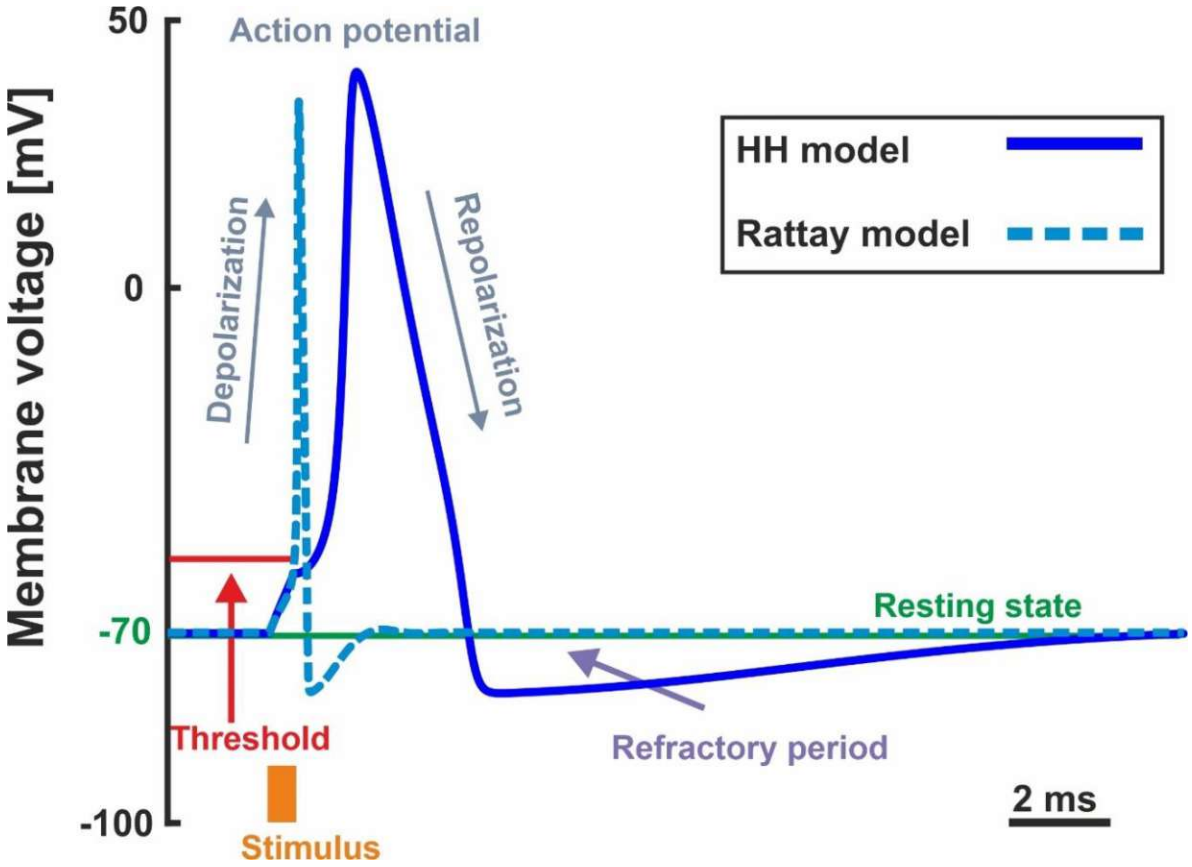

Figure 2.3. A schematic of an action potential during a stimulus is applied. The action potential is generated due to the activation of sodium channels leading to the rise in membrane potential; through the depolarization, sodium channels inactivate, and potassium channels activate, causing a decrease in the membrane potential. Finally, all channels are closed and membrane reaches the resting state.

2.1.4 Compartment models

The signaling of a neuron can be modeled either by a single compartment, in which the neuron is considered as a single unit, or by a multi-compartment (Figure 2.4), in which the conduction of excitation along the neuron can be investigated.

Die approbierte gedruckte Originalversion dieser Dissertation ist an der TU Wien Bibliothek verfügbar.
The approved original version of this doctoral thesis is available in print at TU Wien Bibliothek.
TU Bibliothek Your knowledge hub WIEN

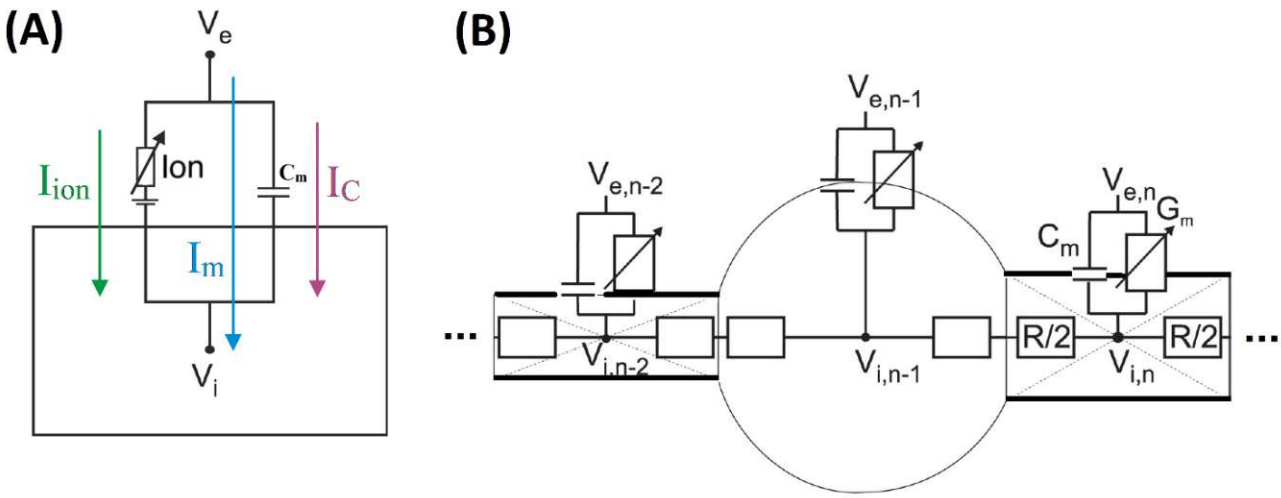

Figure 2.4. Schematic drawing of single- and multi-compartment models. **(A)** Single compartment model includes capacitance and ion currents across the cell membrane. **(B)** Multi-compartment model of soma and its processes. Note that due to potential changes from one subunit to the other, a multi-compartment model consists of an axial current that flows between neighboring compartments. The Figure is adapted from (Rattay et al., 2001b).

Multi-compartment models can mimic the three-dimensional structure of neurons to study the neuron excitation during intra- and extracellular stimulation. Based on this method, a neuron is divided into various segments (multiple compartments) that are connected and described as electric circuits. Moreover, in the multi-compartment model, each compartment is internally connected and identified by internal axial current (I_{Axial}) in the axial direction due to different axial conductivity and potential from neighbor compartments.

The total current of the multi-compartments that consist of nth subunits can be determined by applying Kirchhoff's law

$$I_{ion_n} + I_{Stim_n} + I_{C_n} + I_{Axial_n} = 0 \tag{2.20}$$

Note that all currents and voltages are time-dependent. The axial current for the nth compartment (I_{Axial_n}) is determined as

$$I_{Axial_n} = \frac{V_{i_n} - V_{i_{n-1}}}{R_n/_2 + R_{n-1}/_2} + \frac{V_{i_n} - V_{i_{n+1}}}{R_n/_2 + R_{n+1}/_2} + \cdots \tag{2.21}$$

where $V_{i_{n-1}}$ and $V_{i_{n+1}}$ denote membrane potential of the left and right investigated neighbors compartments. $R_n/_2$ represents the axial resistance (axoplasm resistance) of the nth

Die approbierte gedruckte Originalversion dieser Dissertation ist an der TU Wien Bibliothek verfügbar.
The approved original version of this doctoral thesis is available in print at TU Wien Bibliothek.
TU Bibliothek Your knowledge hub WIEN

compartment from the middle to the end of the compartment in [kΩ] that can be calculated in cylindrical compartments as

$$A_n = r_n^2 \pi \qquad R_n = \frac{\rho_i \, l_n}{A_n}$$
$$R_n/_2 = \frac{\rho_i \, l_n}{2 r_n^2 \pi} \tag{2.22}$$

where A_n denotes cross-section area of the nth compartment, and ρ_i, r_n, as well as l_n indicate the intracellular resistivity, cross-sectional radius, and length of the nth compartment, respectively.

The axial resistance of a spherical soma is determined with (Rattay et al., 2003):

$$A_{Soma} = 4 r_{Soma}^2 \pi - \sum \left(2 r_{Soma} \pi h_j\right) \tag{2.23}$$

$$h_j = r_{Soma} - z_j \qquad z_j = \sqrt{r_{Soma}^2 - r_{Adj}^2} \tag{2.24}$$

$$R_{Soma}/_2 = \frac{\rho_i}{2 r_{Soma} \pi} \ln \frac{r_{Soma} + z_j}{r_{Soma} - z_j} \tag{2.25}$$

where r_{Adj} and r_{Soma} represent the radius of the adjacent compartment and radius of soma in [cm].

2.1.5 Multi-compartment model of human spiral ganglion neuron

The bipolar SGN consists of a peripheral axon (peripheral process), soma, and central axon (central process) (Figure 1.4). The SGN is implemented by an electrical network that includes numerous connected subunits in peripheral and central processes and somatic regions based on the multi-compartments model (Figure 2.5). These connected subunits consist of the non-myelinated terminal, nodes of Ranvier, internodes, pre-somatic, soma, and post-somatic regions that allow the derivation of a system of differential equations for the membrane potential in each compartment. The calculated temporal and spatial changes in membrane potential are used to study the initiation and propagation of an AP.

Die approbierte gedruckte Originalversion dieser Dissertation ist an der TU Wien Bibliothek verfügbar.
The approved original version of this doctoral thesis is available in print at TU Wien Bibliothek.
TU Bibliothek Your knowledge hub WIEN

Over the past decades, several multi-compartment models of human ANF have been established to provide a better understanding of ANFs behavior under different stimulation strategies. The Rattay model (Rattay et al., 2001b) is known as one of the closest models to experimental outcomes. Recently (Bachmaier et al., 2019) published an investigation with the three most cited and famous multi-compartment models of human ANF and reported that the Rattay multi-compartment model replicates many features known from experiments in some of their examinations. Here, the Rattay model is described briefly; however, more information was described in detail (Rattay et al., 2001b).

The model is divided into passive and active compartments. Internodes consist of only leakage current recognized as passive compartments, which have linear resistive membrane current represented by a constant conductance for each membrane layer (grey in Figure 2.5). On the other hand, active sites such as the soma, nodes of Ranvier, pre- and post-somatic compartments includes non-linear sodium and potassium currents, and linear leakage current; all compartments are modeled with Hodgkin Huxley ion channel kinetics (Hodgkin and Huxley, 1952) with some modifications which are explained in the flowing section.

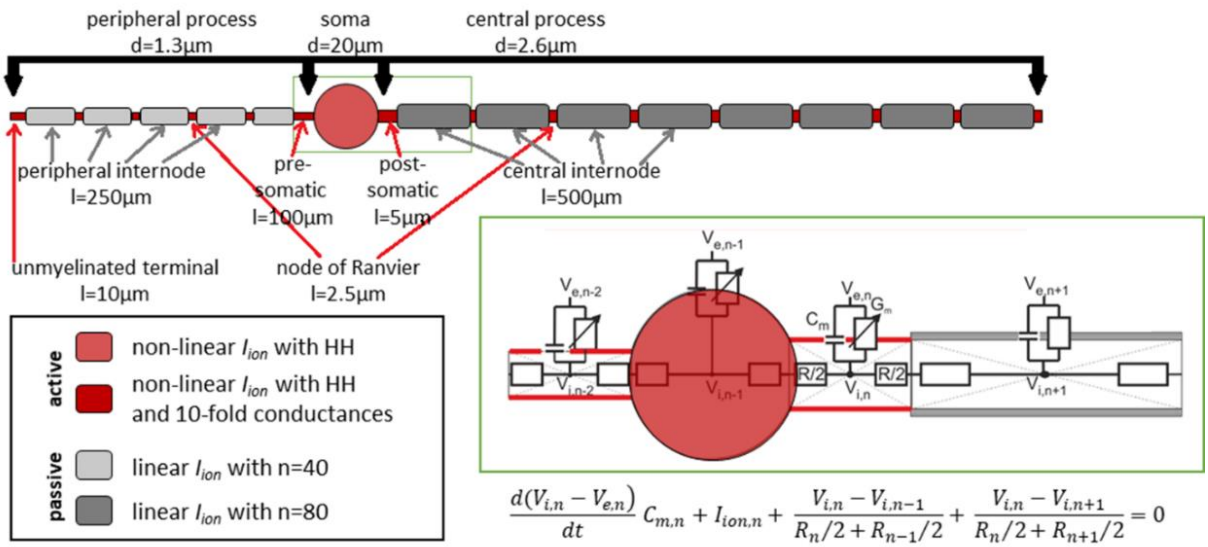

Figure 2.5. Representation of the compartment model of a human SGN. Geometric parameters are indicated in the top part; the colors describe the electrical parameters. The electrical network model of the soma area in the green box is displayed at the right, including the corresponding differential equation in the nth compartment. The currents are defined by extracellular potential V_e, intracellular potential V_i, membrane capacitance C_m, membrane conductance G_m, and intracellular resistance R (Potrusil et al., 2020).

All compartments with non-linear resistive transmembrane currents (red in Figure 2.5) were modeled with Hodgkin Huxley ion channel kinetics adjusted to a temperature of 29 °C, which

Die approbierte gedruckte Originalversion dieser Dissertation ist an der TU Wien Bibliothek verfügbar.
The approved original version of this doctoral thesis is available in print at TU Wien Bibliothek.
TU Bibliothek Your knowledge hub WIEN

fits the AP duration in the human cochlea (Hodgkin and Huxley, 1952; Motz and Rattay, 1986; Rattay et al., 2013). The soma was further surrounded by three membrane layers (Potrusil et al., 2012), and internodes are densely shielded by layers of myelin (n_m), resulting in membrane capacitance and membrane conductance proportional to $1/n_m$. In addition, the peripheral and central processes are considered to have 40 and 80 layers, respectively (Arnesen and Osen, 1978; Arbuthnott et al., 1980; Spoendlin and Schrott, 1989; Rattay, 1990). In all other active compartments, i.e., the nodes of Ranvier and the pre-and post-somatic regions, a 10-fold increase of HH membrane conductance accounted for experimentally reported high ion channel densities (Rattay and Aberham, 1993; Rattay et al., 2002; Hossain et al., 2005).

The peripheral and central processes, as well as soma diameters are 1.3, 2.6, and 20 µm, respectively (Figure 2.5). The length of the active pre- and post-somatic regions are 100 and 5 mm; the peripheral terminal compartment is 10 µm long. The length of a node of Ranvier is 2.5 µm, whereas peripheral and central internodes have a standard length of 250 and 500 µm, except for the last peripheral internode, which has a length of 210 µm.

2.1.6 Extracellular stimulation

Generated electric current with an electrode from the outside of a neuron creates extracellular electrical potentials that may stimulate some regions of the neuron and elicit an AP. In this approach, the position of electrodes and morphology of neurons play critical roles.

The extracellular potential profiles were determined in two approaches, analytical and numerical methods. In the analytical method, the point source method was used for a two-dimensional neuron model. In this method, the electrode is considered as a point and creates a homogeneous electric field. The extracellular potentials were calculated as

$$V_{e_n} = \frac{\rho_e I_e}{4\pi r_{dis}} \tag{2.26}$$

where I_e in [mA] and ρ_e in [Ω.cm] indicate the electrode current and the extracellular resistivity of homogeneous medium. The distance between an active electrode and the nth compartment is denoted with r_{dis}.

In the second approach using the finite element method (FEM), the geometry of the cochlea together with an implant was included as well as the 3D structure of selected SGNs. More details on this method are given in section 2.1.10-11.

Die approbierte gedruckte Originalversion dieser Dissertation ist an der TU Wien Bibliothek verfügbar.
The approved original version of this doctoral thesis is available in print at TU Wien Bibliothek.
TU Bibliothek Your knowledge hub WIEN

In both methods, the excitation of a target neuron was calculated in a two-step procedure. First, the extracellular V_e was calculated for every compartment, and in the second step these V_e values entered the compartment model. The virtual stimulation current and membrane potential can be determined from the extracellular potentials calculated from either a point source or a FEM approach.

$$I_{Stim_n} = \frac{V_{e_n} - V_{e_{n-1}}}{R_n/_2 + R_{n-1}/_2} + \frac{V_{e_n} - V_{e_{n+1}}}{R_n/_2 + R_{n+1}/_2} + \cdots \tag{2.27}$$

where V_{e_n} denotes the extracellular potential at nth compartment. By setting the I_{Stim} then the membrane potential can be calculated as follows

$$\frac{dV_{m_n}}{dt} = \frac{I_{Stim_n} - I_{ion_n} - I_{Axial_n}}{C_{m_n}} \tag{2.28}$$

2.1.7 Activating function

The concept of the activating function (AF) was introduced by Frank Rattay in 1986 (Rattay, 1986) to explain the effect of an electric field during extracellular stimulation. The activating function is proportional to the second derivative of the extracellular voltage V_e along an non-myelinated axon with constant diameter, while for myelinated axons AF is given by the second difference quotient of V_e. The activating function is a robust mathematical conception to get a preliminary understanding of the influence of applied electric field on target neurons without any information about the kinetics of the ion channels.

The activating function AF was also formulated for neurons of arbitrary shape (Rattay, 1999) and can be implemented on multi-compartment models to calculate the direct stimulating influence of the extracellular potential on compartment n as

$$AF_n = \left[\frac{V_{e_{n-1}} - V_{e_n}}{R_{n-1}/_2 + R_n/_2} + \frac{V_{e_{n+1}} - V_{e_n}}{R_{n+1}/_2 + R_n/_2}\right] / C_{m,n} \tag{2.29}$$

where V_{e_n}, R_n, and C_m are the extracellular voltage, the axial resistance, and the membrane capacitance, respectively, at the nth compartment.

Die approbierte gedruckte Originalversion dieser Dissertation ist an der TU Wien Bibliothek verfügbar.
The approved original version of this doctoral thesis is available in print at TU Wien Bibliothek.
TU Bibliothek Your knowledge hub WIEN

The activating function is a good predictor for AP initiation. A region will be depolarized when the activating function is positive (AF > 0). Contrary, a negative activating function (AF < 0) indicates hyperpolarization (Figure 2.6).

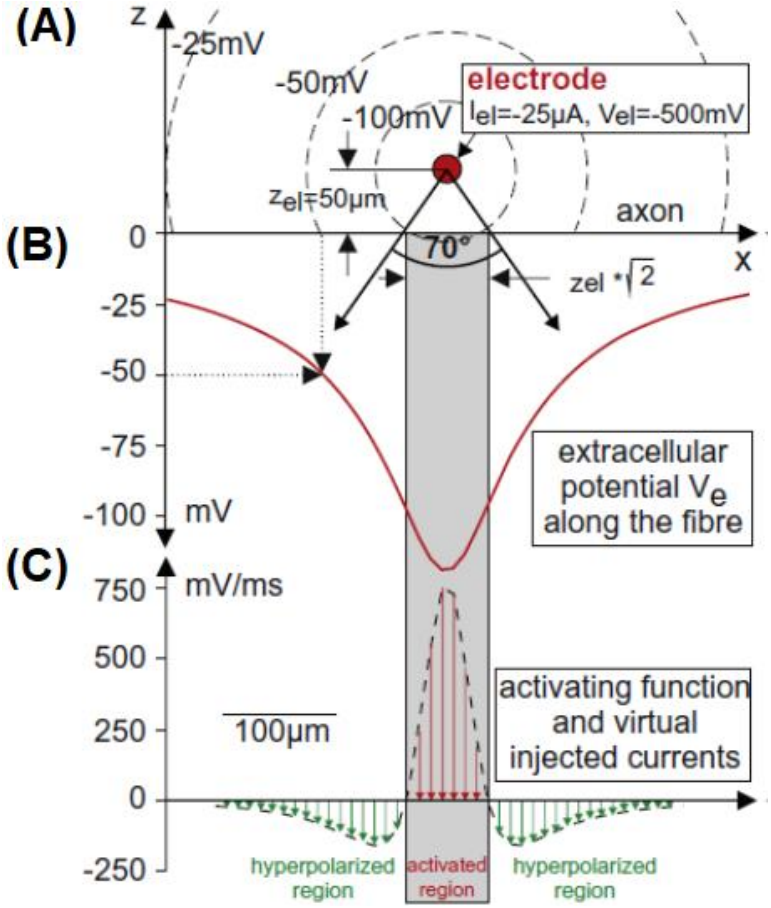

Figure 2.6. Activating function generated by extracellular stimulation of a straight non-myelinated axon with a spherical electrode. **(A)** Geometry and isopotentials for a point source 50 µm above a fiber positioned at the x-axis. **(B)** Calculating activating function by using extracellular potential. **(C)** A fiber with d = 1 µm and compartment length Δx = 10 µm results in a peak activating function value of 740 mV/ms. Figure and caption are slightly adapted from (Rattay et al., 2012).

2.1.8 Numerical solution

Sophisticated and complex dynamic models like neuron simulations are not possible to solve by analytical solution; hence, the numerical method is an alternative to solve ordinary differential equations (ODEs). One commonly used method in computational neuroscience to solve and analyze ODEs is the backward (implicit) Euler method. However, both forward and

Die approbierte gedruckte Originalversion dieser Dissertation ist an der TU Wien Bibliothek verfügbar.
The approved original version of this doctoral thesis is available in print at TU Wien Bibliothek.
TU Bibliothek Your knowledge hub WIEN

backward Euler methods can be used for solving numerical approximations to the solution of time-dependent ODEs.

As the name implies, in the forward Euler method, the approximation at the following time step is presented by a formula depending only on the approximation at the current time step.

$$y_{n+1} = y_n + hf(y_n, t_n) \tag{2.30}$$

The forward Euler method is based on Taylor series expansions. When $t = t_n$:

$$y_{n+1} = y_n + hf(y_n, t_n) + O(h^2) \tag{2.31}$$

where $O(h^2)$ is the local truncation error that happens at every time step based on the Taylor series.

The forward Euler method is simple to implement; however, some drawback appears on the time step size for ensuring numerical stability.

rewriting the forward Euler equation results in

$$\begin{aligned} y_{n+1} = y_n - ay_n h = (1-ah)y_n = (1-ah)^2 y_{n-1} = \cdots = (1-ah)^n y_1 \\ = (1-ah)^{n+1} y_0 \end{aligned} \tag{2.32}$$

To avoid large errors, it is required that $|1 - ah| < 1$ that leads to stability criterion $h < {}^{2}/_{a}$.

On the other hand, an extra equation needs to be solved in the backward Euler method to find the final solution. In contrast to the forward Euler method, the backward method requires solving the non-linear equation at each time step. Based on the Taylor series expansion:

$$y(t_{n+1} - h) = y(t_{n+1}) - h\left(\frac{dy}{dt}\right)_{t_{n+1}} + O(h^2) \tag{2.33}$$

numerically stable is valid for all $h > 0$.

$$y_{n+1} = y_n + hf(y_{n+1}, t_{n+1}) \tag{2.34}$$

where $f(y_{n+1}, t_{n+1})$ is unknown.

The presented simulation results were obtained by the backward Euler method.

Die approbierte gedruckte Originalversion dieser Dissertation ist an der TU Wien Bibliothek verfügbar.
The approved original version of this doctoral thesis is available in print at TU Wien Bibliothek.
TU Bibliothek Your knowledge hub WIEN

2.1.9 Finite Element Method

The AC/DC module of COMSOL (https://www.comsol.com) was used to compute electric fields elicited by CI stimulation under quasi-static conditions. The human inner ear model is a volume conductor, which can be described mathematically by Maxwell's equation. An electric field in dielectric volume conductors can be identified with a potential field (ϕ) gradient

$$E = -\nabla\phi \tag{2.35}$$

Based on Ohm's law, the current density is related to the electric field (E), where J is the current density and σ is the electrical conductivity (S/m) of the components.

$$J = \sigma E \tag{2.36}$$

When stationary electric currents in a conductive medium are studied, and an active source for generating current is available with

$$J = \sigma E + J_e \tag{2.37}$$

where is J_e externally generated current density (A/m^2).

Under quasi-static conditions, it is necessary to generalize the equation that the divergence of the equation should be zero.

$$\nabla . J = 0 \qquad \nabla . \sigma E + \nabla J_e = -\nabla . (\sigma \nabla V - J_e) = 0$$

$$-\nabla . J_e = \nabla . \sigma E \tag{2.38}$$

with interchanging equations (2.35) and (2.38):

$$\nabla . J_e = \nabla . \sigma(\nabla\phi)$$

$$\nabla . (\sigma \nabla \phi) = I_v \tag{2.39}$$

where I_v is the internal current source per unit volume that makes Poisson's equation (Klepfer et al., 1997).

Die approbierte gedruckte Originalversion dieser Dissertation ist an der TU Wien Bibliothek verfügbar.
The approved original version of this doctoral thesis is available in print at TU Wien Bibliothek.
TU Bibliothek Your knowledge hub WIEN

2.1.10 FE Model Configurations

Three-dimensional anatomically detailed FE model of a human cochlea and thirty reconstructed tonotopically organized auditory pathways of type I ANFs (Figure 2.7) were performed in this study, using COMSOL simulation software (versions 5.4 & 5.5, https://www.comsol.com). The FE of the human cochlea model in this dissertation was published first in (Potrusil et al., 2020).

Figure 2.7 demonstrates an electrode array with 12 contacts inserted in the ST of the model with the thirty tonotopically reconstructed nerve fiber bundles. The investigated nerve fiber bundles from basal turn to apical turn are visualized in a color-coded manner. It comprises fourteen nerve fiber bundles (black) representing frequencies from 1166 to 11524 Hz (298° - 28°) over a length of 18.2 mm, which is a proper fraction for the basal turn concerning the overall length of the human organ of Corti (Erixon et al., 2009). In addition, nine nerve fiber bundles from the middle turn (green) represent the next 180° turn along 8.35 mm of the organ of Corti with covering a hearing spectrum from 266 to 976 Hz (592° - 327°). Finally, seven nerve fiber bundles from the apical turn (red) indicate a frequency range of 42 - 228 Hz (928° - 620°) over a distance of 5.7 mm. All nerve fiber bundles information can be found in Table 2.2.

Taking into account the impact of the precise cochlear model, for extracellular stimulation, it was adopted an accurate FE cochlea model and thirty three-dimensional ANF pathways that were reconstructed from tracing real fiber bundles following natural fiber spirality, e.g., highly helical pathway in the peripheral sides of the most apical fiber (up to 900° of overall rotation) systematically decreasing in most basal fiber (to 30° overall rotation).

Die approbierte gedruckte Originalversion dieser Dissertation ist an der TU Wien Bibliothek verfügbar.
The approved original version of this doctoral thesis is available in print at TU Wien Bibliothek.
TU Bibliothek Your knowledge hub WIEN

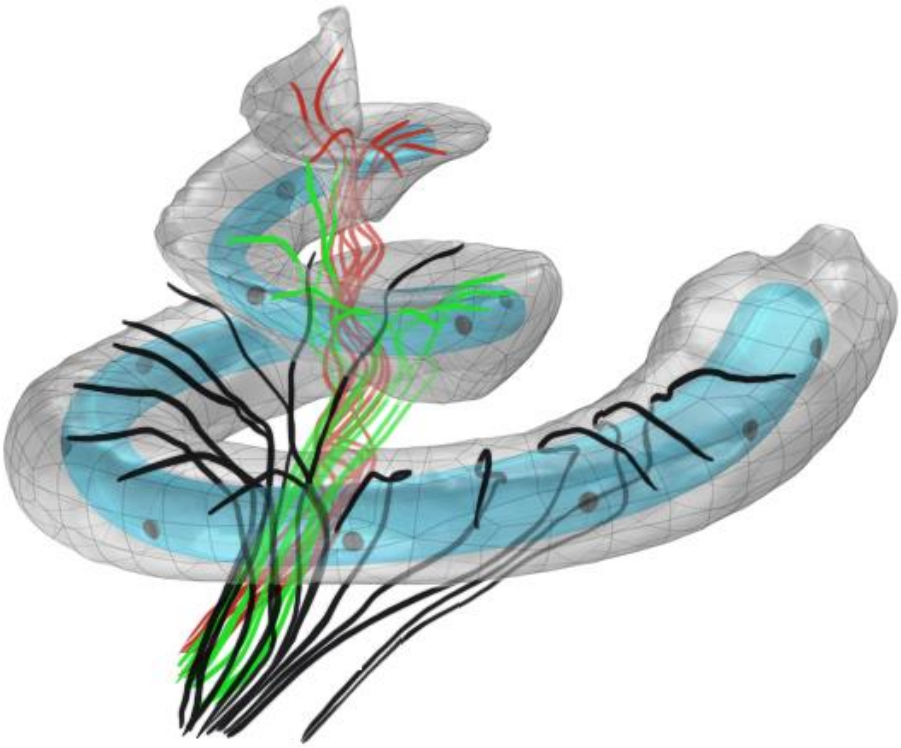

Figure 2.7. 3D visualization of 30 differently colored fibers from the basal (black), middle (green), and apical (red) cochlea turns together with the scala tympani. An electrode array (gray circles) of a 12 channels CI (light blue) is inserted in the scala tympani of the model (Heshmat et al., 2020).

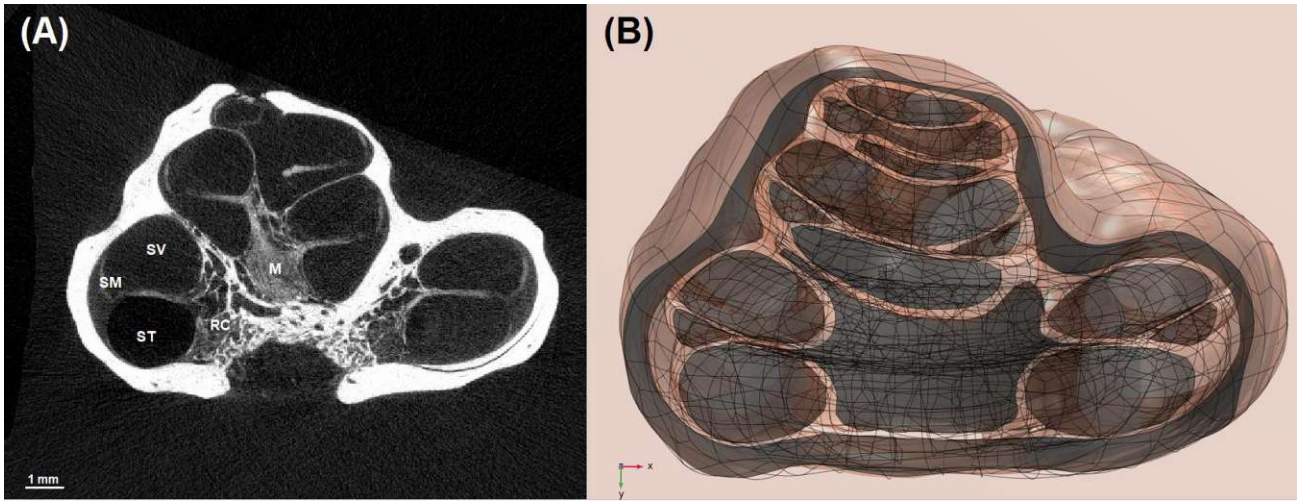

Figure 2.8. A micro-CT image of a human cochlea **(A)** provided the raw data for the COMSOL model **(B)**. **(A)** Scala tympani (ST) is the cave where electrodes are inserted. Scala vestibuli (SV), and scala media (SM) coil up the bony modiolus (M). Rosenthal's canal (RC) within M houses somata of auditory nerve fibers.

Die approbierte gedruckte Originalversion dieser Dissertation ist an der TU Wien Bibliothek verfügbar.
The approved original version of this doctoral thesis is available in print at TU Wien Bibliothek.
TU WIEN Bibliothek Your knowledge hub

The FE human cochlea model was segmented based on a high-resolution micro-CT scan with an isotropic voxel size of 3 µm (Figure 2.8). The model includes scala tympani (ST), scala media (SM), scala vestibuli (SV), compact bone, which is the bony shell surrounding the cochlea, modiolus, and cochlear nerves. The entire segmentation procedure was performed with Amira (Thermo Fisher Scientific, https://www.thermofisher.com). Figure 2.9 shows the segmented components of the human cochlea to have a sketch of segmented micro-CT data; however, more detail is explained in the following section.

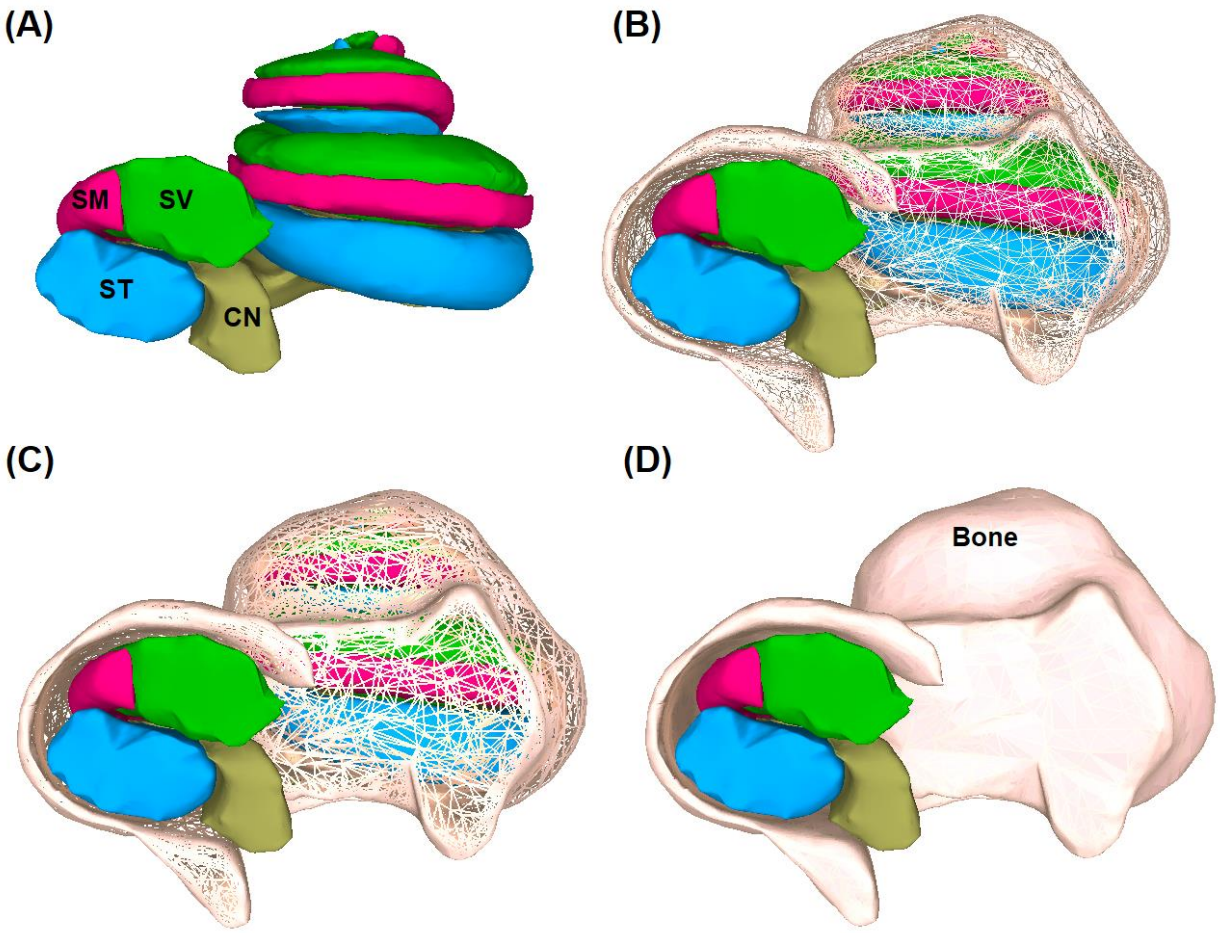

Figure 2.9. The segmented components of the human cochlea model. **(A)** The three scalae presented with blue, light green, and red for scala tympani (ST), scala vestibuli (SV), and scala media (SM), respectively. In addition, the whole cochlear nerves (CN) are indicated by dark green. **(B-D)** The surrounded bone structure of the cochlea is shown gradually with light pink for better visualization.

Die approbierte gedruckte Originalversion dieser Dissertation ist an der TU Wien Bibliothek verfügbar.
The approved original version of this doctoral thesis is available in print at TU Wien Bibliothek.
TU Bibliothek Your knowledge hub WIEN

Nerve fiber bundles	Angle [°]	Corresponding frequency [Hz]
Basal 14 (B14)	28	11524
Basal 13 (B13)	47	9568
Basal 12 (B12)	56	8200
Basal 11 (B11)	79	7492
Basal 10 (B10)	93	6040
Basal 9 (B9)	109	4455
Basal 8 (B8)	123	3845
Basal 7 (B7)	137	3371
Basal 6 (B6)	154	2977
Basal 5 (B5)	169	2607
Basal 4 (B4)	183	2285
Basal 3 (B3)	206	1977
Basal 2 (B2)	253	1519
Basal 1 (B1)	298	1166
Middle 9 (M9)	327	976
Middle 8 (M8)	371	805
Middle 7 (M7)	402	747
Middle 6 (M6)	433	657
Middle 5 (M5)	471	526
Middle 4 (M4)	495	469
Middle 3 (M3)	536	411
Middle 2 (M2)	576	309
Middle 1 (M1)	592	266
Apical 7 (A7)	620	228
Apical 6 (A6)	631	174
Apical 5 (A5)	790	133
Apical 4 (A4)	839	109
Apical 3 (A3)	862	92
Apical 2 (A2)	916	53
Apical 1 (A1)	928	42

Table 2.2. Summary of all nerve fiber bundles along the cochlea in respect to their angle and frequency (Potrusil et al., 2020). All angles are measured from the round window concerning the modiolus axis to the terminal of ANFs.

Die approbierte gedruckte Originalversion dieser Dissertation ist an der TU Wien Bibliothek verfügbar.
The approved original version of this doctoral thesis is available in print at TU Wien Bibliothek.
TU Bibliothek Your knowledge hub WIEN

2.1.11 Modeling cochlear implant array in COMSOL

In this study, CI electrode arrays were modeled using COMSOL. This section gives some details on creating a CI array model and inserting it into the ST and SV of the investigated FE human cochlea model. COMSOL provides to build three-dimensional objects. The modeling procedure is managed through the *Model builder*, which provides an easy way to go from geometry to simulation results.

In the *Global Definition* section, required variables were set in *Parameters* used throughout the entire model. In addition, all values in *Parameters* were saved with name, expression, and description. Subsequently, it is accessible to add a geometry part in one to three-dimension (1D, 2D, or 3D) that was used with new values of the input parameters, which were added to the final model individually. The array model employed the 3D geometry part and inserted all geometry information into the *Local Parameters* section, which was considered for adding parameters locally for the particular geometry.

Since the human cochlea model was available and the coordinate points were known, the *Interpolation Curve* was utilized to include a series of points for creating a curve (Figure 2.10A). The next step is to define the position of electrodes that were performed with the *Partition Edges* module, which delivered a process that partitions selected edges at specified positions (Figure 2.10B). Afterward, the model was converted from a curve to a spiral cylinder. For this purpose, a 2D circle and the sweep were applied for the extended model (Figure 2.10C). After generating the array shape, a sphere shape was used to model all electrode contacts as a ball (Figure 2.10D).

When the modeling of the CI array and electrode contacts were completed, the array parts were separated from the electrode contacts parts. In addition, the detached geometry was used further for identifying domain and boundary sections. Hence, the overlapping parts from the array and electrodes were departed and removed with the *Difference* module, which subtracted geometry objects from other geometry parts. In the next step, the *Delete Entities* module was used to delete geometry objects or geometric entities from objects (Figure 2.10E). Finally, the model was ready and was added to the investigated model, which is an essential part of the model and contains all components.

Die approbierte gedruckte Originalversion dieser Dissertation ist an der TU Wien Bibliothek verfügbar.
The approved original version of this doctoral thesis is available in print at TU Wien Bibliothek.
TU Bibliothek Your knowledge hub WIEN

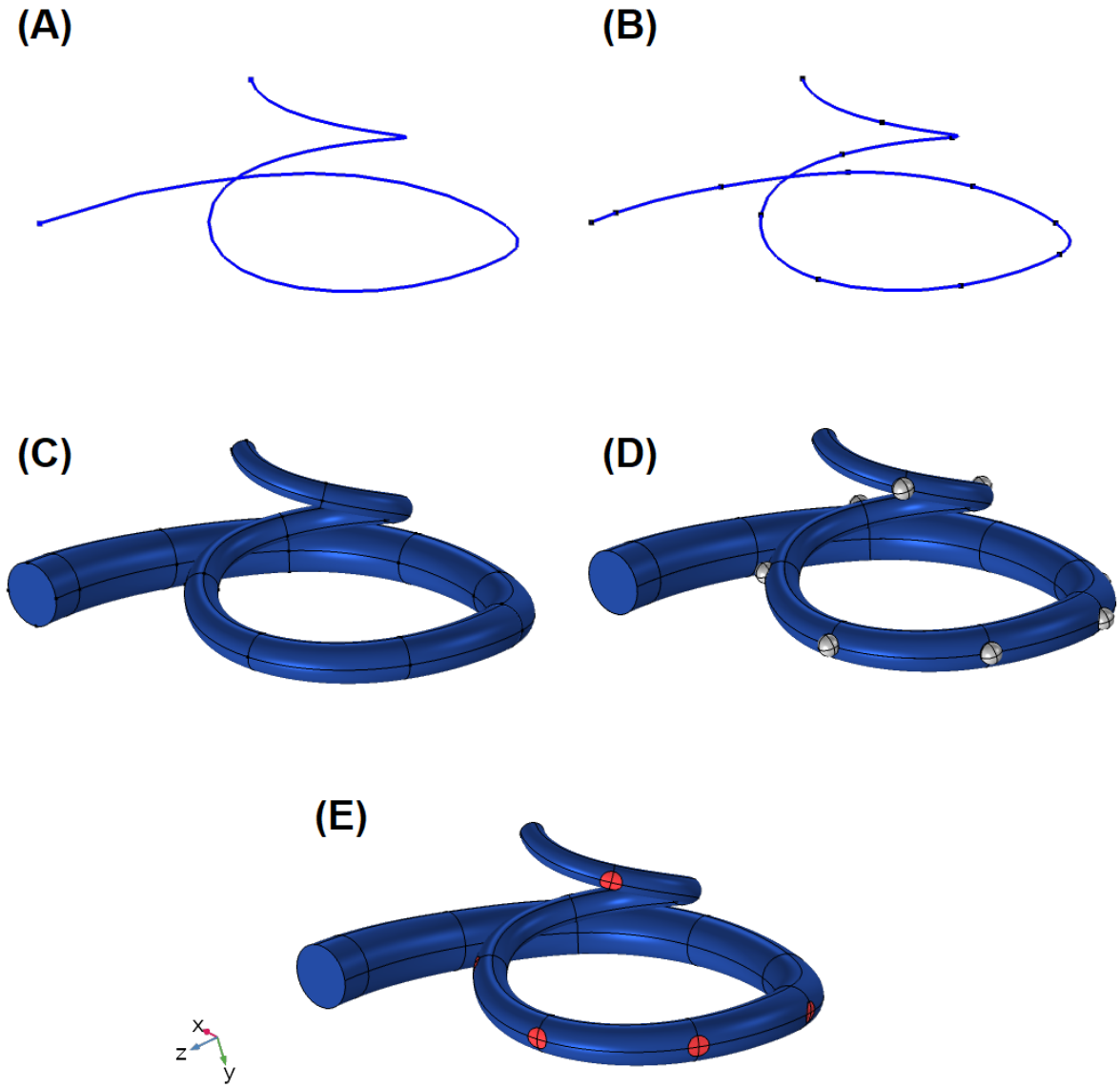

Figure 2.10. Representation of creating a cochlear implant array in COMSOL. **(A)** Using Interpolation Curve for generating a curvature based on a series of coordinates. **(B)** Applying Partition Edges module to model the position of electrode contacts on the curve. **(C)** Converting the curve to the spiral cylinder. **(D)** Adding the sphere shape of electrode contacts to the cylinder model. **(E)** The cochlear implant array separates and deletes the overlapping section. The coordinate system in panel (E) applies to all panels.

Moreover, in the FEM of this study, the human inner ear including different components are considered as a domain, and two different CI electrode arrays, a lateral and a perimodiolar CI system, were modeled as explained earlier and added to our cochlea model to evaluate the excitation profiles of the investigated ANFs. Both CI models are designed according to manufacturer data of a deep-insertion array of *FLEX SOFT*, MED-EL, Innsbruck, Austria,

Die approbierte gedruckte Originalversion dieser Dissertation ist an der TU Wien Bibliothek verfügbar.
The approved original version of this doctoral thesis is available in print at TU Wien Bibliothek.
TU Bibliothek Your knowledge hub WIEN

consisting of 12 electrodes and a perimodiolar array *CI24RE* Contour Advance, Cochlear, Sydney, Australia, including 24 electrodes. Figure 2.11 indicates the top views of both electrode arrays inserted into the ST of the FE human cochlea model.

The *FLEX SOFT* MED-EL CI array has 31.5 mm in length and 26.4 mm in active stimulation range with 1.3 mm diameter at the basal end as well as 0.5 × 0.4 mm dimension at apical. On the other hand, the *CI24RE* Contour Advance CI system comprises three silicon ribs with 0.8 mm and 0.5 mm diameter at the basal and apical end, covering 15 mm as active stimulation range.

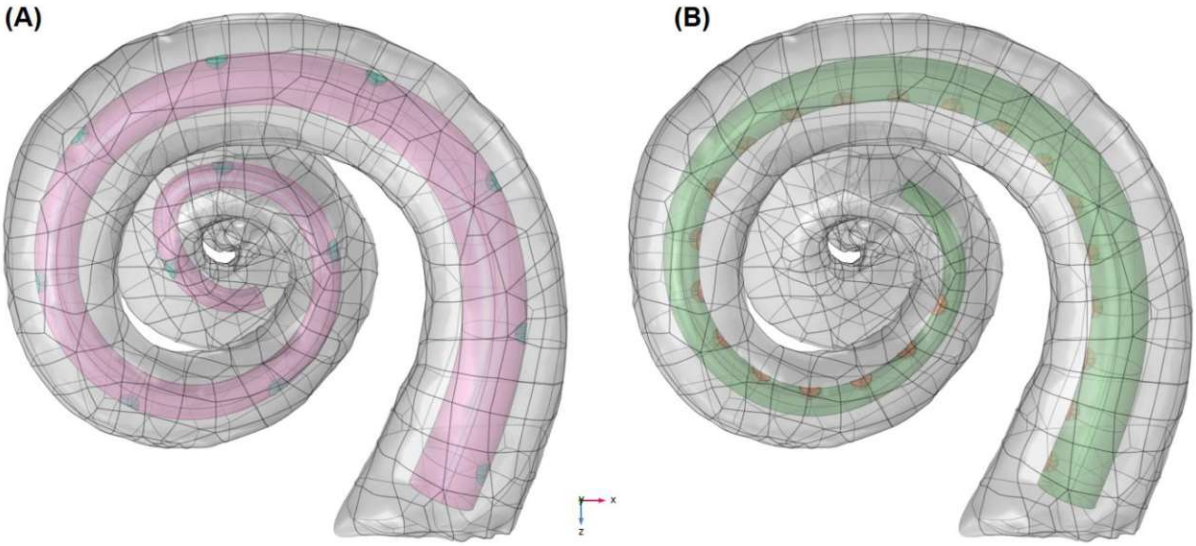

Figure 2.11. 3D model of two investigated cochlear implant electrode arrays were modeled into scala tympani. **(A)** The lateral array includes 12 electrodes shown in green that is close to the lateral wall of the scala tympani and a larger array length that covers the upper-middle and apical turn of the cochlea. **(B)** The perimodiolar array consists of 22 electrodes shown in orange that are close to the medial wall of the scala tympani and near to the cell bodies of the cochlear nerves.

For the effect of ground boundary size on finite element evaluations, first, the cochlea was embedded into a cuboid of bone using its boundary as ground, called old boundary. According to Figure 2.12A, the embedded volume was enlarged and tested the resulting change of the voltage profile of a target neuron. The enlargement of the bony cuboid to a rather large sphere (new boundary) with the same specific conductivity of 0.016 S/m (Table 2.3) caused an increase of the extracellular voltage (Figure 2.12B). The maximum increase was 3% (0.03 V vs. 1 V at the electrode) at the end of the central axon. The larger insulation by the sphere can be approximated by a shift of about 0.064 V (compare dashed gray line vs. the black line).

At first glance, it is surprising that a pure shift of the external voltage profile along a neuron does not affect its excitation. Eq. 2.28 can explain this phenomenon, where the external input

Die approbierte gedruckte Originalversion dieser Dissertation ist an der TU Wien Bibliothek verfügbar.
The approved original version of this doctoral thesis is available in print at TU Wien Bibliothek.
TU Bibliothek Your knowledge hub WIEN

always enters as a difference, e.g., as $V_{e_{n-1}} - V_{e_n}$ and such a difference is not changed by a common shift of V_e. The differences between the shifted original profile and its new evaluation (dashed gray vs. black line in Figure 2.12B) are extremely small, at least in the first (left) part representing peripheral axon, soma region, and the first part of central axon. Consequently, an AP which is elicited in this first part can be expected to need a quite similar electrode threshold voltage for both embedded volumes. On the other hand, in the region where these two curves have large distances, the curves are nearly straight (there is nearly no curvature), which is a sign of bad excitability according to the activating function principle (Rattay et al., 2001a, Eickenscheidt and Zeck 2014).

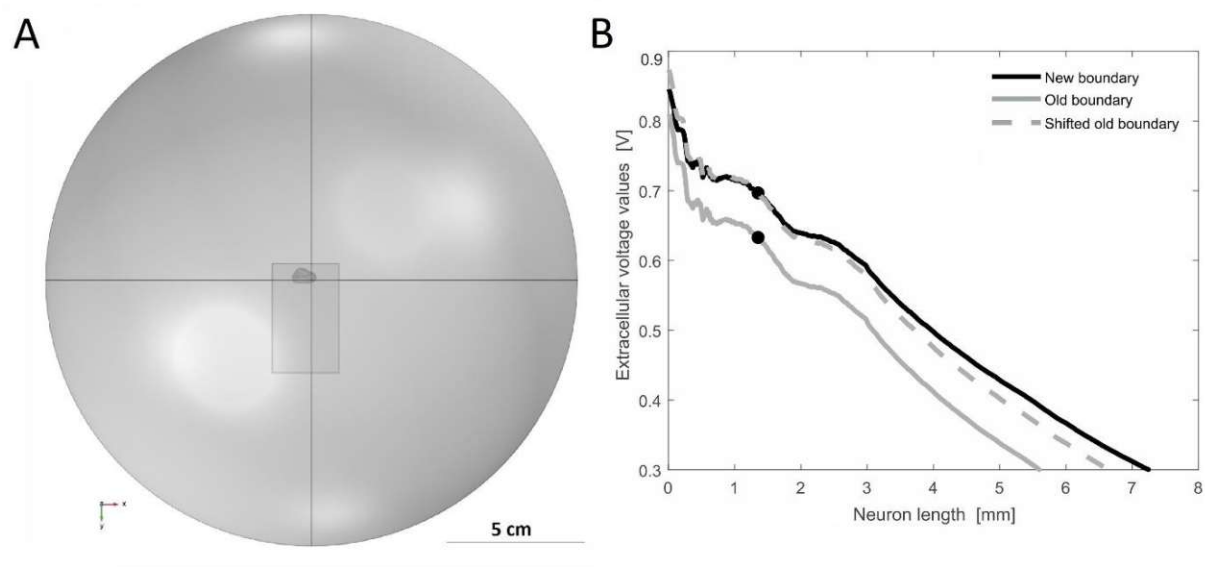

Figure 2.12. Investigating the effect of the ground boundary on extracellular voltage. **(A)** Representation of two ground boundaries, cuboid vs. sphere. **(B)** Showing the external voltage profile along a target neuron with different boundary sizes: cuboid and sphere displayed old and new boundary, respectively.

Finally, changing the size of the boundary surface area causes a change in extracellular potentials, which a common shift can approximate. Since the external voltage is always calculated from the difference between two neighboring compartments, such a general shift has no impact on the calculated excitation profiles of selected intact and degenerated ANFs. Hence, the effect of the outer boundary size does not a significant effect on the excitation profiles.

In this study, a sphere with a radius of 100 mm was used as an outer boundary. This boundary was introduced to the model as the ground (Figure 2.13). The particular electrical conductivity (S/m) of each component was set according to (Rattay et al., 2001a; Potrusil et al., 2020) that can be found in Table 2.3.

Die approbierte gedruckte Originalversion dieser Dissertation ist an der TU Wien Bibliothek verfügbar.
The approved original version of this doctoral thesis is available in print at TU Wien Bibliothek.
TU Bibliothek Your knowledge hub WIEN

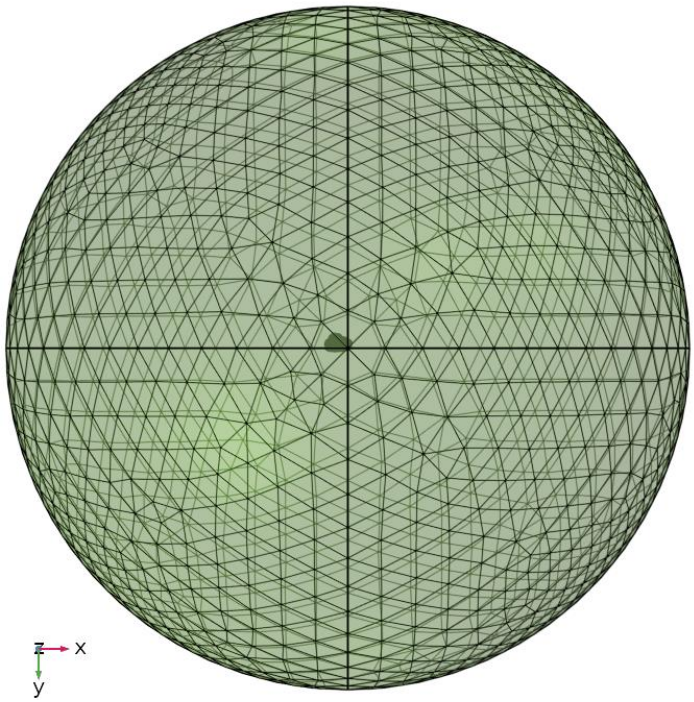

Figure 2.13. The outer boundary of the FE model that was modeled with a sphere and cochlea was placed in the center.

The AC/DC module is used to simulate CI stimulation, i.e., the induced electric potential was calculated under quasi-static conditions for a fixed potential of ±1 V at the surface of a selected active electrode through the CI array systems (Rattay et al., 2001a).

Components	Electrical conductivity (S/m)
Scala tympani	1.43
Scala vestibuli	1.43
Scala media	1.67
Compact bone	0.016
Osseous spiral lamina (Modiolus)	0.0334
Electrodes of CI	1000
Silicon of CI array	~ 0

Table 2.3. Electrical conductivities of the human inner ear components were used in the FEM.

Die approbierte gedruckte Originalversion dieser Dissertation ist an der TU Wien Bibliothek verfügbar.
The approved original version of this doctoral thesis is available in print at TU Wien Bibliothek.
TU Bibliothek Your knowledge hub WIEN

2.1.12 Image processing

Image processing and analysis were performed in Amira visualization software (Thermo Fisher Scientific, https://www.thermofisher.com). Amira delivers the complete set of powerful tools for the generation and post-processing of accurate three-dimensional models. Amira software is used to create a cochlea model that includes all scalae, cochlear nerves, vestibular system, facial nerve, etc. More than ten human inner ear temporal bones were performed to create 3D models for further analysis in computer simulations. All data was provided and prepared by the Inner ear biology laboratory of the Medical University of Innsbruck and analyzed by the Amira work-station located in the inner ear biology laboratory.

High-resolution micro-CT scans with an isotropic voxel size of 15 µm were taken. Image reconstruction was performed using a workstation of the micro-CT system, and reconstructed images were exported in DICOM format, including numerous series of image slices. The DICOM file was used as raw data and opened and loaded directly into Amira software. Before beginning the segmentation of the desired data, it is necessary to apply some modules to the data to prepare it for segmentation. This section briefly describes data segmentation in Amira.

After loading the data, it is possible to look at 3D images at single or multiple orthographic or oblique sections using *Ortho Slice* in different orientations. The *Ortho Slice* module enables arbitrary extracting of orthogonal slices from a 3D image volume. In addition, a region of interest was restricted to the desired area by cropping the unnecessary information or parts of the images using the bounding box tool. The next step modified the data by applying some filtering procedures, editors, and data processing modules. One module was applied before segmentation to reduce the noise of the data and smooth the images; however, this step was done accurately, not to change the necessary information. This step was accomplished by applying a filter module like *Median Filter used* for scattering dots and preserving edges, or *Bilateral Filter,* which applied for balancing smoothing and edge-preserving specifically in sharp angles. In addition, *Unsharp masking* and *Delineate* filters were used to reinforce the contrast at edges and transparentize the details. Volume Rendering was applied to give a 3D impression of the data without segmentation. This module operates based on the emission and absorption of the light to each voxel of the image volume.

Furthermore, when the data were ready for segmentation, it was used *Segmentation Editor*. Amira's Segmentation Editor module allows to segment selected structures in micro-CT datasets. Segmentation of 3D images assigns a label to each pixel of the image. Segmented label data were stored separately from the image data called *Label Field*. Amira *Segmentation Editor* provides a user interface workroom for interactive segmentation assignments. For a

Die approbierte gedruckte Originalversion dieser Dissertation ist an der TU Wien Bibliothek verfügbar.
The approved original version of this doctoral thesis is available in print at TU Wien Bibliothek.
TU Bibliothek Your knowledge hub WIEN

better comprehension of the segmentation tool, the whole procedure of cochlea segmentation is described below.

The region of interest was restricted to the cochlea since the whole inner ear was present in the data; the bounding box tool and an edge-based smoothing filter, Median filter, were applied to reduce the amount of noise in the data. Manual and semi-automatic selection of structures were performed with different tools such as brush (painting), lasso (intelligent scissors), magic wand (region growing), thresholds, etc. It is possible to change the orientation of the image slice from *Segmentation/Orientation* by choosing the Single-viewer in the viewer toolbar to see different 2D planes (XY, YZ, and XZ) and a 3D view. In addition, it is feasible to select two- or four viewer layouts. A four viewer layout enables that observed an image and labeled structures in all planes (XY-XZ-YZ) and 3D volume-rendered view.

The distinct contrast of the ossified cochlear nerve made it possible to use threshold tools to quickly and reliably outline the nerve tissue. Interactive selection of a range of voxel intensities covering osmium tetroxide (OsO_4) stained nerve fibers, masking these voxels, and then manual selection of the regions of interest in 2D slices in every 3rd to the fourth plane results in a stack of label areas. Missing labels in between are interpolated to obtain a gapless stack of labeled structures saved in a Label Field file. Careful checking in all planes and 3D label views is necessary to find accurate structures, avoid staircase artifacts, and bypass blind spots in certain planes.

The Label Field defines materials separately depending on the segmentation parts and assigns a particular name and color. Each step of segmentation was added or removed desired segmented parts into the defined materials; for instance, the materials of the cochlea are defined as ST, SM, SV, cochlear nerve, modiolus, etc., in a color-coded manner.

Specific segmentation filters were used to improve the final segmentation data like *Remove islands*, *Smooth labels, Remove and Fill Holes*. In the next step, Amira constructs a triangular surface of the segmented object by *Generate surface* module. Hence, all surfaces were extracted either separately or all together from Label filed data of segmented data. In addition, the number of triangles produced by the *Generate surface* module is too large for the further steps in a computer simulation; therefore, *Surface Simplification Editor* was used to decrease the triangular numbers. It was manually checked by *the Surface View* module that decreasing triangular numbers did not affect the data information by changing the surface structure. Finally, the generated surface of the data was stored as STL file format, which was used in COMSOL for FE investigations.

Die approbierte gedruckte Originalversion dieser Dissertation ist an der TU Wien Bibliothek verfügbar.
The approved original version of this doctoral thesis is available in print at TU Wien Bibliothek.
TU Bibliothek Your knowledge hub WIEN

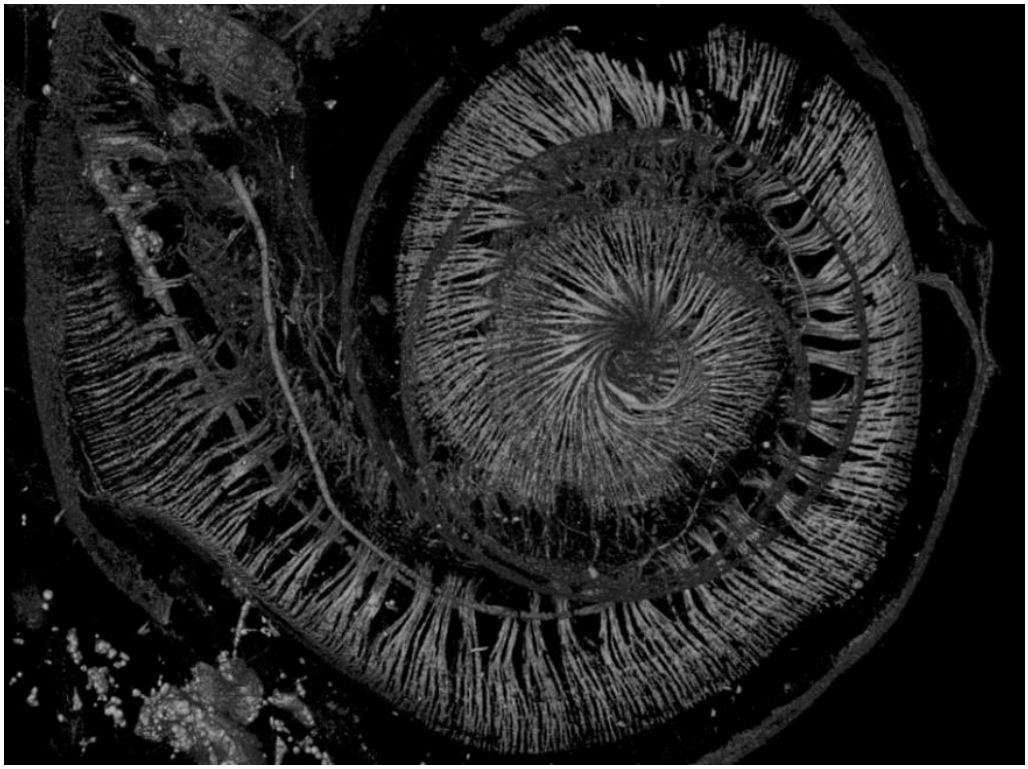

Figure 2.14. High-resolution micro-CT scan with an isotropic voxel size of 2.4 µm of a human cochlear nerve. Figure taken from Inner Ear Biology Laboratory Medical University of Innsbruck.

Since the SGNs have a sophisticated arrangement and spiral shape (Figure 2.14) is very complicated and delicate for segmentation. Therefore, it is required to have proper staining and fixation methods of a cochlea specimen as well as high micro-CT resolution for achieving accurate cochlear nerves segmentation, which can be reliable for further investigations in computer simulations. Figure 2.15 represents one model of a segmented human cochlea from micro-CT with Amira as described above.

Die approbierte gedruckte Originalversion dieser Dissertation ist an der TU Wien Bibliothek verfügbar.
The approved original version of this doctoral thesis is available in print at TU Wien Bibliothek.
TU WIEN Bibliothek Your knowledge hub

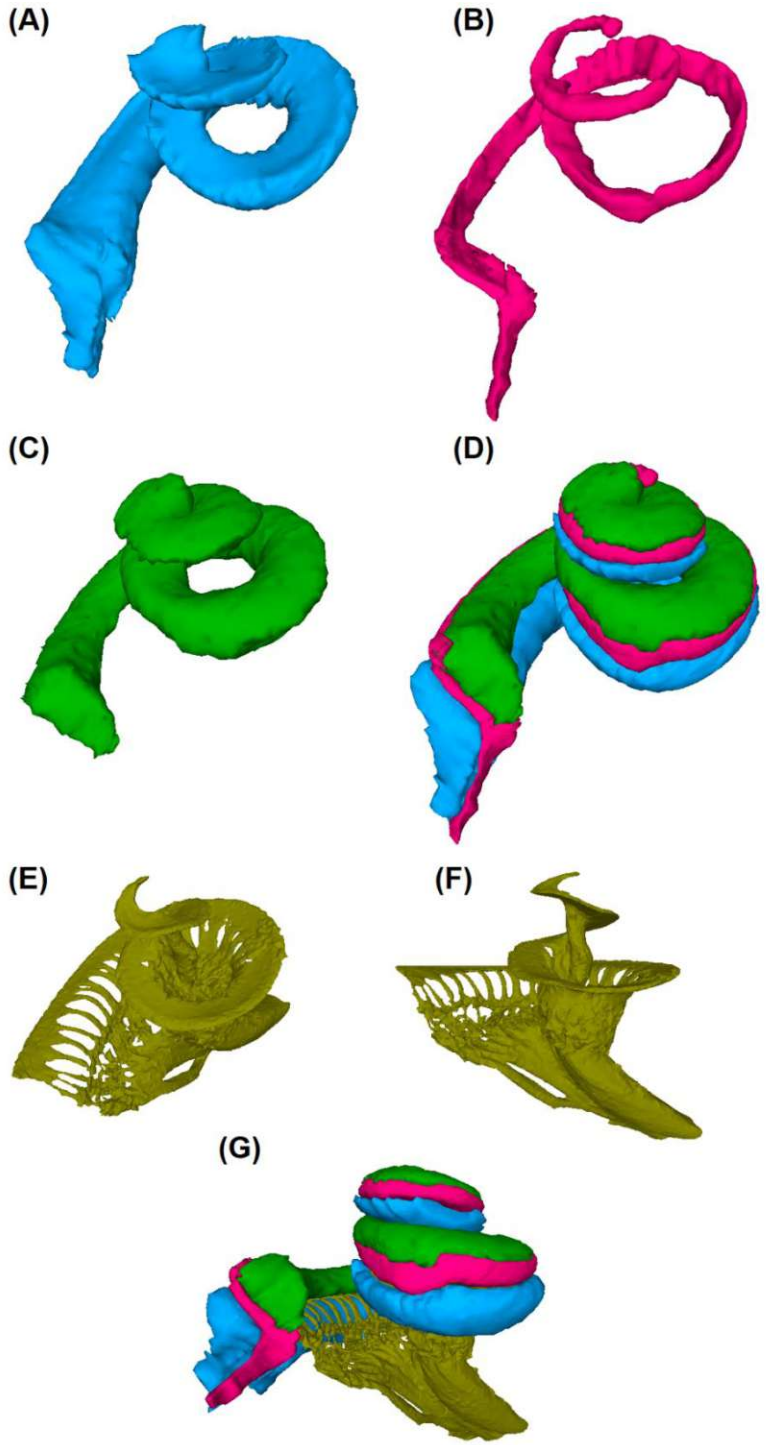

Figure 2.15. Segmentation of human cochlea from high-resolution micro-CT scans with an isotropic voxel size of 15 µm in Amira. Segmented **(A)** scala tympani, **(B)** scala media, and **(C)** scala vestibuli. **(D)** Combined all segmented scalae. **(E-F)** Segmented the whole cochlear nerves projecting to internal acoustic meatus in two different views. **(G)** segmented three scalae and cochlear nerves.

Die approbierte gedruckte Originalversion dieser Dissertation ist an der TU Wien Bibliothek verfügbar.
The approved original version of this doctoral thesis is available in print at TU Wien Bibliothek.
TU WIEN Bibliothek Your knowledge hub

2.2 Distinctive Methods

2.2.1 Degeneration pattern of human cochlear nerves

2.2.1.1 Preparation and Fixation

For investigating the degeneration levels in peripheral axons of human ANFs, four individual human inner ears, one normal (healthy), and three hearing loss cases, were considered in this study. Based on the audiogram evaluations, the hearing impairment differed in three cochlear regions, basal, middle, and apical (Table 2.4). Ethical guidelines were followed according to the Division of Clinical and Functional Anatomy of the Innsbruck Medical University (McHanwell et al., 2008; Riederer et al., 2012).

Prefixation was done with the Karnovsky solution within 1–3 h after death by perilymphatic perfusion through the round and oval windows. During the autopsy, the temporal bones were removed and fixed by immersion and repeated perilymphatic perfusion. After post-fixation with 1.5% osmium tetroxide (OsO_4) for 90 minutes and washing the specimen, the excess bone around the cochlea was removed using a Bien Air CE 0120 driller until only a thin bony shell surrounded the cochlea. The temporal bones were dehydrated with 70% ethanol and embedded without removing the bony shell. Then the block-surface method (Spoendlin and Schrott, 1987) was used. A mid-modiolar cut was performed with a circular saw, and then small disks of the cochlear half turns were dissected and divided into segments. The lamina was re-embedded, and tangential histological sections of the whole segment were determined by counting the cross-sectioned myelinated nerve fibers. The histological sections were done as near as possible to the organ of Corti. The number of myelinated nerve fibers was evaluated by counting the cross-sectioned fibers between the osseous spiral lamina and organ of Corti of each segment.

Die approbierte gedruckte Originalversion dieser Dissertation ist an der TU Wien Bibliothek verfügbar.
The approved original version of this doctoral thesis is available in print at TU Wien Bibliothek.
TU WIEN Bibliothek Your knowledge hub

Specimen-ID	*Audiogram Basal [dB]*	*Hearing-loss level*	*Audiogram Middle [dB]*	*Hearing-loss Level*	*Audiogram Apical [dB]*	*Hearing-loss level*	*Age (years)*	*Audiogram prior to death (months)*
Control	17	Normal	7	Normal	11	Normal	47	10
S1	97	Profound	66	Severe	42	Moderate	67	5
S2	57	Moderate	28	Slight	17	Normal	63	15
S3	57	Moderate	20	Normal	20	Normal	80	1

Table 2.4. Specimen details on hearing deficits as provided by the Innsbruck Medical University, Department of Otorhinolaryngology, Laboratory for Inner Ear Biology.

2.2.1.2 Imaging, Data Processing, and Statistics

Based on the block-surface method (Spoendlin and Schrott, 1987), it is feasible to assess the cochlea quantitatively at a light and electron microscopic level within the osseous spiral lamina and the cochlear nerve. ANFs of all specimens were divided into equal and comparable segmented regions, from basal to apical. Sections were digitized using a Zeiss Axio Imager.M2 equipped with a Zeiss Axiocam 512. Full-resolution images were acquired with a Plan Apochromat 63 × 1.4 lens. Data processing was performed with ImageJ as well as MATLAB (version R2018b, https://mathworks.com), using a toolbox (Zaimi et al., 2016) for semi-automatic segmentation to investigate the peripheral parts of the ANFs. For a systematic comparison, an equal number of ANFs were counted in all three regions.

Figure 2.16 displays a light microscopy image with the corresponding segmentation parts. All light microscopic images were used to segment ANFs based on myelinated and non-myelinated parts to evaluate peripheral axon diameter (PD), myelination thickness (MT), and G-ratio of the ANFs which is, the ratio of the inner to the outer diameter of a myelinated fiber (Figure 2.17).

Die approbierte gedruckte Originalversion dieser Dissertation ist an der TU Wien Bibliothek verfügbar.
The approved original version of this doctoral thesis is available in print at TU Wien Bibliothek.
TU Bibliothek Your knowledge hub WIEN

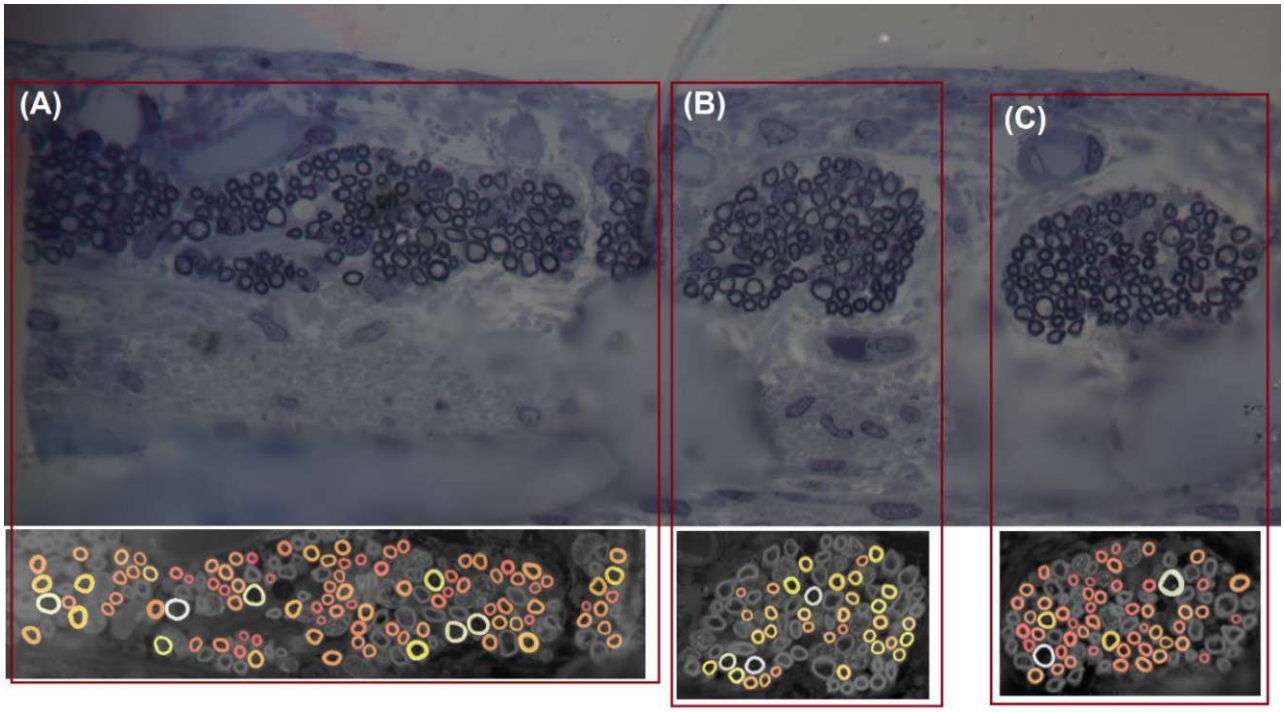

Figure 2.16. Light microscopy image of the peripheral part of ANFs in the healthy human specimen, taken in the Inner Ear Biology lab at the Medical University of Innsbruck. The corresponding segmentation of myelination thickness, peripheral diameter, and fiber diameter was performed in MATLAB using the axon segmentation toolbox.

In this study, a monophasic (cathodic) pulse and a biphasic (cathodic first) of 100 µs per phase were applied to investigate the threshold profile for extracellular stimulation. The monopolar stimulation configuration was chosen as the stimulation strategy. Table 2.5 represents the measured angles from the round window with respect to the modiolus axis for ten investigated electrodes, five from lateral CI and five from perimodiolar CI array, as well as the fiber with the closest distance from its terminal to the center of the electrode named target neuron (TN). Figure 2.18 shows the top views of both electrode arrays inserted into the ST, for better understanding, the basal nerve pathways and electrode positions are added to the figure.

The morphometry of the peripheral process was categorized in three different neural health cases based on our findings in this study (Heshmat et al., 2020): (i) intact case with a peripheral diameter of 2 µm as well as normal myelination, (ii) an intermediate degenerated case with a reduced diameter of 0.5 µm and subsequently a reduced number of myelin layers, and finally (iii) the progressive degenerated case with no peripheral process. In addition, the central diameter was fixed to 4 µm for all cases to have a fair comparison.

Die approbierte gedruckte Originalversion dieser Dissertation ist an der TU Wien Bibliothek verfügbar.
The approved original version of this doctoral thesis is available in print at TU Wien Bibliothek.
TU Bibliothek Your knowledge hub WIEN

Lateral electrode array	Electrode angle[°]	Perimodiolar electrode array	Electrode angle[°]	TN	TN angle[°]
EL1	10	**CA2**	15	Basal14	28
EL3	69	**CA6**	73	Basal11	79
EL5	143	**CA11**	153	Basal7	137
EL8	295	**CA19**	317	Basal1	298
EL9	343	**CA20**	332	Middle9	327

Table 2.5. Angles of the investigated electrodes and the corresponding target neurons (TN) were measured from the round window with respect to the modiolus axis.

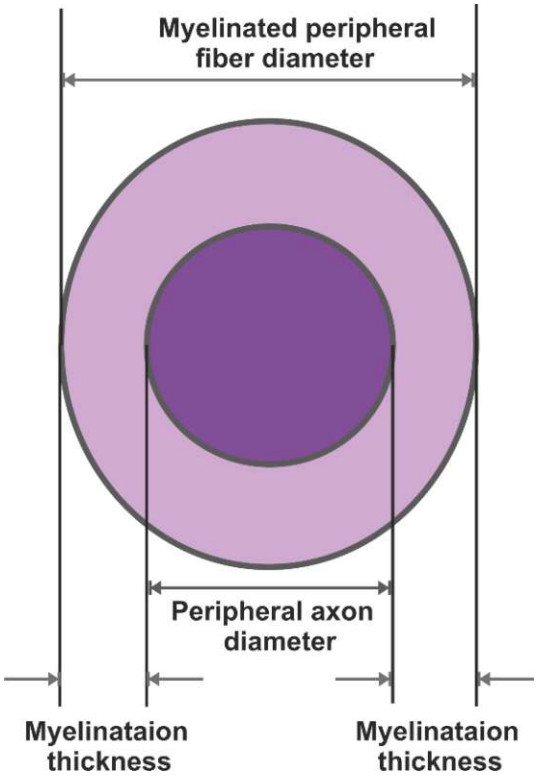

Figure 2.17. A schematic cross-section of a peripheral axon of the cochlear nerve demonstrates myelinated and non-myelinated parts of the fiber. G-ratio can be determined by the ratio of the

Die approbierte gedruckte Originalversion dieser Dissertation ist an der TU Wien Bibliothek verfügbar.
The approved original version of this doctoral thesis is available in print at TU Wien Bibliothek.
TU Bibliothek Your knowledge hub WIEN

peripheral axon diameter to the myelinated peripheral fiber diameter (the inner to the outer diameter of a myelinated fiber).

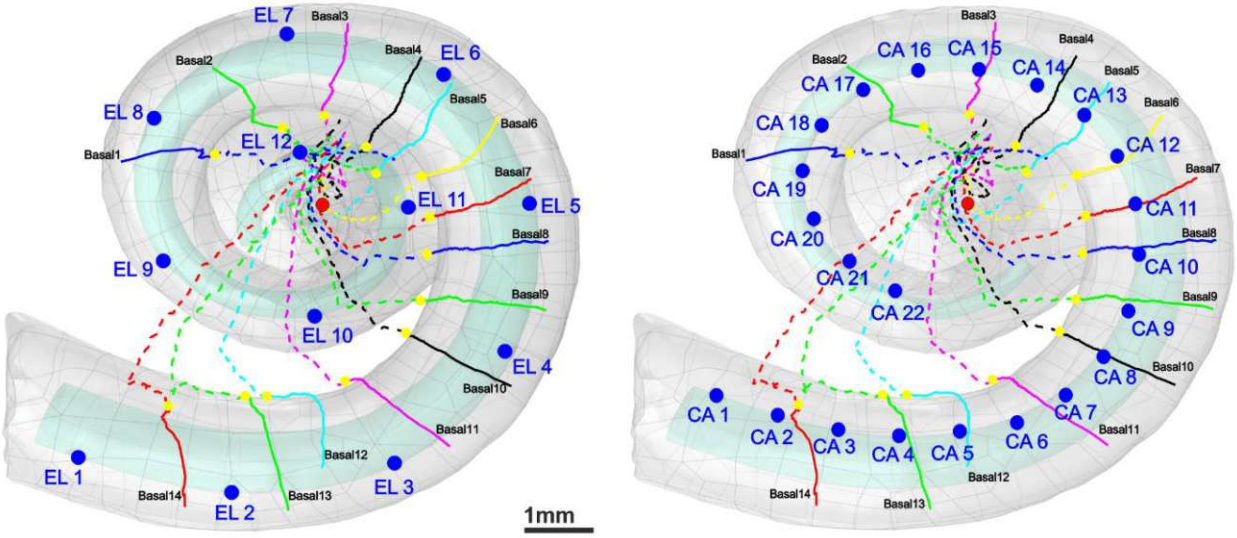

Figure 2.18. 3D model of scala tympani includes 12 electrodes of a lateral CI (left) and 22 electrodes of a perimodiolar CI (close to the center, right) and the 14 pathways of ANFs in the basal turn. The peripheral axons, soma positions, and central axons of the nerve pathways are represented with colored solid lines, yellow spheres, and colored dashed lines, respectively. For the sake of clarity, all electrode positions are shown as blue spheres, although in calculations, each active electrode is a hemisphere. The axis of modiolus is marked as a red sphere. The Figure and caption are taken from (Heshmat et al., 2020).

Statistical analyses were conducted using MATLAB and Python programming language (version 2.7, https://www.python.org). All data shown in Table 2.4 were collected based on the degree of hearing loss at three regions of the basal, middle, and apical with 450, 520, and 150 fiber numbers, respectively. The data were compared with the healthy specimen as the control.

Moreover, The Kruskal–Wallis test was used to determine if there were significant differences between groups in each region, separately. Pairwise Conover test was applied to compare the medians of all groups significance levels were set as follows: $p < 0.05$ *, $p < 0.01$ **, $p < 0.001$ ***. The data was visualized in histograms, and the fit kernel distribution was applied. Scatter plot was used to study the correlation of the peripheral axon diameters vs. myelination thickness as well as G-ratio. The related results are shown in section 3.1.

Die approbierte gedruckte Originalversion dieser Dissertation ist an der TU Wien Bibliothek verfügbar.
The approved original version of this doctoral thesis is available in print at TU Wien Bibliothek.
TU Bibliothek Your knowledge hub WIEN

2.2.2 Impact pulse shapes, CI stimulation strategies, and array types on polarity behavior of human auditory nerve fibers

In this part of the study, some influential parameters on the CI outcomes such as pulse shape, CI stimulation strategy, the distance between channels of CI as well as the electrode distance to the modiolus axis were studied. Moreover, the polarity effect was analyzed based on the parameters mentioned above and proposed a better indicator for detecting neural health status. Results related to this section are demonstrated in section 3.2.

Two electrode arrays, a lateral and a perimodiolar CI, were inserted in the ST of the human cochlea FE model, including reconstructed pathways of type I ANFs (Figure 2.19). In the first simulation step, the stimulating voltage profiles along the ANFs were computed for active CI electrode contacts using COMSOL. In the second step, excitations of selected ANFs were simulated with a multi-compartment model (Rattay et al., 2001b).

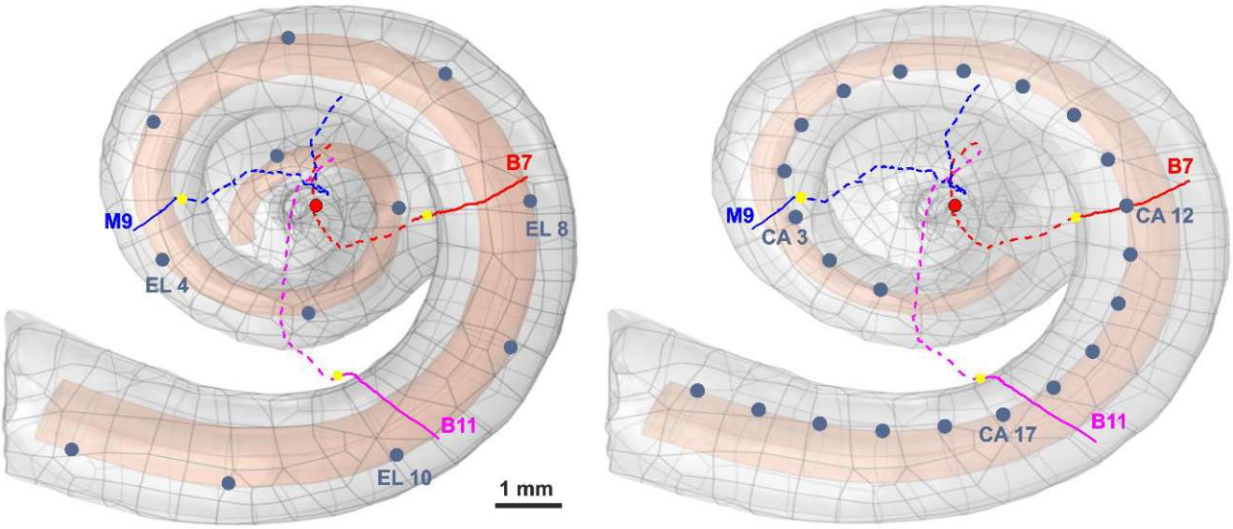

Figure 2.19. The 3D model of scala tympani includes 12 electrodes of the lateral CI (left) and 22 electrodes of the perimodiolar CI (electrodes are close to the center, right) and the three investigated pathways ANFs. The peripheral part, soma position, and central part of the nerve pathways are represented with colored solid lines, yellow spheres, and colored dashed lines, respectively. For the sake of clarity, all electrode positions are shown by dark blue circles. In calculations, however, each active electrode is considered a hemisphere. The axis of the modiolus is marked with a red circle.

The investigated ANFs, named target neurons (TN), were selected based on the closest distance from their peripheral terminal site to the center of the electrodes. Table 2.6 represents the angles measured from the round window with respect to the modiolus axis for the six investigated

Die approbierte gedruckte Originalversion dieser Dissertation ist an der TU Wien Bibliothek verfügbar.
The approved original version of this doctoral thesis is available in print at TU Wien Bibliothek.
TU Bibliothek Your knowledge hub WIEN

electrodes (three from each CI array system) and TNs in different cochlear turns (basal, middle, and upper-middle).

Lateral electrode array	Electrode angle [◦]	Perimodiolar electrode array	Electrode angle [◦]	TN	TN angle [◦]
EL4	343	**CA3**	332	M9	327
EL8	143	**CA12**	153	B7	137
EL10	69	**CA17**	73	B11	79

Table 2.6. Angles of the investigated electrodes and the corresponding target neurons (TN) measured from the round window with respect to the modiolus axis; compare Figure 2.19.

Our previous clinical study (Heshmat et al., 2020) investigated critical morphometry parameters such as diameter and myelination thickness of the peripheral parts of ANFs for several human cochleae at various ages with different hearing loss levels. According to observations of different distributions in diameter and myelination thickness, the study suggested a degeneration pattern for peripheral parts of human ANFs based on hearing loss levels. Therefore, the peripheral process morphometry was divided into six groups indicating different neural health statuses (Table 2.7) according to the different varieties of the peripheral parts of human ANFs.

ANF state	Degeneration levels	Peripheral diameter [µm]
AS1	intact	2
AS2	slight	1.5
AS3	moderate	1
AS4	severe	0.75
AS5	profound	0.5
AS6	progressive	without peripheral

Table 2.7. Six ANFs statuses based on degeneration levels of peripheral diameter.

Die approbierte gedruckte Originalversion dieser Dissertation ist an der TU Wien Bibliothek verfügbar.
The approved original version of this doctoral thesis is available in print at TU Wien Bibliothek.
TU Bibliothek Your knowledge hub WIEN

In this section of the investigation, symmetric and asymmetric pulses, including four pulse shapes, were implemented. Monophasic, pseudo-monophasic, triphasic, and biphasic pulses were applied for both polarities, a negative phase called cathodic (CAT) and a positive phase named anodic (ANO) (Figure 2.20). The phase duration was set to 100 µs, except for the second phase of the pseudo-monophasic pulse, in which the duration was increased by a factor of four, and its amplitude decreased by the same factor to keep the charge balanced (Macherey et al., 2011). All multi-compartment model evaluations were performed in MATLAB (version R2020a, https://mathworks.com).

In this section, excitations of selected ANFs were simulated with Rattay's multi-compartment model (Rattay et al., 2001b). The geometry of the peripheral process was varied in six different neural health cases based on our findings in degeneration pattern study (Heshmat et al., 2020): (i) An intact case with a diameter of 2 µm as well as normal myelination, (ii) a slight degenerated case with a reduced diameter of 1.5 µm and subsequently a reduced number of myelin layers, (iii) a moderate degenerated case with a reduced diameter of 1 µm and consequently a reduced number of myelin layers, (iv) a sever degenerated case with a reduced diameter of 0.75 µm and subsequently a reduced number of myelin layers, (v) a profound degenerated case with a reduced diameter of 0.5 µm and consequently a reduced number of myelin layers, and finally (vi) the progressive degenerated case with no peripheral process.

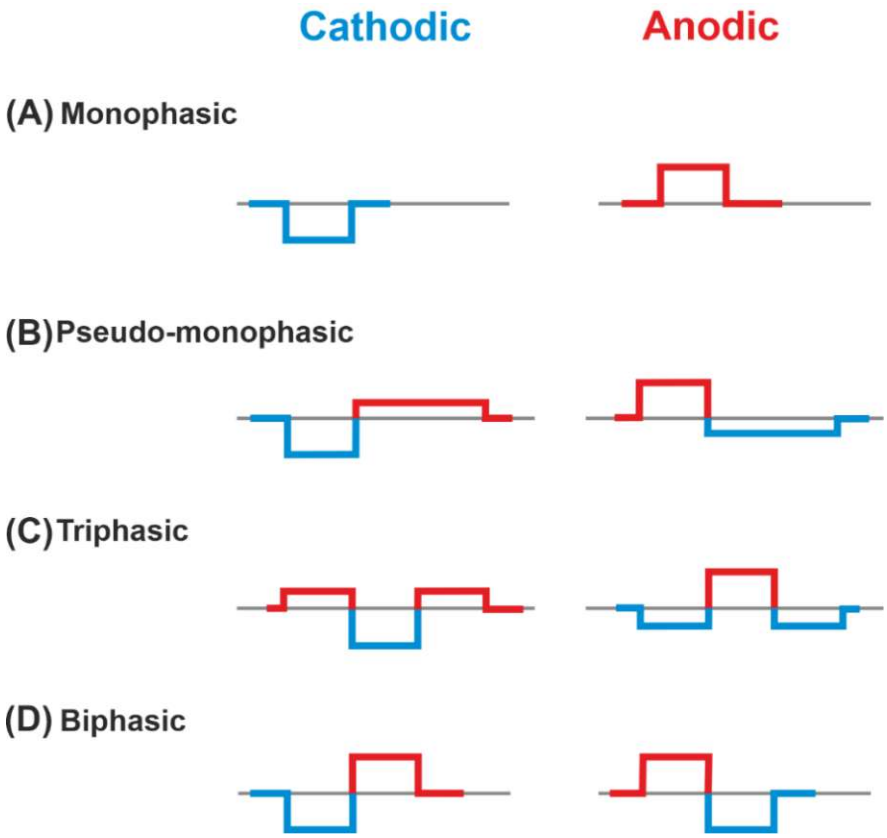

Die approbierte gedruckte Originalversion dieser Dissertation ist an der TU Wien Bibliothek verfügbar.
The approved original version of this doctoral thesis is available in print at TU Wien Bibliothek.
TU Bibliothek Your knowledge hub WIEN

Figure 2.20. Illustration of symmetric and asymmetric pulse shapes in both anodic and cathodic polarity. **(A-C)** represent the asymmetric pulse shapes: monophasic, pseudo-monophasic, and triphasic. **(D)** demonstrates symmetric pulse shape, biphasic commonly used in cochlear implants.

Moreover, four CI stimulation strategies were used in this dissertation that varied depending on the return electrode (ground electrode) position:

i) A monopolar strategy (MP) is used, in which the return electrode is located outside the cochlea, usually behind the ear.
ii) A bipolar strategy (BP) with a return electrode placed next to the stimulating electrode, adjacent active electrode.
iii) A tripolar strategy (TP) is applied. In this strategy, the return electrodes are two neighboring electrodes, and each electrode takes half of the current delivered to the stimulating electrode.
iv) A partial tripolar strategy (PTP) is used, which is a combined configuration of MP and TP. In PTP, part of the stimulating current (defined by the coefficient σ, $0 < \sigma < 1$) returns to the two neighboring electrodes and the rest to the common ground (Figure 2.21). The investigated PTP configuration was considered with 75% of the current returning to the neighboring electrodes and 25% to the ground, according to (Jolly et al., 1996; Litvak et al., 2007; Mesnildrey et al., 2020).

Two geometrical parameters are important in order to compare the lateral and the perimodiolar CI: (i) the center-to-center distance of adjacent channels and (ii) the electrode distance to the modiolus axis. These parameters are different in lateral and perimodiolar array systems. In the lateral CI, the distance between electrodes as well as the electrode distance to the modiolus axis are larger compared to the perimodiolar CI array. Therefore, to perceive the impact of parameters, the CI systems were first modeled with features reported by the manufacturer. In the next step, a similar distance between channels was applied in both CI arrays, and finally, the results were compared between the manipulated and the original arrays. For this aim, in perimodiolar CI, the second basal adjacent channels were considered (Figure 2.21B), whereas, in lateral CI, an extra electrode was set between two investigated electrodes each time, which was used as the new ground electrode (Figure 2.21C).

Die approbierte gedruckte Originalversion dieser Dissertation ist an der TU Wien Bibliothek verfügbar.
The approved original version of this doctoral thesis is available in print at TU Wien Bibliothek.
TU Bibliothek Your knowledge hub WIEN

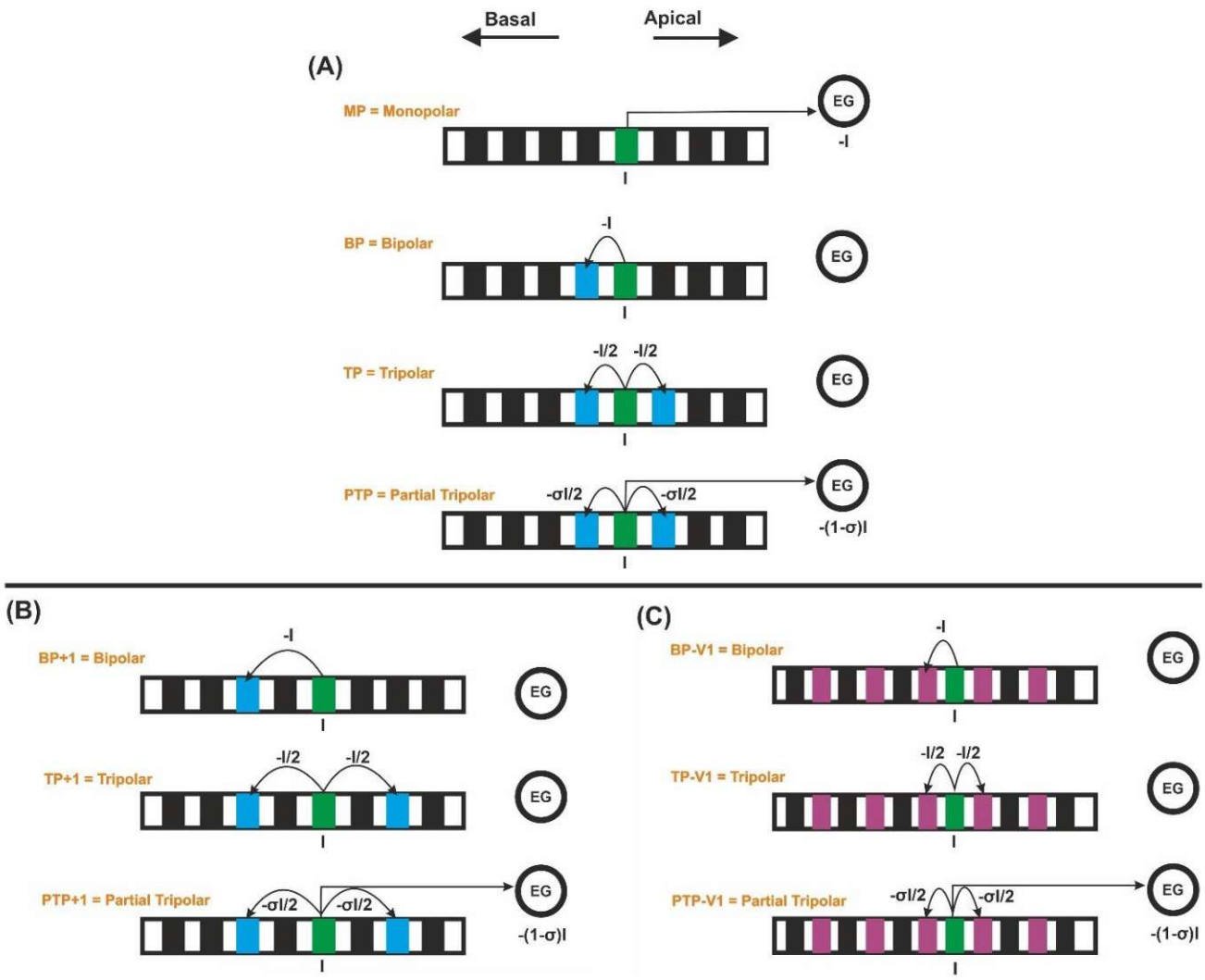

Figure 2.21. Forced current flow (I) from the stimulating CI channel for monopolar, bipolar, tripolar, and partial tripolar configuration. **(A)** Monopolar and multipolar strategies by considering the adjacent basal channel. **(B)** Multipolar strategies by considering the second basal adjacent channel in perimodiolar CI. **(C)** Multipolar strategies by considering a shorter inter-channel distance in the lateral CI.

Die approbierte gedruckte Originalversion dieser Dissertation ist an der TU Wien Bibliothek verfügbar.
The approved original version of this doctoral thesis is available in print at TU Wien Bibliothek.
TU Bibliothek Your knowledge hub WIEN

2.2.3 Scala tympani vs. scala vestibuli implantations

2.2.3.1 Modeling electrodes inside of scala tympani and scala vestibuli

In this section, the same three-dimensional cochlea model and six (out of the thirty) reconstructed pathways of tonotopically organized type I auditory nerve bundles were studied (Table 2.8). In addition, six electrodes were modeled as platinum spheres with a realistic radius of 0.1 mm and placed in the ST as well as SV, 12 electrodes in total. For a fair comparison between two scalae, it was necessitated to consider the same condition; hence, the evaluated distances from the center of the active electrode to a specific position at the peripheral part of the closest ANF were deliberately chosen equivalent for ST vs. SV electrodes (Figure 2.22). The results related to this section are presented in section 3.3.

TN	TN angle[°]
B12	56
B7	137
B2	253
M7	402
M4	495
M1	592

Table 2.8. Names and angles of the investigated auditory nerve fibers as target neurons (TN) were measured from the round window with respect to the modiolus axis.

At the active electrode surface, the AD/DC module with a fixed potential of ±1 V was used in COMSOL Multiphysics (version 5.5) to calculate the extracellular potential distribution of the active electrode within the cochlea. The positions of the compartment centers were extracted from the nerve pathways and applied to the COMSOL to calculate the induced extracellular potentials at these points and finally applied to the multi-compartment model of each ANF.

Die approbierte gedruckte Originalversion dieser Dissertation ist an der TU Wien Bibliothek verfügbar.
The approved original version of this doctoral thesis is available in print at TU Wien Bibliothek.
TU Bibliothek Your knowledge hub WIEN

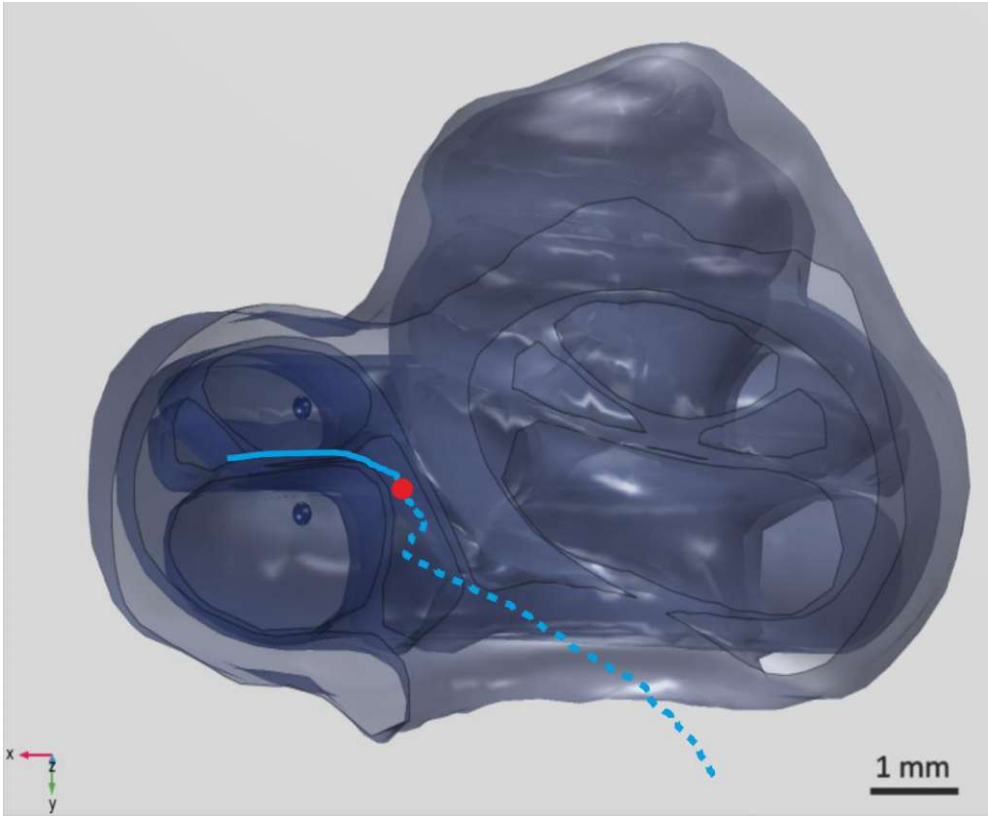

Figure 2.22. 3D view of the FE of the human cochlea model with one ANF (in cyan), the electrodes inside the scala vestibuli and scala tympani are shown in blue spheres and the soma in red.

Rattay's multi-compartment model (Rattay et al., 2001b) was chosen and implemented on the selected ANF pathways. More details on the geometry and kinetics parameters of the human cochlear neuron multi-compartment model related to this part can be found in Table 2.9.

The geometry of the peripheral process was varied in three different neural health cases based on our findings in degeneration pattern study (Heshmat et al., 2020): (i) intact case with a diameter of 1.3 µm as well as normal myelination, (ii) an intermediate degenerated case with a reduced diameter of 0.5 µm and subsequently a reduced number of myelin layers, and finally the (iii) progressive degenerated case with no peripheral process. To investigate and compare the spiking behavior of the selected ANFs in ST vs. SV electrode positions, a monophasic pulse of both polarities, cathodic pulse (CAT), and anodic pulse (ANO), with a 100 µs duration were applied. All simulations in this section were performed in MATLAB (version 2020a).

Die approbierte gedruckte Originalversion dieser Dissertation ist an der TU Wien Bibliothek verfügbar.
The approved original version of this doctoral thesis is available in print at TU Wien Bibliothek.
TU Bibliothek Your knowledge hub WIEN

Length		
	Non-myelinated terminal	10 [µm]
	Pre-somatic region	100 [µm]
	Post-somatic region	5 [µm]
	Nodes of Ranvier	2.5 [µm]
	Internode in peripheral/ central process	250 (except for the last internode) /500 [µm]
Diameter		
	Peripheral process	intact: 1.3 [µm] intermediate: 0.5 [µm]
	Soma	20 [µm]
	Central process	2.6 [µm]
Resistivity		
	Intracellular	0.1 [kΩ.cm]
	Extracellular	0.3 [kΩ.cm]
	Capacitance of cell membrane	1 [µF.ms^{-2}]
Membrane conductance		
	Non-myelinated terminal	10-fold of HH model
	Pre-somatic region	10-fold of HH model
	Post-somatic region	10-fold of HH model
	Nodes of Ranvier	10-fold of HH model
Internode conductance		
	Passive membrane conductance	0.1 [mS.ms^{-2}]
	Number of myelination layers	Peripheral /Central process: 40/80

Table 2.9. Standard parameters for human cochlear neurons.

Die approbierte gedruckte Originalversion dieser Dissertation ist an der TU Wien Bibliothek verfügbar.
The approved original version of this doctoral thesis is available in print at TU Wien Bibliothek.
TU Bibliothek Your knowledge hub WIEN

2.2.3.2 Modeling cochlear implant inserted into scala tympani and scala vestibuli

In this part, the same three-dimensional human cochlea model and four (out of the thirty) reconstructed pathways of tonotopically organized type I auditory nerve bundles were studied. In addition, two CI systems, a lateral and a perimodiolar with 12 and 22 electrode contacts, respectively, were modeled. Based on the different CI insertions in the ST and SV (Figure 2.23), in each step of the calculations, the CI insertion was individually applied, that means when ST array was used, the SV did not exist and the other way around. In addition, for a systematic comparison between ST and SV CI array insertions, the same TNs in both CI array insertions depending on the cochlear regions were chosen (Table 2.10).

TN	TN angle [°]	Corresponding frequency [Hz]
B14	28	11524
B5	169	2607
B3	206	1977
M9	327	976

Table 2.10. Names, frequencies, and angles of the investigated auditory nerve fibers as target neurons (TN) were measured from the round window concerning the modiolus axis.

To investigate and compare the threshold excitation of the selected ANFs and spike behavior of the TNs in ST vs. SV CI array insertions, a biphasic pulse and a pseudo-monophasic pulse were applied. The phase duration of pulses was 100 µs, except for the second phase of the pseudo-monophasic pulse, in which the duration was increased by a factor of four, and its amplitude decreased by the same factor to keep the charge-balanced, in both polarities, CAT and ANO pulses. All simulations in this section were performed in MATLAB (version 2020a).

For a fair comparison between two scalae, it was required to consider the same condition; hence, the evaluated distances from the center of the active electrode from each CI insertion array to the terminal of the closest ANF were chosen equivalent for ST vs. SV CI arrays. The results related to this section are presented in section 3.3.5.

Die approbierte gedruckte Originalversion dieser Dissertation ist an der TU Wien Bibliothek verfügbar.
The approved original version of this doctoral thesis is available in print at TU Wien Bibliothek.
TU Bibliothek Your knowledge hub WIEN

ANF state	Peripheral axon diameter [µm]
Intact	2
Severe	0.5
Progressive	without peripheral

Table 2.11. Three ANFs statuses based on degeneration levels of peripheral axon diameter.

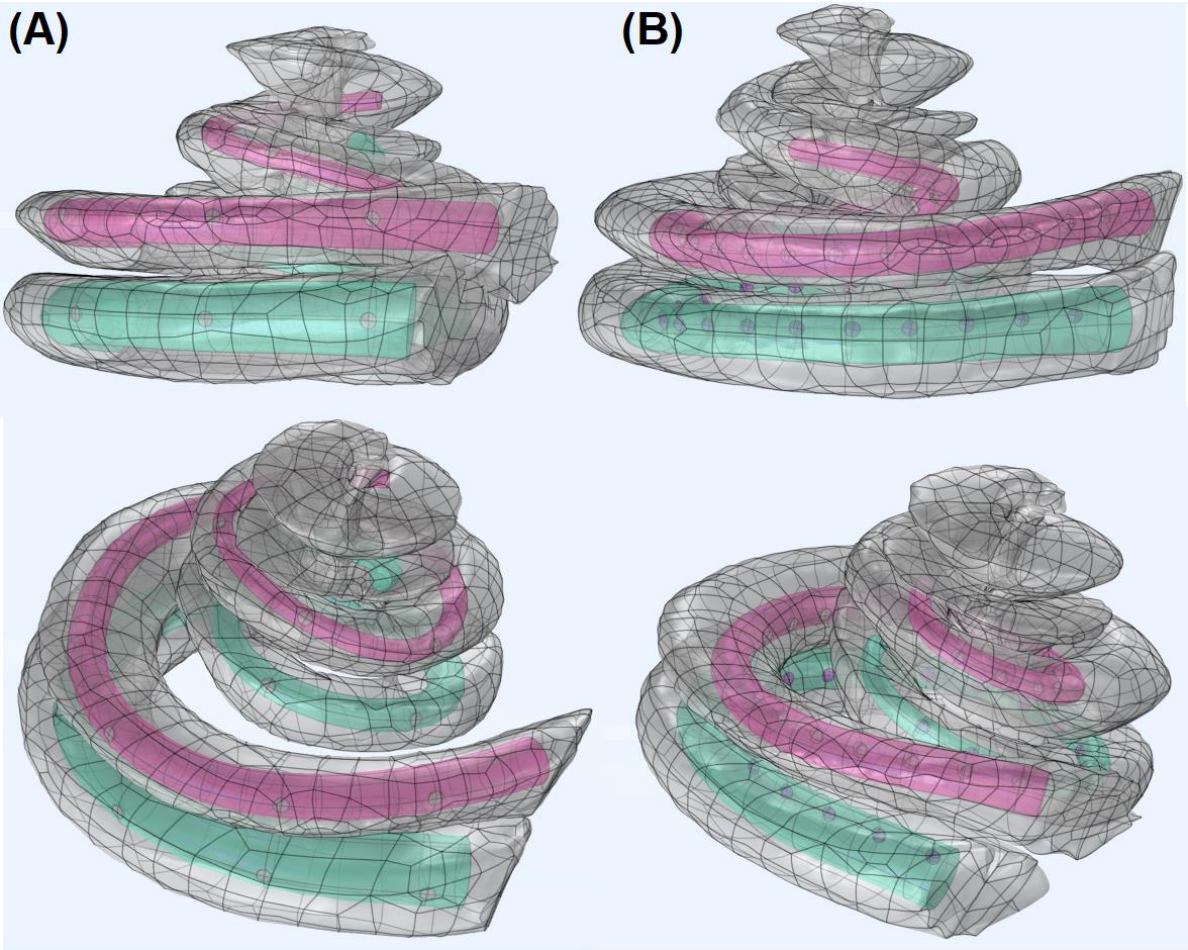

Figure 2.23. Cochlear implants inserted in scala tympani (ST) and scala vestibuli (SV). **(A)** Insert a lateral array with 12 electrode contacts in the ST (green) and SV (dark pink). **(B)** Insertion of perimodiolar array with 22 electrode contacts in the ST (green) and SV (dark pink). Noted that each CI array insertion (ST vs. SV) is used separately in calculations.

Die approbierte gedruckte Originalversion dieser Dissertation ist an der TU Wien Bibliothek verfügbar.
The approved original version of this doctoral thesis is available in print at TU Wien Bibliothek.
TU Bibliothek Your knowledge hub WIEN

Chapter 3

Results

Based on the three objectives of this dissertation, the results section is divided into three main parts. Each part describes individually the all findings related to the topic of the aims:

I. The degeneration patterns of human auditory nerves depending on the hearing loss levels are explained. Results presented in this part (section 3.1) were first published in (Heshmat et al., 2020).

II. Estimation of the neural health status of human ANFs is described. In addition, the impact of several parameters such as pulse shapes, CI arrays, CI stimulation configurations, and pulse polarity is investigated and analyzed their behavior related to polarity sensitivity. Results demonstrated in this section (3.2) were first published in (Heshmat et al., 2021).

III. A comparison between the ST versus SV implantations is performed to investigate ANFs excitation in both scalae. In addition, the similarities and dissimilarities are analyzed in both implantations.

3.1 Degeneration pattern of peripheral axon of human ANFs based on hearing loss levels

The first section of the results describes the clinical evaluation of peripheral axon diameter, myelination thickness, and G-ratio of four human cochleae with different hearing loss levels. This part of the investigation involved four human inner ears (cochleae), one normal case as the control, and three hearing loss cases (S1, S2, and S3) with hearing impairment differing in three cochlear regions based on the audiogram evaluations (Table 2.4) were used.

All data were collected based on the degree of hearing loss from three regions of the basal, middle, and apical turns. The control data compared to hearing loss cases depending on hearing loss levels to investigate the geometrical parameters. Finally, the obtained geometrical parameters were implemented into the model to investigate the impact on the behavior of ANFs under intracellular and extracellular stimulations.

Die approbierte gedruckte Originalversion dieser Dissertation ist an der TU Wien Bibliothek verfügbar.
The approved original version of this doctoral thesis is available in print at TU Wien Bibliothek.
TU Bibliothek Your knowledge hub WIEN

3.1.1 Variations in peripheral axon diameter and myelination thickness

Figure 3.1 demonstrates a histogram with fit kernel distribution for peripheral axon diameter (PD) for each hearing loss case compared to the control in the basal turn. The control data has a unimodal shape and spread from about 1.3 to 3.5 µm, with a peak at about 2 µm. In contrast, the data become a multimodal shape in the hearing loss cases depending on the hearing loss levels.

The PD range varies from 0.3 to 3.5 µm with several peaks at about 0.4, 1, 1.5, and 2 µm showing a multimodal distribution in the S1 (Profound impairment) (Figure 3.1A). In addition, as shown in Figure 3.1B-C, the other two specimens S2 and S3, with moderate impairment, represent similar PD distributions, spreading from about 0.4 to 3.5 µm with peaks at 0.5, 1.5, and 2 µm. Moreover, the PD distributions between profound and moderate impairment cases display a similar distribution pattern; however, the fibers with smaller diameters appear less in the lower hearing loss cases (moderate case).

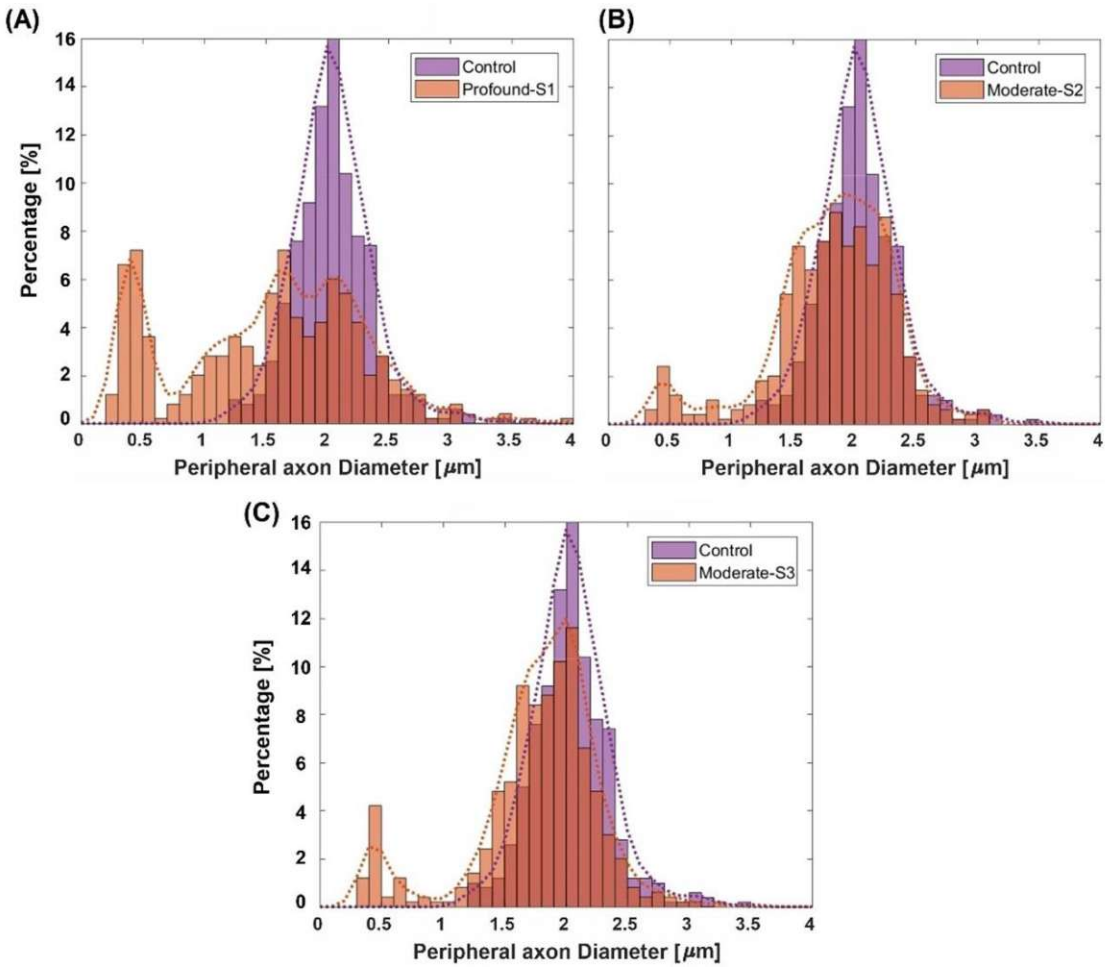

Die approbierte gedruckte Originalversion dieser Dissertation ist an der TU Wien Bibliothek verfügbar.
The approved original version of this doctoral thesis is available in print at TU Wien Bibliothek.

Figure 3.1. Histograms and fit kernel distributions (dashed lines) for peripheral axon diameter of the ANFs in the basal turn for control vs. specimens with determined hearing loss level. **(A)** Profound impairment case (S1). **(B-C)** Moderate impairment specimens (S2 and S3).

Figure 3.2 represents a histogram with fit kernel distribution for myelination thickness (MT) for each hearing loss case compared to the control in the basal turn. The MT of the control case has a unimodal form similar to the PD histogram and spreads from about 0.35 to 1.2 µm, with a peak at about 0.6 µm. The MT values are clustered on the right side of the histogram, demonstrating a right-skewed form. In contrast, the data become a multimodal shape in the S1 case, where MT spreads from about 0.1 to 1.1 µm with peaks occurring at about 0.1, 0.3, and 0.55 µm (Figure 3.2A). In addition, MT becomes wider that indicates more variety.

As shown in Figure 3.2B-C, MT spread from about 0.15 to 1.1 µm in the S2 and S3 cases, with peaks at 0.2 and 0.55 µm for both cases. Furthermore, MT represents a bimodal behavior in moderate cases whereas, MT becomes multimodal in the profound impairment case. This behavior indicates the MT decreases more in higher hearing loss levels compared to less hearing loss (S1 vs. S2 & S3).

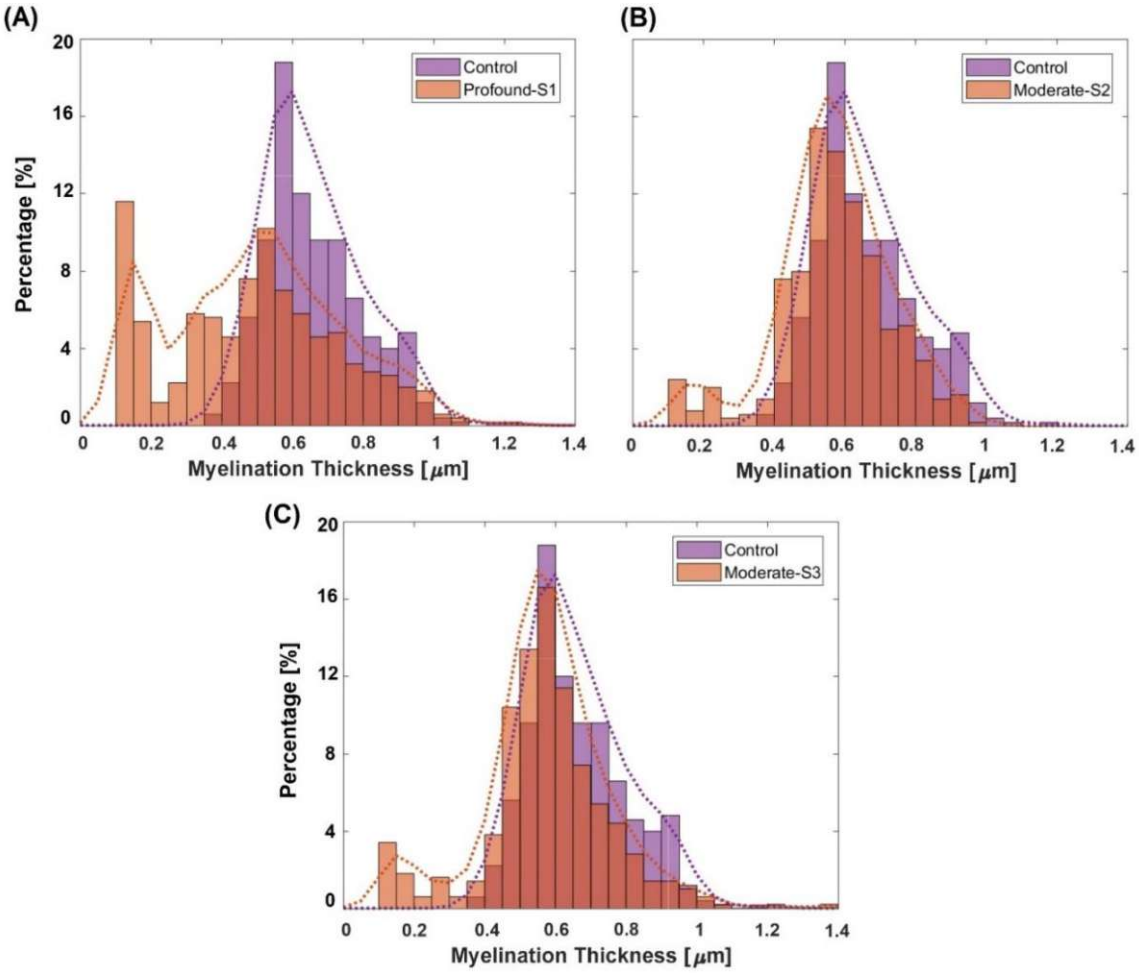

Die approbierte gedruckte Originalversion dieser Dissertation ist an der TU Wien Bibliothek verfügbar.
The approved original version of this doctoral thesis is available in print at TU Wien Bibliothek.

Figure 3.2. Histograms and fit kernel distributions (dashed lines) for myelination thickness (MT) of the ANFs in the basal turn for control vs. specimens with determined hearing loss level. **(A)** Profound impairment case (S1). **(B-C)** Moderate impairment specimens (S2 & S3).

There were two impairment cases in the middle turn of the cochlea, one with severe impairment (S1) and the other had slightly hearing loss (S2). The PD and MT distributions are represented in the upper and lower panels of Figure 3.3, respectively. The PD of S1 expands from 0.3 to 3.5 µm with peaks at about 0.4, 1.3, and 2 µm representing a multimodal distribution behavior (Figure 3.3A). On the other hand, PD expands about 1 to 3.5 µm (Figure 3.3B) in the S2 case, representing similar trends as the control case, where almost the PD distributions in control and slight impairment cases are overlapped.

Figure 3.3C shows MT spreads from about 0.1 to 1.1 µm with similar peaks as the profound case (S1) of the basal turn that happens at about 0.1, 0.3, and 0.55 µm. However, MT expands from 0.3 to 1.1 µm with a peak of about 0.6 µm in the S2 case, which has the same distribution as the control (Figure 3.3D). Both PD and MT parameters indicate that a higher level of hearing loss induces a reduction in diameter and myelination thickness of the peripheral parts of ANFs that happen the same as in the basal turn.

Die approbierte gedruckte Originalversion dieser Dissertation ist an der TU Wien Bibliothek verfügbar.
The approved original version of this doctoral thesis is available in print at TU Wien Bibliothek.
TU Bibliothek Your knowledge hub WIEN

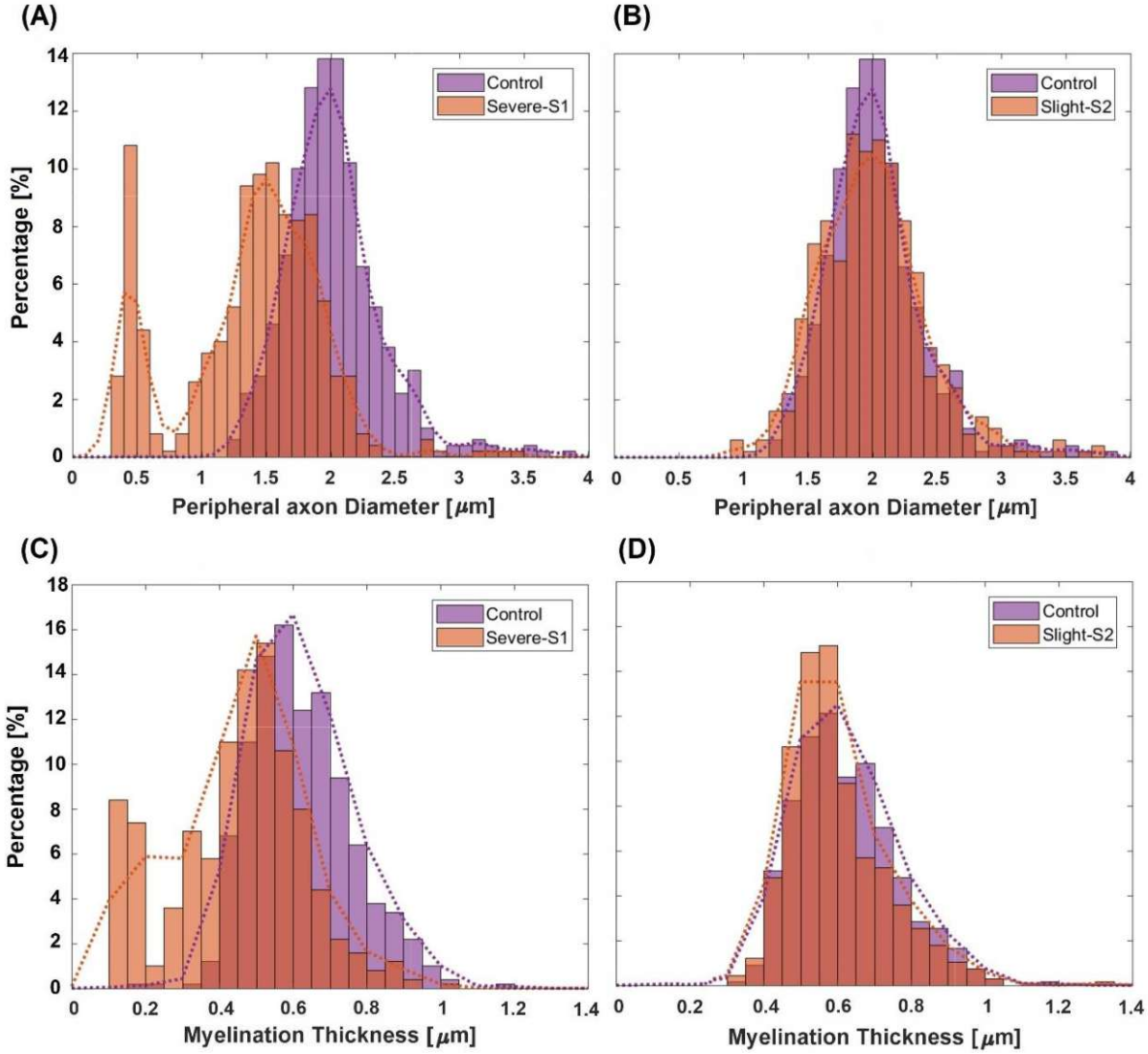

Figure 3.3. Histograms and fit kernel distributions (dashed lines) for PD and MT of the ANFs in the middle turn for control vs. specimens with determined hearing loss level. **(A)** Showing PD distribution of severe impairment case (S1). **(B)** Representing PD distribution of slight impairment case (S2). **(C)** Showing MT distribution of S1 case. **(D)** Indicating MT distribution of S2 case.

Figure 3.4 demonstrates a histogram with fit kernel distribution for the PD and MT distributions of control vs. impairment case for the apical turn. The control data spread from about 1.1 to 3.5 µm, with a peak at about 2 µm. In contrast, PD data of moderate impairment (S1) shows spreading from about 0.4 to 3.5 µm with peaks arising in about 0.5, 1.5, and 2 µm that is indicating multipolar (multi-peaks) behavior same as other turns in impairment cases (Figure 3.4A).

Besides, the MT of the control case has a unimodal form similar to the PD histogram and spreads from about 0.35 to 1.1 µm, with a peak at about 0.6 µm. However, in the mild

Die approbierte gedruckte Originalversion dieser Dissertation ist an der TU Wien Bibliothek verfügbar.
The approved original version of this doctoral thesis is available in print at TU Wien Bibliothek.
TU Bibliothek Your knowledge hub WIEN

impairment case, the MT distribution spreads from about 0.15 to 1.1 µm and with only one peak of about 0.5 µm that represents unimodal form similar to the control, but with a little skewed to the left (Figure 3.4B).

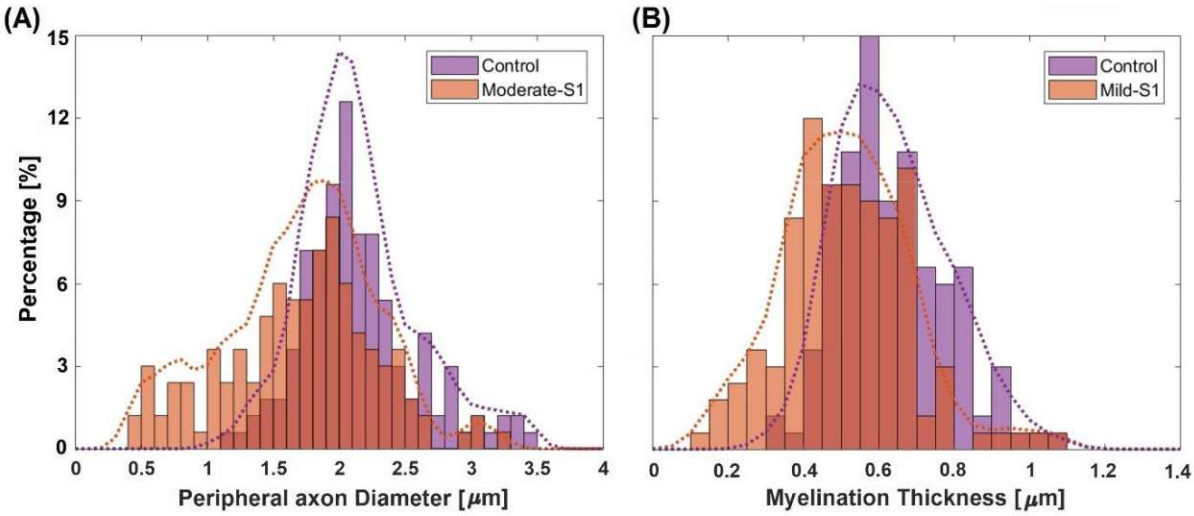

Figure 3.4. Histograms and fit kernel distributions (dashed lines) for PD and MT of the ANFs in the apical turn for control vs. specimen with determined hearing loss level. **(A)** Showing PD distribution of moderate impairment case (S1). **(B)** Representing MT distribution of mild impairment case (S1).

3.1.2 Correlation between peripheral axon diameter, myelination thickness, and G-ratio

In this section, the scatter plot with the best-fit linear regression is used for better visualization and comparing the control group with hearing loss cases. Scatter plot is employed to analyze the correlation between investigated morphological parameters of peripheral parts of ANFs. Therefore, For this purpose, MT and G-ratio are plotted against PD to investigate the relationship of the most important geometrical parameters of ANF.

Figure 3.5 represents the scatter plot with linear regression of the MT against PD in the basal turn for control and three impairment cases. The control case shows a weak positive linear relationship with r^2 = 0.22 between PD against MT. However, MT and PD have a strong positive linear relationship in all three impairment cases. In the S1 case (Figure 3.5A), the linear relationship is the most strong case with r^2 = 0.83, whereas, in S2 and S3 (Figure 3.5B-C), the linear relationship becomes weak with r^2 = 0.63 and 0.64, respectively. Hence, it can be understood that degeneration of diameter and myelination layers are directly related, which means that by decreasing the PD or MT, the other parameter decreases.

Die approbierte gedruckte Originalversion dieser Dissertation ist an der TU Wien Bibliothek verfügbar.
The approved original version of this doctoral thesis is available in print at TU Wien Bibliothek.
TU Bibliothek Your knowledge hub WIEN

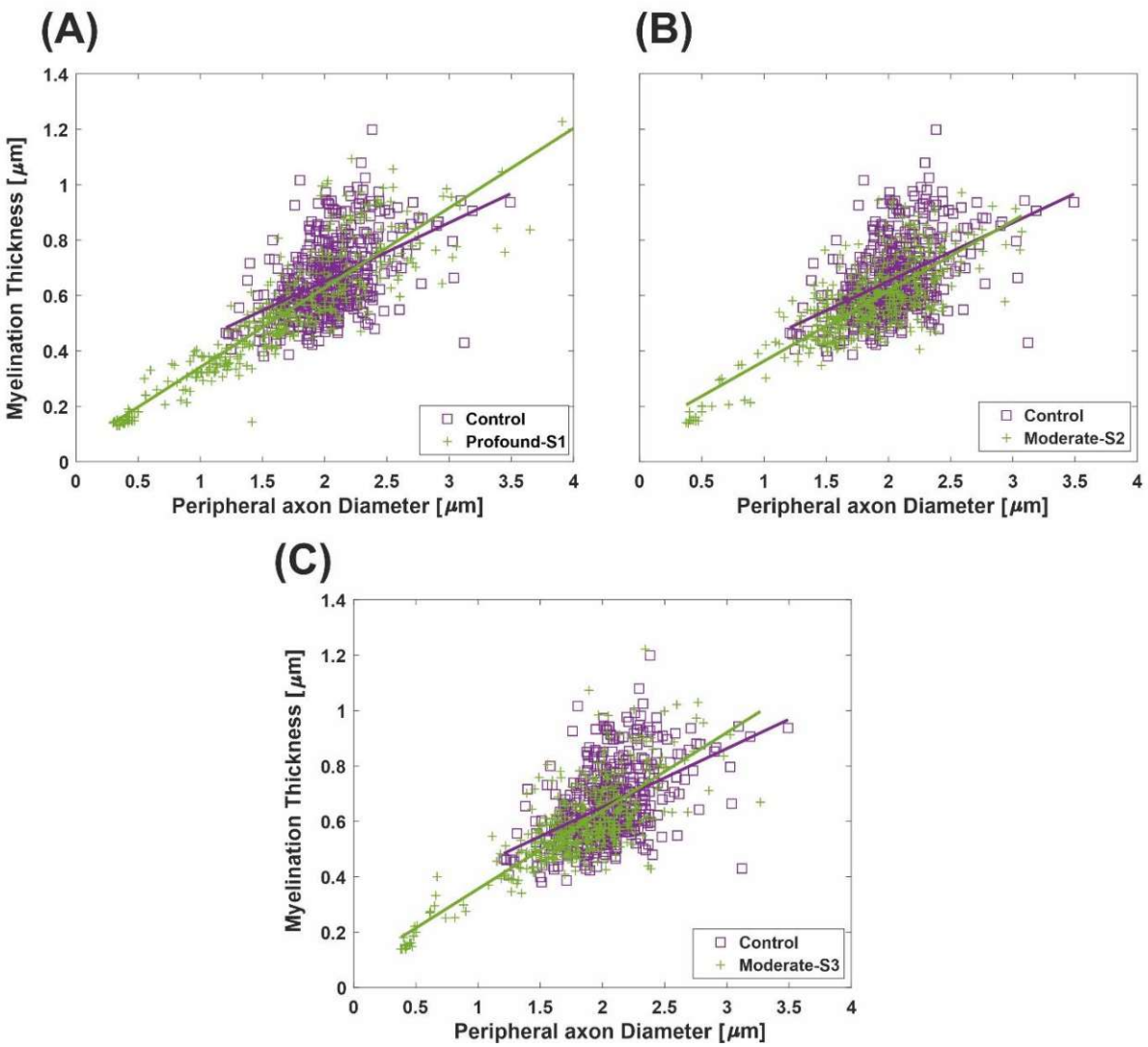

Figure 3.5. Scatter plot for the MT against PD of the ANFs in the basal turn for control and three specimens with determined hearing loss level. **(A)** Profound case. **(B-C)** Moderate cases. The best-fit linear regression to each scatterplot is included.

Figure 3.6 demonstrates the scatter plot with linear regression of the G-ratio (GR) against PD in the basal turn for control and three impairment cases. The control case shows a very weak linear relationship with r^2= 0.07 between PD against GR. The changes in PD and MT are negligible, and consequent changes in GR are insignificant. However, GR and PD have a weak linear relationship in all three impairment cases (S1, S2, and S3), with r^2 = 0.2, 0.16, and 0.12, respectively. The data implies that the GR has a known range regardless of the degeneration levels because PD and MT diminish simultaneously.

Die approbierte gedruckte Originalversion dieser Dissertation ist an der TU Wien Bibliothek verfügbar.
The approved original version of this doctoral thesis is available in print at TU Wien Bibliothek.

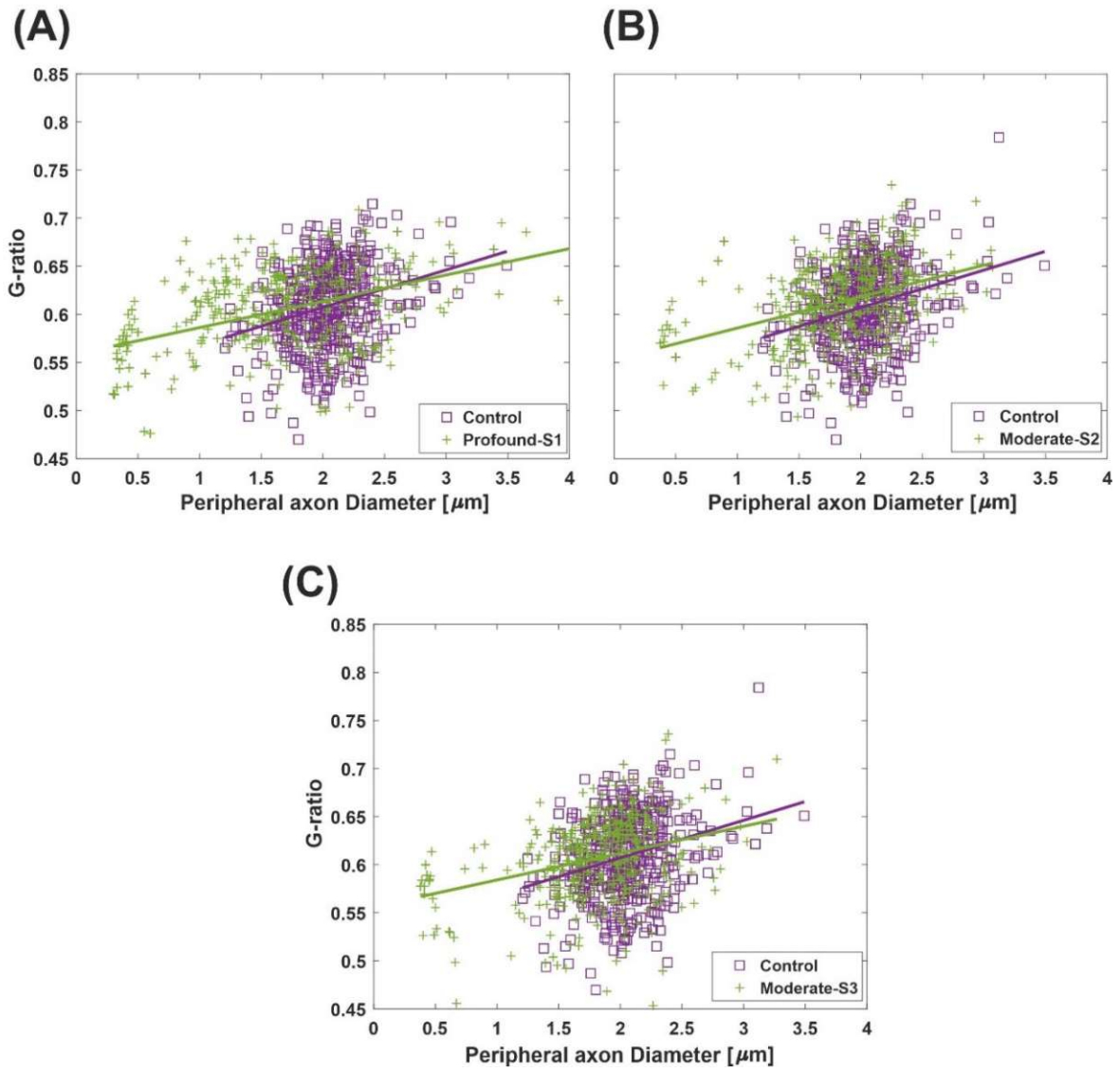

Figure 3.6. Scatter plot for the G-ratio against PD of the ANFs in the basal turn for control and three specimens with determined hearing loss level. **(A)** Profound case. **(B-C)** Moderate cases. The best-fit linear regression to each scatterplot is included.

Figure 3.7 represents the scatter plot with linear regression of the GR and MT against PD in the middle turn for control and two impairment cases, S1 and S2. The control case shows a weak positive linear relationship between GR and MT against PD with r^2 = 0.16 and 0.21, respectively. In addition, both hearing loss cases also display a positive linear relationship with r^2 = 0.15 and 0.18, respectively (Figure 3.7A-B). In MT against PD scatter plot, a positive linear relationship is observed in the severe case with r^2= 0.73 whereas, in the slight hearing loss case, the relationship is small with r^2 = 0.33 (Figure 3.7C-D).

Die approbierte gedruckte Originalversion dieser Dissertation ist an der TU Wien Bibliothek verfügbar.
The approved original version of this doctoral thesis is available in print at TU Wien Bibliothek.

The scatter plot with linear regression of the GR and MT against PD in the apical turn for the control and hearing loss case is demonstrated in Figure 3.8. The control case shows a weak positive linear relationship between GR against PD with r^2 = 0.16, whereas the moderate impairment case (S1) displays a stronger positive linear relationship (r^2 = 0.3). In addition, Figure 3.8B shows MT against PD with a weak positive linear relationship for the control with r^2 = 0.26, whereas in the S1 case, the relationship becomes stronger (r^2 = 0.39) as expected due to the direct reduction correlation between PD and MT.

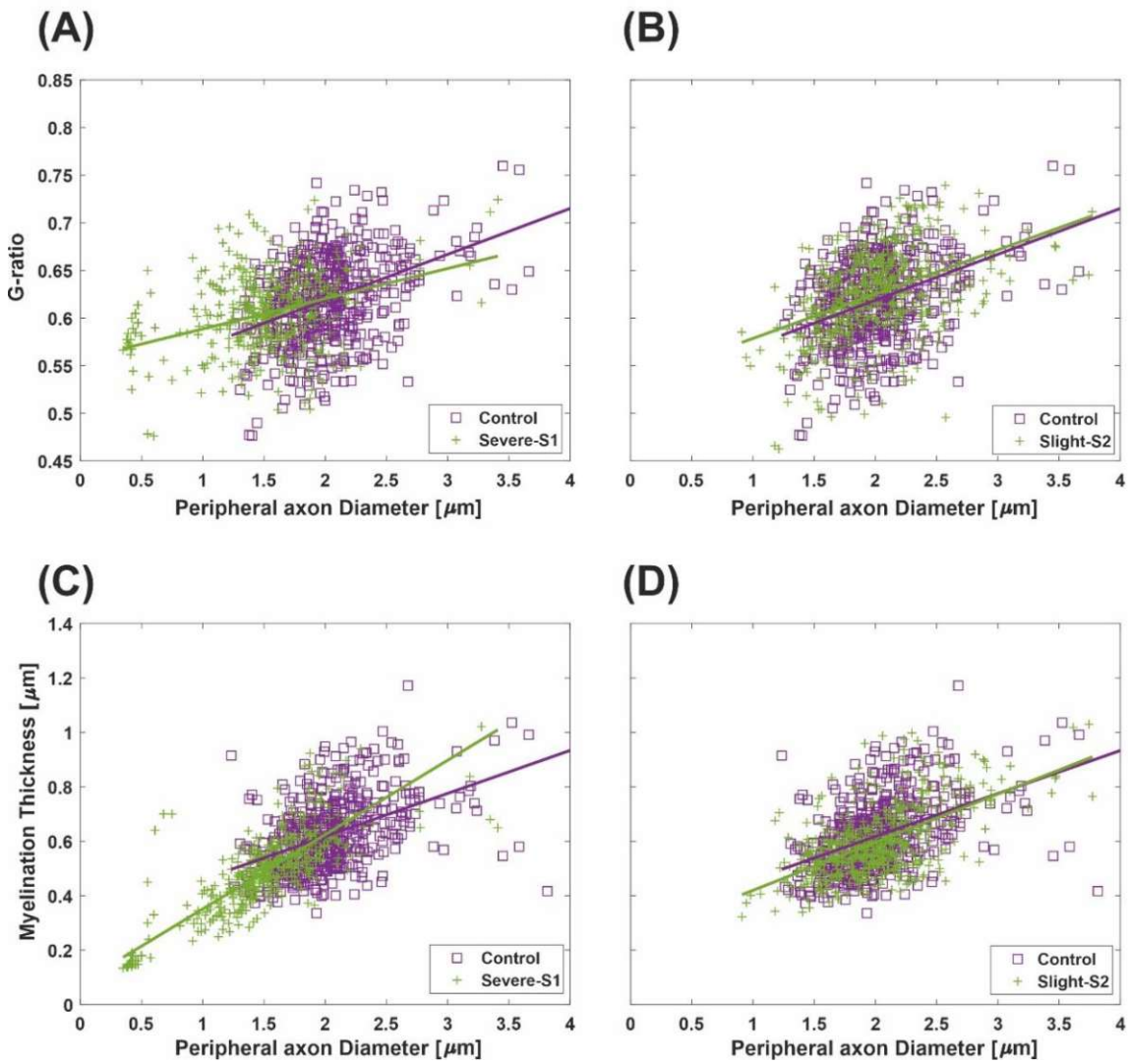

Figure 3.7. Scatter plot for the G-ratio and MT against PD of the ANFs in the middle turn for control and two specimens with determined hearing loss level. **(A-B)** Showing scatter plot for the G-ratio

Die approbierte gedruckte Originalversion dieser Dissertation ist an der TU Wien Bibliothek verfügbar.
The approved original version of this doctoral thesis is available in print at TU Wien Bibliothek.

against PD for S1 and S2 cases. **(C-D)** representing scatter plot for the MT against PD for S1 and S2 cases. The best-fit linear regression to each scatterplot is included.

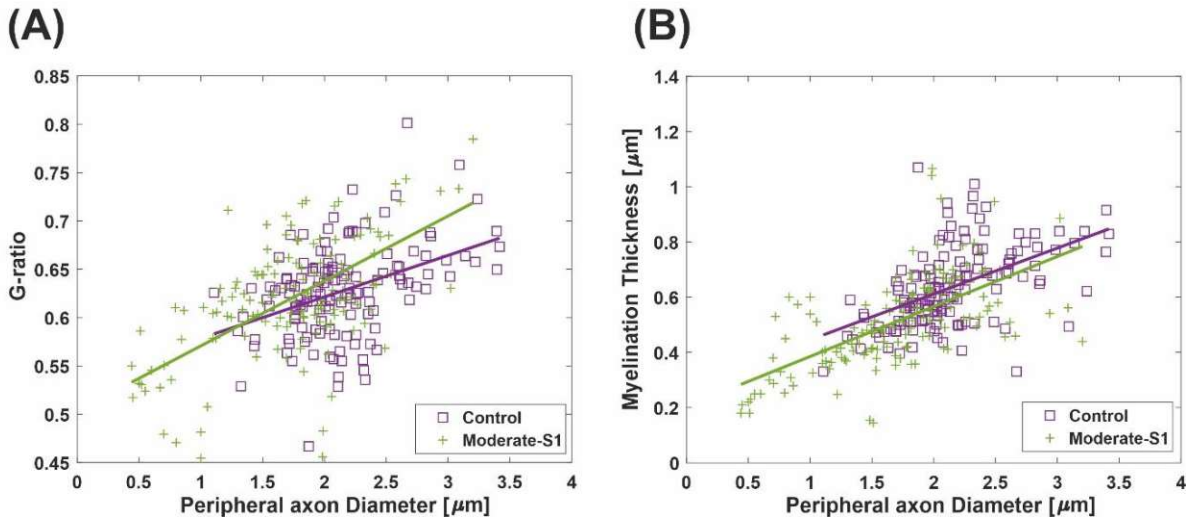

Figure 3.8. Scatter plot for the G-ratio and MT against PD of the ANFs in the apical turn for control and a determined hearing loss level specimen. **(A)** Illustrating scatter plot for the G-ratio against PD. **(B)** Demonstrating scatter plot for the MT against PD. The best-fit linear regression to each scatterplot is included.

The following section presents the PD, MT, and GR results of the control and hearing loss cases in the basal, middle, and apical turns in boxplots. In all boxplots, each box's bottom and top blue horizontal lines are the 25th and 75th percentiles of the data, respectively, and the distance between the top and bottom is the interquartile range. The red line in the middle of each box represents the median. In addition, whiskers, long single vertical dashed lines, indicate variability from maximum and minimum of the data. Any values beyond the whisker length, which lie outside the interquartile range, are shown in gray circles.

Figure 3.9 demonstrates boxplots for PD, MT, and GR in the basal turn between control and three hearing loss cases. Figure 3.9A shows the PD boxplots that the median of the control in the PD data is 2 µm, whereas the medians for S1, S2, and S3 are about 1.63, 1.88, and 1.85 µm, respectively. In addition, significant differences were observed with a p-value < 0.001 in all three hearing loss cases versus the control.

Figure 3.9B represents the MT boxplots of the basal turn for control and three impairment cases with median 0.63, 0.5, 0.57, and 0.57 µm, respectively. Significant differences were found with a p-value < 0.001 in all three hearing loss cases versus the control. Moreover, no significant differences were observed in the GR case except only between control and the profound case (S1) with a p-value < 0.001.

Die approbierte gedruckte Originalversion dieser Dissertation ist an der TU Wien Bibliothek verfügbar.
The approved original version of this doctoral thesis is available in print at TU Wien Bibliothek.
TU Bibliothek Your knowledge hub WIEN

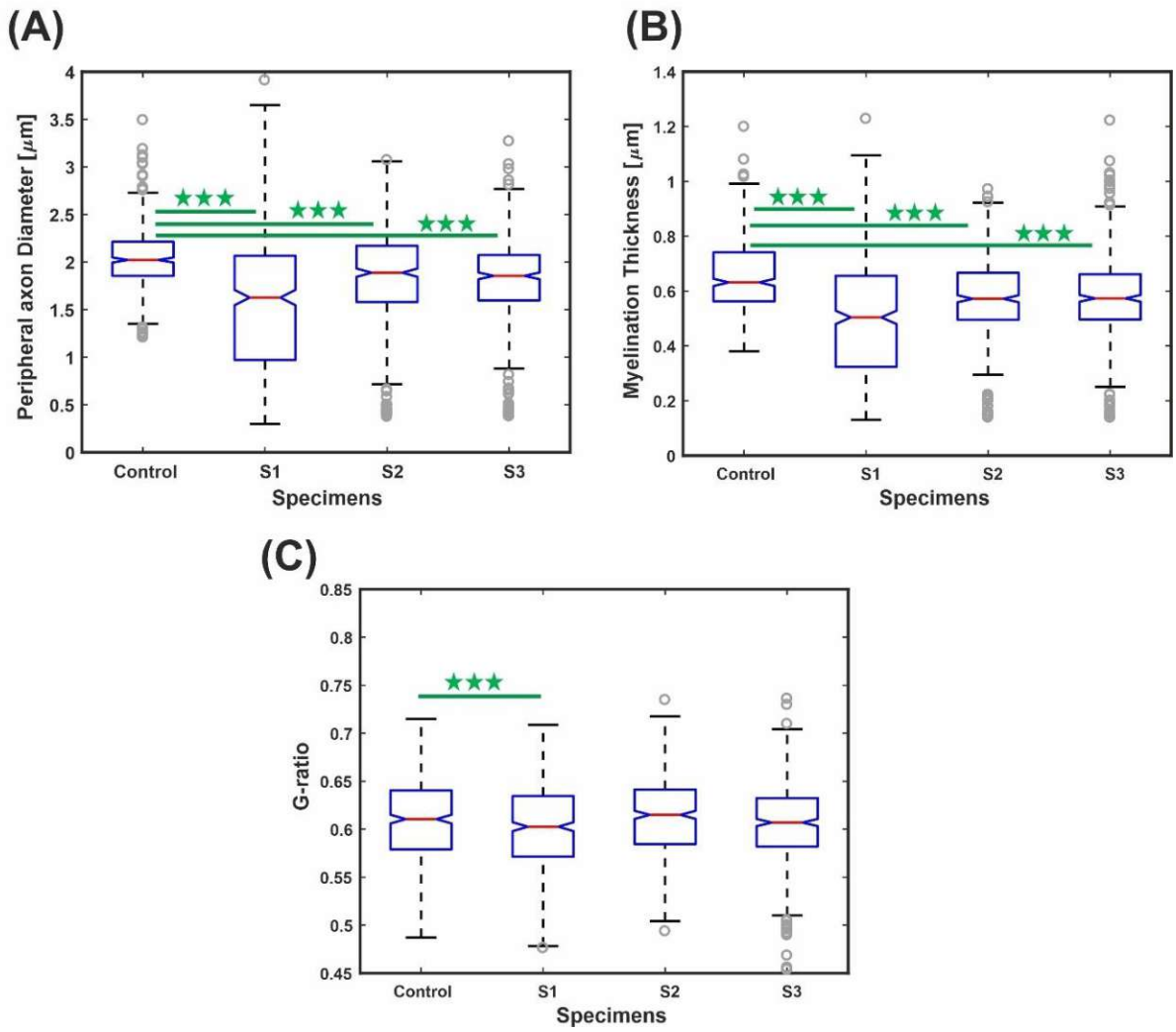

Figure 3.9. Boxplot of peripheral axon diameter **(A)**, myelination thickness **(B)**, and G-ratio **(C)** for the control and three hearing loss cases (S1, S2, and S3) in the basal turn. The red horizontal line represents the median of the data, the box includes 50% of the data, and the whiskers reach the highest and lowest values within 95% of the distribution. Open gray circles represent single values outside 95% of the distribution.

Figure 3.10 displays PD, MT, and GR boxplots between control and two hearing loss cases in the middle turn. The median of the control in the PD data is about 2 µm, whereas the medians for S1 and S2 are about 1.47 and 1.98 µm, respectively (Figure 3.10A). In addition, a significant difference was seen with a p-value < 0.001 between the control and severe case (S1).

The MT boxplots of the middle turn are depicted in Figure 3.10B for control and two impairment cases with median 0.6, 0.47, and 0.57 µm, respectively. In addition, a significant difference was found with a p-value <0.001 between the severe case and the control. Finally, the GR data have a median of about 0.62, 0.6, and 0.62 µm for the control and two impairment

Die approbierte gedruckte Originalversion dieser Dissertation ist an der TU Wien Bibliothek verfügbar.
The approved original version of this doctoral thesis is available in print at TU Wien Bibliothek.
TU Bibliothek Your knowledge hub WIEN

cases, respectively. Again, a significant difference was observed only between the control and severe case with a p-value < 0.001.

Figure 3.11 displays PD, MT, and GR boxplots in the apical turn between control and one hearing loss case. The median of the control and moderate case are about 2 and 1.77 µm (Figure 3.11A). A significant difference was noted in the PD between the control and impairment with a p-value < 0.001.

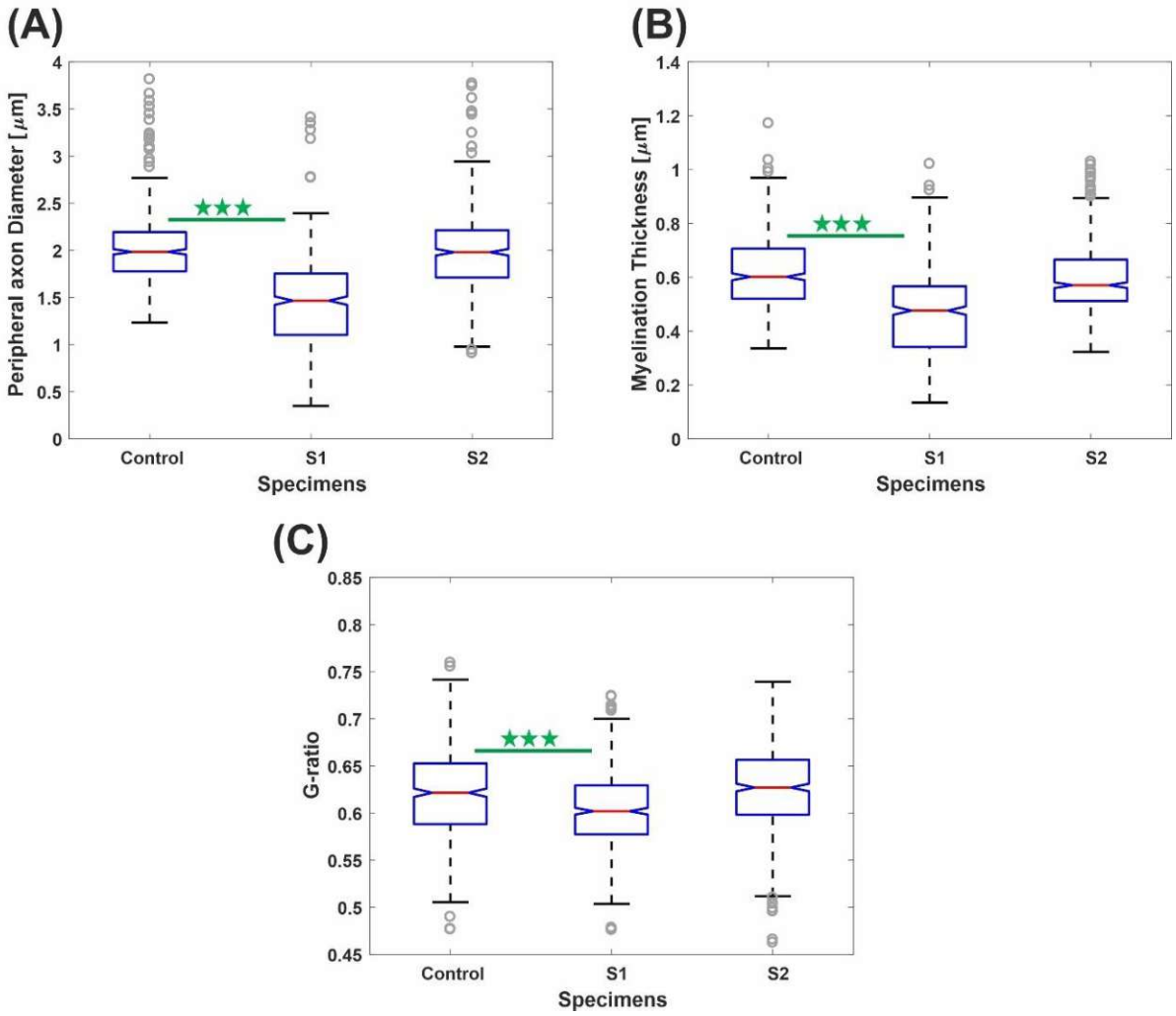

Figure 3.10. Boxplot of peripheral axon diameter **(A)**, myelination thickness **(B)**, and G-ratio **(C)** for the control and two hearing loss cases (S1, S2) in the middle turn. Same configuration as Figure 3.9.

The MT boxplots of the apical turn are represented in Figure 3.11B for control and impairment cases with a median of 0.62 and 0.51 µm. In addition, a significant difference was detected with a p-value < 0.001 between the control and the moderate hearing loss case. Finally, the GR data have the same median of about 0.62 µm for the control and hearing loss cases; however, no significant differences were observed between both data.

Die approbierte gedruckte Originalversion dieser Dissertation ist an der TU Wien Bibliothek verfügbar.
The approved original version of this doctoral thesis is available in print at TU Wien Bibliothek.

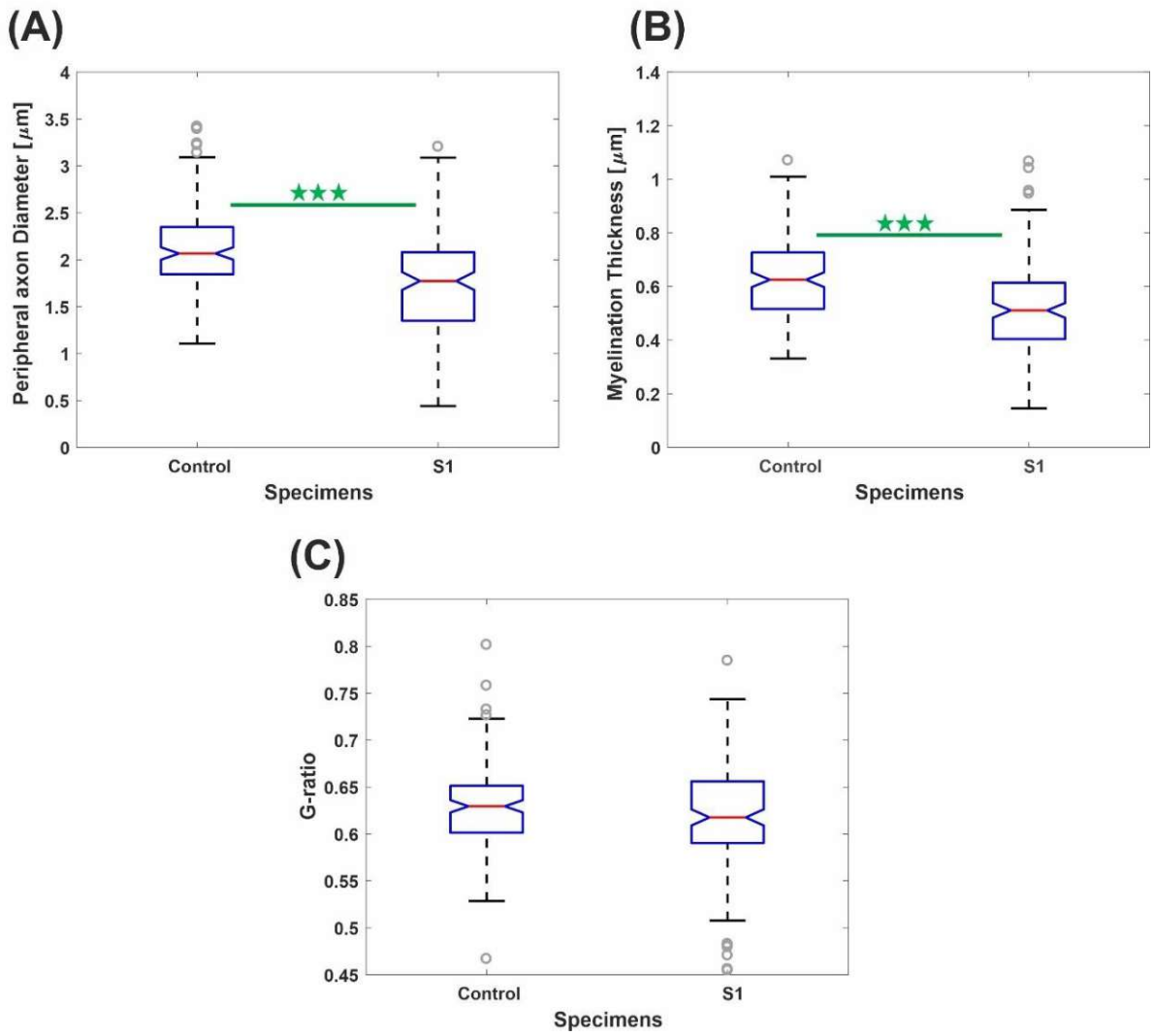

Figure 3.11. Boxplot of peripheral axon diameter **(A)**, myelination thickness **(B)**, and G-ratio **(C)** for the control and a hearing loss case (S1) in the apical turn. Same configuration as Figure 3.9.

Die approbierte gedruckte Originalversion dieser Dissertation ist an der TU Wien Bibliothek verfügbar.
The approved original version of this doctoral thesis is available in print at TU Wien Bibliothek.
TU Bibliothek Your knowledge hub WIEN

3.1.3 Impact of peripheral axon diameter and myelination thickness on synaptic threshold current and action potential arrival time in the axon

The first computer experiments concentrate on the impact of PD and MT on the excitation and the arrival time of the AP at the soma for physiological hearing in contrast to stimulation with a CI. Synaptic IHC excitation and spike conduction along the ANF were simulated by a 100 µs pulse of 300 pA injected into the first compartment, the peripheral terminal (Figure 3.12A). Thin fibers need weak postsynaptic currents to generate a spike, and consequently, a fixed stimulus amplitude causes earlier AP peaks for smaller PD. Comparing blue APs depicting first compartment excitations, the violet vertical dashed line demonstrates the earliest AP peak for the thinnest diameter in Figure 3.12A.

In contrast to this advantage for thin fibers, the AP conduction velocity of myelinated fibers is proportional to fiber diameter. Tiny fibers lose any temporal benefit of AP generation during slow AP conduction (nine gray lines for six nodes of Ranvier and three black lines for non-myelinated pre-somatic compartments) before AP arrives at the soma (orange line, Figure 3.12A).

The impact of PD on the AP conductance time to the soma is rather small for peripheral axons of the control group in contrast to the presented multimodal histograms (Figure 3.12B). The threshold current for AP initiation is inverse to PD (Figure 3.12C) because small myelinated fibers need small intracellular current flow for AP conductance (Rattay, 1990).

However, the high capacitance of the soma cannot be loaded with such a small intracellular current delivered by PD < 0.4 µm, although there is support from a non-myelinated pre-somatic region. This pre-somatic region, represented by three compartments and marked by the arrowhead in the lowest graph of Figure 3.12A, amplifies the intracellular current flow but causes an additional AP delay at soma that increases when PD is reduced (compare the middle and lower graph of Figure 3.12A).

In conclusion, as PD of fibers decreases, the AP needs more time to load the high capacitance of soma and consequently pass the soma; however, in the deterministic model of this study, AP conduction into the axon is not feasible for fibers with PD less than 0.4 µm.

To estimate the probability of spike conductance as functions of PD and G-ratio, ion current fluctuations were included in all active membrane compartments, and 20 runs were performed with an amplitude of 300 pA for all cases. Although the probability of spike arrival in the central axon is 100% for PD larger than 1 µm, it reduces by decreasing PD (Figure 3.12D).

Die approbierte gedruckte Originalversion dieser Dissertation ist an der TU Wien Bibliothek verfügbar.
The approved original version of this doctoral thesis is available in print at TU Wien Bibliothek.
TU Bibliothek Your knowledge hub WIEN

The spike probability reduced from 100% to about 5% in the case of PD = 0.5 µm with G-ratio = 0.45 to 0.7, respectively (Figure 3.12D, blue curve). In addition, the decreasing trend is more noticeable with a steeper slope in the case of the PD = 0.4 µm (Figure 3.12D, red curve), which the spike probability from 100% with G-ratio= 0.45 reaches to 0% with G-ratio = 0.65.

Finally, in the case of the PD = 0.3 µm (Figure 3.12D, green curve), the maximum spike probability of 20% happens with G-ratio = 0.45 and shows the substantial decline in the spike probability to compared with larger PD (PD ≥ 1 µm, orange curve).

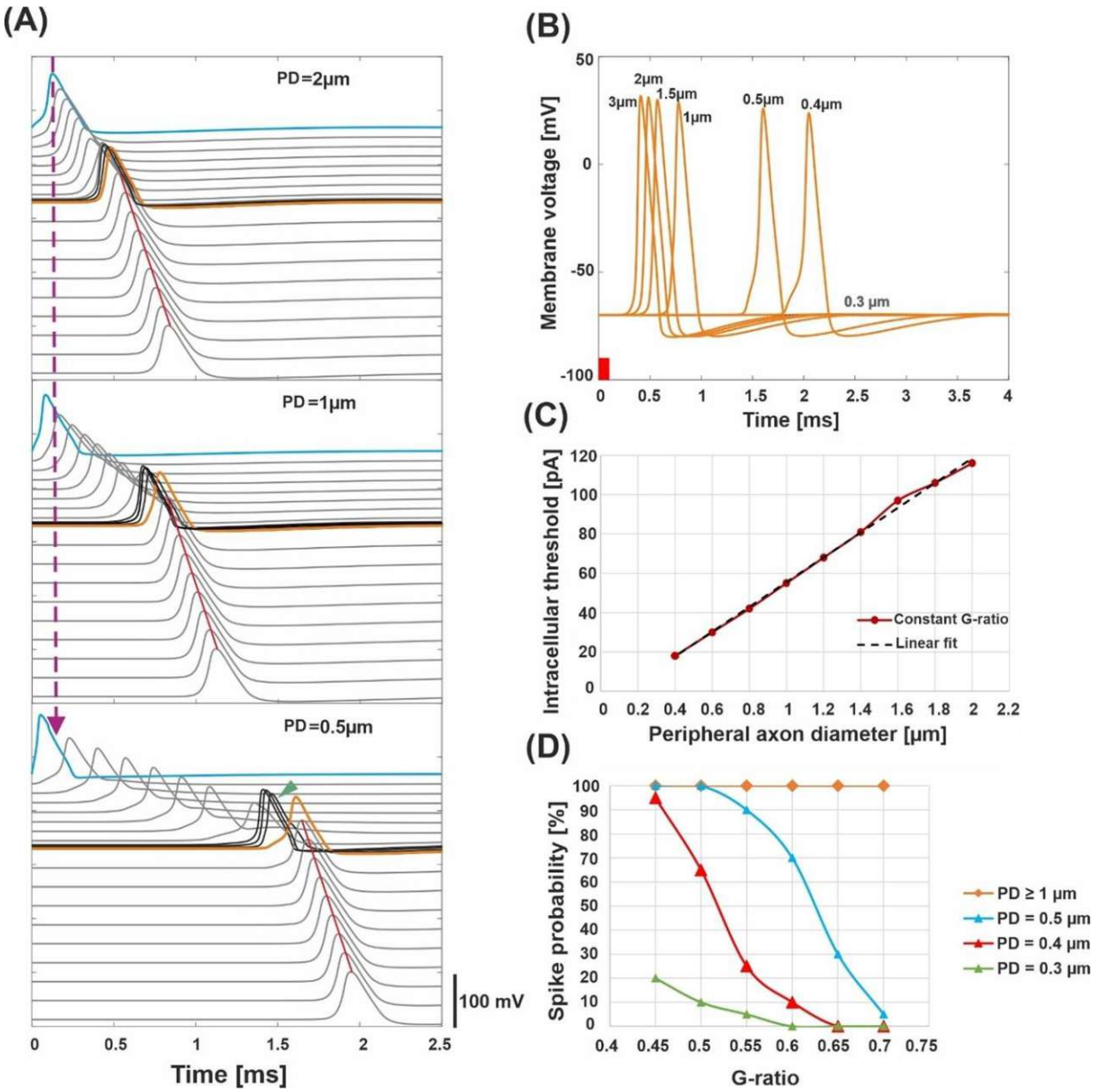

Figure 3.12. Intracellular ANF stimulation simulating synaptic excitation. **(A)** Excitation and AP conduction along the ANF (300 pA, 100 µs). AP is initiated in the first compartment (blue; note the quicker excitation when PD is reduced marked by dashed vertical line; pre-somatic compartments are

Die approbierte gedruckte Originalversion dieser Dissertation ist an der TU Wien Bibliothek verfügbar.
The approved original version of this doctoral thesis is available in print at TU Wien Bibliothek.
TU Bibliothek Your knowledge hub WIEN

marked with arrowhead for PD = 0.5 µm and show slow conduction velocity for thin fibers). Conducted APs are shown for all active compartments with a vertical shift indicating the compartment's location. The arrival time of the AP in the soma (orange) increases when PD decreases. Axon's conduction velocity (marked by the red line at AP peaks) outmatches all dendritic cases as a consequence of the larger central axon diameter (4 µm). **(B)** Membrane voltage in the soma for varied PD demonstrates increased latency when PD is reduced; no AP for PD = 0.3 µm. **(C)** Synaptic threshold current for AP conduction as a function of PD (red) and linear fit (black dashed line). **(D)** Probability of spike conduction across the soma as a function of G-ratio for various PD. In panels A–C, G-ratio = 0.625 (mean value of the control). (A-B) were calculated without noise (C-D) with the stochastic model that included current fluctuations in the active membrane.

Figure 3.13 displays the loss of AP for the healthy case (PD = 2 µm) and degenerated cases (PD = 0.5 and 0.3 µm) with two G-ratio values. The investigation loss of APs was performed for weak stimulation, namely, at the threshold (I_{th}) and 1.2 times threshold (I_0).

In the healthy case with G-ratio = 0.625, the spiking pattern shows the only 10 spikes by applying 20 runs can pass the soma and reaches the central axon with threshold stimulation (Figure 3.13A, first row), whereas, by increasing the amplitude (I_0 = 139 pA), the jitter and delay decrease, and 20 spikes reach the central axon (Figure 3.13B, first row).

In contrast, in the degenerated case (PD = 0.5 µm), although the threshold value is substantially about 136% decreased, but the sharply synchronized spiking pattern is reduced compared to the healthy case, and consequently causes the enhancement of delay and jitter. In addition, by generating 17 spikes in the peripheral axon, only 6 spikes arrive at the central axon (Figure 3.13A, second row). Furthermore, by increasing the threshold (I_0 = 26 pA), the delay and jitter are reduced by about 5%, and the spikes in the peripheral axon and arriving at the central axon are increased (Figure 3.13B, second row).

By applying the G-ratio = 0.5 in the degenerated case for PD = 0.5 µm (Figure 3.13A-B, third row), the jitter and delay are about 20% decreased compared with the same degeneration level but with G-ratio = 0.625 for the threshold and 1.2 times threshold. In addition, the arriving spikes at the central axon significantly increased about 85% and 61% for the threshold and 1.2 times threshold stimulations, respectively.

Furthermore, by decreasing the diameter (PD = 0.3 µm) with the G-ratio = 0.5 (Figure 3.13A-B, last row), the threshold value about 58% decreased in comparison with the PD = 0.5 µm. However, the number of spikes at the central axon is about 152% decreased in comparison with the case of PD = 0.5 µm. Surprisingly, spikes are generated more in the peripheral axon by increasing the threshold (I_0 = 14 pA), but only 2 spikes can reach the central axon, which is similar to the threshold case (Figure 3.13A vs. 3.13B, last row).

Die approbierte gedruckte Originalversion dieser Dissertation ist an der TU Wien Bibliothek verfügbar.
The approved original version of this doctoral thesis is available in print at TU Wien Bibliothek.
TU Bibliothek Your knowledge hub WIEN

Overall, the healthy (normal) fiber (PD= 2 µm) shows a sharply synchronized spiking pattern with a reduced delay for the higher amplitude. Increasing the amplitude causes a decrease in jitter and delay. The case of PD = 0.5 µm demonstrates that synchronization becomes higher, and the delay becomes shorter when the G-ratio is reduced (increasing of MT). For the higher G-ratio, only 30 – 45% of spikes can pass the soma. The case PD = 0.3 µm generates no AP for G-ratio higher than 0.55 (simulated but not shown). However, by shortening the internodal lengths to half of its standard length (250 µm), the AP is generated in the peripheral axon even with the standard G-ratio of 0.625, yet the small intracellular current is unable to load the soma capacitance enough to initiate a spike in the soma.

Die approbierte gedruckte Originalversion dieser Dissertation ist an der TU Wien Bibliothek verfügbar.
The approved original version of this doctoral thesis is available in print at TU Wien Bibliothek.
TU Bibliothek Your knowledge hub WIEN

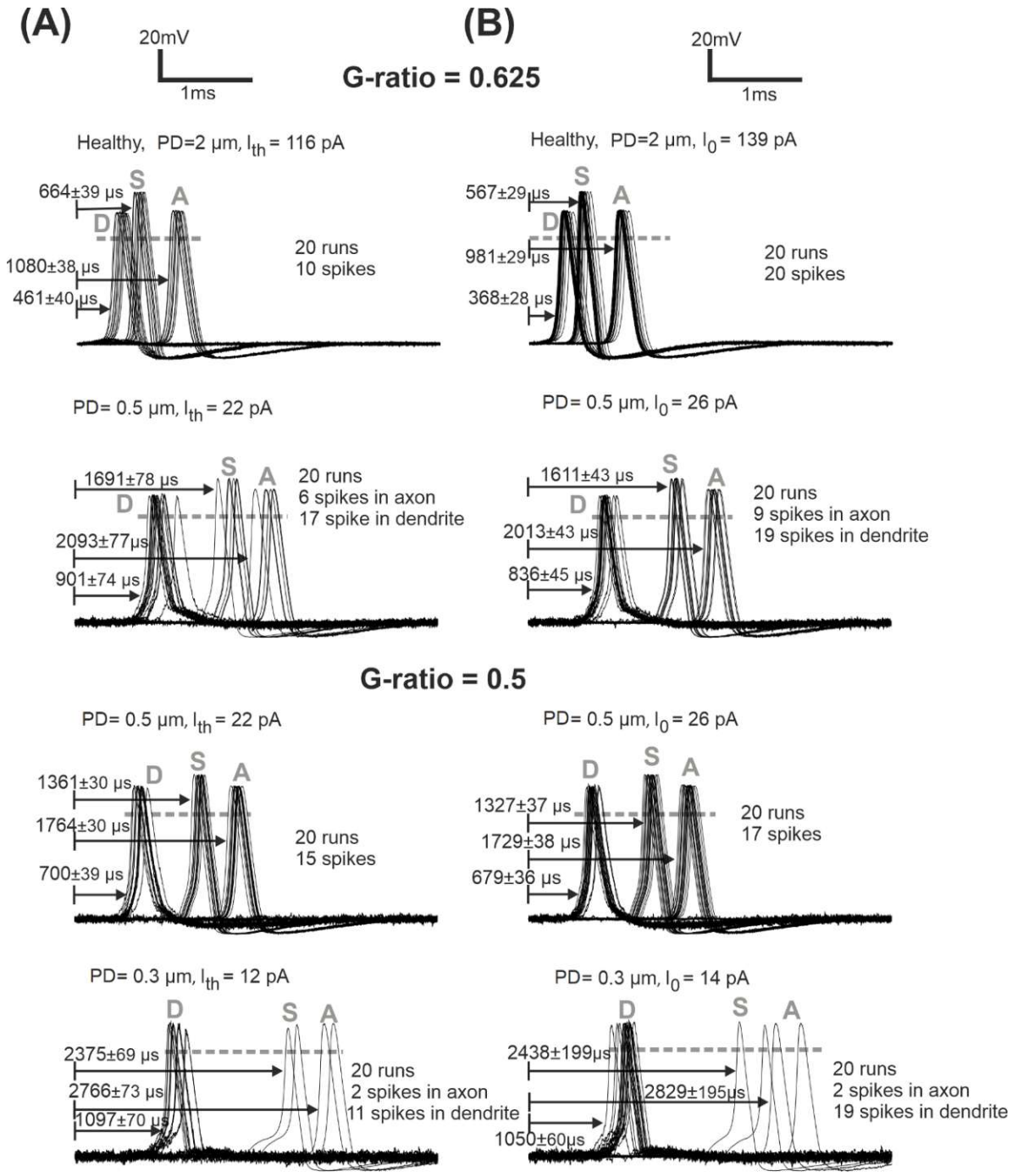

Figure 3.13. ANF responses at peripheral terminal (first compartment), soma, and axon (last compartment) are marked with D, S, and A, respectively. **(A)** Later APs and larger jitters for synaptic stimuli at threshold (I_{th}) versus **(B)** more synchronized responses for synaptic stimuli at I_0 = 1.2 × threshold are represented for G-ratios = 0.625 and 0.5. While the arrows start at the stimuli onset, the delays represent the time when the membrane voltage reaches 0 mV (shown with gray dashed horizontal lines). Recording point A of simulations corresponds with the axonal terminal from the micro-CT sample (Potrusil et al., 2020).

Die approbierte gedruckte Originalversion dieser Dissertation ist an der TU Wien Bibliothek verfügbar.
The approved original version of this doctoral thesis is available in print at TU Wien Bibliothek.
TU Bibliothek Your knowledge hub WIEN

The following experiments show the expected AP delays in the soma as a function of PD (Figure 3.14A) and, according to the PD histograms, which show the different PD distributions for different cochlear regions based on hearing loss levels (Figure 3.14B–E). Figure 3.14A shows exponential decay of mean delays of AP in the soma with various PD values. The thinnest fibers (PD < 0.5 µm) indicate the most extensive delay, and the mean AP delays become less by increasing the PD, and by reaching the PD ≥ 2 µm, the shorter delays occur.

Figure 3.14B demonstrates the spiking pattern of the control (healthy) case compared with the degenerated cases in different hearing loss levels based on the cochlear turns (Figure 3.14C-E). The most significant delay and jitter values occur for very thin fibers that are found in the profound hearing loss case with 1.816 ms and 0.405 ms, respectively. When the degeneration levels become moderate, the latency and jitter (1.664 ± 0.257) decrease in a similar PD range (Table 3.1). When fiber diameter increases and becomes close to the control group, the delay becomes less. However, the fiber numbers with larger diameters do not appear as much as the control case.

PD [µm]	**Mean delay ± STD [ms]**			
	Control (basal)	**Profound (basal)**	**Severe (middle)**	**Moderate (apical)**
0.3≤ PD <1.3	-	1.816± 0.405	1.800± 0.387	1.664± 0.257
1.3≤ PD ≤2	1.248 ± 0.032	1.279± 0.044	1.284± 0.043	1.270± 0.045
2<PD ≤3	1.197 ± 0.014	1.191± 0.016	1.201± 0.013	1.192± 0.015
PD >3	1.159 ± 0.006	1.162± 0.010	1.163± 0.007	1.157± 0.006

Table 3.1. Mean delay ± STD (jitter) for the counted fibers in each specimen. For calculations an intracellular stimulus of 300 pA and a various run numbers, based on each fiber group quantity, are chosen.

Moreover, for the thickest group of fibers (PD > 3 µm), the mean delay and jitter values are the smallest compared with the other fiber groups. The successful spike conduction of thicker fibers is based on a high density of sodium channels in the nodes of Ranvier and an adequate number of insolating myelination sheets covering the internodes, which limit the transmembrane currents.

Die approbierte gedruckte Originalversion dieser Dissertation ist an der TU Wien Bibliothek verfügbar.
The approved original version of this doctoral thesis is available in print at TU Wien Bibliothek.
TU Bibliothek Your knowledge hub WIEN

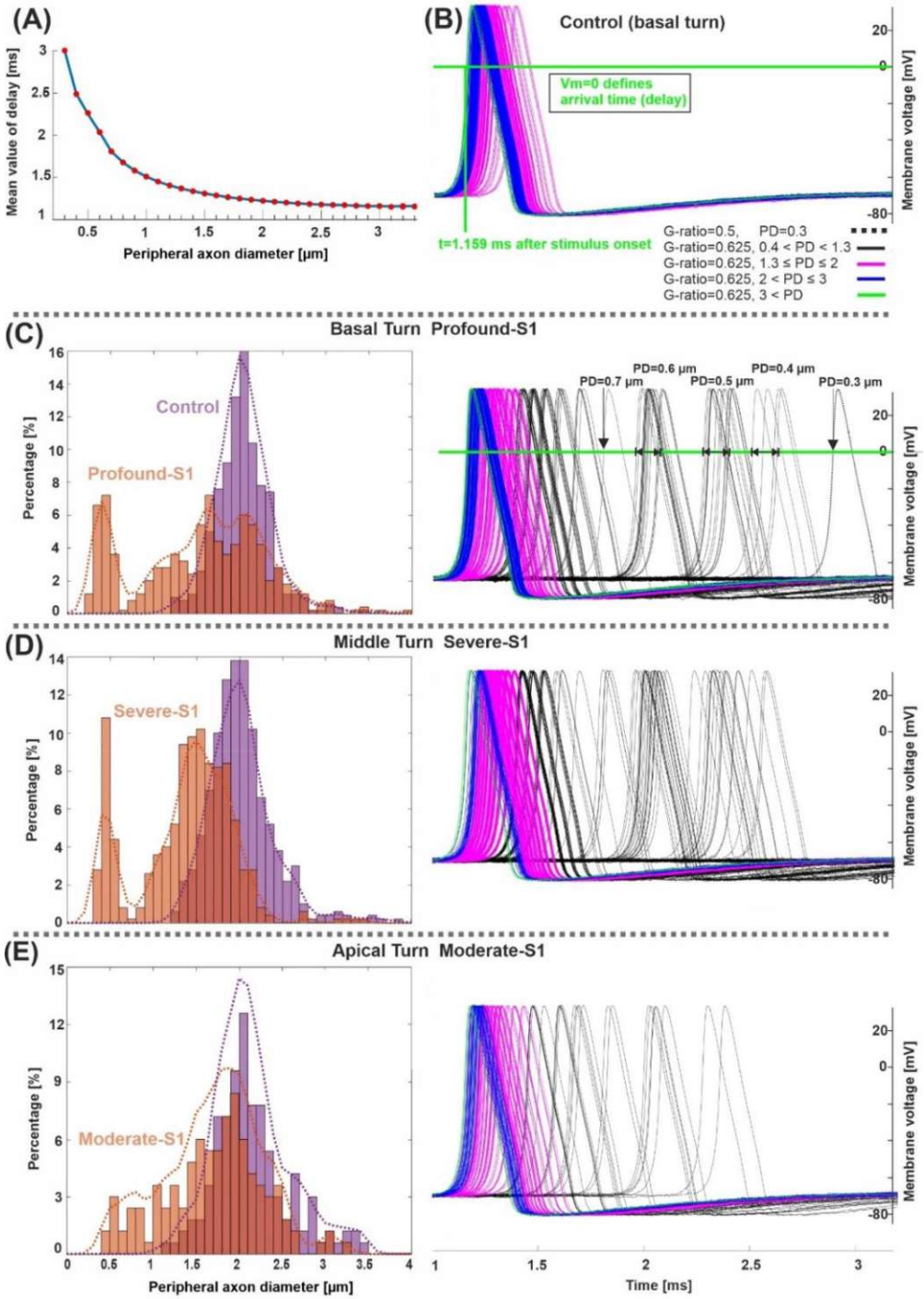

Figure 3.14. Spike pattern comparison between control and hearing loss cases in three cochlear regions. **(A)** Delay (mean values) as a function of PD (20 runs per PD). **(B–E)** Spiking patterns of the investigated specimens (S1 vs. control) based on the number of counted fibers in different cochlear regions, the basal, middle, and apical, stimulated with 300 pA. The horizontal and vertical green lines in panel B represent the membrane voltage value at 0 mV and the corresponding time (delay) at soma after the stimulus onset, respectively. The color code in panel **(B)** applies to **(C–E)**. Recording point at axonal terminal. The x-axis of the right panel in panel E applies to all spike pattern graphs.

Die approbierte gedruckte Originalversion dieser Dissertation ist an der TU Wien Bibliothek verfügbar.
The approved original version of this doctoral thesis is available in print at TU Wien Bibliothek.
TU Bibliothek Your knowledge hub WIEN

3.1.4 Extracellular stimulation

By considering one ANF (basal7) in the position 137°, synaptic excitation of a monophasic anodic pulse and extracellular stimulation of a monophasic cathodic pulse from lateral CI, EL5 (143°), and its corresponding perimodiolar electrode CA11 (153°) were compared (Figure 3.15). In contrast to synaptic excitation Figure 3.15A, where the AP is initiated in the first compartment, it is more complicated to understand the AP generation and propagation during extracellular stimulation (Figure 3.15B-C).

Depending on the cell geometry, cochlear region, electrode position, and pulse intensity, there are several sites along the fiber where spikes can be generated, and, moreover, excitation is possible both with cathodic (negative) and anodic (positive) pulses. An indicator for possible spike initiation sites is the membrane voltage profile along the ANF under subthreshold conditions, e.g., the full blue line in Figure 3.15B-C, which has its maximum within different parts of peripheral axon for both PD = 2 µm (left) and PD = 0.5 µm (middle).

As mentioned before, thinner fibers are easier to excite with intracellular stimuli, but the opposite, known as reversed recruitment order (Blair and Erlanger, 1933), is seen for extracellular stimulation. Comparing values of threshold currents in Figure 3.15A–C demonstrates that the fiber with PD = 2 µm needs 116 pA current whereas for thinner fiber (PD = 0.5 µm), the stimulation current significantly about 136% is decreased with intracellular stimuli.

Furthermore, applying intracellular stimulation makes the thinner fibers easier to excite; however, this behavior does not happen in the extracellular. As shown in Figure 3.15B, the ANF is stimulated with a current of about 109 µA in the healthy case with PD = 2 µm, whereas in the degenerated case with PD = 0.5 µm, the required current for excitation ANF becomes larger just about 24%, which is about 139 µA, in the lateral CI system. On the other hand, in the perimodiolar case, the same behavior occurs but with less current intensity (Figure 3.15C). The needed current in the healthy and degenerated cases is about 64 µA and 86 µA, which is approximately a 30% difference between healthy and degenerated excitation thresholds.

Die approbierte gedruckte Originalversion dieser Dissertation ist an der TU Wien Bibliothek verfügbar.
The approved original version of this doctoral thesis is available in print at TU Wien Bibliothek.
TU Bibliothek Your knowledge hub WIEN

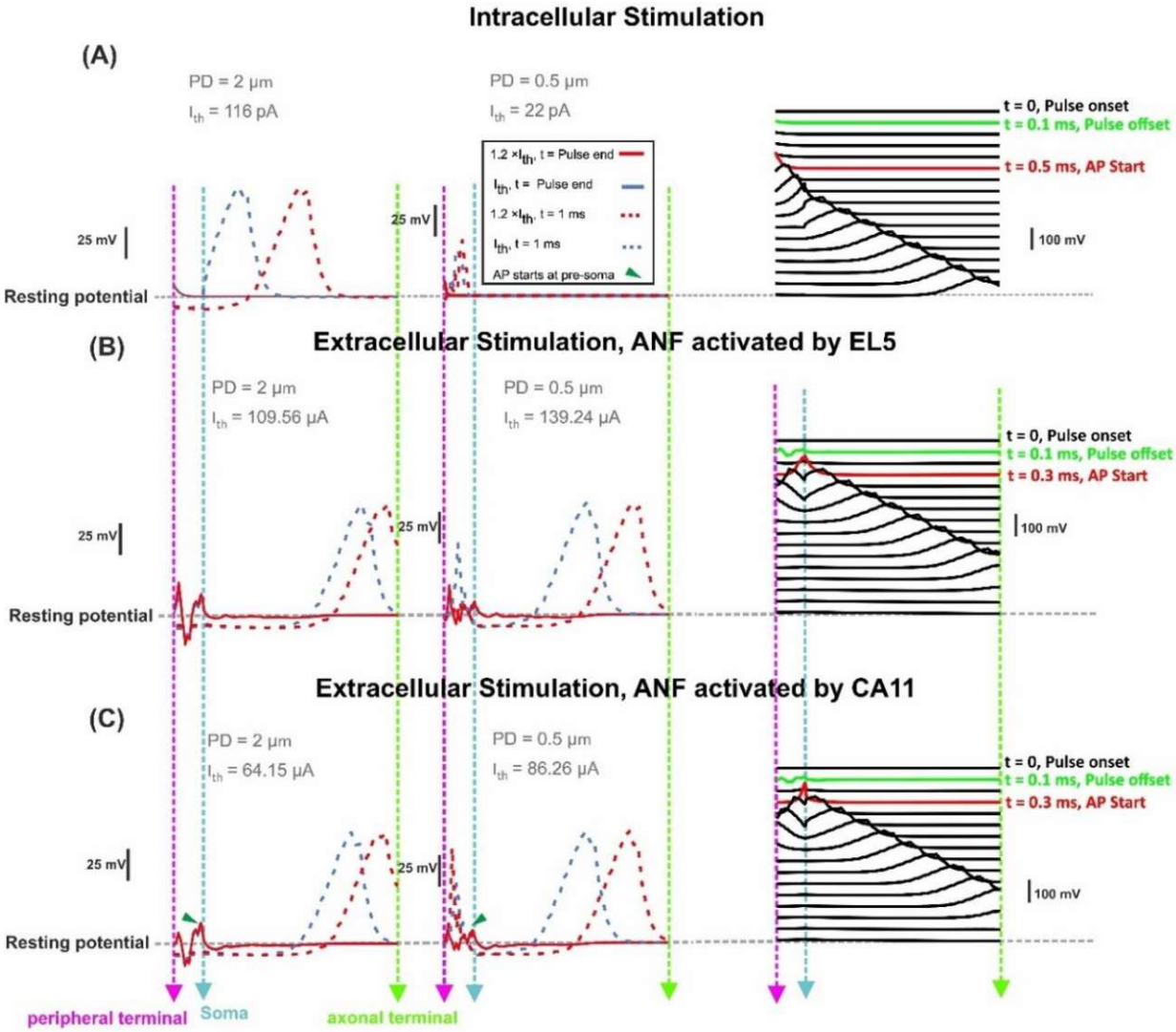

Figure 3.15. Membrane voltage along ANF basal7 (137°, G-ratio = 0.625) as a response of intra- and extracellular stimulation. **(A)** Membrane voltage for PD = 2 vs. 0.5 µm at pulse offset (0.1 ms) and 1 ms after intracellular stimulus onset with a pulse amplitude at threshold (I_{th}) and 1.2 × threshold. Right panel: AP propagation along the ANF with PD = 2 µm at the threshold. Each line shows the membrane voltage at a fixed time. The green and red lines represent the times corresponding to stimulus offset and the first achievement of the AP peak, respectively. **(B)** Same configuration for extracellular stimulation of lateral electrode EL5 and **(C)** perimodiolar electrode CA11. Vertical dashed pink, cyan, and green lines represent the positions of the peripheral terminal, soma, and axonal terminal, respectively. Arrowheads indicate that the firing starts at presoma.

Die approbierte gedruckte Originalversion dieser Dissertation ist an der TU Wien Bibliothek verfügbar.
The approved original version of this doctoral thesis is available in print at TU Wien Bibliothek.
TU Bibliothek Your knowledge hub WIEN

To investigate the impact of the neural pathway on the threshold profiles, five electrodes from each CI array system were selected (Table 2.5 and Figure 2.18). Two electrodes in basal (EL1, EL3, CA2, and CA6), one electrode in the middle (EL5 and CA11), and two electrodes in the upper-middle (EL8, EL9, CA19, and CA20) in each CI system. A fixed potential of 1 V was applied at the surface of the active electrode, and the V_e distribution along the interested pathways was calculated with the FE model.

Moreover, all calculations were implemented for three different peripheral axon geometries: a healthy fiber of PD = 2 µm and two degeneration levels with PD = 0.5 µm and without peripheral axon case (profound degeneration). At each level of calculations, all ANFs were considered with the same geometry.

Figure 3.16 demonstrates the electrode distances (upper panel) and the inverse relationship of V_e (lower panel) along the fiber of five TNs in blue and red, which were stimulated with perimodiolar and lateral CI systems, respectively.

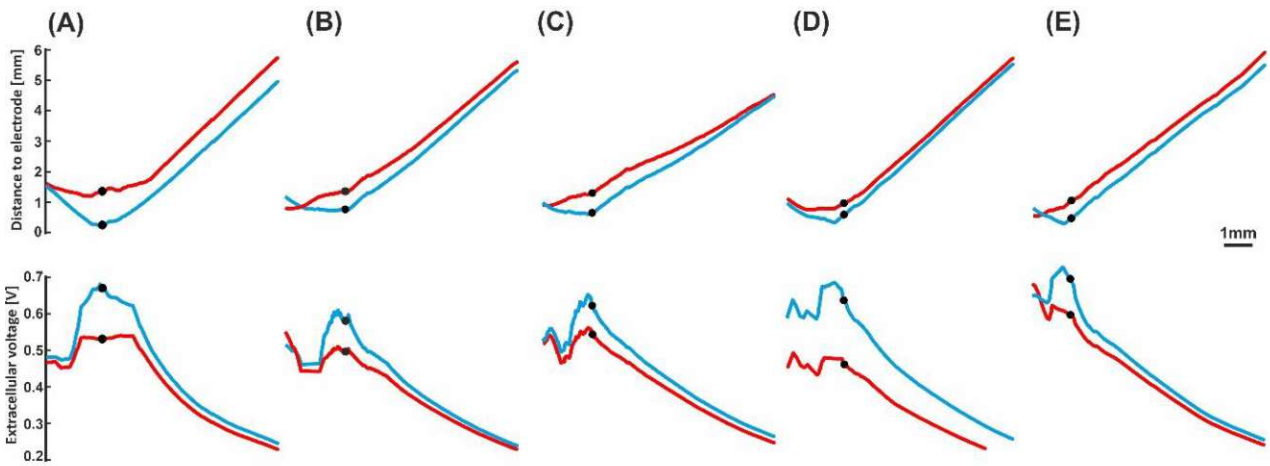

Figure 3.16. Demonstrates the electrode distances (upper panel) and the inverse relationship of extracellular voltage (lower panel) along the fiber of five target neurons in blue and red, which were stimulated with perimodiolar and lateral CI systems, respectively.

Die approbierte gedruckte Originalversion dieser Dissertation ist an der TU Wien Bibliothek verfügbar.
The approved original version of this doctoral thesis is available in print at TU Wien Bibliothek.

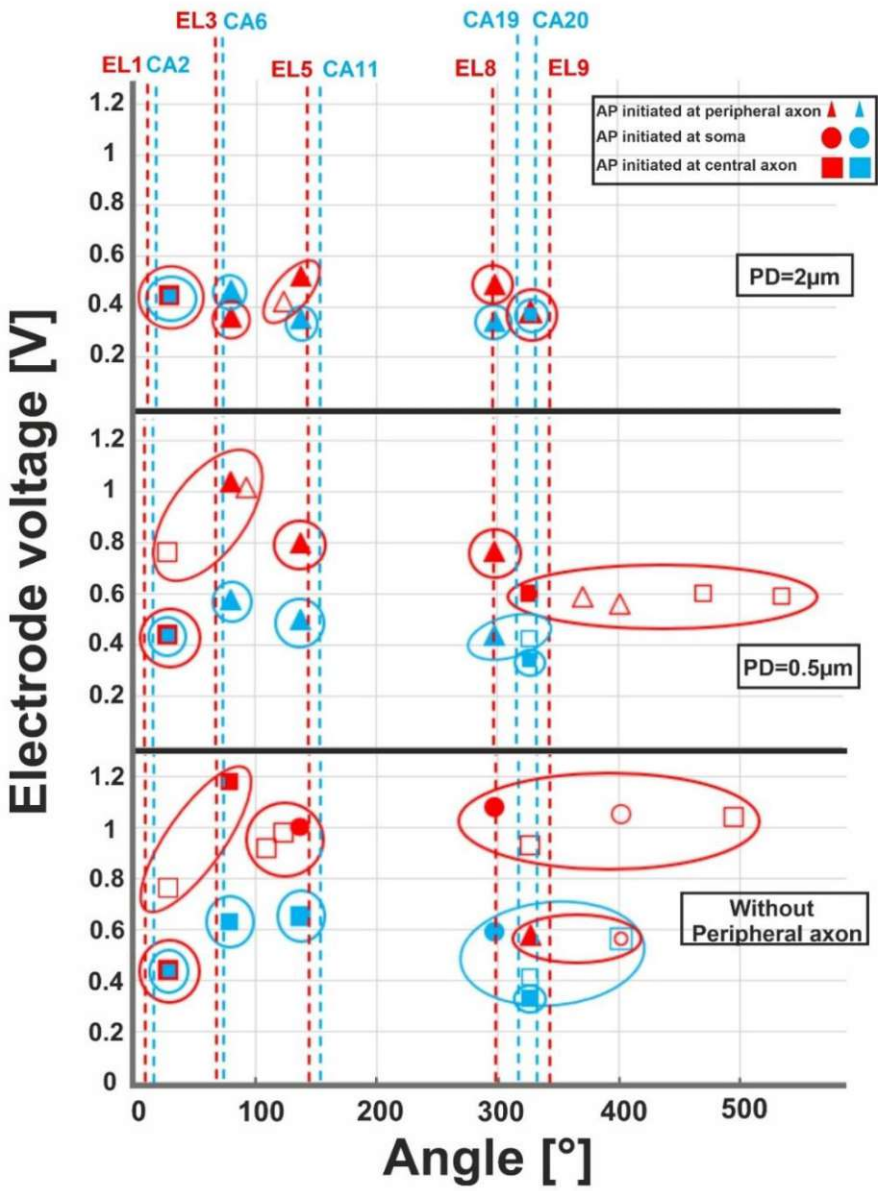

Figure 3.17. Excitation thresholds of TNs and co-stimulated ANFs along the fiber angles calculated for ten electrodes. The electrode thresholds for three PD of 2, 0.5, and 0 µm (without peripheral axon) is demonstrated in the upper, middle, and lower panel, respectively. Note that all investigated ANFs are considered with the same peripheral axon, soma, and central axon diameters at each level of calculation. Vertical dashed lines indicate the angle of electrodes, filled symbols TN, unfilled co-stimulated neurons (blue for perimodiolar, red for lateral CI system).

The threshold profiles for the selected electrodes are shown in Figure 3.17 for biphasic (cathodic first) stimulation with 100 µs per phase. Applying the threshold current of the closest TN (ANF 28°), the basal electrodes (EL1 and CA2) stimulated only one of the 30 investigated fibers. There was no co-stimulated ANF in this region. The threshold is the same for the three

Die approbierte gedruckte Originalversion dieser Dissertation ist an der TU Wien Bibliothek verfügbar.
The approved original version of this doctoral thesis is available in print at TU Wien Bibliothek.
TU Bibliothek Your knowledge hub WIEN

investigated PD (2 µm, 0.5 µm, and without peripheral axon) because the AP is initiated in this case at the central axon. Contrarily, the second investigated basal electrode from the lateral array (EL3) stimulated another group of fibers before the TN basal11 (79°) in the case of PD = 0.5 µm and without peripheral axon, whereas the corresponding perimodiolar electrode (CA6) stimulates only the TN.

For the middle electrodes EL5 and CA11, co-stimulation of ANFs depend on peripheral axon condition and CI system: EL5 stimulated another group of fibers before TN basal7 (137°) in the case of PD = 2 µm, but no co-stimulation when PD = 0.5 µm and two co-stimulated neurons under the assumption that ANFs are without peripheral axon. For each level of degeneration, it was assumed that all 30 ANFs had the same peripheral axon, soma, and central axon diameter and, subsequently, different co-stimulated neurons might appear when only the PD parameter is changed. For instance, basal6 is a co-stimulated neuron in the case of lateral electrode EL5 when PD is 2 µm. However, this ANF does not appear in the next level of degeneration (PD = 0.5 µm) because its electrode voltage threshold is essentially larger than the threshold of TN, basal7 (Figure 3.17, upper and middle panels).

In the upper-middle turn, active electrodes from lateral CI (EL8, EL9) were compared with perimodiolar CI (CA19, CA20). The stimulation of ANFs of this region becomes less selective mostly for the lateral electrode system when peripheral axon degeneration increases (Figure 3.17, middle and lower panels). With increasing peripheral axon degeneration levels, higher thresholds are needed to activate the TN, leading to disruption of the electrode selectivity and cochlea tonotopic function in this region.

Table 3.2 indicates threshold values, spike initiation sites, and co-stimulated ANFs. The values increase with increasing degeneration level of the TN, resulting in stimulating more neurons in the neighborhood, particularly in the case of the lateral electrode system.

The mean values of standard deviation (STD) for threshold variations of the investigated electrodes during peripheral axon degeneration of each TN were 0.22 V for lateral electrode array and 0.07 V for perimodiolar array. Moreover, the perimodiolar array requires a lower threshold than the lateral electrode system in most cases, which is in line with findings in clinical studies (Cohen et al., 2001; Long et al., 2014; Lee et al., 2019).

Die approbierte gedruckte Originalversion dieser Dissertation ist an der TU Wien Bibliothek verfügbar.
The approved original version of this doctoral thesis is available in print at TU Wien Bibliothek.
TU Bibliothek WIEN Your knowledge hub

Lateral CI system						
PD = 2 µm						
Electrode array	**TN**	**Threshold [V]**	**AP location TN**	**Co-stimulated neuron**	**Threshold [V]**	**AP location Co-stimulated**
EL1	basal14	0.44	Central	-	-	-
EL3	basal11	0.36	Peripheral	-	-	-
EL5	basal7	0.52	Peripheral	basal8	0.42	-
EL8	basal1	0.49	Peripheral	-	-	-
EL9	middle9	0.38	Peripheral	-	-	-
PD = 0.5 µm						
EL1	basal14	0.44	Central	-	-	-
EL3	basal11	1.04	Peripheral	basal14/basal10	0.76/1.02	central/central
EL5	basal7	0.8	Peripheral	-	-	-
EL8	basal1	0.77	Presoma	-	-	-
EL9	middle9	0.6	Central	middle7/middle3/ middle8/middle5	0.56/0.59/ 0.59/0.6	presoma/central/ presoma/postsoma
Without peripheral axon						
EL1	basal14	0.44	Central	-	-	-
EL3	basal11	1.18	Central	basal14	0.76	central
EL5	basal7	1	Soma	basal9/basal8	0.92/0.98	central/central/
EL8	basal1	1.08	Soma	middle9/middle4/ middle7	0.93/1.04/ 1.05	central/central/ soma
EL9	middle9	0.58	Central	middle7	0.56	soma
Perimodiolar CI system						
PD = 2 µm						
CA2	basal14	0.44	Central	-	-	-
CA6	basal11	0.46	Peripheral	-	-	-

Die approbierte gedruckte Originalversion dieser Dissertation ist an der TU Wien Bibliothek verfügbar.
The approved original version of this doctoral thesis is available in print at TU Wien Bibliothek.
TU Bibliothek Your knowledge hub WIEN

CA11	basal7	0.35	Presoma	-	-	-
CA19	basal1	0.34	Peripheral	-	-	-
CA20	middle9	0.37	Central	-	-	-
PD = 0.5 µm						
CA2	basal14	0.44	Central	-	-	-
CA6	basal11	0.58	Presoma	-	-	-
CA11	basal7	0.5	Presoma	-	-	-
CA19	basal1	0.44	Peripheral	middle9	0.42	central
CA20	middle9	0.34	Central	-	-	-
Without peripheral axon						
CA2	basal14	0.44	Central	-	-	-
CA6	basal11	0.63	Central	-	-	-
CA11	basal7	0.65	Central	-	-	-
CA19	basal1	0.59	Soma	middle9/middle7	0.41/0.56	central/central
CA20	middle9	0.33	Central	-	-	-

Table 3.2. Thresholds of TNs and the co-stimulated neurons for ten investigated electrodes for the lateral and perimodiolar electrode array systems.

Die approbierte gedruckte Originalversion dieser Dissertation ist an der TU Wien Bibliothek verfügbar.
The approved original version of this doctoral thesis is available in print at TU Wien Bibliothek.
TU Bibliothek Your knowledge hub WIEN

3.2 Impact different parameters on threshold current and polarity sensitivity

In the second part of the results, different parameters such as CI array system (Figure 2.19), pulse shape (Figure 2.20), stimulation strategy (Figure 2.21) were considered to investigate excitation threshold currents based on different degeneration levels of the peripheral process of ANFs. For this purpose, three ANFs were selected from different regions of the cochlear and named as TNs (Table 2.6). In addition, six different geometry of peripheral parts of each TN were used to analyze the excitation threshold individually and compare TNs excitation behavior based on all the above-mentioned parameters.

3.2.1 Impact of type of array, pulse shape, stimulus strategy, and degeneration level on threshold current

Figure 3.18 summarizes excitation thresholds of three investigated TNs in the basal, middle, and upper-middle turn for the perimodiolar CI with pulse shapes: monophasic, pseudo-monophasic, triphasic, and biphasic in the MP and three multipolar strategies: BP, TP, and PTP. In all panels, six ANF statuses based on degeneration levels (Table 2.7) were considered with a circle (intact), rectangle, triangle, cross, diamond, and plus, for AS1, AS2, AS3, AS4, AS5, and AS6, respectively.

Figure 3.18A shows the excitation thresholds of the monophasic pulse for three TNs, B11 (blue), B7 (green), and M9 (red), in four stimulation strategies. The MP strategy needs the lowest currents in both polarities. The deviation between ANO and CAT thresholds is small for each degeneration case. This is obvious as most cases accumulated over the black dotted line where the polarity ratio (ANO/CAT) is one. In addition, the threshold increases in both polarities by increasing the degeneration levels of TNs except in M9, which has almost the same ANO threshold for all degenerated levels because in all status cases AP initiation site is the central process.

Moreover, in contrast to MP strategy, the ANO threshold ranges increase negligibly in BP, TP, and PTP; however, the CAT threshold ranges increase significantly. The investigated TNs have almost equal ANO thresholds for different ANFs degenerated cases, which indicates the AP initiates from nearly the same site of the central process of TNs. In contrast, the CAT threshold variations are substantial and increased significantly in each level of degeneration, especially in AS5 and AS6 cases. Finally, the behavior of the fibers in TP and PTP strategies are similar to each other.

Die approbierte gedruckte Originalversion dieser Dissertation ist an der TU Wien Bibliothek verfügbar.
The approved original version of this doctoral thesis is available in print at TU Wien Bibliothek.
TU Bibliothek Your knowledge hub WIEN

Another important point is the excitation threshold behavior of each TN depending on the cochlear turns. Each TN demonstrates particularly CAT and ANO thresholds that significantly occur only in multipolar strategies, especially in TP and PTP strategies. This means ANFs from different turns of the cochlea are stimulated by individual current ranges. To summarize, using monophasic pulse in four stimulation strategies shows that all threshold cases are densely accumulated in MP, whereas, in multipolar strategies, each TN individually forms a cluster that can be distinguished by degeneration levels.

Figure 3.18B represents the excitation thresholds for the pseudo-monophasic pulse. The ANFs behavior is almost similar to monophasic pulse (Figure 3.18A) for all strategies. Furthermore, the ANO threshold variations in the BP, TP, and PTP are minimal between degeneration cases of individual TNs compared to MP strategy, and again, the clustering behavior is formed in multipolar strategies compared to MP. Interestingly, the CAT threshold ranges are decreased by half compared to monophasic pulse, as in Figure 3.18A. This threshold difference can be understood from the voltage membrane changes induced by the two pulse shapes, as shown in Figure 3.19A. The pseudo-monophasic pulse has a lower negative slope at the onset of the CAT-leading phase compared to the monophasic pulse represented with the pink rectangle (Figure 3.19A). Therefore, the pulse makes the transmembrane voltage less negative (20 vs. 55 mV hyperpolarized). The second charge-balanced phase of the pseudo-monophasic pulse has a positive effect, causing the transmembrane voltage to depolarize more and faster to the excitation threshold level. For a better understanding, the voltage membrane changes by applying a monophasic pulse are displayed over time for a progressively degenerated fiber (Figure 3.19B) and a healthy fiber (Figure 3.19C).

Die approbierte gedruckte Originalversion dieser Dissertation ist an der TU Wien Bibliothek verfügbar.
The approved original version of this doctoral thesis is available in print at TU Wien Bibliothek.
TU Bibliothek Your knowledge hub WIEN

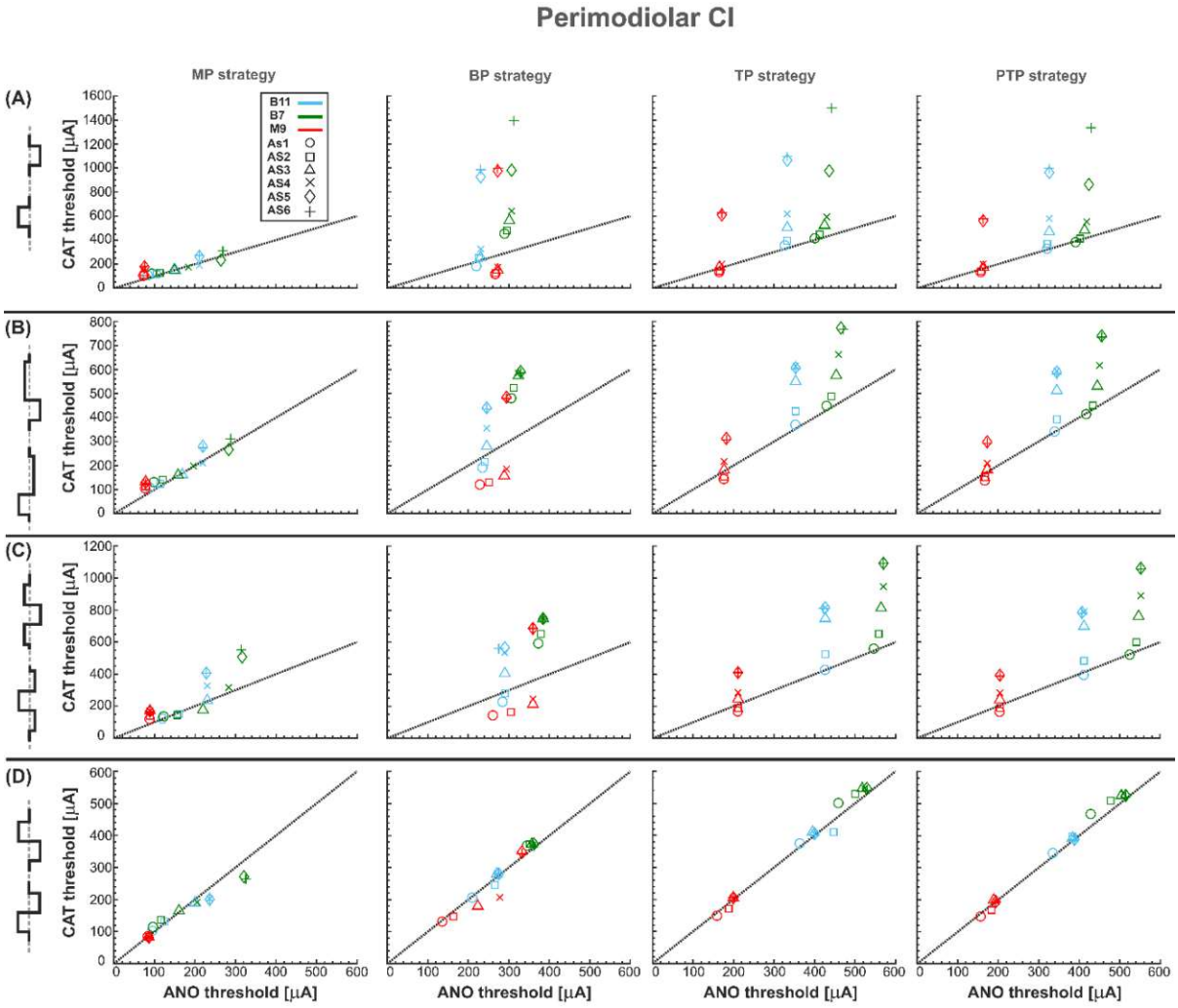

Figure 3.18. Threshold profiles of three TNs for perimodiolar CI. Thresholds are shown for four stimulation configurations: MP, BP, TP, and PTP with **(A)** monophasic, **(B)** pseudo-monophasic, **(C)** triphasic, and **(D)** biphasic pulse. Blue, green, and red colors represent B11, B7, and M9, respectively, in all panels. ANFs status based on degeneration levels are indicated with circle, rectangle, triangle, cross, diamond, and plus shapes for AS1, AS2, AS3, AS4, AS5, and AS6, respectively. Black dotted lines represent the ANO/CAT = 1. Legend from top-left panel A applies to all panels.

Figure 3.18C demonstrates the excitation thresholds with the triphasic pulse. The ANFs behavior is almost comparable to previous pulse shapes in all stimulation strategies, and again, the clustering behavior is formed in multipolar strategies compared to MP. Moreover, in multipolar strategies, the CAT threshold ranges of the triphasic pulse are about 50% higher than pseudo-monophasic and 50% lower than the monophasic pulse.

Die approbierte gedruckte Originalversion dieser Dissertation ist an der TU Wien Bibliothek verfügbar.
The approved original version of this doctoral thesis is available in print at TU Wien Bibliothek.

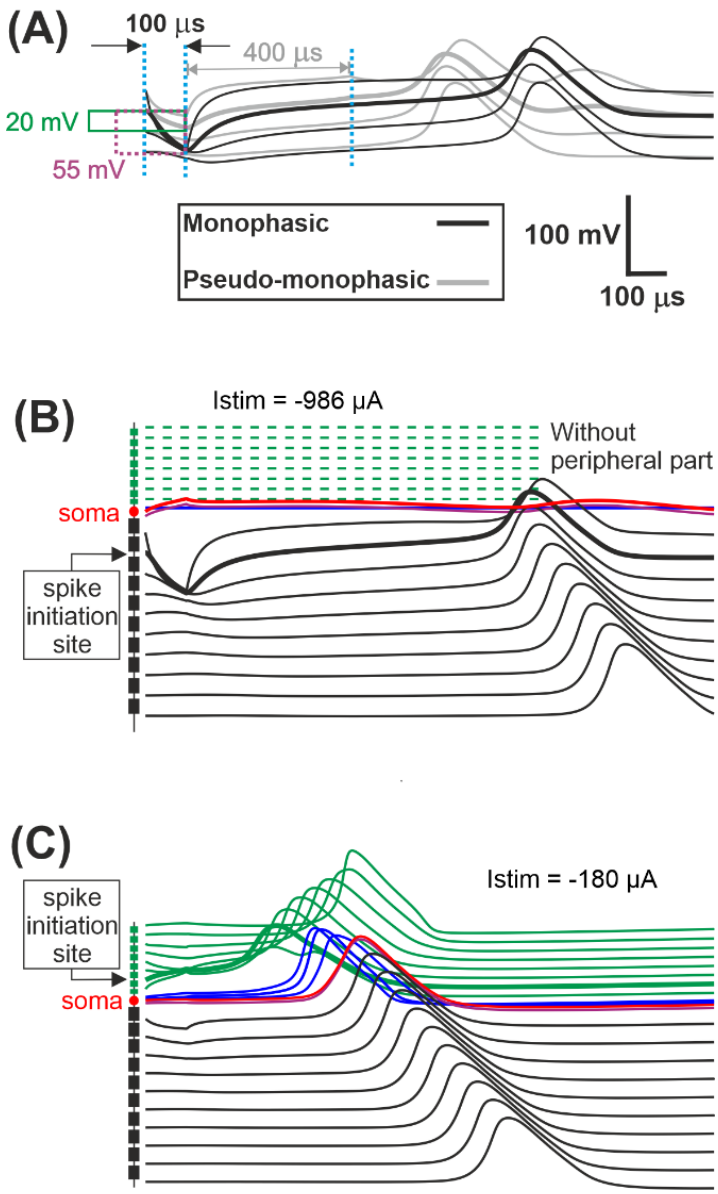

Figure 3.19. Comparison of the transmembrane voltage just above the threshold. **(A)** Comparison between excitation of the initiation sites for both pulse shapes. During the first cathodic phase, the strongest deviations from the resting voltage appear in a central process region close to the soma. Hyperpolarization of the monophasic pulse (55 mV) is almost three times larger than for the pseudo-monophasic pulse (20 mV). In monophasic stimulation, the central process compartment with the strongest hyperpolarization elicits the spike by break excitation (thick black line), and this spike is conducted in both directions (thin black lines). Break excitation is an overshoot of membrane voltage in the direction of the resting potential after a strong hyperpolarization. This overshooting trend is strongly supported by the weak second phase of the pseudo-monophasic pulse (gray lines). Consequently, the pseudo-monophasic stimulation needs less hyperpolarization during the first phase.

Die approbierte gedruckte Originalversion dieser Dissertation ist an der TU Wien Bibliothek verfügbar.
The approved original version of this doctoral thesis is available in print at TU Wien Bibliothek.
TU Bibliothek Your knowledge hub WIEN

(B) Degeneration status AS6, without peripheral process, when monophasic pulse is applied. **(C)** Excitation of fiber with healthy status for monophasic pulse.

Figure 3.18D displays the excitation thresholds with biphasic pulse. The behavior in the MP strategy is similar to the previous pulse shapes but with less variability, polarity ratio almost close to one. However, the cluster form based on degeneration levels among individual TNs is not visible anymore. The TN thresholds mostly accumulate over the black dotted line, resulting from the same AP initiation site of TNs in different degeneration levels in both polarities. As a result of losing the CAT threshold variations in multipolar strategies by applying the biphasic pulse, it is challenging to distinguish TNs response based on different degeneration levels, which differs from the previous pulse shapes (Figure 3.18A-C).

Figure 3.20 shows excitation thresholds as Figure 3.18 but for a lateral CI. Subsequently, Figure 3.20A displays the excitation thresholds of monophasic pulse for the three investigated TNs in the four stimulation strategies. The MP strategy needs significantly lower currents, especially in CAT thresholds, compared to the other strategies. In addition, the ANO and CAT thresholds do not change substantially by increasing degeneration levels. However, both ANO and CAT thresholds increase significantly in multipolar strategies compared to the MP strategy. The ANO threshold variations between the TNs are small in the BP strategy compared to TP and PTP strategies. However, the cluster behavior is not formed in multipolar strategies in lateral CI, as they formed in the perimodiolar CI (Figure 3.18A).

Figure 3.20B represents the excitation thresholds with the pseudo-monophasic pulse. The trend is similar to monophasic pulse (Figure 3.20A) for all strategies, although CAT thresholds in the BP are significantly lower and more concentrated compared to monophasic pulse in severe degenerated cases (Figure 3.20A, BP strategy). Surprisingly, the similar CAT threshold ranges between monophasic and pseudo-monophasic pulses (Figure 3.20A vs. Figure 3.20B) are in contrast to the CAT threshold behavior in the perimodiolar CI case (Figure 3.18A vs. Figure 3.18B). Since the CAT thresholds in the perimodiolar CI are significantly decreased, but the CAT thresholds reduction is not notable in the lateral CI.

Figure 3.20C displays the excitation thresholds with the triphasic pulse with a similar structure as Figure 3.20A-B. The ANFs behavior is comparable to previous asymmetric pulses, especially with pseudo-monophasic. The CAT threshold ranges of triphasic pulses are about 25% larger than monophasic and pseudo-monophasic pulses.

Figure 3.20D demonstrates the excitation threshold with the biphasic pulse. The ANO and CAT threshold ranges are almost doubled compared to the perimodiolar case (Figure 3.18D). The

Die approbierte gedruckte Originalversion dieser Dissertation ist an der TU Wien Bibliothek verfügbar.
The approved original version of this doctoral thesis is available in print at TU Wien Bibliothek.
TU Bibliothek Your knowledge hub WIEN

threshold characteristics in both polarities are comparable in all four stimulation strategies for all TNs, except in some severe degenerated cases.

To summarize, the excitation thresholds in the lateral CI are totally distinct from the perimodiolar CI case. The excitation thresholds based on different degeneration levels of all three TNs in lateral CI demonstrate an unrecognized pattern regardless of the pulse shapes and stimulation strategies.

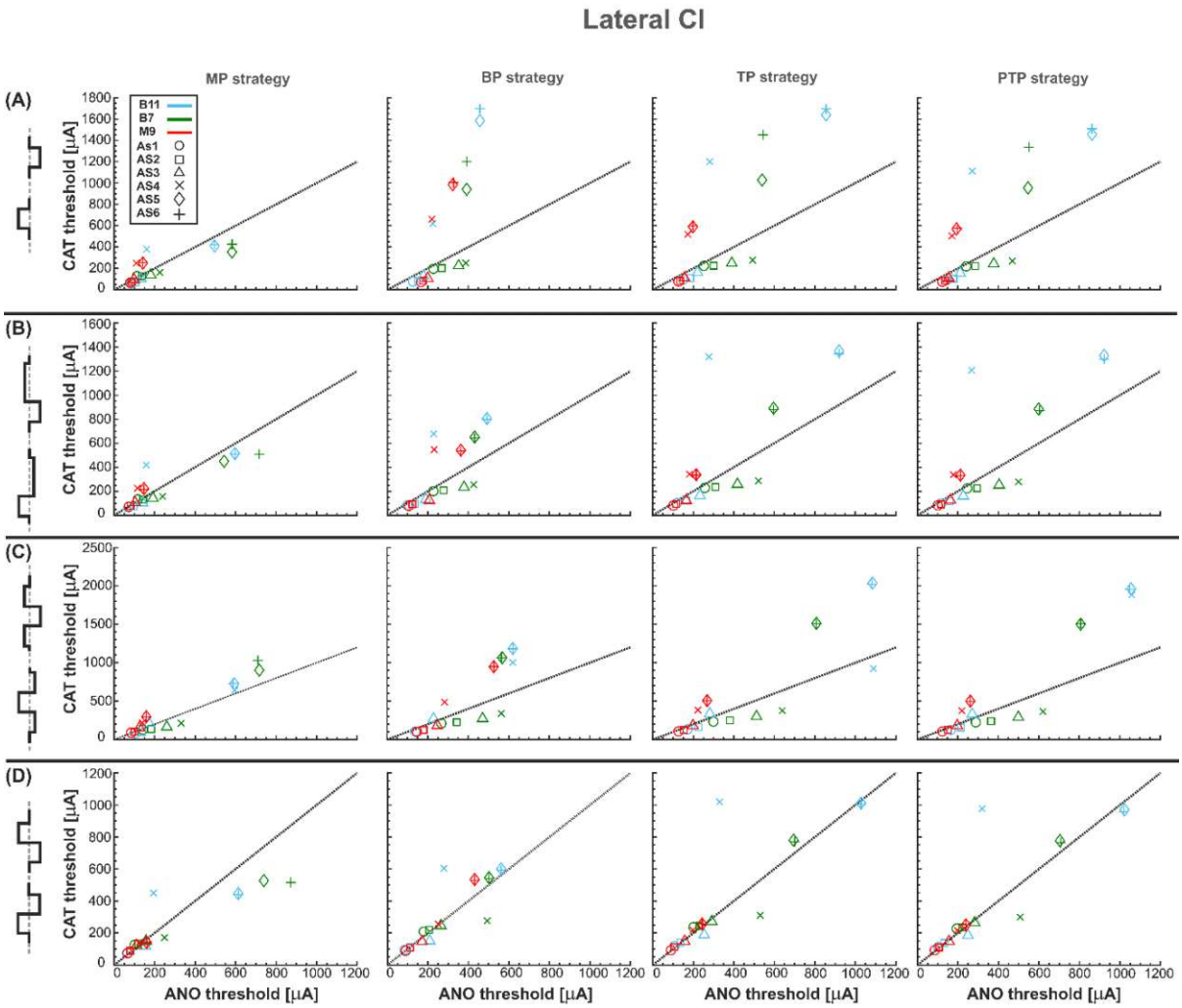

Figure 3.20. Threshold profiles of three TNs for lateral CI. Layout as in Figure 3.18.

Die approbierte gedruckte Originalversion dieser Dissertation ist an der TU Wien Bibliothek verfügbar.
The approved original version of this doctoral thesis is available in print at TU Wien Bibliothek.

3.2.2 Impact of type of array, pulse shape, stimulus strategy, and degeneration level on polarity ratios and polarity sensitivity

Figure 3.21-24 summarize the polarity sensitivity defined by the ANO/CAT threshold ratios of three investigated TNs for the perimodiolar CI (left panels) and lateral CI (right panels) with pulse shapes: monophasic (Figure 3.21), pseudo-monophasic (Figure 3.22), triphasic (Figure 3.23), and biphasic (Figure 3.24), in the MP and the three multipolar strategies for the six degeneration levels (Table 2.7).

In this study, It is used the ANO/CAT ratio for polarity investigation instead of the different CAT and ANO thresholds known as the polarity effect. The polarity ratio provides a better insight into degeneration pattern recognition of ANFs. The trend ANO/CAT < 1, indicating the lower ANF threshold for anodic stimulation, is related to the degeneration level and the modiolus distance of the stimulating electrode. Polarity sensitivity is much more pronounced for monophasic (Figure 3.21), pseudo-monophasic (Figure 3.22), and triphasic (Figure 3.23) vs. biphasic (Figure 3.24) stimulation.

Figure 3.21illustrates the polarity threshold ratios with monophasic pulse for two CI systems. In the MP strategy (Figure 3.21A), ANO sensitivity (ANO/CAT<1) in the perimodiolar CI occurred more frequently except in four cases that can be related to nearer distance electrode to modiolus wall. A declining trend in ratios appears from intact to more degenerated cases in both CI array systems only for the upper middle TN, M9.

Figure 3.21B-D displays the polarity ratios in multipolar strategies for both CI systems. Interestingly, a declining trend in ratios always happens for all three TNs in the case of the perimodiolar array. Despite, in the perimodiolar array, regardless of degeneration level, most cases show ANO sensitivity. On the other hand, more degenerated cases (AS4 - AS6) become ANO sensitive in the lateral system, whereas CAT sensitivity happens in intact and less degenerated cases for all three multipolar strategies.

Die approbierte gedruckte Originalversion dieser Dissertation ist an der TU Wien Bibliothek verfügbar.
The approved original version of this doctoral thesis is available in print at TU Wien Bibliothek.
TU Bibliothek Your knowledge hub WIEN

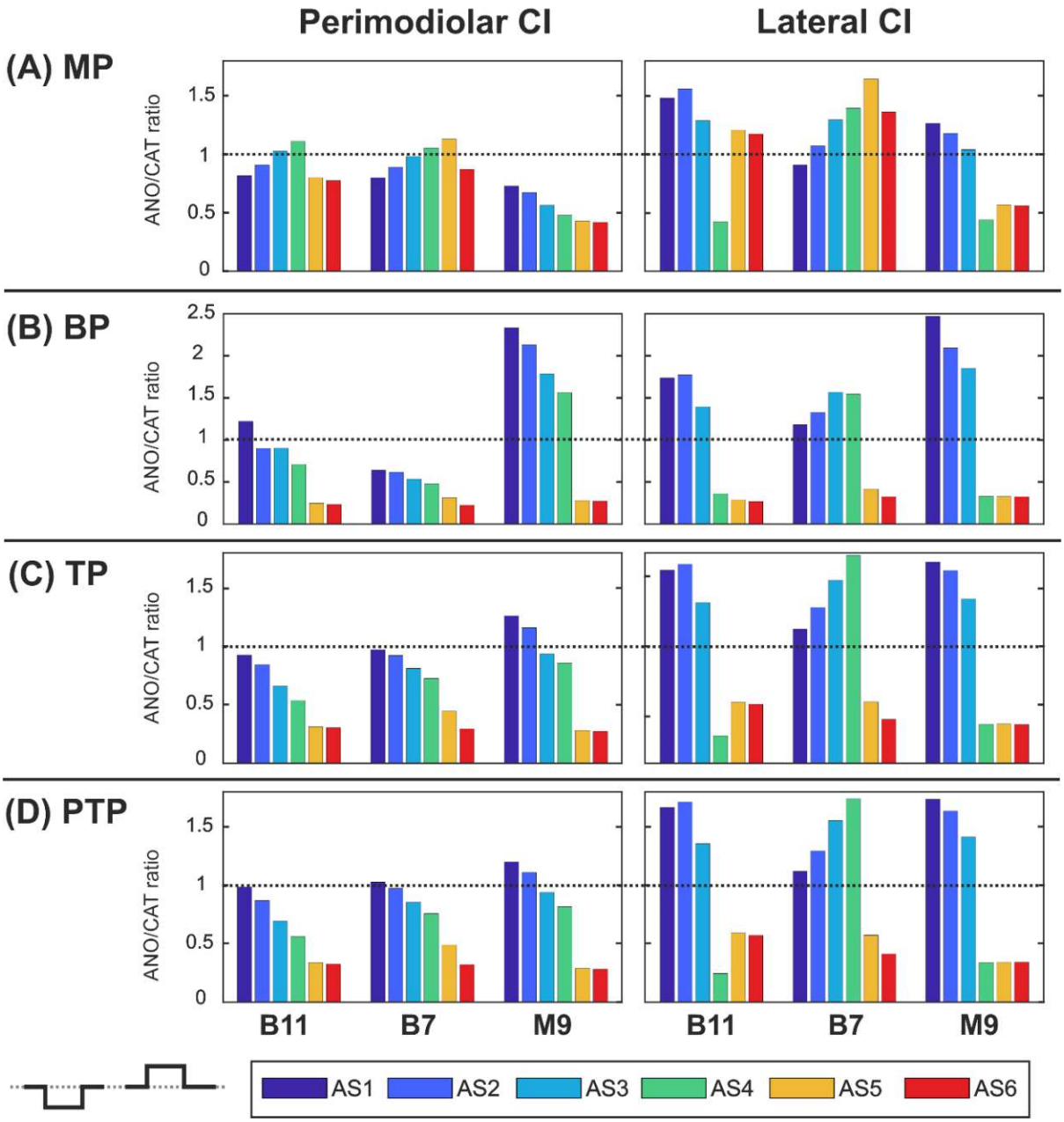

Figure 3.21. Polarity ratios for different degeneration levels stimulated with the monophasic pulse. Threshold ratios are shown for the TNs B11, B7, and M9 with color-coded degeneration levels **(A)** monopolar (MP), **(B)** bipolar (BP), **(C)** tripolar (TP), **(D)** partial tripolar (PTP) stimulation strategies. The horizontal dotted lines indicate the polarity ratio ANO/CAT = 1.

Figure 3.22 shows the polarity threshold ratios for pseudo-monophasic pulse. The behavior is very similar to monophasic pulse (Figure 3.21A-D). Interestingly, again the decreasing trend can be observed in the perimodiolar array for all TNs in the three investigated multipolar strategies. In contrast, in the lateral array system, ANO vs. CAT sensitivity occurs mainly in AS4 - AS6 degenerated cases vs. intact, slight, and moderate degenerated cases (AS1 - AS3).

Die approbierte gedruckte Originalversion dieser Dissertation ist an der TU Wien Bibliothek verfügbar.
The approved original version of this doctoral thesis is available in print at TU Wien Bibliothek.
TU Bibliothek Your knowledge hub WIEN

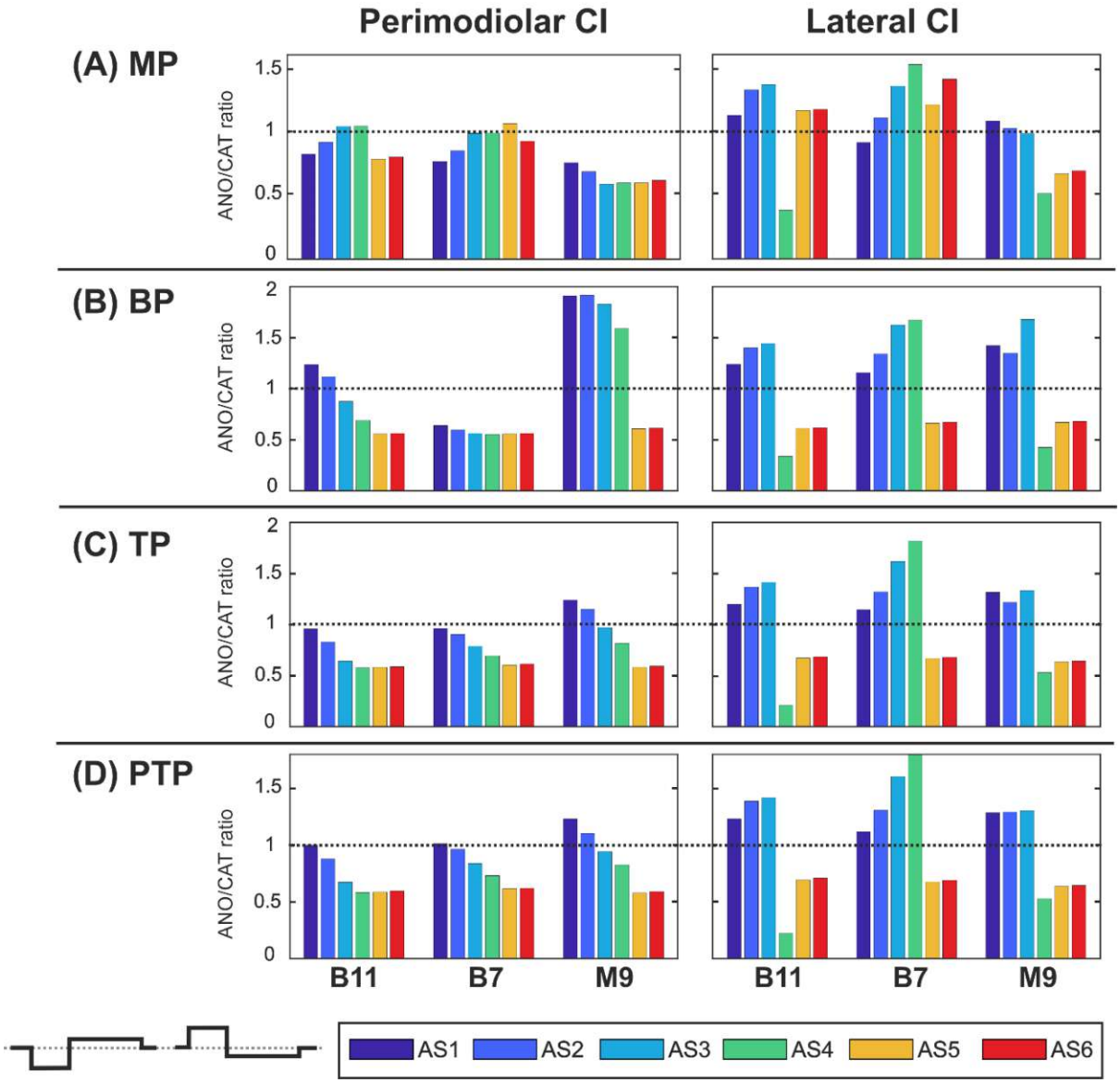

Figure 3.22. Polarity ratios for different degeneration levels stimulated with the pseudo-monophasic pulse. Layout as in Figure 3.21.

Figure 3.23 demonstrates the polarity threshold ratios for triphasic pulse. The behavior is similar to monophasic and pseudo-monophasic pulses (Figure 3.21 and Figure 3.22). Again the decreasing trend can be noticed in the perimodiolar array for all TNs in the three investigated multipolar strategies. In contrast, in the lateral array system, ANO vs. CAT sensitivity occurs mainly in AS4 - AS6 vs. AS1- AS3.

Die approbierte gedruckte Originalversion dieser Dissertation ist an der TU Wien Bibliothek verfügbar.
The approved original version of this doctoral thesis is available in print at TU Wien Bibliothek.

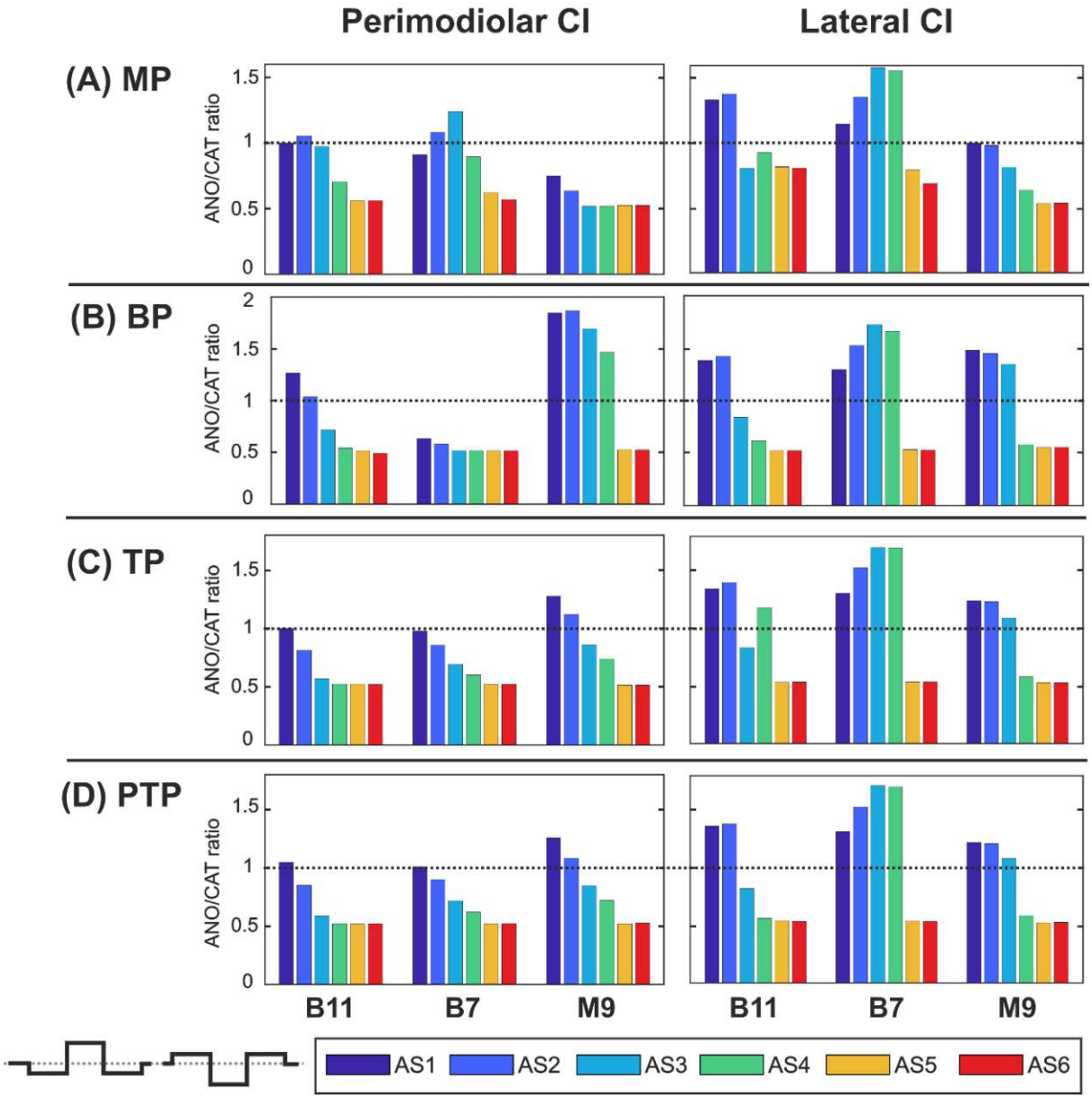

Figure 3.23. Polarity ratios for different degeneration levels stimulated with the triphasic pulse. Layout as in Figure 3.21.

Figure 3.24 shows the polarity threshold ratios with biphasic pulse for both CI systems. Contrary to the previous pulses, for the biphasic pulse in the lateral array, the ANO sensitivity of the high degeneration vs. CAT sensitivity for intact and less degenerated cases is not observed anymore. In most cases of the perimodiolar array, the polarity ratio is close to one; hence, the declining behavior in perimodiolar CI from intact to progressive degeneration does not occur in the biphasic pulse.

Die approbierte gedruckte Originalversion dieser Dissertation ist an der TU Wien Bibliothek verfügbar.
The approved original version of this doctoral thesis is available in print at TU Wien Bibliothek.

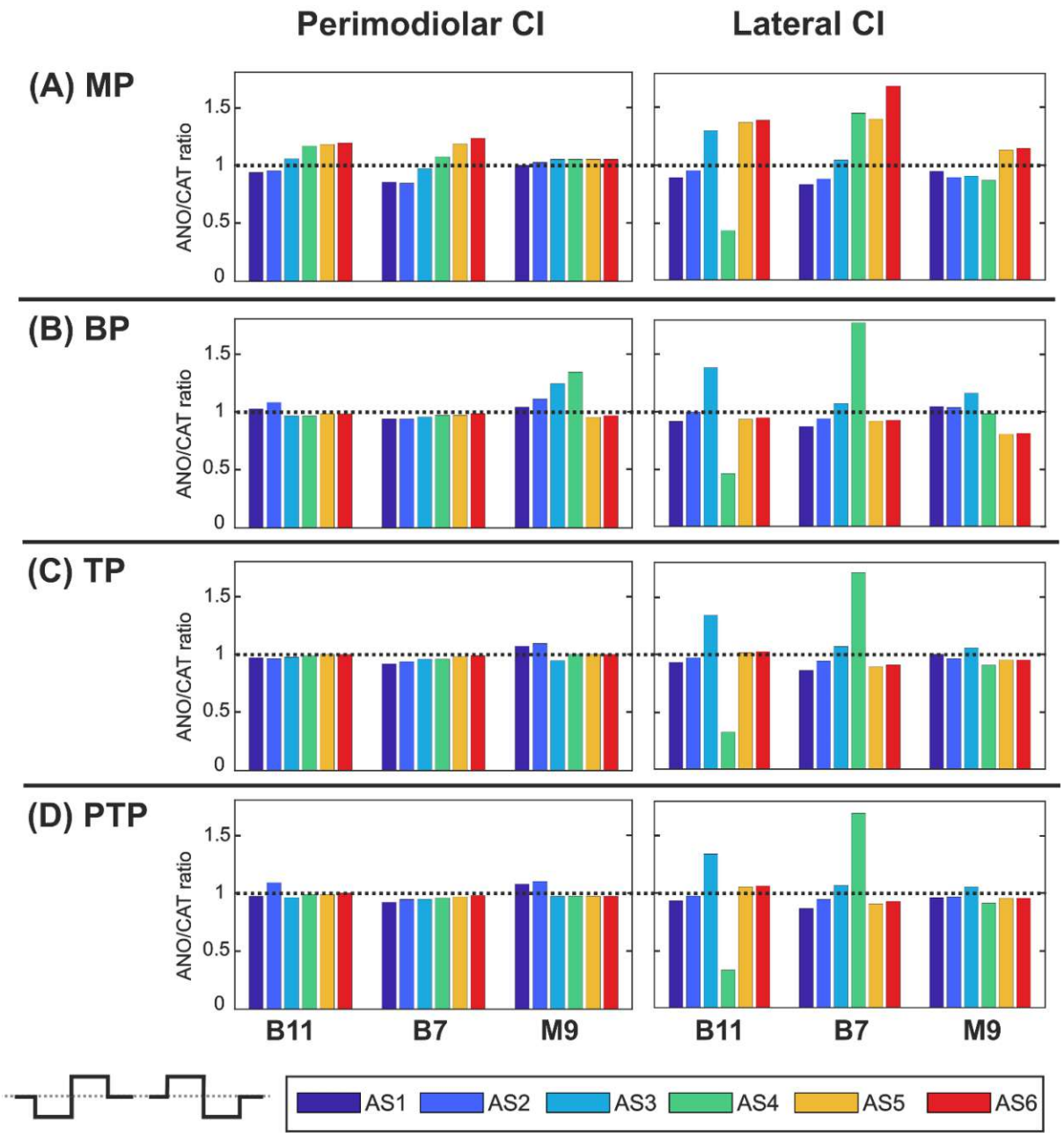

Figure 3.24. Polarity ratios for different degeneration levels stimulated with the biphasic pulse. Layout as in Figure 3.21.

To summarize, asymmetric pulses display individual patterns based on polarity threshold ratio in perimodiolar and lateral array systems when the multipolar strategies were used. In the perimodiolar case, a declining trend was observed between degeneration levels that can be useful for detecting neural status. Also, the CAT and ANO sensitivity idea is noticed in healthy to mild degeneration cases versus moderate to profound degeneration cases in the lateral case. However, by using symmetric pulse shape like biphasic pulse, the polarity sensitivity and declining trend disappear in both CI array systems, and regardless of degeneration levels,

Die approbierte gedruckte Originalversion dieser Dissertation ist an der TU Wien Bibliothek verfügbar.
The approved original version of this doctoral thesis is available in print at TU Wien Bibliothek.
TU Bibliothek Your knowledge hub WIEN

stimulation strategy, and array system, the polarity threshold ratios occurred near to one (ANO/CAT ~ 1) in most cases.

3.2.3 Impact of type of array, pulse shape, pulse polarity, stimulus strategy, and degeneration level on action potential initiation sites

Figure 3.25 displays AP initiation sites at ANO and CAT threshold levels for the three investigated TNs in the basal, middle, and upper-middle turn for the perimodiolar CI (blue) and the lateral CI (red) with monophasic pulse shape in the MP and the three multipolar strategies, BP, TP, and PTP. In all panels, the y-axis represents the six ANF statuses based on the degeneration levels, as in Table 2.7.

Figure 3.25 shows AP initiation sites when a monophasic pulse is applied. In the lateral CI, AP mostly initiates at the peripheral sites regardless of the pulse polarity, stimulation strategy, and degeneration levels, except for progressive cases, which are considered without peripheral process. On the other hand, in the primordial CI, the AP initiates in the peripheral process parts when CAT pulse is applied in MP and all multipolar strategies except for the progressive cases. However, in the case of ANO pulses, the AP initiation sites occur only in the central processes in multipolar strategies, and with MP strategy, most AP initiation sites happen in the central parts of ANFs.

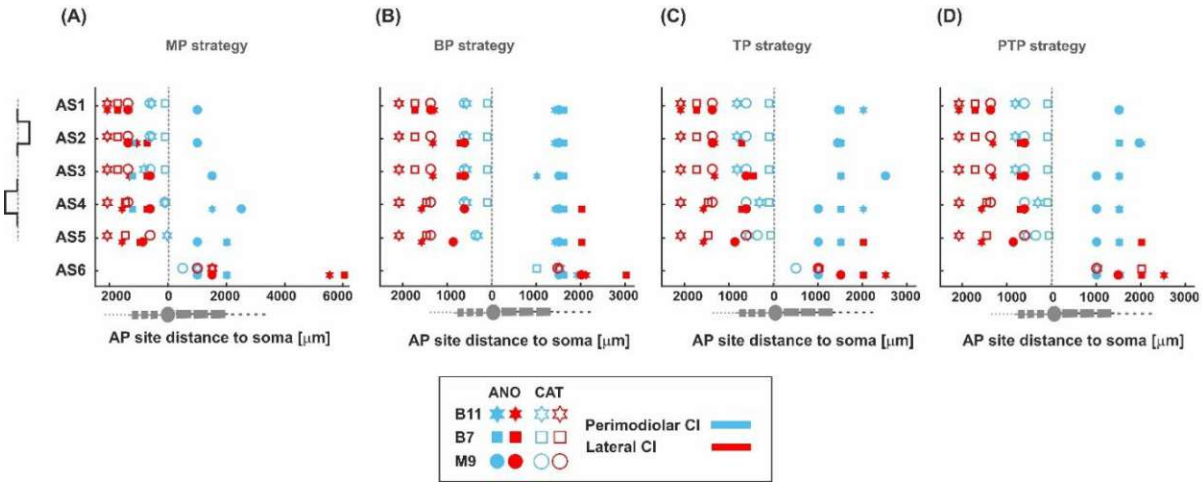

Figure 3.25. AP initiation sites at ANO and CAT thresholds for monophasic pulse in four stimulation strategies **(A)** MP, **(B)** BP, **(C)** TP, **(D)** PTP. The TNs: B11, B7, and M9 are demonstrated with star, rectangle, and circle, respectively. In addition, the lateral and perimodiolar CI systems are indicated

Die approbierte gedruckte Originalversion dieser Dissertation ist an der TU Wien Bibliothek verfügbar.
The approved original version of this doctoral thesis is available in print at TU Wien Bibliothek.

with red and blue colors. Pulse polarity is identified by filled (ANO) and unfilled shapes (CAT). Gray dashed lines show the soma positions.

Figure 3.26 displays the AP initiation sites when pseudo-monophasic is applied. The same behavior in AP initiation sites can be observed in the lateral array as in Figure 3.25. AP initiation sites in the lateral CI mainly happen in the peripheral parts regardless of pulse polarity and stimulation strategy except for profound degeneration cases. However, by using the perimodiolar array, AP initiation sites differ for ANO vs. CAT thresholds. When TP and PTP strategies are used, AP initiation sites mainly differ between peripheral and central parts related to CAT and ANO polarity.

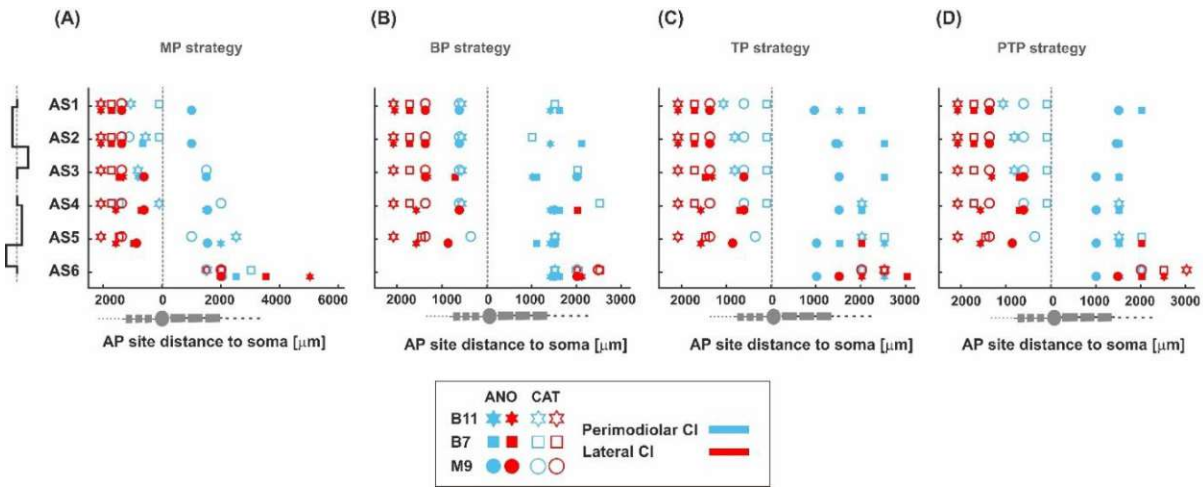

Figure 3.26. AP initiation sites at ANO and CAT thresholds for pseudo-monophasic pulse in four stimulation strategies **(A)** MP, **(B)** BP, **(C)** TP, **(D)** PTP. Layout as in Figure 3.25.

Figure 3.27 demonstrates the AP initiation sites when triphasic is applied. The same behavior in AP initiation sites can be observed in the perimodiolar and lateral array systems as in Figure 3.25. In lateral array, AP initiation sites mainly happen in the peripheral parts regardless of pulse polarity and stimulation strategy. By using the perimodiolar array, AP initiation sites differ for ANO vs. CAT thresholds.

Die approbierte gedruckte Originalversion dieser Dissertation ist an der TU Wien Bibliothek verfügbar.
The approved original version of this doctoral thesis is available in print at TU Wien Bibliothek.
TU Bibliothek Your knowledge hub WIEN

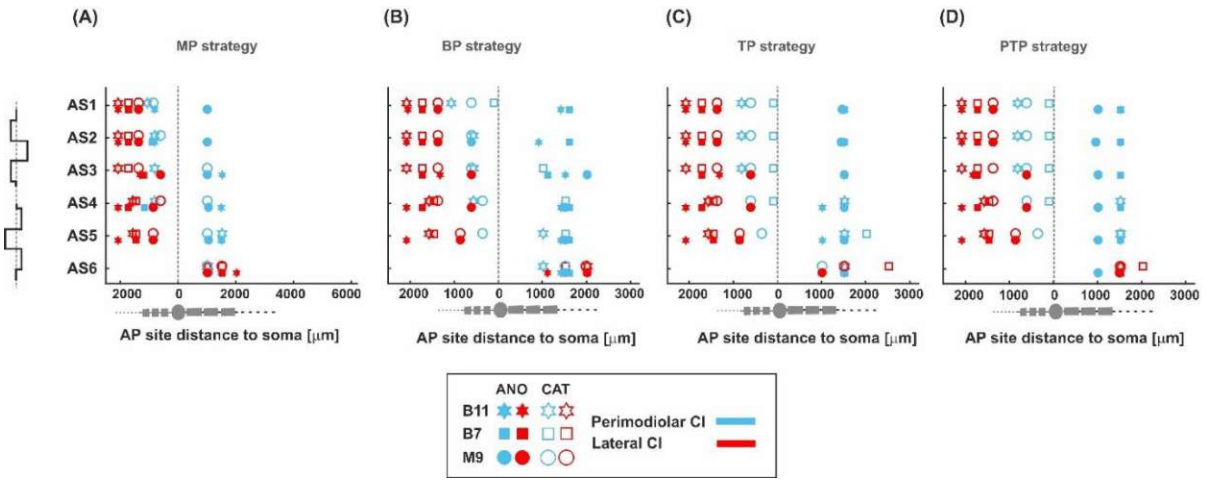

Figure 3.27. AP initiation sites at ANO and CAT thresholds for triphasic pulse in four stimulation strategies **(A)** MP, **(B)** BP, **(C)** TP, **(D)** PTP. Layout as in Figure 3.25.

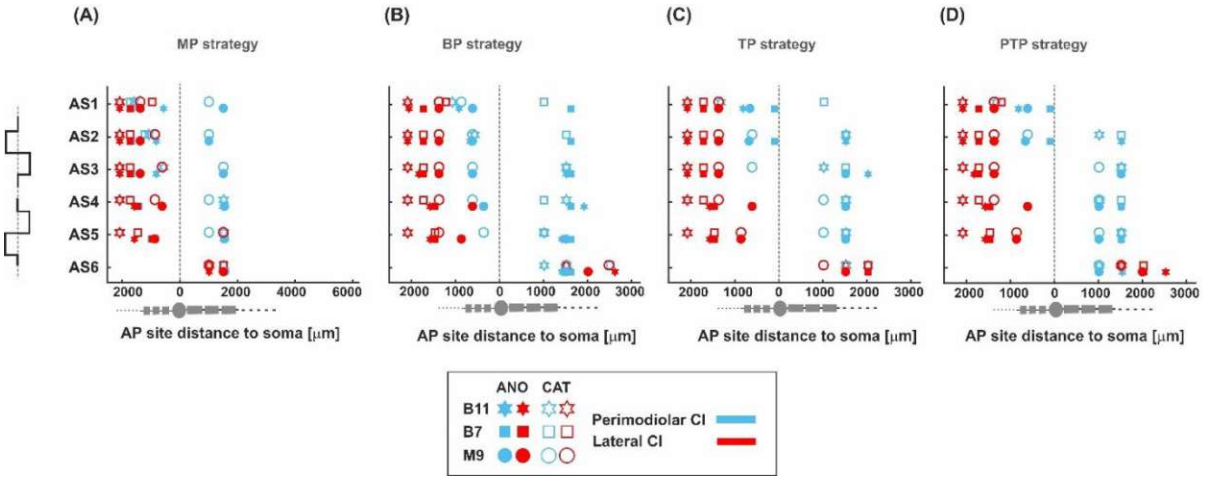

Figure 3.28. AP initiation sites at ANO and CAT thresholds for biphasic pulse in four stimulation strategies **(A)** MP, **(B)** BP, **(C)** TP, **(D)** PTP. Layout as in Figure 3.25.

By applying a symmetric biphasic pulse (Figure 3.28), the lateral CI keeps the AP initiation sites in the peripheral sites regardless of pulse polarity, degeneration levels, and stimulation strategy. While in the perimodiolar array, the AP initiation sites are mostly the same in both CAT and ANO thresholds regardless of TN degeneration levels.

Die approbierte gedruckte Originalversion dieser Dissertation ist an der TU Wien Bibliothek verfügbar.
The approved original version of this doctoral thesis is available in print at TU Wien Bibliothek.
TU Bibliothek Your knowledge hub WIEN

3.2.4 Impact of distance between channels and distance to modiolus wall on polarity sensitivity

Differences in threshold characteristics between perimodiolar and lateral CIs result from the electrode to modiolus distance and the distance between channels. To investigate the impact of distance between channels, one channel gap is considered in perimodiolar CI by increasing the distance between channels from 0.7 to 1.4 mm (Figure 2.21B). In addition, for the lateral CI, it was decreased the distance between channels from 2.4 to about 1.3 mm (Figure 2.21C).

The effect of doubled channel separation is evident for multipolar configurations in perimodiolar array; compare Figure 3.18 and Figure 3.29. For monophasic pulses, the ANO and CAT threshold ranges are reduced by a factor of 2 when the distance of returning electrode is increased (Figure 3.29A vs. Figure 3.18A). The clustering behavior is also noticeable in all three multipolar strategies. The investigated TNs have individually similar ANO thresholds in all degeneration cases; in contrast, the CAT thresholds are increased in each level of degeneration, similar as in Figure 3.18A but with lower thresholds (Figure 3.29A).

Figure 3.29B shows similar characteristics of pseudo-monophasic pulses as in monophasic pulse yet with lower CAT thresholds dropped by half (Figure 3.29A vs. Figure 3.29B), as Figure 3.18A-B for multipolar strategies. The same clustering behavior can be observed as in Figure 3.18B.

Triphasic pulse (Figure 3.29C) displays similar behavior with previous pulses with the almost same CAT threshold ranges as in monophasic pulse (Figure 3.29A) and higher CAT thresholds than pseudo-monophasic pulse (Figure 3.29B). In addition, the ANO and CAT threshold ranges are reduced by a factor of 2 when the distance of returning electrode is increased compared to Figure 3.18C.

For biphasic pulse again, the ANO and CAT threshold ranges in the multipolar strategies are decreased by a factor of about two (Figure 3.29D vs. Figure 3.18D). However, the cluster form based on degeneration levels among individual TNs is not visible anymore, and the threshold ratios are mostly close to one, as in Figure 3.18D. Overall, both polarity threshold ranges are decreased by increasing the returning electrode distance in all multipolar strategies, which are related directly to current shunting between electrodes.

Die approbierte gedruckte Originalversion dieser Dissertation ist an der TU Wien Bibliothek verfügbar.
The approved original version of this doctoral thesis is available in print at TU Wien Bibliothek.
TU WIEN Bibliothek Your knowledge hub

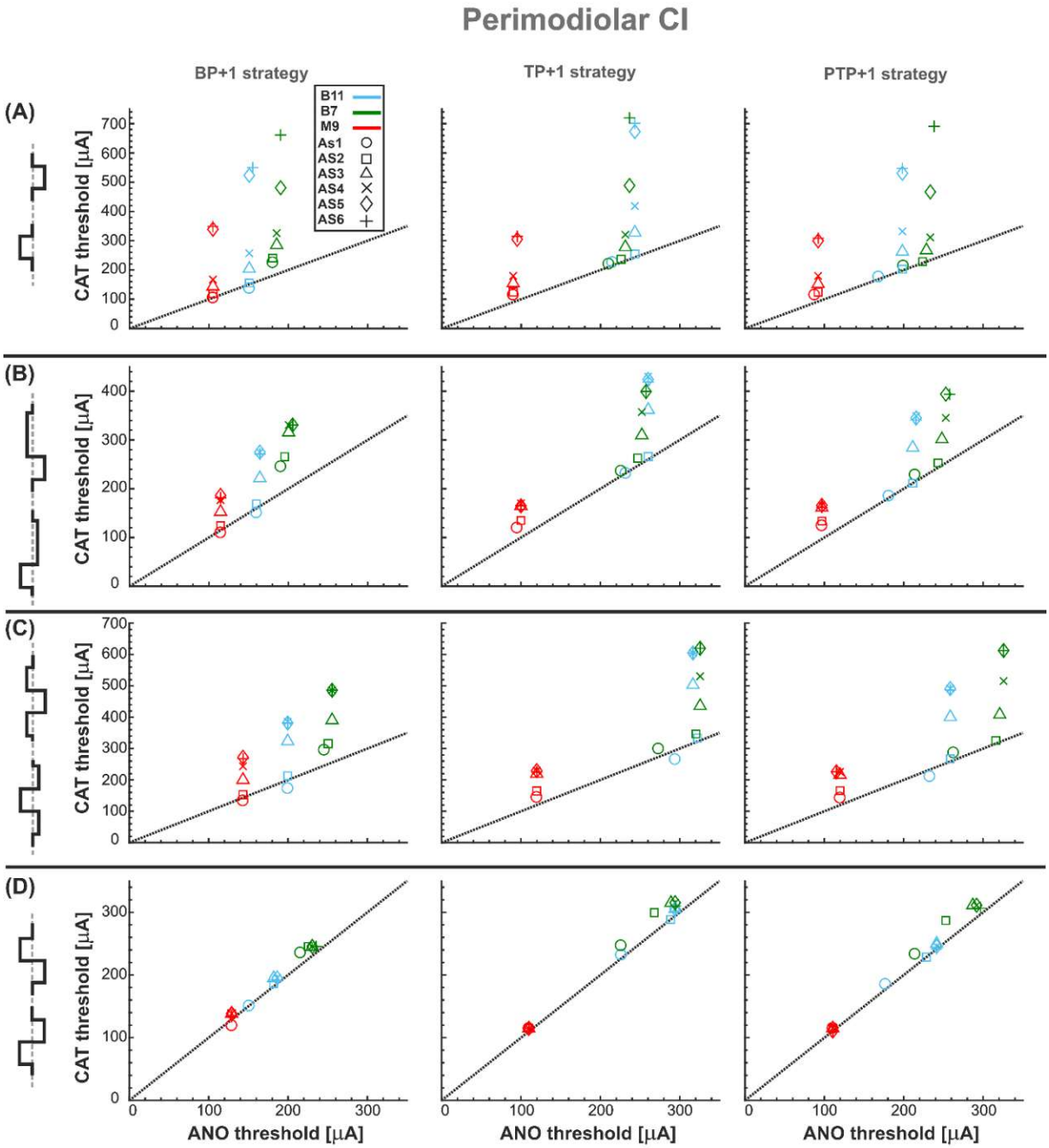

Figure 3.29. Threshold of three TNs for perimodiolar CI for four different pulse types and three multipolar strategies (BP+1, TP+1, and PTP+1) by changing the distance between channels of both CI systems. **(A)** Monophasic, **(B)** pseudo-monophasic, **(C)** triphasic, and **(D)** biphasic pulse. Layout as in Figure 3.18.

The effect of halving channel distance is studied and shown in Figure 3.30 for multipolar strategies in the lateral CI. As displayed in Figure 3.30A-D, except for the threshold ranges, which are significantly increased compared to Figure 3.20A-D, the threshold characteristics

Die approbierte gedruckte Originalversion dieser Dissertation ist an der TU Wien Bibliothek verfügbar.
The approved original version of this doctoral thesis is available in print at TU Wien Bibliothek.

are very similar to multipolar strategies in Figure 3.20A-D. The ANO/CAT ratios are again close to one (Figure 3.20D and Figure 3.30D) for the biphasic pulse, and no cluster is formed regardless of pulse shape and stimulus strategies as before.

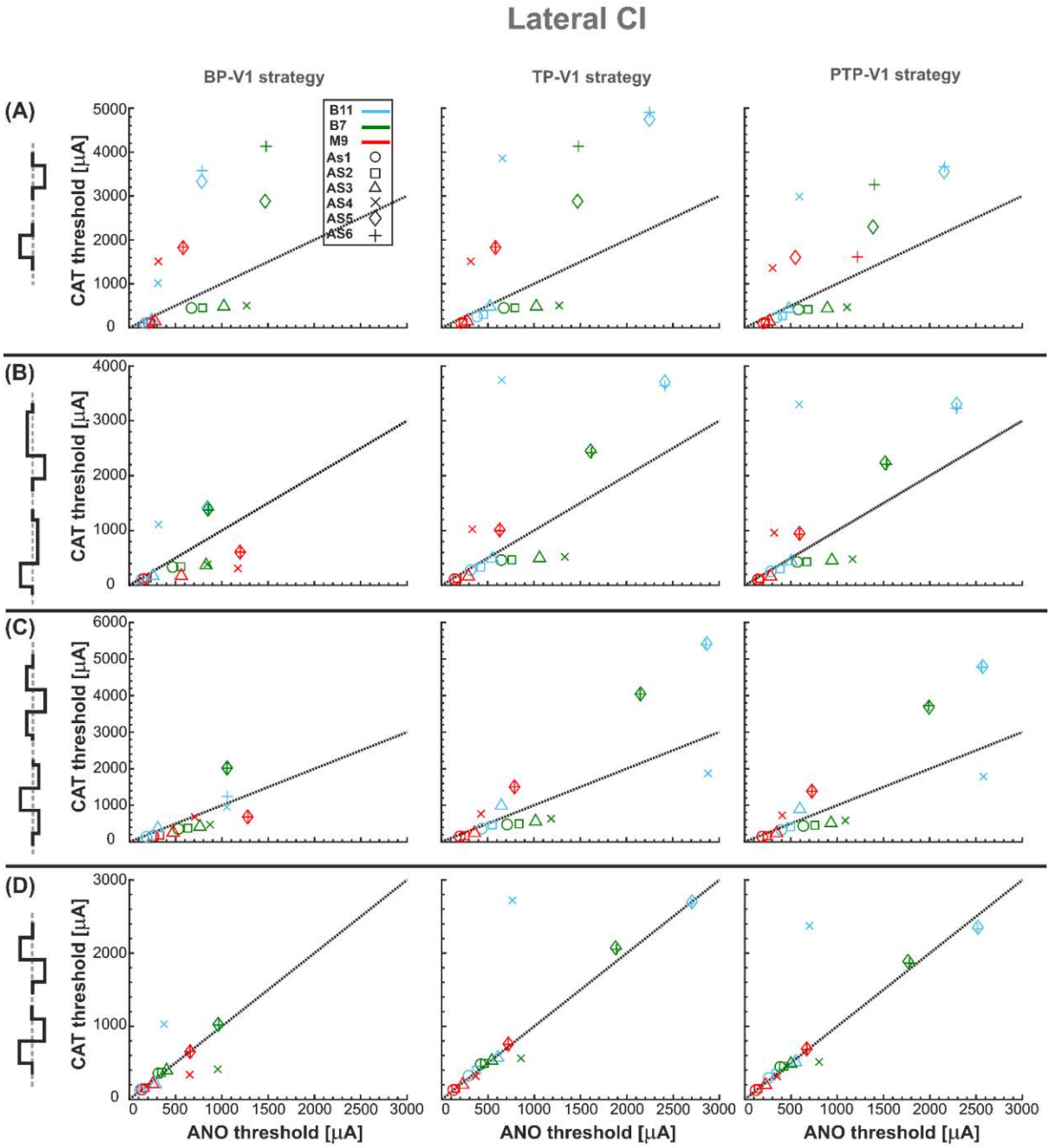

Figure 3.30. Threshold of three TNs for lateral CI for four different pulse types and three multipolar strategies (BP-V1, TP-V1, and PTP-V1) by changing the distance between channels of both CI systems. **(A)** Monophasic, **(B)** pseudo-monophasic, **(C)** triphasic, and **(D)** biphasic pulse. Layout as in Figure 3.18.

Die approbierte gedruckte Originalversion dieser Dissertation ist an der TU Wien Bibliothek verfügbar.
The approved original version of this doctoral thesis is available in print at TU Wien Bibliothek.
TU Bibliothek Your knowledge hub WIEN

Figure 3.31 represents the polarity ratios for monophasic stimulation. The polarity ratio in perimodiolar CI is significantly decreased by doubling the distance between channels compared to Figure 3.21B-D, left panels. Interestingly, the declining trend is also again visible between intact and different degenerated cases, similar to Figure 3.21B-D (left panels). In contrast, the polarity ratio substantially increased by halving the distance between channels in the lateral CI. However, the polarity behavior of all TNs in intact and different degenerated levels is similar to Figure 3.21B-D (right panels).

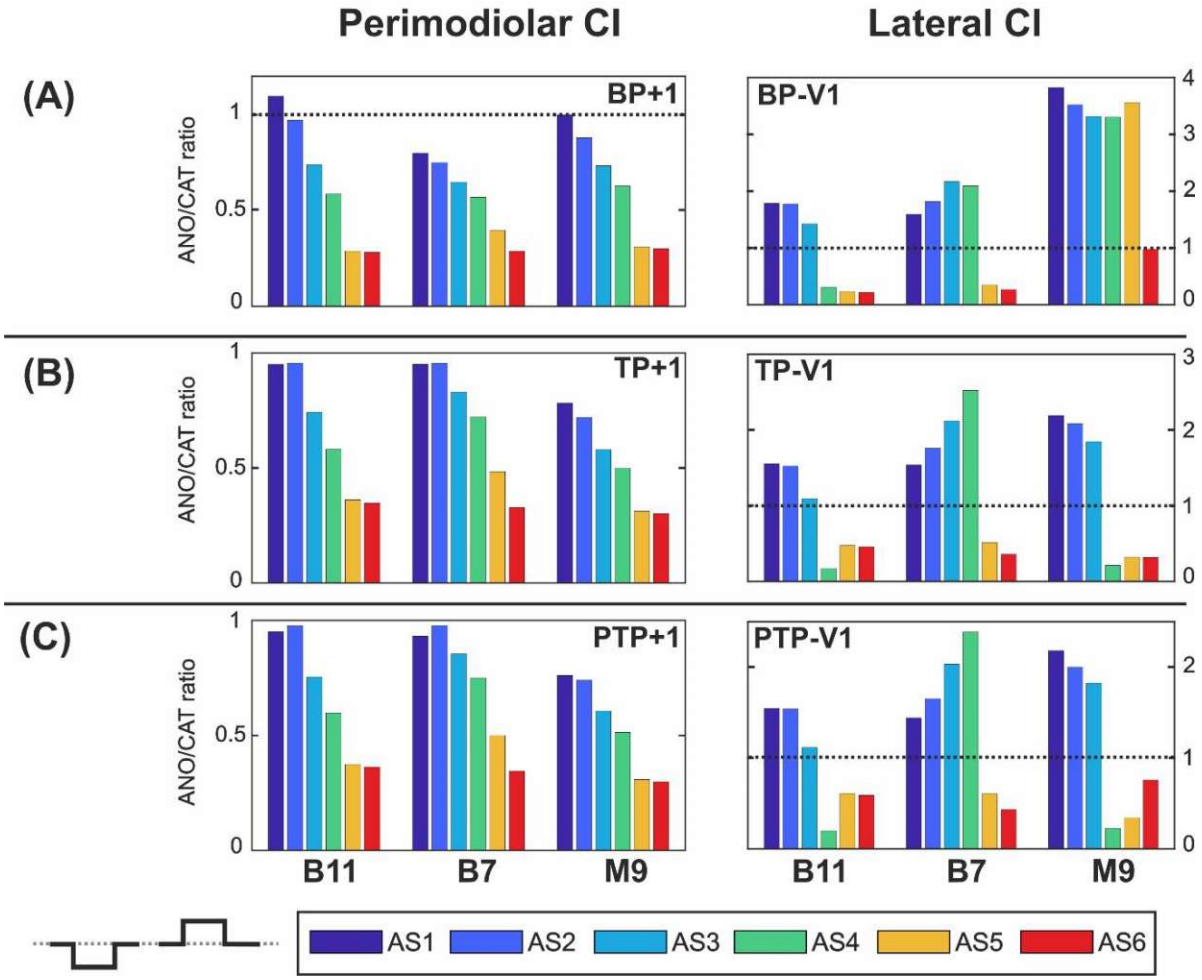

Figure 3.31. Polarity ratios for different degeneration levels stimulated with the monophasic pulse by changing the distance between channels of both CI systems. **(A)** bipolar (BP), **(B)** tripolar (TP), and **(C)** partial tripolar (PTP) stimulation strategies. The horizontal dotted lines show the polarity ratio is equal to one (ANO/CAT = 1).

Die approbierte gedruckte Originalversion dieser Dissertation ist an der TU Wien Bibliothek verfügbar.
The approved original version of this doctoral thesis is available in print at TU Wien Bibliothek.

Figure 3.32 illustrates the polarity ratios with the same structure as Figure 3.31 but for pseudo-monophasic stimulation. The polarity ratio is significantly decreased by doubling the distance between channels compared to Figure 3.22B-D (left panels). The declining trend is again visible between intact and most degenerated cases, similar to Figure 3.22B-D (left panels). On the other hand, lateral CI shows similar polarity behavior as monophasic pulse (Figure 3.31 and Figure 3.22B-D, right panels).

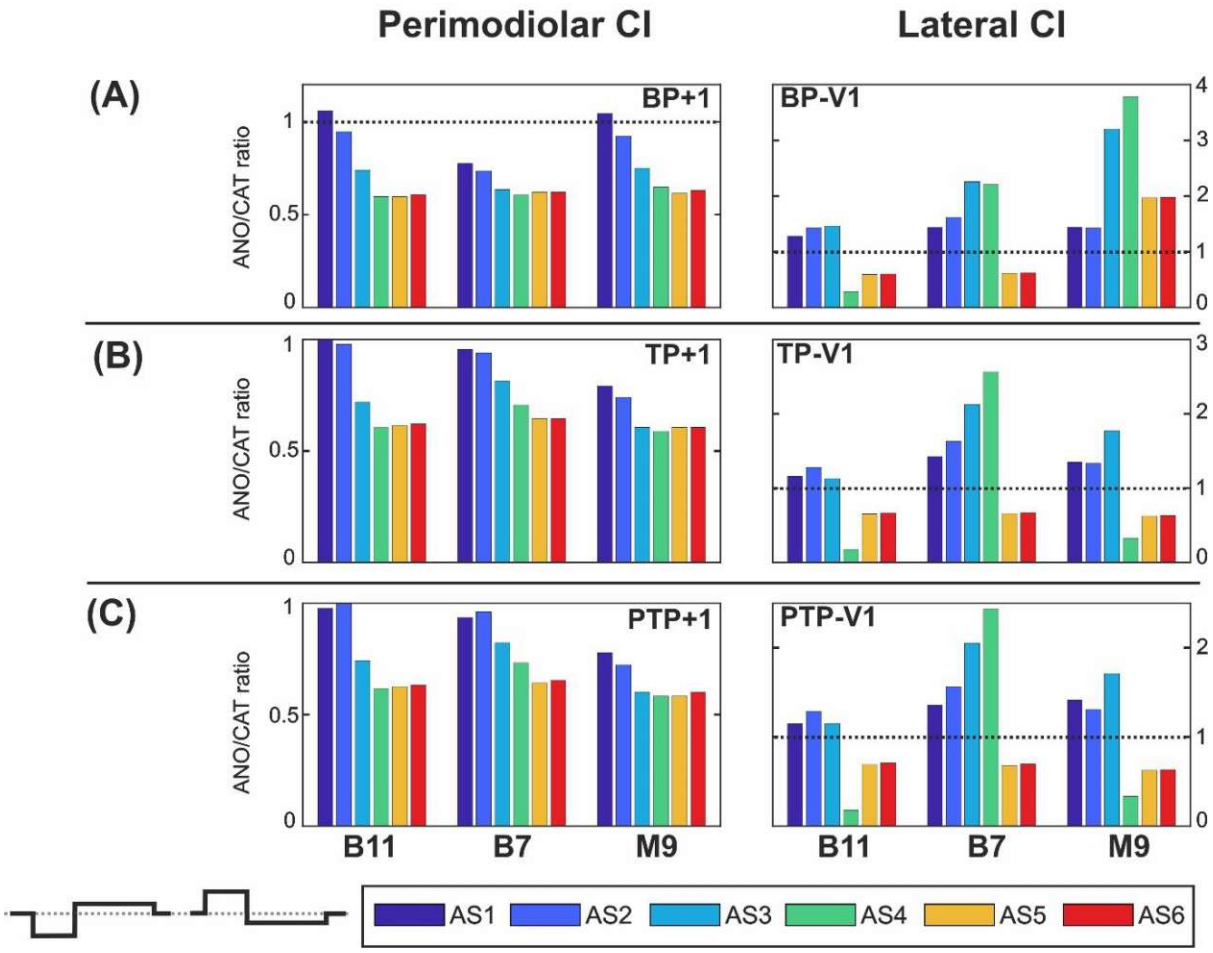

Figure 3.32. Polarity ratios for different degeneration levels stimulated with the pseudo-monophasic pulse by changing the distance between channels of both CI systems. Layout as in Figure 3.31.

Figure 3.33 demonstrates the polarity ratios with the same configuration as Figure 3.31 but for triphasic stimulation. The polarity ratio is significantly decreased by doubling the distance between channels compared to Figure 3.23B-D, left panels. Again, the declining trend is noticeable between intact and most degenerated cases, similar to Figure 3.23B-D, left panels. Lateral CI represents similar polarity behavior as previous pulses (Figure 3.31-32, right panels) and Figure 3.23B-D, right panels.

Die approbierte gedruckte Originalversion dieser Dissertation ist an der TU Wien Bibliothek verfügbar.
The approved original version of this doctoral thesis is available in print at TU Wien Bibliothek.
TU Bibliothek Your knowledge hub WIEN

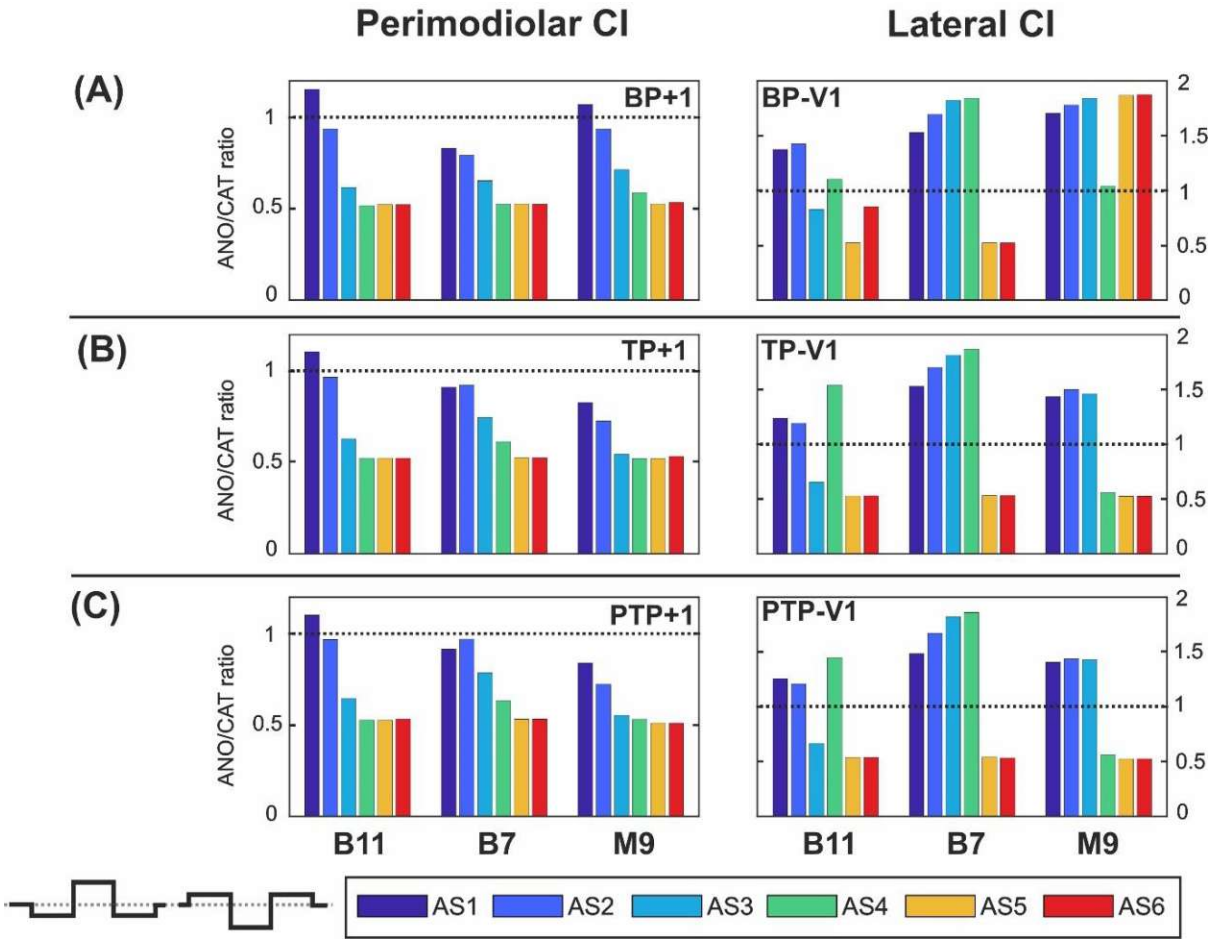

Figure 3.33. Polarity ratios for different degeneration levels stimulated with the triphasic pulse by changing the distance between channels of both CI systems. Layout as in Figure 3.31.

Figure 3.34 shows the polarity ratios for biphasic stimulation. In contrast to the previous pulse shapes, by applying the biphasic pulse in the lateral CI array (Figure 3.34, right panels), the polarity effect is lost, similar as in Figure 3.24B-D, right panels. The declining trend in perimodiolar CI (Figure 3.34, left panels) from intact to progressive degeneration does not occur by applying this pulse shape, same as in Figure 3.24B-D, left panels.

Die approbierte gedruckte Originalversion dieser Dissertation ist an der TU Wien Bibliothek verfügbar.
The approved original version of this doctoral thesis is available in print at TU Wien Bibliothek.

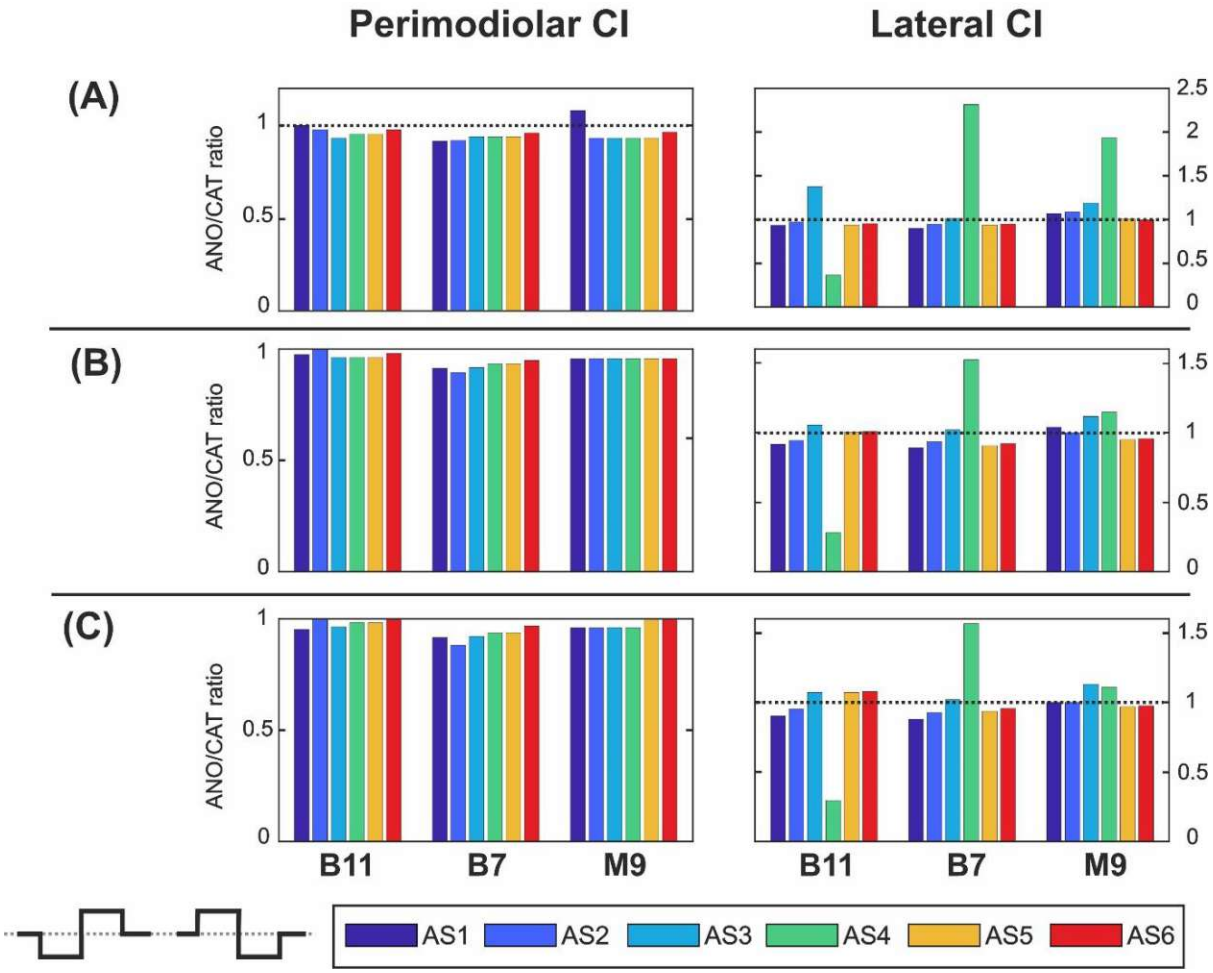

Figure 3.34. Polarity ratios for different degeneration levels stimulated with the biphasic pulse by changing the distance between channels of both CI systems. Layout as in Figure 3.31.

Die approbierte gedruckte Originalversion dieser Dissertation ist an der TU Wien Bibliothek verfügbar.
The approved original version of this doctoral thesis is available in print at TU Wien Bibliothek.

3.3 Scala tympani versus scala vestibuli electrodes

3.3.1 Stimulation at threshold

The extracellular stimulations for six ANFs (named as target neuron: TN) from different cochlear regions (Table 2.8) for the electrode placed in the scala tympani (ST) vs. in scala vestibuli (SV) were investigated. Three different neural statuses: intact, intermediate, and progressive degenerated, are studied by the excitation of the nearest electrode. In addition, ANO and CAT thresholds are considered for the excitation threshold of TNs in all three degenerated levels.

Figure 3.35 displays the excitation profiles of TN=B12 (α =56°) from the lower-middle of the basal turn in three ANF statuses for threshold stimulation with ST electrode (left) and SV electrode (right); the corresponding threshold values for AP initiation are shown on top. In the intact case (Figure 3.35A), both ANO and CAT thresholds for the SV electrode are smaller than the corresponding ST electrode (up to 50% in CAT). The AP initiation sites of all six cases are at the peripheral process shown with golden color.

Figure 3.35B represents the intermediate case where the ANO threshold for ST is about 50% lower than the CAT threshold (ANO sensitivity). On the other hand, the CAT threshold is about 5% lower than the ANO threshold (CAT sensitivity) in the SV case. In this degeneration level of ANF, first AP is generated in the peripheral process in all panels, but the AP cannot load the large capacitance of the soma and pass through the soma since the fiber diameter is reduced; except for the CAT stimulus in the ST. Then, the second (real) AP initiation happens for the three remaining cases at the central process. Figure 3.35C represents the progressive status of TN where the excitation thresholds for all cases are similar to the intermediate case (Figure 3.35B), but the AP initiation sites are in the central process since their peripheral parts are lost.

Die approbierte gedruckte Originalversion dieser Dissertation ist an der TU Wien Bibliothek verfügbar.
The approved original version of this doctoral thesis is available in print at TU Wien Bibliothek.
TU Bibliothek Your knowledge hub WIEN

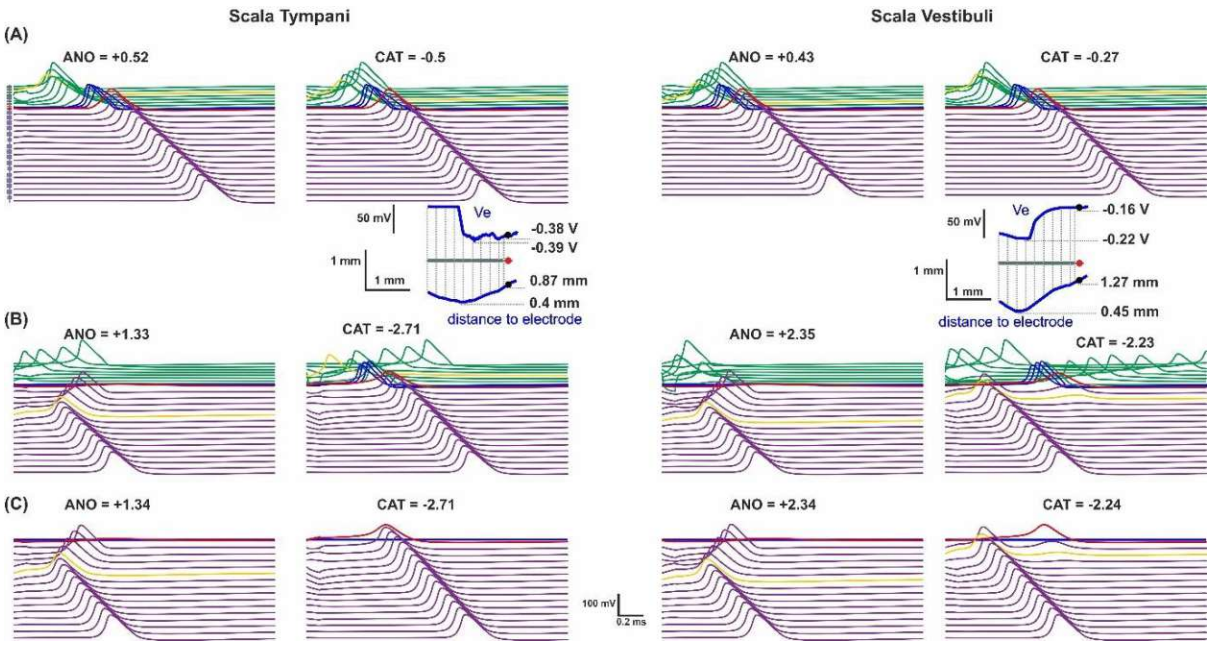

Figure 3.35. Threshold stimulation of TN B12 for intact **(A)**, intermediate **(B)**, and progressive case **(C)** for the scala tympani electrode (left) and the scala vestibuli electrodes (right). In each panel, traces represent the membrane voltage over time in selected compartments for ANO (left) and CAT (right) pulses. The green, blue, red, and violet lines represent peripheral nodes, pre-somatic compartments, soma, and central nodes, respectively. Corresponding threshold values are displayed on the top of each panel. The bottom part in panel **(A),** the CAT pulse shows the extracellular potential V_e for CAT along the first part of the TN (blue line), the soma positions (black spheres), the largest (negative) V_e and V_e of soma (horizontal black dashed lines); the vertical black dashed lines indicate the positions of nodes of Ranvier, and the blue curves show the distances of the compartment centers to the electrodes. The golden curves indicate the spike initiation compartments.

The next TN=B7 (α = 137°) investigates excitation profiles based on the ANFs status and electrode position (Figure 3.36). In the intact case, CAT thresholds are about 30% and 50% lower than the ANO thresholds (CAT sensitive) in the ST and SV, respectively (Figure 3.36A). AP initiation sites happen at the peripheral process in both polarities in ST and SV cases. The CAT threshold is about 20% lower than ANO in the intermediate level despite the real AP site of both polarities at the same compartment from the central process (Figure 3.36B, left). Also, in the SV case, the CAT threshold is about 74% smaller than the ANO threshold, and the second and real AP initiation sites are in the central process (Figure 3.36B, right).

Figure 3.36C represents the progressive case of the ST and SV electrodes. The ANO threshold and AP site remain the same as the intermediate case in the ST (Figure 3.36B, left), whereas the CAT threshold is almost double compared to the intermediate case with the same AP site. At this degenerated level, ANO sensitivity occurs for the ST electrode. On the other hand, the

Die approbierte gedruckte Originalversion dieser Dissertation ist an der TU Wien Bibliothek verfügbar.
The approved original version of this doctoral thesis is available in print at TU Wien Bibliothek.
TU Bibliothek Your knowledge hub WIEN

thresholds and AP sites in both polarities in the SV are similar to the previous degeneration level (Figure 3.36B vs. Figure 3.36C, right). In addition, in the SV, CAT sensitivity occurs in contrast to the ST case (ANO sensitivity).

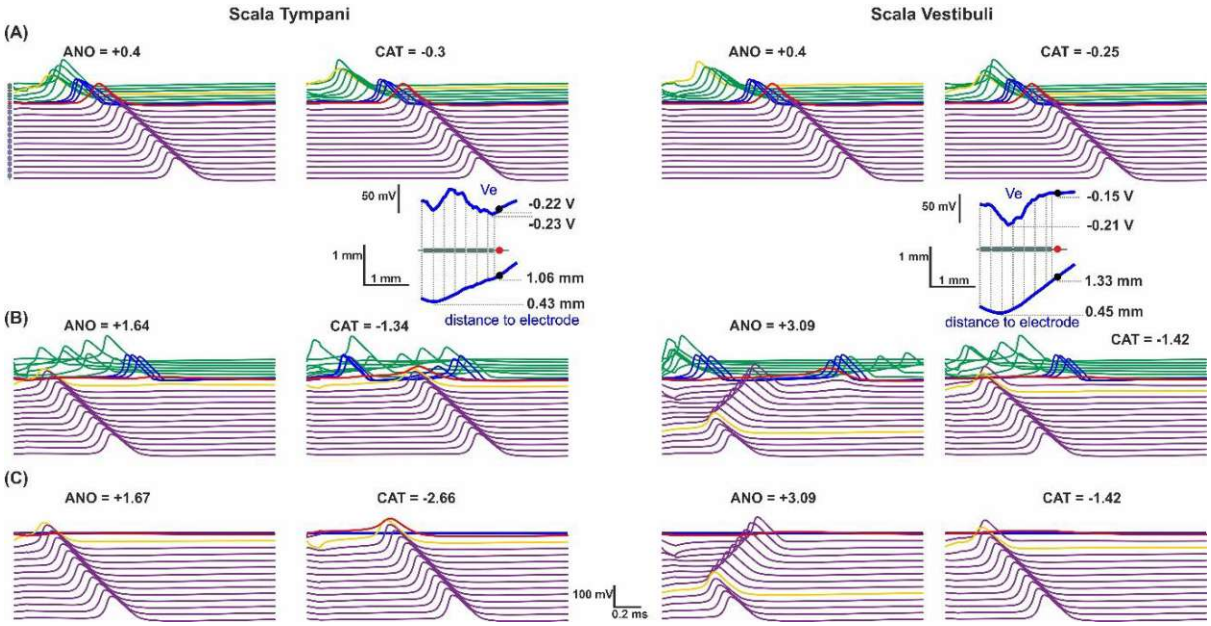

Figure 3.36. Threshold stimulation of TN=B7 for intact **(A)**, intermediate **(B)**, and progressive **(C)** for the scala tympani electrode (left) and the scala vestibuli electrodes (right). Layout as in Figure 3.34.

The third selected fiber is TN=B2 (α = 253°), which shows the threshold stimulation behavior depending on the degeneration level and electrode position in Figure 3.37. In the intact, CAT thresholds are lower than ANO thresholds, and the threshold ranges are almost similar in both ST and SV electrodes (Figure 3.37A). The AP initiation sites in this level happen at the peripheral process (golden compartment).

Figure 3.37B displays the intermediate case where the CAT excitation thresholds need less than ANO thresholds in the ST (with 25%) and SV (with 50%). The AP initiation sites are similar between the ST and SV, corresponding to ANO and CAT pulses individually. In the progressive case (Figure 3.37C), the thresholds are almost comparable to the intermediate case since the AP initiation sites happen at the same central process compartments with respect to the CAT and ANO pulses (Figure 3.37B vs. Figure 3.37C).

Die approbierte gedruckte Originalversion dieser Dissertation ist an der TU Wien Bibliothek verfügbar.
The approved original version of this doctoral thesis is available in print at TU Wien Bibliothek.
TU Bibliothek Your knowledge hub WIEN

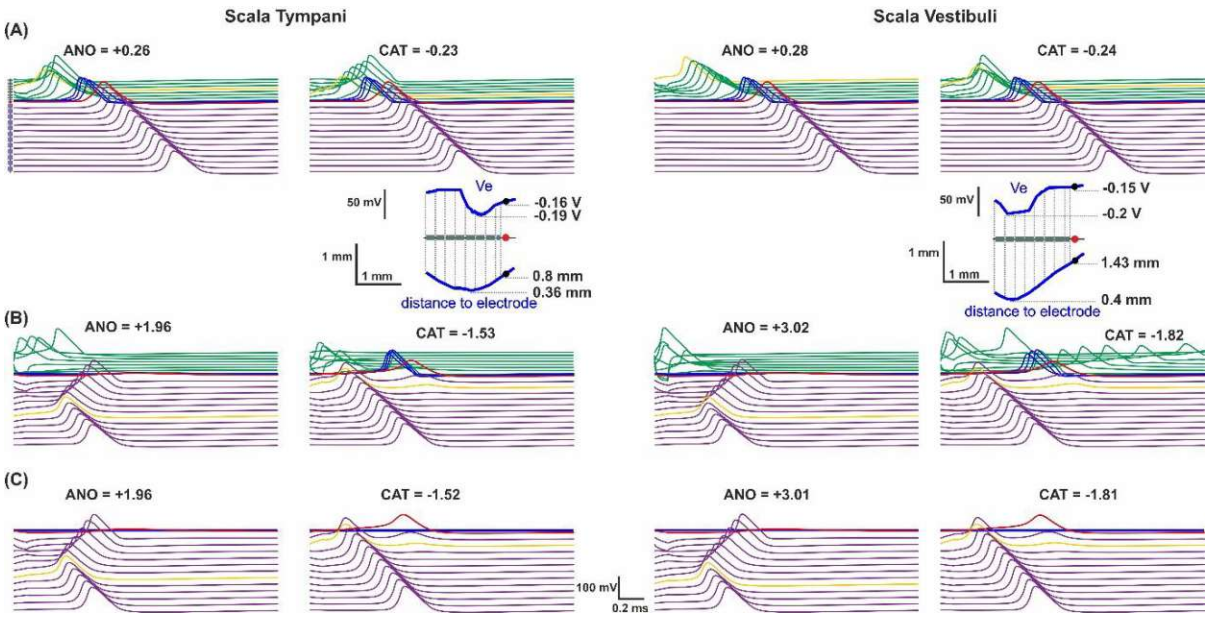

Figure 3.37. Threshold stimulation of TN=B2 for intact **(A)**, intermediate **(B)**, and progressive **(C)** for the scala tympani electrode (left) and the scala vestibuli electrodes (right). Layout as in Figure 3.34.

Concerning cochlear turns, the next investigated TN is selected from the middle turn, TN = M7 ($\alpha = 402°$). In the intact case, the ANO threshold is almost triple the CAT threshold in the ST, while the AP sites are in the peripheral process (Figure 3.38A, left).

On the other hand, the CAT sensitivity appears in the SV electrodes, but the difference between ANO and CAT thresholds (36%) is not significant as in the ST case. In addition, the AP initiation site happens in the peripheral part as expected (Figure 3.38A, right). In the intermediate state (Figure 3.38B), CAT sensitivity happens in ST and SV electrodes. Both thresholds increased slightly in the ST case, but significantly threshold enhancement happened in the SV case compared to the intact case (Figure 3.38A vs. Figure 3.38B). In addition, the AP initiation sites in the intermediate level occur in the central process in all cases. Figure 3.38C shows the progressive case where the ANO and CAT excitation thresholds and AP sites are equal to the previous degenerated levels (Figure 3.38B, intermediate case).

Die approbierte gedruckte Originalversion dieser Dissertation ist an der TU Wien Bibliothek verfügbar.
The approved original version of this doctoral thesis is available in print at TU Wien Bibliothek.
TU Bibliothek Your knowledge hub WIEN

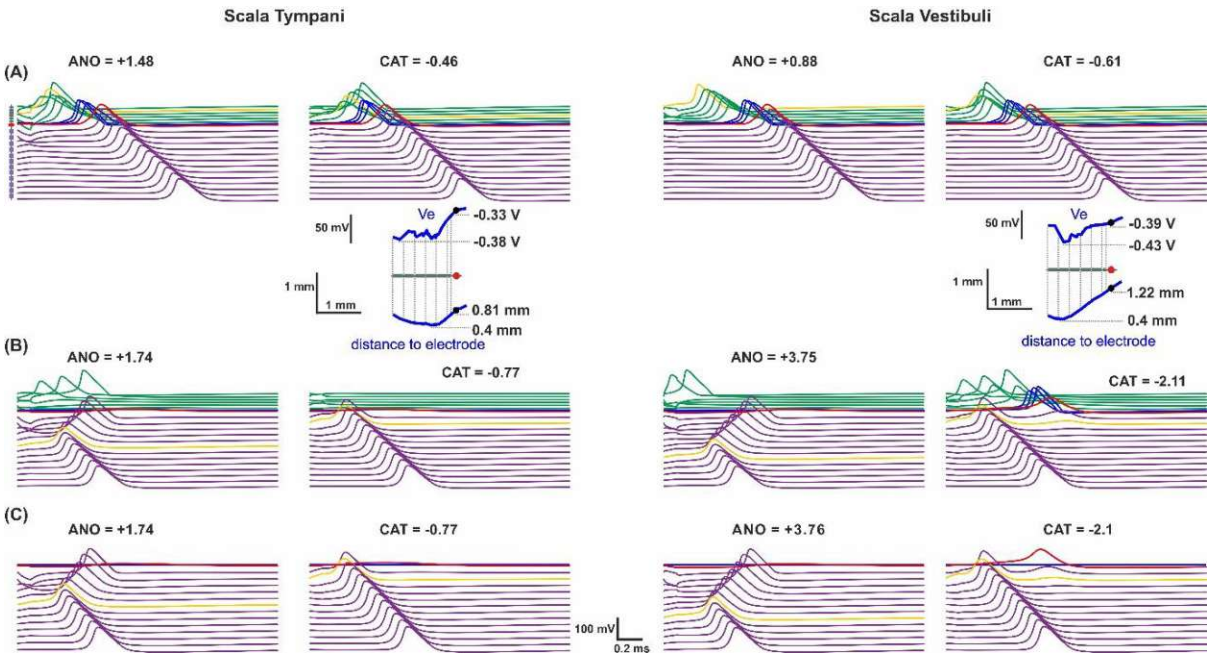

Figure 3.38. Threshold stimulation of TN=M7 for intact **(A)**, intermediate **(B)**, and progressive **(C)** for the scala tympani electrode (left) and the scala vestibuli electrodes (right). Layout as in Figure 3.34.

The fifth TN is M4 (α= 495°) which is located almost in the upper-middle turn and illustrates the excitation profiles based on electrode location and fiber state in Figure 3.39.

The intact case of the ST (Figure 3.39A, left) represents CAT sensitivity where the ANO threshold is almost quadruple to the CAT threshold. In addition, the AP initiation sites of CAT and ANO are located at peripheral and central processes, respectively. In contrast, in the SV case (Figure 3.39A, right), the CAT threshold is smaller than ANO, the same as the ST case, but since the distance of electrode to TN increased needs a higher current than the ST. Again, the AP sites are similar to the ST case (CAT at peripheral process and ANO at central process).

In the intermediate state (Figure 3.39B), the ANO thresholds and AP sites remain the same as the intact case (Figure 3.39A) in the ST and SV cases. However, the CAT thresholds are noticeably increased up to six times larger than the intact case (Figure 3.39A vs. Figure 3.39B, left). The intermediate degenerated level (Figure 3.39B) shows ANO sensitivity in the ST and SV cases, and AP sites are located in the central processes except for the CAT pulse of the ST. In the progressive level (Figure 3.39C), the thresholds and AP initiation sites are comparable to the previous degenerated level (intermediate case, Figure 3.39B).

Die approbierte gedruckte Originalversion dieser Dissertation ist an der TU Wien Bibliothek verfügbar.
The approved original version of this doctoral thesis is available in print at TU Wien Bibliothek.
TU Bibliothek Your knowledge hub WIEN

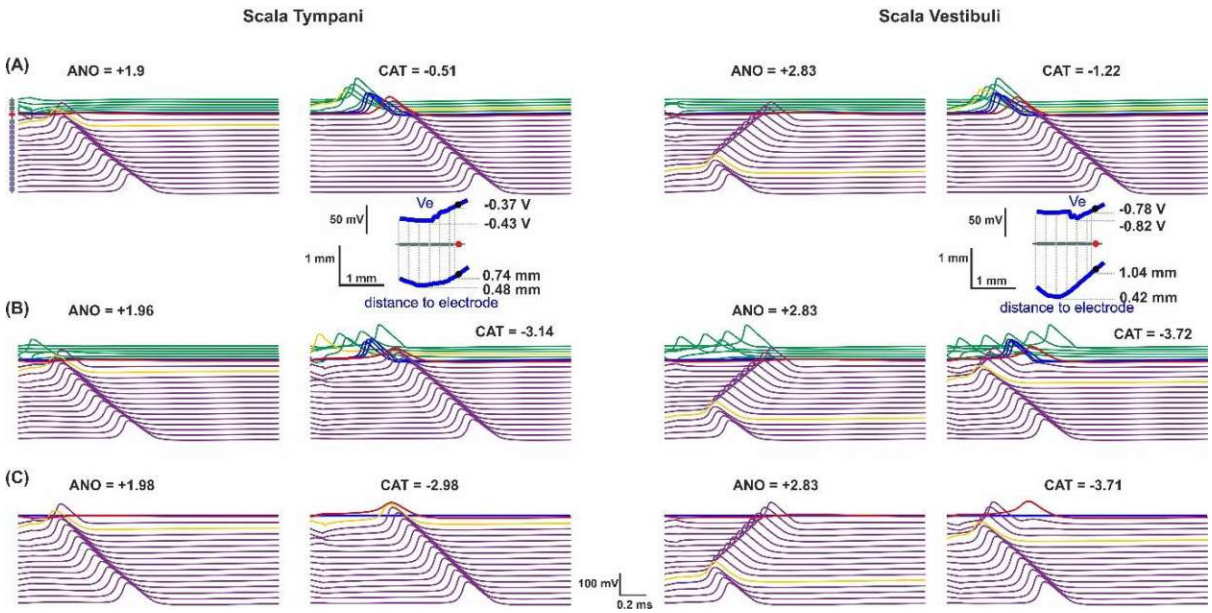

Figure 3.39. Threshold stimulation of TN=M4 for intact **(A)**, intermediate **(B)**, and progressive **(C)** for the scala tympani electrode (left) and the scala vestibuli electrodes (right). Layout as in Figure 3.34.

The last TN is selected from the beginning of the apical turn, M1 (α = 592°). In the intact (Figure 3.40A), CAT thresholds are smaller than ANO thresholds, and all AP initiation sites are located at the peripheral parts. The threshold and AP initiation site of the ANO pulse of the ST is similar to the CAT pulse of the SV.

The intermediate case demonstrates ANO sensitivity in both ST and SV cases. The CAT threshold in the ST case (Figure 3.40B, left) is almost triple, and in the SV case (Figure 3.40B, right), almost 46% increases compared to the ANO thresholds. The AP initiation sites happen in the central processes except for the CAT pulse of the ST (peripheral process). Figure 3.40C displays ANO sensitivity in the ST and SV cases for the progressive degenerated level. The thresholds and AP sites (except CAT in ST) are almost similar to the intermediate case (Figure 3.40B vs. Figure 3.40C).

Die approbierte gedruckte Originalversion dieser Dissertation ist an der TU Wien Bibliothek verfügbar.
The approved original version of this doctoral thesis is available in print at TU Wien Bibliothek.
TU Bibliothek Your knowledge hub WIEN

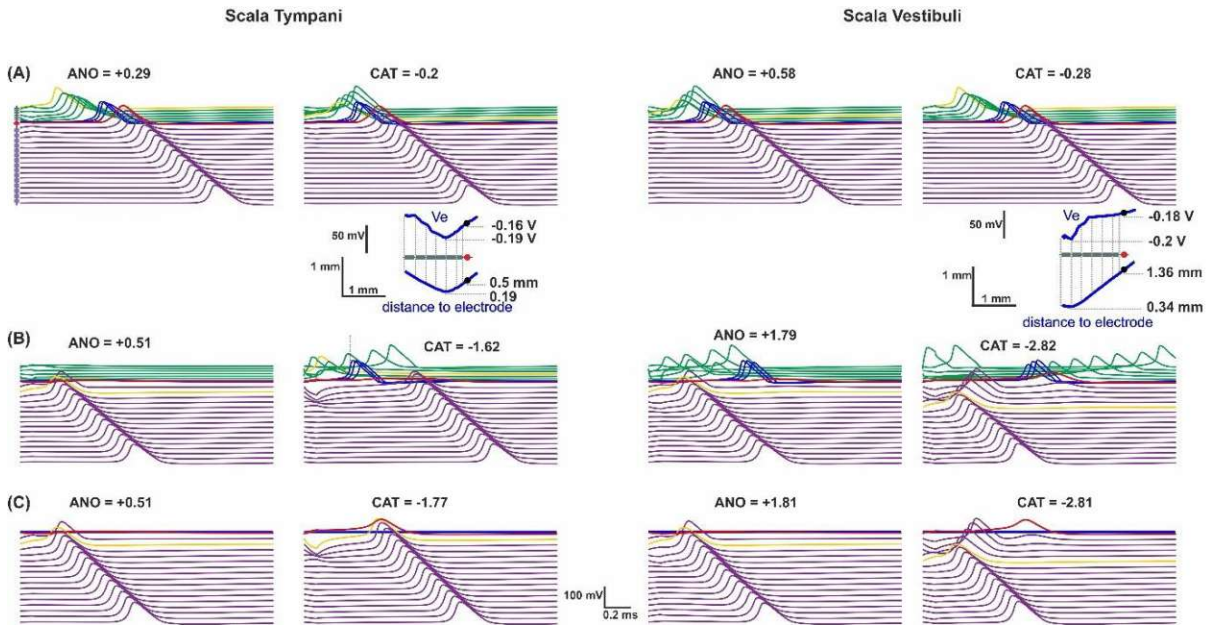

Figure 3.40. Threshold stimulation of TN=M1 for intact **(A)**, intermediate **(B)**, and progressive **(C)** for the scala tympani electrode (left) and the scala vestibuli electrodes (right). Layout as in Figure 3.31.

3.3.2 Stimulation of intact auditory nerve fibers

This section selects only three TNs (B12, B2, and M1) from the six investigated TNs for a more detailed investigation. The three TNs are chosen based on the cochlear turns with similar CAT excitation thresholds in ST and SV or less SV thresholds. These three TNs are stimulated with the electrode located in comparable positions in ST and SV. In all investigated cases, the AP initiated from the peripheral process, which was sensitive to CAT pulse.

Figure 3.41 demonstrates the membrane voltage over time for selected compartments of three intact cases located in the basal, middle, and apical turns for the ST (left panel) vs. SV stimulations (right panel). The color-coded manner of compartments is similar to Figure 3.35. The voltage profiles of the V_e (blue) against the distance to electrode (green) curves in all cases demonstrate that the closest part of the fiber possesses the highest voltage value. However, this does not necessarily mean that the closest part can initiate the AP. According to the voltage membrane equation, there are three forces to change the transmembrane potential (V_m):

i) Activating function (AF), which is proportional to the second derivative of the extracellular voltage in every compartment with two neighbors and inversely proportional to its intracellular resistance and capacitance (Rattay et al., 1986, 1999).
ii) Axial force which is the current flow of the neighbor compartments and again inversely proportional to its intracellular resistance and capacitance.

Die approbierte gedruckte Originalversion dieser Dissertation ist an der TU Wien Bibliothek verfügbar.
The approved original version of this doctoral thesis is available in print at TU Wien Bibliothek.
TU Bibliothek Your knowledge hub WIEN

iii) The ionic current force which is acting due to opening of channels.

AF is the most important driving force in extracellular stimulation, whose values estimate the candidate sites of AP initiation. However, depending on the AF values of the neighbors, a node with the highest AF may not initiate the AP, especially for the intact fibers at the threshold stimulation since the voltage values are low. In these cases, investigating the second force may help explain and understand the initiation of AP even in non-expected sites. However, before the pulse onset, the cell is in the resting state, and for the AP initiation, the most critical time is the stimulus onset, when the ionic forces do not start to act yet. At this time, the axial force of each compartment is affected mainly by the AFs of other neighboring compartments.

The AP can be initiated even at a site with negative AF, shown in Figure 3.41A, left. In the intact case of investigated ANF for the ST stimulating electrode, the AP starts in the fourth node, which possesses a negative AF value shown with the orange star, while both internode neighbors have the highest positive AF values according to the V_e curvature. The dashed orange curve demonstrates the axial force of the same compartment that initiates the AP. In the first half of the stimulus time, the axial force is dominant by a high positive value resulting from the positive AF of the neighbor internodes that initiates the AP in this compartment even with a high negative AF. In contrast, the threshold for the SV case is half of the ST threshold, and AF has less oscillation in the SV case than ST.

Figure 3.41B-C displays other cases, and again the AP initiates in a node where the AF is not as high as in the neighboring compartments. The AF vs. axial forces in all three cases demonstrate that the net driving force in the nodes with the highest value of AF is almost zero because the high positive value of AF is surrounded by large negative values of AF neighbors that result in all together becoming small, almost zero. Whereas the winner nodes have a positive net driving force, especially at the first half of the stimulus time (vertical gray dashed line), which results in AP initiation in these non-expected compartments (orange). However, the depolarized regions during the stimulus onset in blue and purple V_m curves result from the positive AF, where the V_e curves also show a positive curvature.

Die approbierte gedruckte Originalversion dieser Dissertation ist an der TU Wien Bibliothek verfügbar.
The approved original version of this doctoral thesis is available in print at TU Wien Bibliothek.
TU Bibliothek Your knowledge hub WIEN

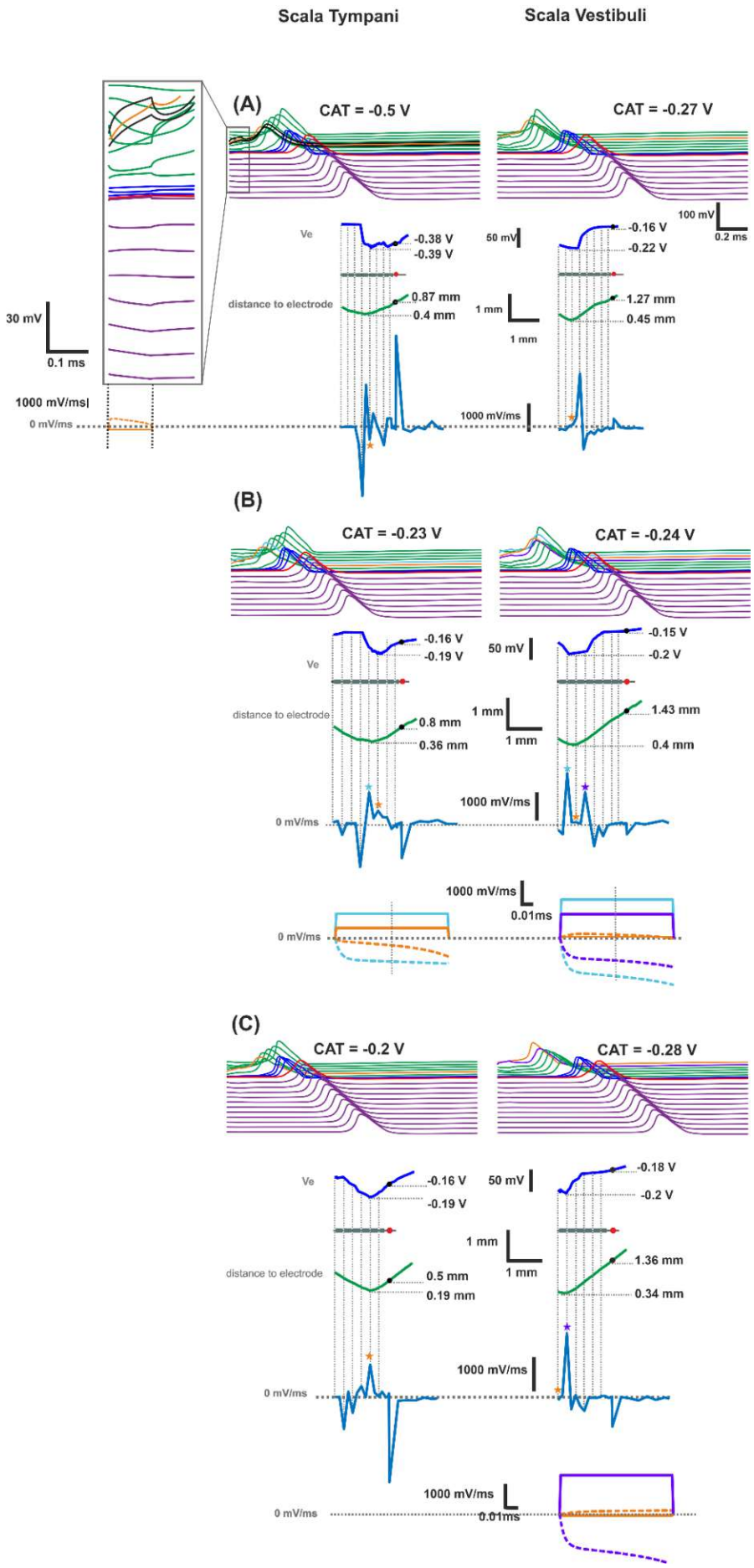

Die approbierte gedruckte Originalversion dieser Dissertation ist an der TU Wien Bibliothek verfügbar.
The approved original version of this doctoral thesis is available in print at TU Wien Bibliothek.
TU Bibliothek Your knowledge hub WIEN

Figure 3.41. Threshold stimulation of intact target fibers, B12 (top), B2(middle), and M1(bottom) for the scala tympani electrodes (left) and scala vestibuli electrodes (right). In each panel, upper traces represent the membrane voltage over time in selected compartments for CAT pulse. The green, blue, red, violet, black (only in A), and orange lines represent peripheral nodes, pre-somatic compartments, soma, central nodes, internodes, and AP initiation sites, respectively. Corresponding threshold values are displayed on the top. The lower part in each panel shows the extracellular potential (V_e) distribution for CAT along the peripheral process of the ANFs (blue line) and the soma position (black spheres), the soma and largest (negative) V_e (horizontal grey dashed lines); the vertical grey dashed lines indicate the positions of nodes of Ranvier; a schematic illustration between the blue and the green curves shows the compartments with internodes in grey, nodes in black and soma in red circle. The green curves show the distance to the electrode center along the peripheral process; the corresponding AF (light blue curve, I_{ext}/C) is reproduced with its zero line (horizontal grey dashed line); the stars in color coded manner represent the AP starting node in orange, the possible winner in the right and left neighborhoods in purple and light blue, respectively; the last colored traces show the corresponding AF (solid line) and the axial voltage changes, $\frac{dV_m}{dt}$, (dashed line) of the same compartments during the stimulus time with the same color code as in the stars: AP initiation compartment in orange, right and left possible winners in purple and light blue, respectively.

3.3.3 Stimulation of intermediate vs. progressive degenerated auditory nerve fibers

The same simulation of three TNs from the previous section investigated the ANFs behavior in detail under degeneration conditions as the intermediate and progressive levels based on ST and SV electrodes.

In both cases (intermediated vs. progressive degeneration), the voltage membrane behavior along the ANFs as well as the AF curves for the three from six TNs (B12, B2, and M1) are shown for the electrodes positioned in the ST vs. in the SV. Depending on the nerve positions, both sensitivities occurred in degenerated cases; therefore, both CAT and ANO pulses are shown in Figure 3.42. Surprisingly, in all degenerated cases (from investigated ANFs), when the electrode is located in SV, the propagated AP initiated from the central process; however, for the ST case, the AP initiation sites occur at different parts of ANFs depending on the degeneration level and the polarity of the pulse. However, contrary to the intact fiber's behavior, in degeneration cases, the AP initiation can perfectly be explained only by AF behavior as a result of high extracellular potentials required for the degenerated fiber excitation that accordingly causes high AF values.

Die approbierte gedruckte Originalversion dieser Dissertation ist an der TU Wien Bibliothek verfügbar.
The approved original version of this doctoral thesis is available in print at TU Wien Bibliothek.
TU Bibliothek Your knowledge hub WIEN

Figure 3.42 demonstrates the V_m over time for the same selected compartments and with the same color codes as in Figure 3.41. In addition, the AF curves are shown in blue, and the AP positions are indicated with orange and green stars in the case of propagated AP and the peripheral initiated AP, respectively. This figure shows the V_m behavior in intermediate (plots above in each section) and progressive cases (plots below in each section) for the selected ANFs located in the basal (A), middle (B), and apical turns (C), for the ST (left) vs. SV stimulations (right).

Figure 3.42A left (ST stimulation) displays ANO sensitivity in both degenerated cases; the AP starts at a central node about 2.5 mm away from soma, which possesses a positive AF value (the orange star). Although in the intermediate case, the first AP started in the middle of the peripheral process, yet the thin peripheral process was not strong enough to load the soma capacitance and pass the soma.

The right panel of Figure 3.42A demonstrates CAT sensitivity in both degenerated cases for the SV stimulation. The AP starts in a central node about 1 mm away from the soma, which has a positive AF value (orange star). However, again in the intermediate case, the first AP occurs in the third peripheral node with the highest positive AF value (green star), but the AP cannot propagate due to collision block. In addition, the AP starts in a central node about 2.5 mm away from the soma in both degenerated cases, in the ANO pulse.

Die approbierte gedruckte Originalversion dieser Dissertation ist an der TU Wien Bibliothek verfügbar.
The approved original version of this doctoral thesis is available in print at TU Wien Bibliothek.
TU Bibliothek Your knowledge hub WIEN

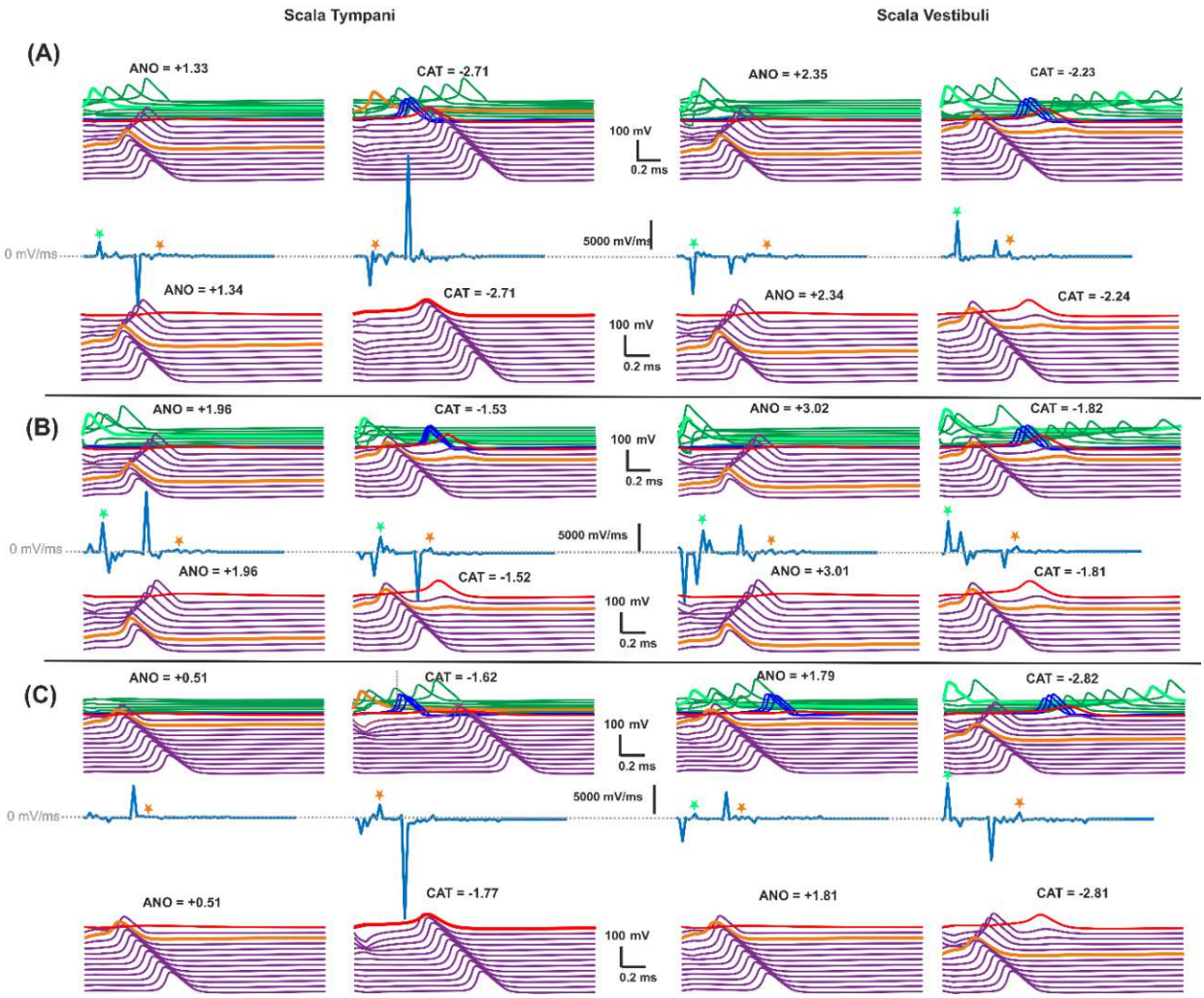

Figure 3.42. Threshold stimulation of intermediate and progressive degeneration target fibers top and bottom of each panel, respectively, for B12 **(A)**, B2 **(B)**, and M1 **(C)** for the scala tympani electrodes (left) and scala vestibuli electrodes (right). In each panel, traces represent the membrane voltage over time in selected compartments for ANO and CAT pulses. The green, blue, red, violet, and orange lines represent peripheral nodes (intermediate degeneration), pre-somatic compartments (intermediate degeneration), soma, central nodes, and AP initiation sites, respectively. Corresponding threshold values are displayed on the top for both polarities. The middle traces represent the corresponding AF (light blue curve, I_{ext}/C) with its zero line (horizontal grey dashed line); the stars in a color-coded manner represent the AP starting node in orange and the first AP initiation site in green.

Figure 3.42B displays the middle ANF for ST (left panel) and SV (right panel). Both degenerated cases showed CAT sensitivity for both electrode locations in ST, SV, and the APs initiated at the second node of the central process (orange), which is about 1 mm away from the soma. Although for the intermediate degeneration in both SV and ST cases, the first AP starts at the fourth and first node in the peripheral process with the highest AF value, respectively, but due to the faster propagation of the central initiated AP (green), the peripheral

Die approbierte gedruckte Originalversion dieser Dissertation ist an der TU Wien Bibliothek verfügbar.
The approved original version of this doctoral thesis is available in print at TU Wien Bibliothek.
TU Bibliothek Your knowledge hub WIEN

AP is stopped as a result of collision block. In addition, in the ANO pulse, the APs occur at about the same position in the central processes. However, in the intermediate cases, another AP occurs in the peripheral process with the highest AF value (green star), although due to the thin diameter of the peripheral processes, the AP is not strong enough to load the soma capacitance and pass the soma.

Figure 3.42C illustrates ANO sensitivity in the intermediate and progressive degenerated apical ANF for both electrodes locations in ST (left panel) and SV (right panel); the APs occur at about 1 mm away from the soma in the central processes (orange). In the intermediate case of SV, the first AP happens at the middle of the peripheral process, with the highest AF value (green star), but it stops again due to collision block. In addition, in the case of CAT pulse for SV stimulation, in both degenerated cases, the AP happens at the same central node of about 2.5 mm away from the soma (orange), whereas in the ST stimulation, AP initiates at different positions in the intermediate vs. progressive cases.

3.3.4 Strong versus weak stimulation

The intact and degenerated ANFs exist in a damaged cochlea, yet the number of intact fibers is expected to be often reduced according to the level of hearing loss. For electrical hearing stimulus strength may increase inversely with peripheral axon diameter and the local density of ANFs. In this section, the ANO and CAT thresholds as well as the AP initiation sites of intact and degenerated ANFs are studied for both electrode positions (ST vs. SV).

Figure 3.43 shows the stimulation of the three investigated neural statuses for six investigated ANFs when the electrode is located in ST vs. SV. In Figure 3.43A, the ANFs are stimulated at their threshold values; a color shows each nerve for intact, intermediate, and progressive degenerated cases represented with diamond, circle, and triangle, respectively. Marks above and below the black dashed line indicate a higher sensitivity to ANO and CAT, respectively. The right plot (SV) shows the same threshold values for both degeneration cases, resulting from the same AP initiation sites, whereas these thresholds are more deviated when the electrode is located in the ST.

Die approbierte gedruckte Originalversion dieser Dissertation ist an der TU Wien Bibliothek verfügbar.
The approved original version of this doctoral thesis is available in print at TU Wien Bibliothek.
TU Bibliothek Your knowledge hub WIEN

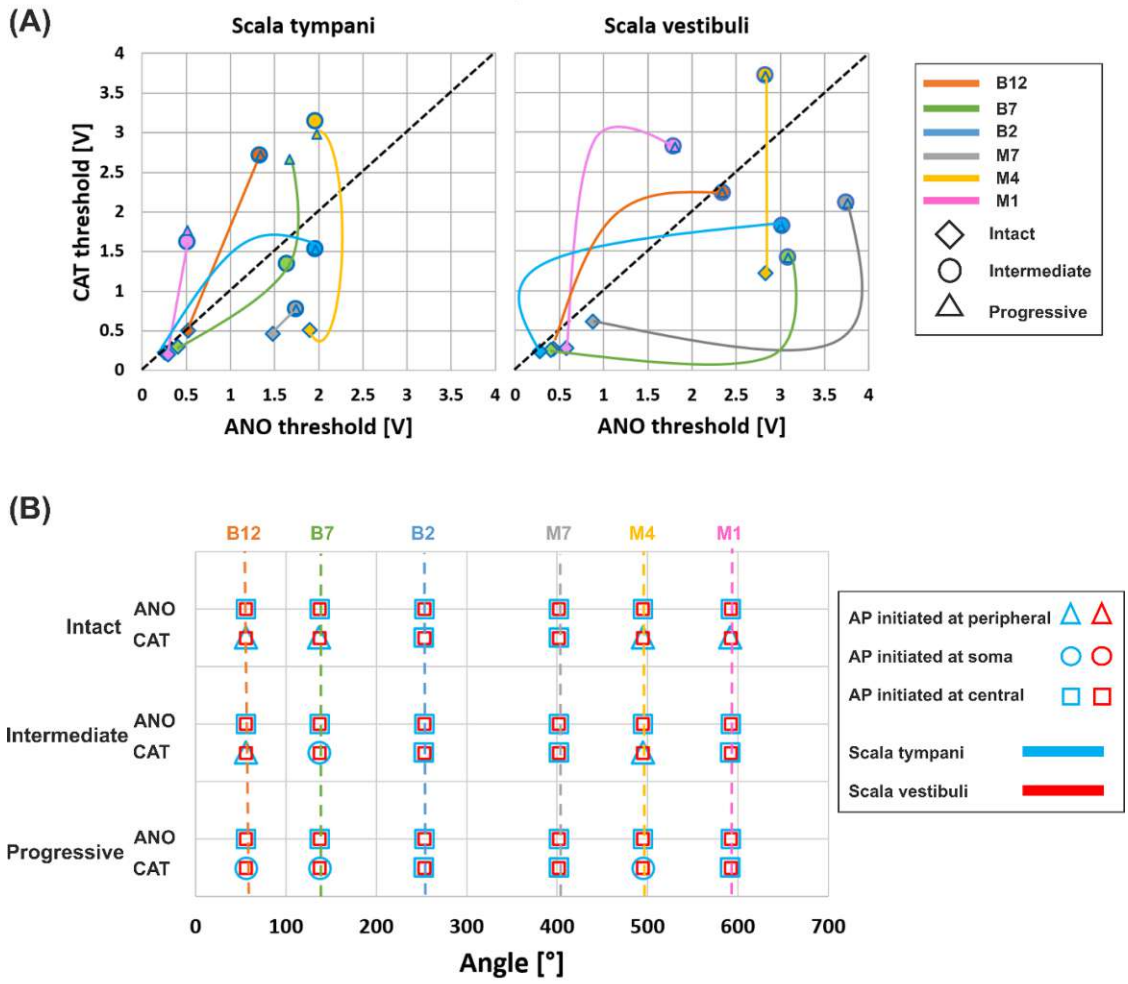

Figure 3.43. (A) ANO/CAT threshold values for six color-coded target fibers **(B)** The AP initiation sites for the strong amplitudes (progressive degeneration thresholds) of both ANO and CAT pulses on the intact, intermediate, and progressive degenerated ANFs are displayed for the six target fibers for scala tympani electrodes (blue) vs. scala vestibuli (red).

On the other hand, Figure 3.43B demonstrates the AP initiation sites for both polarities when the pulse amplitude is set to the strongest value of the threshold of the same progressive case. The SV and ST stimulation cases are shown in red and blue marks, respectively. While the electrodes in ST stimulate different positions of the ANFs (depending on the level of degeneration), the SV electrodes, interestingly, excite the central sites in all investigated fibers. By comparing the AP initiation sites for the threshold case versus the strong stimuli, the AP initiation sites change when strong stimuli were applied in the intact case for all six target fibers. Applying the ANO threshold, the AP sites shift when located at the peripheral part to the central process in both ST and SV electrodes. In addition, CAT thresholds demonstrate the same AP sites behavior as ANO thresholds for the SV stimulating electrodes and in two fibers B2 and M7, for the ST electrodes.

Die approbierte gedruckte Originalversion dieser Dissertation ist an der TU Wien Bibliothek verfügbar.
The approved original version of this doctoral thesis is available in print at TU Wien Bibliothek.
TU Bibliothek Your knowledge hub WIEN

3.3.5 Scala tympani versus scala vestibuli cochlear implant arrays

In this section, two types of CI arrays, perimodiolar and lateral CIs, were used to investigate the excitation behavior of ANFs based on ST and SV electrode array insertion. Therefore, for a systematic comparison, four ANFs (Table 2.10) from different cochlear regions were selected based on the closest distance of the terminal part of ANF to the center of the stimulating electrodes and called TN, which are similar in both types of CIs with ST and SV insertions.

Two different pulse shapes, a biphasic pulse as symmetric and a pseudo-monophasic pulse as asymmetric, were applied. In addition, both polarities, ANO and CAT, were involved. Moreover, three ANF health statuses, one intact (healthy) and two degenerated cases based on the various morphometry of the peripheral axon (Table 2.11), were considered to study the ANF excitation behavior based on array types, CI insertion in ST and SV, and polarity sensitivity.

Figure 3.44A shows the distance of B14 to the stimulating electrodes in the ST and SV for the perimodiolar and lateral CIs. In the perimodiolar array, the TN distance to the center of the SV electrode is about 25% farther than the ST electrode. However, in the lateral CI, the distance from the terminal to the soma of TN is similar in both ST and SV; however, the distance of the central parts of TN in SV becomes about 30% larger than ST.

The extracellular voltage (Ve) of TN, B14, is displayed in Figure 3.44B. In the perimodiolar CI, the terminal part of TN is about 15% larger in the ST compared to SV (Figure 3.44B, left panel). In addition, the peak value of Ve in ST is about 0.67 V occurs in the soma region. In comparison, the highest value of Ve in the SV is about 0.5 V and happens 0.9 mm away from the terminal.

In contrast, in the lateral CI (Figure 3.44B, right panel), the Ve in the terminal of TN is about 15% larger in SV than ST, which is inversed behavior compared to perimodiolar CI (Figure 3.44B, left panel vs. right panel). In addition, the Ve of ST and SV from the terminal to soma are opposite from each other. However, the Ve is similar from the soma to the end of the fiber; only the Ve of ST is about 30% larger than the SV.

Figure 3.44C demonstrates the excitation thresholds of B14 for ST (blue symbols) and SV (green symbols) perimodiolar (left) and lateral (right) CIs with biphasic (black unfilled symbols) and pseudo-monophasic (red unfilled symbols) pulses. In the perimodiolar CI (Figure 3.44C left), the ST thresholds are lower than the SV in all status of ANF in both pulse shapes. Considering ANO/CAT = 1 shown with the black dashed line, the excitation thresholds represent CAT sensitivity in all ANF status regardless of pulse shapes, ST and SV stimulating

Die approbierte gedruckte Originalversion dieser Dissertation ist an der TU Wien Bibliothek verfügbar.
The approved original version of this doctoral thesis is available in print at TU Wien Bibliothek.
TU Bibliothek Your knowledge hub WIEN

electrodes except the intact case of ST, which shows ANO sensitivity. The ST thresholds with biphasic pulse need about 24% and 35% less current than SV in the intact and degenerated cases, respectively. By changing the pulse shape to pseudo-monophasic, again, ST thresholds are smaller than SV with 24% and 30% for the intact and both degenerated cases, respectively.

By comparing the biphasic and pseudo-monophasic pulses, the excitation currents become less about 6% in the intact case (for ST and SV) and up to 11% (in the SV case) in degenerated cases when pseudo-monophasic applied.

On the other hand, the lateral CI (Figure 3.44C, right) demonstrates CAT sensitivity in all cases regardless of ANF health status, the position of the stimulating electrodes, and pulse shapes. By applying the biphasic pulse, the ST needs about 14% and 41% less CAT current than the SV in intact and degenerated cases. However, by applying the pseudo-monophasic pulse, the excitation currents in ST are less than SV with 25% and 44% in the intact and both degenerated cases.

Die approbierte gedruckte Originalversion dieser Dissertation ist an der TU Wien Bibliothek verfügbar.
The approved original version of this doctoral thesis is available in print at TU Wien Bibliothek.
TU Bibliothek Your knowledge hub WIEN

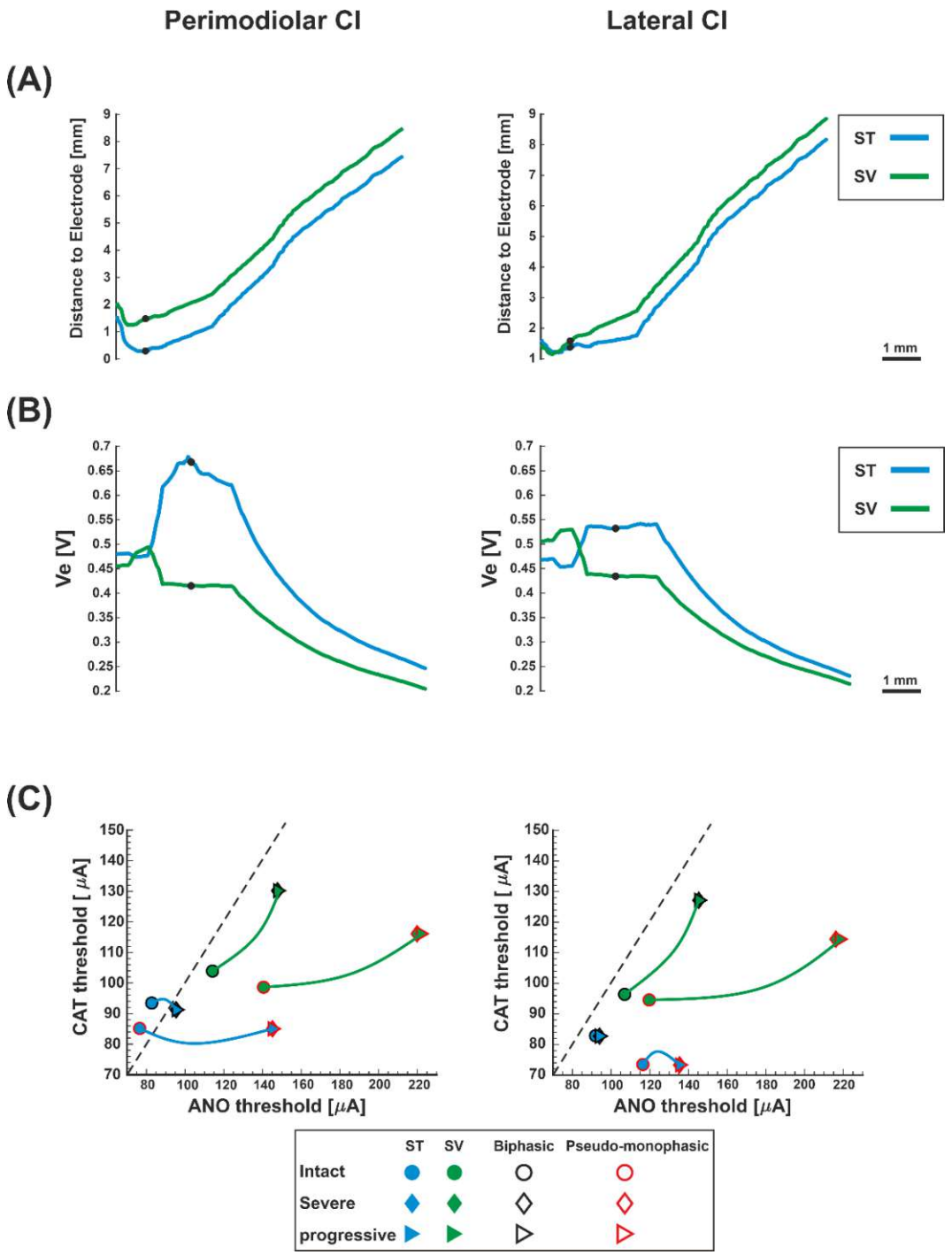

Figure 3.44. Excitation profile of B14. **(A)** Fiber distance to the stimulating electrodes. **(B)** the extracellular voltage Ve versus length of the fiber in ST and SV are shown with blue and green curves, respectively. **(C)** Threshold profiles of B14. The intact (healthy) ANF is displayed as circles, and the degenerated ANF is indicated with diamonds and triangles for severe and progressive cases. The blue and green-filled symbols show thresholds for ST and SV CIs. The black and red unfilled symbols represent biphasic and pseudo-monophasic pulse shapes. Black dashed lines represent the ANO/CAT=1.

Die approbierte gedruckte Originalversion dieser Dissertation ist an der TU Wien Bibliothek verfügbar.
The approved original version of this doctoral thesis is available in print at TU Wien Bibliothek.
TU Bibliothek Your knowledge hub WIEN

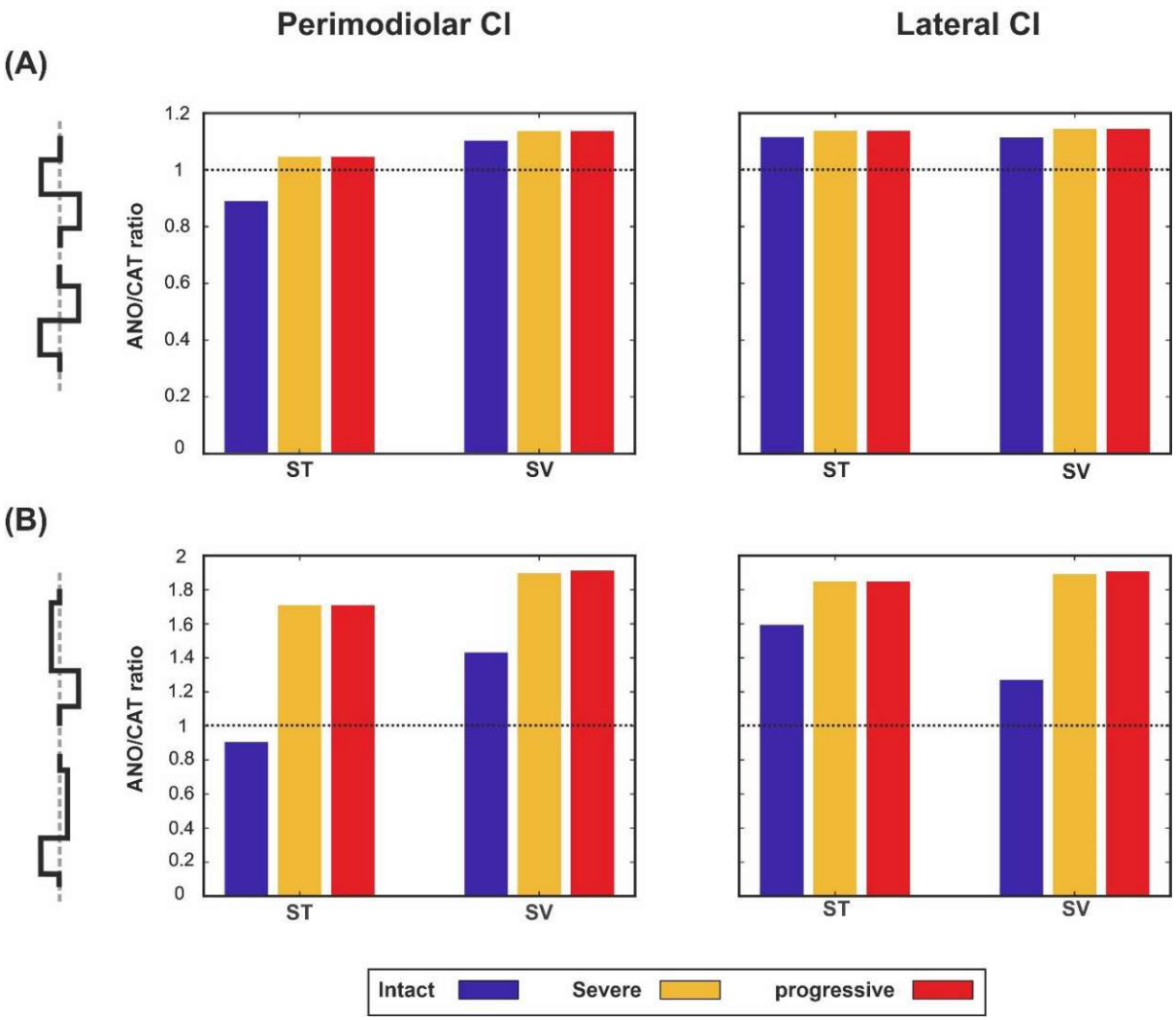

Figure 3.45. Polarity ratios for the perimodiolar (left) and lateral (right) CI arrays for intact and two degeneration levels for ST and SV active electrodes. **(A)** Biphasic pulse and **(B)** pseudo-monophasic pulses stimulated both CI arrays within ST and SV. Threshold ratios are shown for B14. The horizontal dotted lines indicate the polarity ratio ANO/CAT = 1.

Polarity ratios (ANO/CAT) for active electrodes of ST and SV based on perimodiolar and lateral CI arrays are shown in Figure 3.45. By applying biphasic (Figure 3.45A) and pseudo-monophasic (Figure 3.45B) pulses, CAT sensitivity happens in perimodiolar and lateral CI arrays for ST and SV in all ANF status except the intact case of the ST stimulating electrode for the perimodiolar CI. Figure 3.45A demonstrates the polarity ratios are close to one (no difference in polarity ratio between ANF status levels) in all cases regardless of array types and degeneration levels of ANFs in both ST and SV stimulating electrodes. However, applying the pseudo-monophasic pulse makes the polarity ratios more distinguishable between intact and degenerated cases. Overall, by employing pseudo-monophasic pulse, the polarity ratio variations are more significant compared to the biphasic pulse, and an increase of ratio is

Die approbierte gedruckte Originalversion dieser Dissertation ist an der TU Wien Bibliothek verfügbar.
The approved original version of this doctoral thesis is available in print at TU Wien Bibliothek.
TU Bibliothek Your knowledge hub WIEN

observed in degenerated cases in comparison with the intact cases that allow detecting ANF health status better; however, it is challenging to be functional for detecting ANF health status.

Figure 3.46A demonstrates the distance of the TN, B5, to the stimulating electrodes in the ST and SV with the same layout as Figure 3.44. In the perimodiolar array (Figure 3.46A, left), the TN distance to the center of the SV and ST electrodes from the terminal to the soma are almost equivalent, but the distance increased up to 15% in the SV compared to ST in the central parts. However, in the lateral CI, the distance from the terminal to the soma of TN is similar in both ST and SV, but after 0.5 mm away from the terminal, the distance to the SV electrode becomes larger, about 22% compared to the ST.

The Ve of TN, B5, for ST and SV stimulating electrodes with both CI systems is shown in Figure 3.46B. In the perimodiolar and lateral CIs, The Ve value of the terminal part of TN is about 8% larger in the SV than ST. In addition, the peak values of Ve in the SV and ST are about 1 mm and 1.4 mm away from the terminal in the perimodiolar CI. In contrast, in the lateral CI, the maximum value of Ve happens 0.2 mm away from the terminal in SV, but in the ST, the maximum of Ve occur at about 1.4 mm far away from the terminal, which is similar to the perimodiolar CI case (Figure 3.46B, left vs. right blue curve).

Figure 3.46C indicates the excitation thresholds of B5 with the same layout as Figure 3.44C. In the perimodiolar CI (Figure 3.46C, left), by considering ANO/CAT = 1, the excitation thresholds represent CAT sensitivity in all ANF status regardless of pulse shapes and position of the active electrodes in ST and SV. The CAT threshold of the intact case of SV needs about 64% and 71% less current than the ST threshold in biphasic and pseudo-monophasic pulses, respectively. Moreover, the degenerated cases of SV need about 7% and 10% less CAT currents than the ST with biphasic and pseudo-monophasic pulses, respectively.

On the other hand, the lateral CI (Figure 3.46C, right) shows ANO sensitivity for the intact case of the ST with both pulse shapes, whereas the degenerated cases of the ST and all ANF status of the SV represent CAT sensitivity in both pulses. By applying biphasic pulse, the difference between excitation current of the intact case of ST and SV is about 4% which is less in ST. However, the CAT thresholds are about 10% larger in the ST case than SV in the degenerated cases. Moreover, pseudo-monophasic pulse demonstrates a threshold difference between ST and SV with 15% less current in the intact case of the ST. In addition, the CAT thresholds in both degenerated cases are about 10% larger in the ST than SV, which is similar to the biphasic pulse.

Overall, both CI arrays demonstrate that stimulating the SV electrode requires less current than the ST electrode in both degenerated cases, which may impact of ANF pathway.

Die approbierte gedruckte Originalversion dieser Dissertation ist an der TU Wien Bibliothek verfügbar.
The approved original version of this doctoral thesis is available in print at TU Wien Bibliothek.
TU Bibliothek Your knowledge hub WIEN

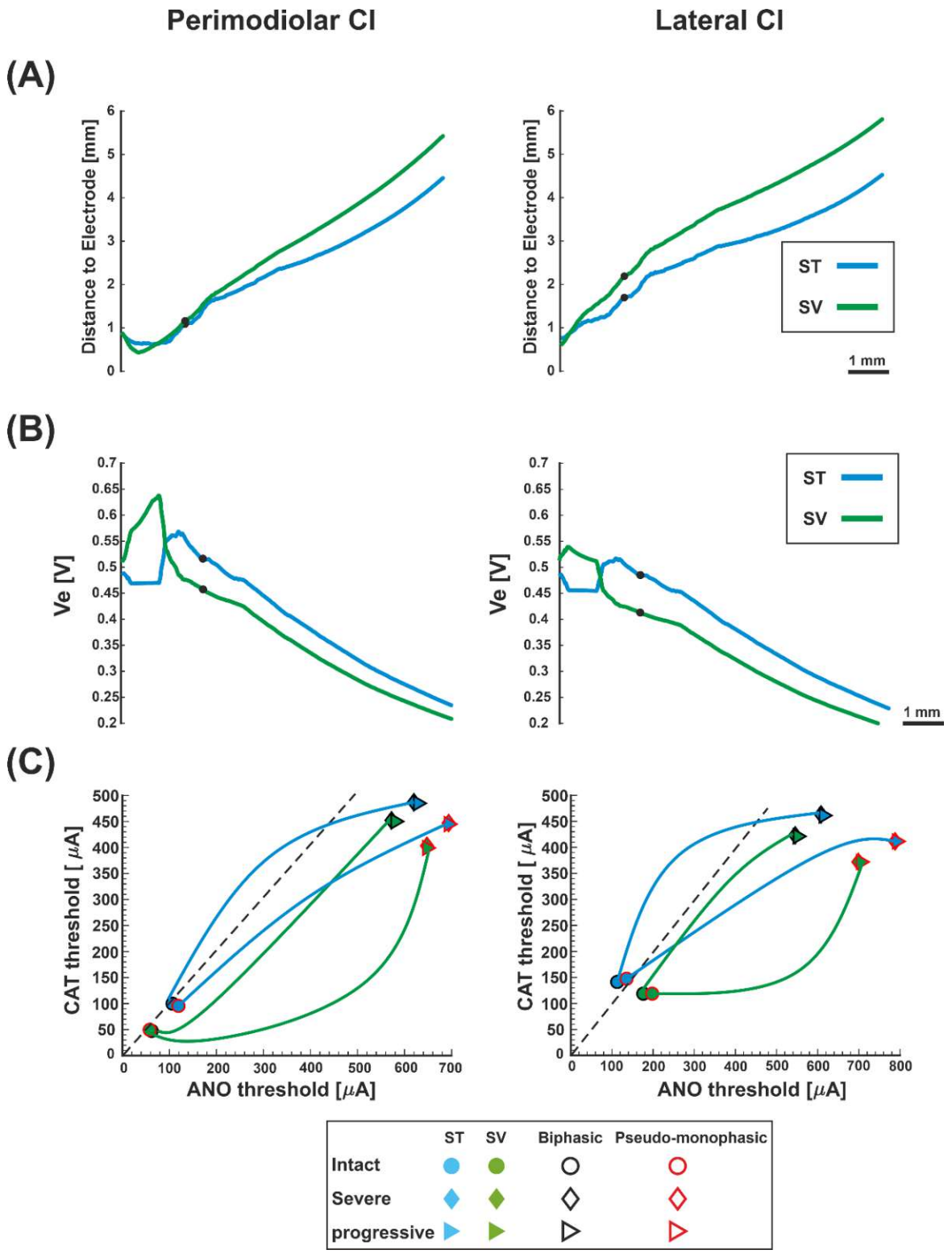

Figure 3.46. Excitation profile of B5 for perimodiolar CI (left) and lateral CI (right). Layout as in Figure 3.44.

Die approbierte gedruckte Originalversion dieser Dissertation ist an der TU Wien Bibliothek verfügbar.
The approved original version of this doctoral thesis is available in print at TU Wien Bibliothek.

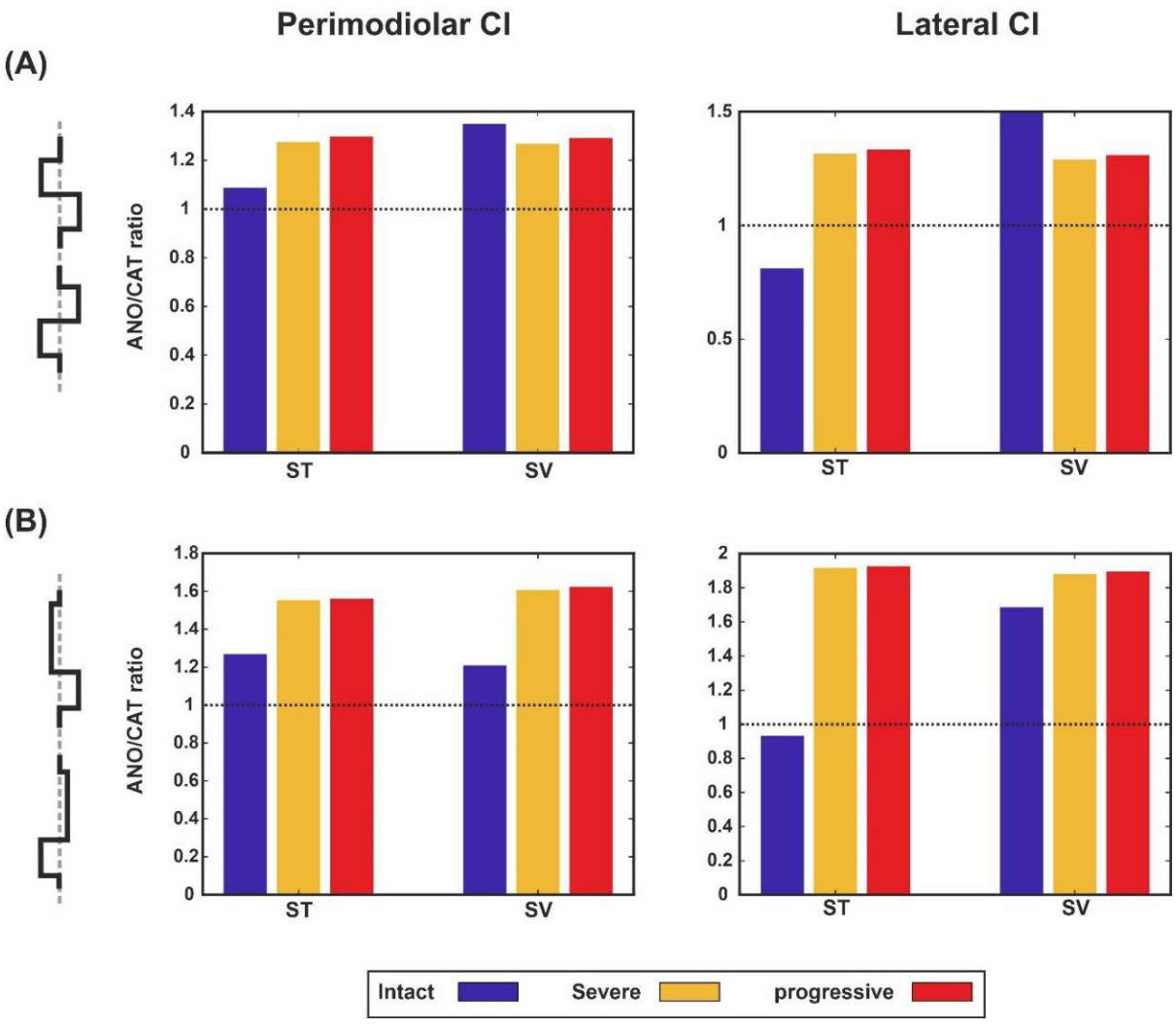

Figure 3.47. Polarity ratios are demonstrated for B5. Layout as in Figure 3.45.

Figure 3.47 represents polarity ratios of TN (B5) for ST and SV stimulating electrodes with biphasic and pseudo-monophasic pulses for the perimodiolar CI (left panels) and lateral CI (right panels). By utilizing biphasic (Figure 3.47A) and pseudo-monophasic (Figure 3.47B) pulses, CAT sensitivity happens in perimodiolar and lateral CI arrays for ST and SV in all ANF status except the intact case of the ST stimulating electrode for the lateral CI.

Figure 3.47A demonstrates the polarity ratios with biphasic pulse and the ratios almost similar in both ST and SV stimulating electrodes for both arrays. In addition, by changing the pulse to pseudo-monophasic (Figure 3.47B), the polarity ratios are almost comparable between both arrays, and by comparing to the biphasic pulse (Figure 3.47A), the ratio trends are similar but with an about 20% higher ratio.

Die approbierte gedruckte Originalversion dieser Dissertation ist an der TU Wien Bibliothek verfügbar.
The approved original version of this doctoral thesis is available in print at TU Wien Bibliothek.
TU Bibliothek Your knowledge hub WIEN

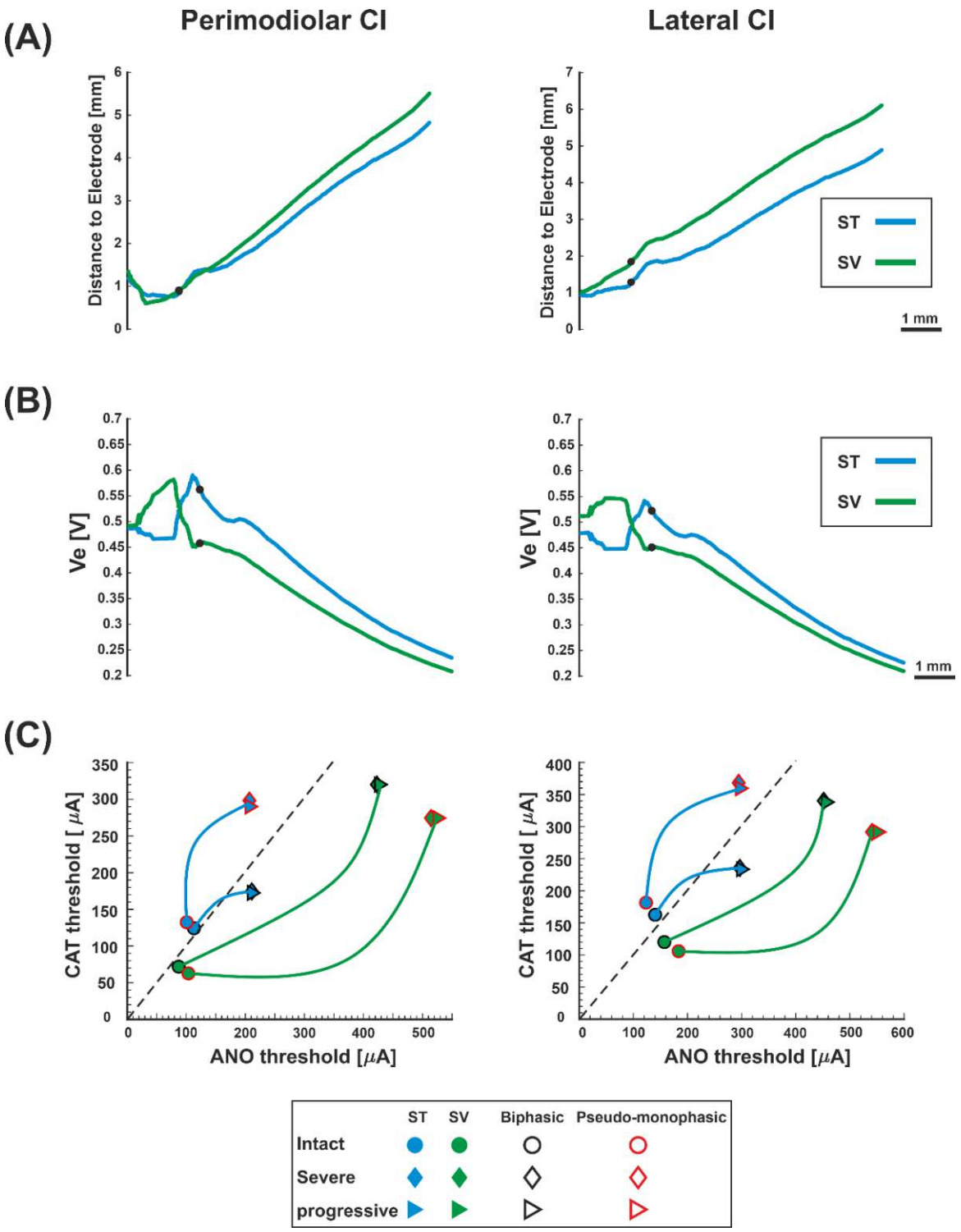

Figure 3.48. Threshold profiles of B3 for perimodiolar CI (left) and lateral CI (right). Layout as in Figure 3.44.

Die approbierte gedruckte Originalversion dieser Dissertation ist an der TU Wien Bibliothek verfügbar.
The approved original version of this doctoral thesis is available in print at TU Wien Bibliothek.

Figure 3.48A displays the distance of the B3 to the stimulating electrodes in the ST and SV with the same layout as Figure 3.44. In the perimodiolar array (Figure 3.48A, left), the TN distance to the center of the SV and ST electrodes from the terminal to the soma is almost comparable, but the distance increased up to 10% in the SV compared to ST in the central parts. However, in the lateral CI (Figure 3.48A, right), the ST and SV electrodes distance of the terminal of TN are similar, but the distance of SV electrode increased about 15%, 35%, and 27% in the peripheral, soma, and central regions, respectively, in compared with ST electrode.

The Ve of TN, B3, for ST and SV stimulating electrodes with perimodiolar and lateral CIs is shown in Figure 3.48B. In the perimodiolar CI, the Ve value of the terminal part of TN is similar in both ST and SV stimulating electrodes (Figure 3.48B, left). In addition, the maximum Ve happens with the same vale about 0.59 V in both stimulating electrodes at 1.6 mm in the ST case and 1.1 mm in the SV case far away from the terminal. On the other hand, in the lateral CI (Figure 3.48B, right), the Ve of the stimulating SV electrode is about 8% larger than ST at the terminal of TN; however, the peak value of Ve is about 0.55 V in both stimulating electrodes and occur at 1.6 mm in ST case and about 0.8 mm in SV case far away from the terminal.

Figure 3.48C shows the excitation thresholds of B3 with the same layout as Figure 3.44C. In the perimodiolar CI (Figure 3.48C, left), by taking ANO/CAT = 1, the excitation thresholds represent CAT sensitivity in all ANF status in the SV stimulating electrode regardless of pulse shapes. However, the ST stimulating electrode demonstrates ANO sensitivity in the intact case with biphasic pulse and all ANF statuses by applying pseudo-monophasic pulse.

Surprisingly, the excitation threshold of the intact case with the SV electrode demands 47% less current than the ST electrode in both pulses. However, in the degenerated cases, the stimulating ST electrode requires less current than the SV electrode with 59% and 28% for biphasic and pseudo-monophasic pulses, respectively.

On the other hand, the lateral CI (Figure 3.48C, right) demonstrates the CAT sensitivity in the SV regardless of pulse shape and ANF status levels, whereas the CAT sensitivity occurs in the ST only in the degenerated cases for the biphasic pulse. The threshold excitation polarity of the lateral CI is comparable to the perimodiolar CI. However, the SV needs about 16% less current than the ST in the intact case regardless of the pulse shapes.

Although, by applying the biphasic pulse, the SV requires about 36% higher current compared to the ST, but surprisingly, by changing pulse shape to pseudo-monophasic, the threshold difference between ST and SV stimulating electrodes is less than 2% that means the excitation thresholds by ST and SV stimulating electrodes are almost similar but with different polarity (ANO for ST, CAT for SV).

Die approbierte gedruckte Originalversion dieser Dissertation ist an der TU Wien Bibliothek verfügbar.
The approved original version of this doctoral thesis is available in print at TU Wien Bibliothek.
TU Bibliothek Your knowledge hub WIEN

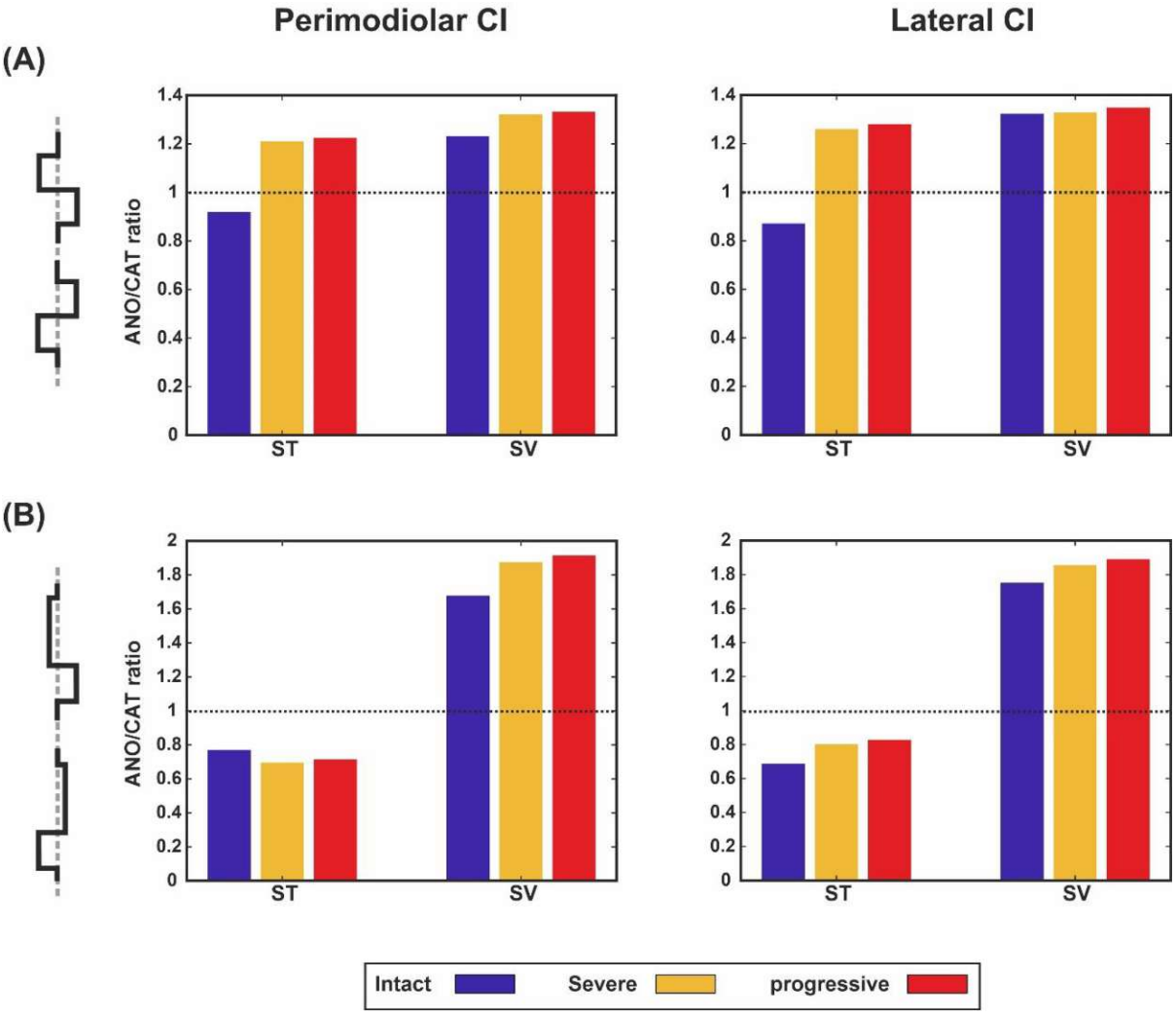

Figure 3.49. Polarity ratios are shown for B3. Layout as in Figure 3.45.

Figure 3.49 demonstrates polarity ratios of TN (B3) for ST and SV stimulating electrodes with biphasic and pseudo-monophasic pulses for the perimodiolar CI (left panels) and lateral CI (right panels).

Using biphasic (Figure 3.49A) and pseudo-monophasic (Figure 3.49B) pulses, CAT sensitivity happens in perimodiolar and lateral CI arrays for ST and SV in all ANF status except the intact case of the ST stimulating electrode for both CI systems. The polarity ratios are almost equivalent between the perimodiolar and lateral arrays when the biphasic is applied (Figure 3.49A, right vs. left).

Figure 3.49B shows the polarity ratios with pseudo-monophasic pulse and indicates the ANO sensitivity in ST stimulating electrodes regardless of ANF status and array systems; however, in contrast, the ST stimulating electrodes display CAT sensitivity in all ANF status and both CI arrays.

Die approbierte gedruckte Originalversion dieser Dissertation ist an der TU Wien Bibliothek verfügbar.
The approved original version of this doctoral thesis is available in print at TU Wien Bibliothek.
TU Bibliothek Your knowledge hub WIEN

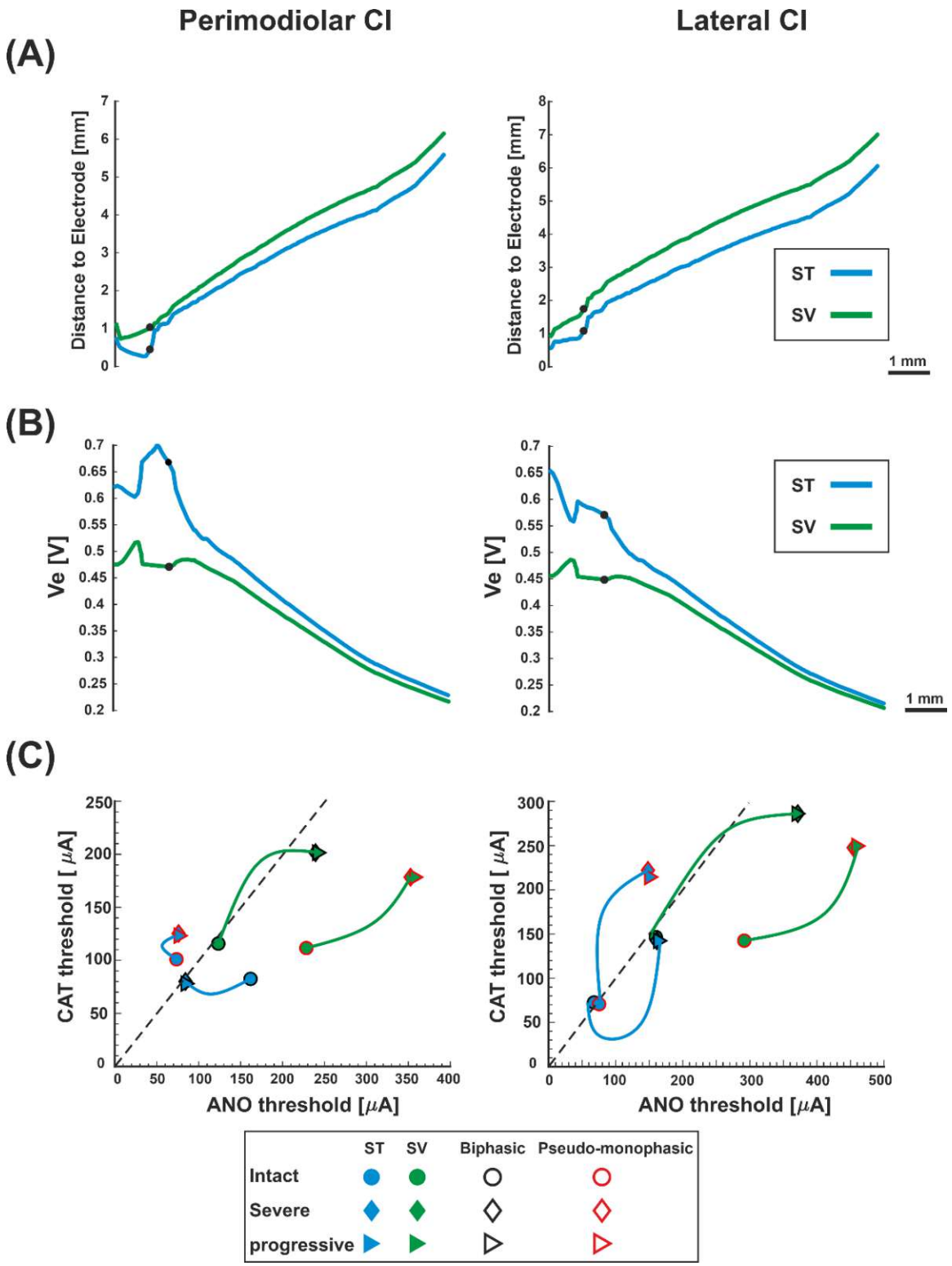

Figure 3.50. Threshold profiles of M9 for perimodiolar CI (left) and lateral CI (right). Layout as in Figure 3.44.

Die approbierte gedruckte Originalversion dieser Dissertation ist an der TU Wien Bibliothek verfügbar.
The approved original version of this doctoral thesis is available in print at TU Wien Bibliothek.

Figure 3.50A displays the distance of the TN, M9, to the stimulating electrodes in the ST and SV with the same layout as Figure 3.44. In the perimodiolar array (Figure 3.50A, left), the distance of the terminal of TN to the center of the SV stimulating electrode is about 40% larger than the ST electrode. In addition, the TN distance to SV electrodes increases up to 80% at the soma and 32% in the central parts compared to ST. In contrast, in the lateral CI (Figure 3.50A, right), the distance of TN's terminal to the center of the SV electrode is about 45% larger than the ST stimulating electrode. This distance difference between ST and SV is noticeable through the whole fiber, which the SV case is larger than the ST case with 45% at the soma and 15% at the central parts.

The Ve of TN, M9, for ST and SV stimulating electrodes with perimodiolar and lateral CIs, is shown in Figure 3.50B. In the perimodiolar CI (Figure 3.50B, left), the Ve value of the terminal of TN in the ST stimulating electrode is about 27% higher than the SV stimulating electrode. In addition, the maximum Ve happens with a value of about 0.7 V in the ST stimulating electrode at 1 mm far away from the terminal; however, in the SV case, the highest Ve appears about 0.5 mm away from the terminal with a value of 0.52 V. In contrast, in the lateral CI (Figure 3.50B, right), the Ve of the terminal for the ST electrode is larger than the SV electrode with the difference about 33%. In addition, the maximum Ve of the ST electrode happens at the terminal with 0.65 V whereas, for the SV stimulating electrode occurs 0.5 mm far away from the terminal with about 0.46 V.

Figure 3.50C indicates the excitation thresholds of M9 with the same layout as Figure 3.44C. In the perimodiolar CI (Figure 3.50, left), concerning ANO/CAT = 1, the excitation thresholds represent CAT sensitivity with the biphasic pulse in the ST and SV stimulating electrode regardless of ANF health status. However, by applying pseudo-monophasic pulse, the polarity sensitivity is opposite between ST and SV stimulating electrodes regardless of the ANF health status (ANO sensitivity in ST vs. CAT sensitivity in SV). Moreover, the ST stimulating electrode needs about 33% and 86% less current compared to SV stimulating electrode for the intact and degenerated cases, respectively with the biphasic pulse, whereas applying pseudo-monophasic pulse, the ST stimulating electrode needs about 40% and 80% less current compared to SV stimulating electrode for the intact and degenerated cases, respectively.

On the other hand, in the lateral CI (Figure 3.50C, right), the SV stimulating electrode represents CAT sensitivity regardless of pulse shapes and ANF health status. However, the ST stimulating electrode shows CAT sensitivity only in the degenerated cases for the biphasic pulse and the intact case for the pseudo-monophasic pulse. The excitation threshold of the intact cases in the ST stimulating electrode requires about 70% less current than the SV electrodes for both pulse shapes. In addition, the excitation thresholds of degenerated cases with ST

Die approbierte gedruckte Originalversion dieser Dissertation ist an der TU Wien Bibliothek verfügbar.
The approved original version of this doctoral thesis is available in print at TU Wien Bibliothek.
TU Bibliothek Your knowledge hub WIEN

electrodes need about 67% and 50% less currents than SV electrodes with biphasic and pseudo-monophasic pulses, respectively.

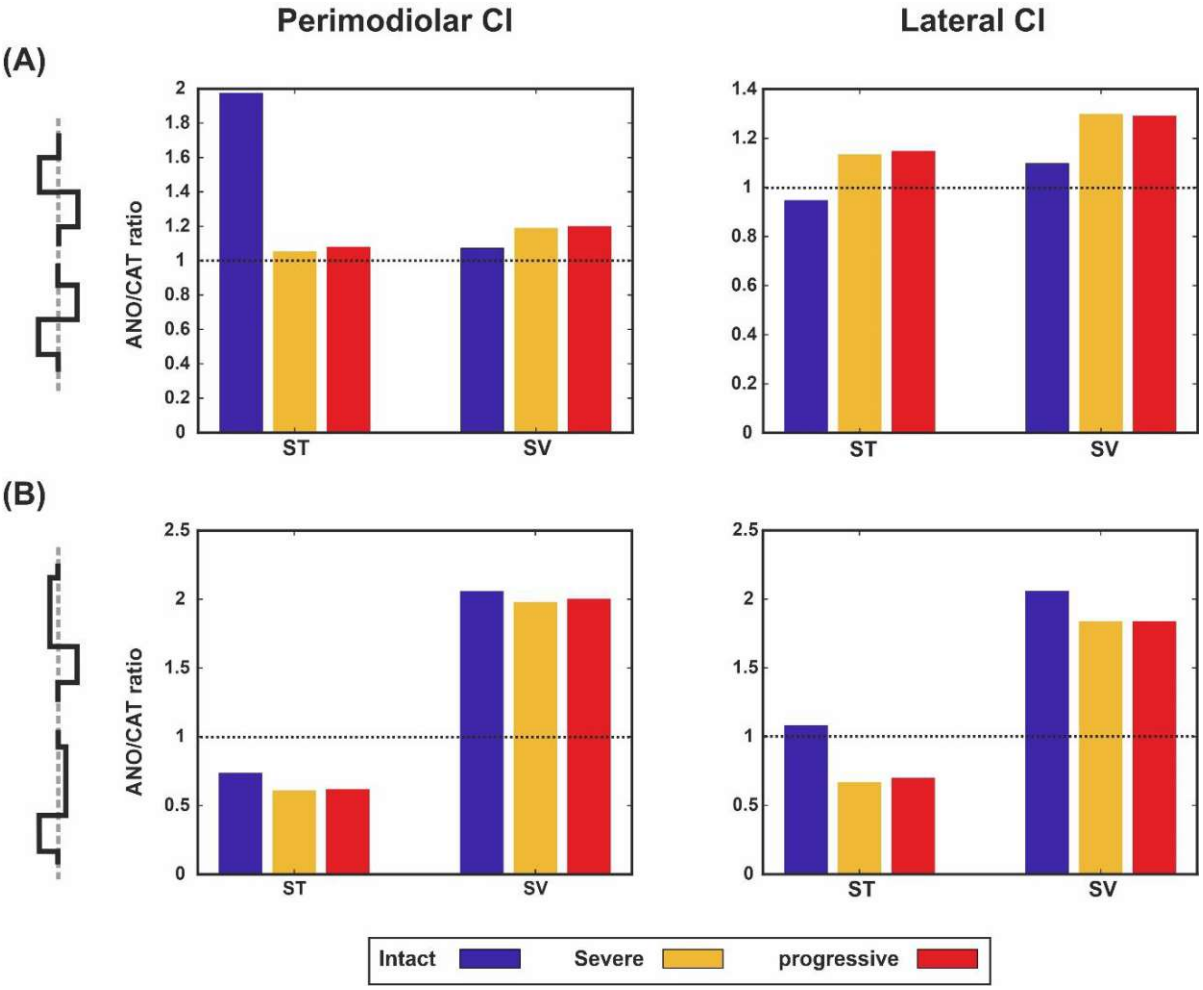

Figure 3.51. Polarity ratios are shown for M9. Layout as in Figure 3.45.

Figure 3.51 indicates polarity ratios of TN (M9) for ST and SV stimulating electrodes with the same layout as Figure 3.45. By applying biphasic pulse (Figure 3.51A), CAT sensitivity appears in all cases in both CI arrays except the intact case of the ST stimulating electrode in the lateral CI.

All ratios are almost similar between CI systems except the intact case of ST for the perimodiolar CI, which is almost doubled. In the perimodiolar CI (Figure 3.51B, left), when the pseudo-monophasic is applied, ANO sensitivity occurs in all ANF status for the ST stimulating electrodes, and the inversed polarity appears for the SV stimulating electrode (CAT sensitivity). In contrast, in the lateral case (Figure 3.51B, right), ANO sensitivity happens only in the degenerated cases of the ST stimulating electrode.

Die approbierte gedruckte Originalversion dieser Dissertation ist an der TU Wien Bibliothek verfügbar.
The approved original version of this doctoral thesis is available in print at TU Wien Bibliothek.
TU Bibliothek Your knowledge hub WIEN

Perimodiolar CI		Biphasic pulse				Pseudo-monophasic pulse			
		ANO [µA]		CAT [µA]		ANO [µA]		CAT [µA]	
ANFs status	TNs	ST	SV	ST	SV	ST	SV	ST	SV
Intact	B14	92	107	83	96	117	120	73	94
	B5	114	177	141	118	137	199	147	118
	B3	141	158	162	119	124	184	181	105
	M9	68	160	72	146	76	292	70	142
Intermediate	B14	94	145	83	127	135	216	73	114
	B5	608	545	463	423	788	699	412	372
	B3	297	452	236	340	295	541	368	292
	M9	161	371	142	286	148	455	222	248
Progressive	B14	94	145	83	127	135	218	73	114
	B5	608	545	463	423	792	705	412	372
	B3	297	452	236	340	297	550	360	292
	M9	161	371	142	286	150	459	215	250

Table 3.3. Excitation currents of TNs in both polarities for different degeneration levels for investigated scala tympani (ST) and scala vestibuli (SV) electrodes for perimodiolar array system with biphasic and pseudo-monophasic pulses.

Die approbierte gedruckte Originalversion dieser Dissertation ist an der TU Wien Bibliothek verfügbar.
The approved original version of this doctoral thesis is available in print at TU Wien Bibliothek.
TU Bibliothek Your knowledge hub WIEN

lateral CI		Biphasic pulse				Pseudo-monophasic pulse			
		ANO [µA]		CAT [µA]		ANO [µA]		CAT [µA]	
ANFs status	**TNs**	**ST**	**SV**	**ST**	**SV**	**ST**	**SV**	**ST**	**SV**
Intact	**B14**	83	114	93	104	77	141	85	99
	B5	108	63	99	47	120	59	95	49
	B3	114	88	124	71	101	104	132	62
	M9	162	124	82	116	74	229	101	111
Intermediate	**B14**	95	148	91	130	145	220	85	116
	B5	620	572	487	452	694	648	447	403
	B3	211	423	175	320	207	514	298	275
	M9	84	293	80	202	76	353	125	178
Progressive	**B14**	95	148	91	130	145	222	85	116
	B5	628	580	485	450	694	648	445	399
	B3	211	426	175	320	207	525	290	275
	M9	84	241	78	202	76	357	123	178

Table 3.4. Excitation currents of TNs in both polarities for different degeneration levels for investigated scala tympani (ST) and scala vestibuli (SV) electrodes for lateral array system with biphasic and pseudo-monophasic pulses.

Die approbierte gedruckte Originalversion dieser Dissertation ist an der TU Wien Bibliothek verfügbar.
The approved original version of this doctoral thesis is available in print at TU Wien Bibliothek.
TU WIEN Bibliothek Your knowledge hub

Die approbierte gedruckte Originalversion dieser Dissertation ist an der TU Wien Bibliothek verfügbar.
The approved original version of this doctoral thesis is available in print at TU Wien Bibliothek.
TU Bibliothek Your knowledge hub WIEN

Chapter 4

Discussion

4.1 Degeneration pattern of human cochlear nerves

Only a small number of human subject studies were performed on the morphometry of degenerated ANFs. Analysis of the signaling of the human ANFs is of great interest to pathophysiology and a better understanding of CI stimulation. Due to limitations of human in vivo studies, detailed computational models enable understanding the neural signaling in the degenerated auditory system and CIs. In the first part of this study, four human cochleae with normal hearing and different hearing loss levels were investigated, and their ANFs were evaluated concerning diameters and myelination thickness of their peripheral axons. The extracted morphometric data were used as input in a multi-compartment model to compare neural signal conduction in normal and degenerated TNs for synaptic excitation from IHCs. In addition, two CI systems were added to the FE model to investigate the impact of peripheral axon degeneration on signaling during extracellular stimulation.

4.1.1 Variation in peripheral axon diameter

Unimodal distribution in peripheral of ANF diameters of mammalian species such as cat, guinea pig, and monkey were reported (Gacek and Rasmussen, 1961; Arnesen and Osen, 1978; Friede, 1984; Gleich and Wilson, 1993). Similar to animals, Spoendlin and Schrott reported unimodal diameter distribution for humans with normal hearing (Spoendlin and Schrott, 1989). The group has reported the same range of diameter for three cochlear regions, basal, middle, and apical. They suggested this similarity results from the almost similar peripheral length of human ANFs in all three regions compared to other species. The current study shows a unimodal distribution in normal hearing specimen vs. multimodal distribution for hearing loss cases. Our reported diameter range for the normal hearing case is in agreement with our recent study in all three cochlear regions (Potrusil et al., 2020).

4.1.2 Appearance of small fibers in hearing loss specimens and consequences

A massive number of fibers with PD < 1 µm was found in subjects with high levels of hearing loss and poor speech discriminations (Spoendlin and Schrott, 1989). It was found similar fiber ranges in our hearing loss cases and extremely thin fibers (smaller than 0.5 µm) in severe and profound cases. Peripheral axon diameter variation leads to changed spike conduction velocity that may affect speech discrimination (Rattay and Motz, 1987; Rattay et al., 2013). According to our modeling study, the spike conductance of such thin peripheral axon diameter fibers with G-ratio = 0.6 (about mean value of G-ratio) resulted in loss of signals and thus in a significantly reduced axonal spiking probability, e.g., 10% (PD = 0.4 µm, Figure 3.12D); jitter and spike latencies increase versus control up to 0.4 and 1 ms, respectively (Figure 3.14 and Table 3.1). Such high delays in spike patterns (see Figure 3.14B vs. C) are expected to affect the temporal fine structure in the neural pattern of the cochlear nerve and, consequently, auditory perception (Rattay and Lutter, 1997). These extended latencies and jitters, calculated for intracellular stimulation to mimic the synaptic excitation, affect also the neural status between the ears and by larger variations in interaural time differences they contribute to poor sound localization and speech discrimination, especially in a noisy environment (Zwislocki and Feldman, 1956; Rosen, 1992; Saberi and Perrott, 1999; Bernstein and Trahiotis, 2015).

4.1.3 Degeneration level affects cochlear implant outcomes

Techniques such as electrocochleography, polarity sensitivity, electrically evoked compound action potential (eCAP), and eCAP responses to changing interphase gap are used to evaluate the residual neural health (Santarelli et al., 2008; Garadat et al., 2012; Long et al., 2014; Pfingst et al., 2015; Hughes et al., 2018; Shearer et al., 2018; He et al., 2020). A recent study on lateral and perimodiolar CI systems reported a lower eCAP threshold in the apical region (Lee et al., 2019). Although their findings are in agreement with some studies (Cohen et al., 2001; Parkinson et al., 2002), others found the opposite result for the apical region (Polak et al., 2004; Brill et al., 2009; Van de Heyning et al., 2016). Table 3.2 demonstrates that both higher and lower thresholds in the apical turn are possible, but the correlation depends on the cochlear geometry, electrode position, neural status, and degeneration level of the ANFs.

In a study of 10 cats, better localized neural excitation for electrodes close to the modiolus compared with the lateral wall was reported (Shepherd et al., 1993). Similar investigations were performed for human subjects that suggest lower threshold, better localization of the nerve

Die approbierte gedruckte Originalversion dieser Dissertation ist an der TU Wien Bibliothek verfügbar.
The approved original version of this doctoral thesis is available in print at TU Wien Bibliothek.
TU Bibliothek Your knowledge hub WIEN

stimulations, broader dynamic range, and less channel interactions are possible for electrode array systems close to modiolus compared with those close to the lateral wall of ST (Cohen et al., 2001; Donaldson et al., 2001; Tykocinski et al., 2001; Saunders et al., 2002; Hughes and Abbas, 2006; Lee et al., 2019). In agreement, it was showed lower thresholds for the TNs in most investigated electrodes located close to modiolus compared with the lateral array (Table 3.2). According to our findings, insignificant channel interaction (concerning the tonotopic principle) occurred for lateral CI and no interaction for perimodiolar array in case of fibers with PD = 2 µm (Figure 3.17, upper panel), whereas with severe levels of degenerations, a lateral CI shows poorer focal stimulation efficiency compared with a perimodiolar CI (Figure 3.17, middle and lower panels).

4.1.4 Clinical implications

In studies related to cochlear insults such as noise and drug exposure, it was reported that soma and axonal degeneration were less and slower than the loss of IHCs and peripheral axons (Johnsson, 1974; Johnsson and Hawkins, 1976; Hinojosa et al., 2001). On the other hand, in a series of histological studies by Spoendlin and Schrott (1988; 1989; 1990), they found that the number of peripheral axons highly correlated with the number of somata in hearing loss as well as normal-hearing specimens. These findings suggest that simply excluding the peripheral axon is no general rule, and the type of degeneration is highly dependent on the origin of the impairment. However, recent valuable models in computational studies mostly eliminate the peripheral part of the ANFs to simulate the degeneration of ANFs (Briaire and Frijns, 2006; Snel-Bongers et al., 2013; Kalkman et al., 2014). This study may shed more light on the impact of ANF degeneration on neural signaling, demonstrating that more realistic models should be considered for improving CI performance.

4.1.5 Modeling details and limitations

The goal of this study was to find trends in the excitability of human ANFs when their peripheral axons are degenerated. Limitations of this study were a small number of available human cochleae, missing geometric parameters such as internode lengths, positions, and surfaces of nodes of Ranvier, lengths of pre-somatic sections, as well as complete individual data sets for every ANF concerning the connected soma and axon. Due to lack of these data, for all ANFs, it was simply assumed constant values for the length of the non-myelinated pre-somatic section (100 µm), the diameters of the spherical soma (20 µm) and the axon (4 µm) independent of the degree of degeneration. Although in a previous study, a quite constant

Die approbierte gedruckte Originalversion dieser Dissertation ist an der TU Wien Bibliothek verfügbar.
The approved original version of this doctoral thesis is available in print at TU Wien Bibliothek.
TU Bibliothek Your knowledge hub WIEN

diameter ratio of 2 was found for healthy subjects for (central axon diameter)/(peripheral axon diameter) in the whole cochlea (Rattay et al., 2013). The vagueness on these post-dendritic data affects predictions such as "Is a spike elicited in the peripheral axon, soma or central axon?".

Other points of interest were the choice of the membrane model and the estimate of spiking probability. Biophysically based neuronal membrane models typically follow the pioneers Hodgkin and Huxley to quantify the ionic transmembrane currents via gating probabilities (Rattay et al., 2003). This method uses deterministic probabilities, which means running a model several times under the same conditions always produces exactly the same results. As spikes simulated with this method will not create any jitter seen in experiments, it was added a noise term which can be interpreted as current fluctuations in the ANF (Hochmair-Desoyer et al., 1984; Rattay, 2000). Although other models for human ANF membranes are published, a review (Bachmaier et al., 2019) and some tests showed that Rattay modified the Hodgkin Huxley model replicates many features known from experiments (Motz and Rattay, 1986; Rattay et al., 2013; Rattay and Danner, 2014). However, features not included in this simple membrane model are, e.g., accommodation effects during repetitive stimulation (Boulet et al., 2016) or the impact of I_h currents, which influence excitation during hyperpolarization phases (Hossain et al., 2005; Negm and Bruce, 2014).

Despite the mentioned shortcomings, combining the FE approach with our compartment model is in good quantitative agreement with experimental CI data. Calculated threshold current range for the active electrode was from 40 to 300 µA depending on the electrode array system and level of degeneration. This range is in agreement with clinical data from (Kawano et al., 1998; van den Honert and Kelsall, 2007; Long et al., 2014). Additionally, the intracochlear potential decrement along a CI array of the standard conductivity parameters was in line with clinical data from (Tang et al., 2011; Kalkman et al., 2014).

4.1.6 Conclusion

Degeneration models of the human auditory system are of great concern for better understanding and recognizing influence factors to improve the functionality of the CIs, which provides better sound perception for CI recipients. In the first part of this study, degeneration patterns of the peripheral part of human ANFs investigations were accomplished based on hearing loss levels of several human temporal bones. In addition, synaptic excitation via IHCs and the excitation properties of electrical potential distribution induced by two CI were analyzed. The main findings suggested:

Die approbierte gedruckte Originalversion dieser Dissertation ist an der TU Wien Bibliothek verfügbar.
The approved original version of this doctoral thesis is available in print at TU Wien Bibliothek.
TU Bibliothek Your knowledge hub WIEN

I. The unimodal distribution of control peripheral axon diameters becomes multimodal for hearing loss cases; a group of thin peripheral axon fibers with diameters between 0.3 and 1 µm with a peak at 0.5 µm appeared.

II. Postsynaptic currents from IHCs excite such thin peripheral axon fibers easier and earlier than under control conditions. However, this advantage is lost as their conduction velocity decreases proportionally with the diameter and causes increased spike latency and jitter in soma and central axon. Firing probability reduces through the soma passage due to the low intracellular current flow in thin peripheral axon fibers during spiking.

III. Compared with peripheral axon diameter, variations in myelination thickness have a small impact on spiking performance.

IV. Contrary to synaptic excitation, CIs cause several spike initiation sites in peripheral axon, soma region, and central axon; moreover, fiber excitability reduces with fiber diameter. In a few cases, where weak stimuli elicit spikes of a TN in the central axon, peripheral axon diameter reduction has no effect. However, in many cases, a spike in a TN is first initiated in peripheral axon, and consequently, peripheral axon degeneration demands an increase in threshold currents.

V. Threshold currents of a TN and co-stimulation of degenerated ANFs in other frequency regions depend on the electrode position, including its distance to the outer wall, the cochlear turn, and the three-dimensional pathway of the TN.

Die approbierte gedruckte Originalversion dieser Dissertation ist an der TU Wien Bibliothek verfügbar.
The approved original version of this doctoral thesis is available in print at TU Wien Bibliothek.
TU Bibliothek Your knowledge hub WIEN

4.2 Impact different parameters on threshold current and polarity sensitivity

Neural health is of great interest to determine individual degeneration patterns for improving speech perception in CI recipients. Therefore, in recent years, several studies tried to identify and quantify neural survival in CI users. Among all proposed techniques, polarity sensitivity is a promising way to evaluate the neural status of ANFs in CI users. Nevertheless, investigating neural health based on polarity sensitivity is a challenging and complicated task that involves various parameters, and the outcomes of many studies show contradictory results of polarity sensitivity behavior. In this study, the computational investigations benefit from an accurate three-dimensional finite element model of a human cochlea with realistic human ANFs and determined ANFs degeneration pattern of peripheral part with a diminishing of peripheral axon diameter and myelination thickness based on degeneration levels. In order to see how different parameters may impact the polarity sensitivity behavior of ANFs, it was investigated polarity behavior under the application of symmetric and asymmetric pulse shapes, monopolar and multipolar CI stimulation strategies, and a perimodiolar and lateral CI array system.

Our main findings: (1) AP initiation sites occurred mainly in the peripheral site in the lateral system regardless of stimulation strategies, pulse polarities, pulse shapes, cochlear turns, and ANF degeneration levels. However, in the perimodiolar system, AP initiation sites varied between peripheral and central processes depending on stimulation strategies, pulse shapes, and pulse polarities. (2) In perimodiolar array, clusters formed in threshold values based on cochlear turns and degeneration levels for multipolar strategies only when asymmetric pulses were applied. (3) In the perimodiolar array, a declining trend in polarity ratio (ANO threshold / CAT threshold) with multipolar strategies was observed between intact or slight degenerated cases and more severe degenerated cases. Whereas, in the lateral array, CAT sensitivity was noticed for intact and less degenerated cases and ANO sensitivity for cases with high degrees of degeneration. The results suggest that a combination of asymmetric pulse shapes, focusing more on multipolar stimulation strategies, as well as considering the distances to the modiolus wall allows us to distinguish the degeneration patterns of ANFs across the cochlea.

4.2.1 Effect of pulse shape

Biphasic symmetric charge balance pulse is widely used as a standard pulse shape to stimulate the surviving ANFs in CIs. According to numerous clinical studies, pulse shape is a critical factor for studying neural status (Undurraga et al., 2010; Bahmer and Baumann, 2012a, 2012b,

Die approbierte gedruckte Originalversion dieser Dissertation ist an der TU Wien Bibliothek verfügbar.
The approved original version of this doctoral thesis is available in print at TU Wien Bibliothek.
TU Bibliothek Your knowledge hub WIEN

2013; Hughes et al., 2018; Luo et al., 2020). In consistent with several clinical studies, which reported that asymmetric pulse shapes are more effective than symmetric biphasic pulse for evaluating polarity sensitivity in CI users (Macherey et al., 2006, 2008, 2017; Carlyon et al., 2013; Guérit et al., 2018; Jahn and Arenberg, 2019b), presented results showed that when a symmetric biphasic pulse is applied, recognition of peripheral changes based on polarity sensitivity was not feasible. It was found threshold variations, and consequently, polarity sensitivity between degeneration levels could not be detected with symmetric biphasic pulses. As a symmetric biphasic pulse consists of phases with equal amplitude and duration but opposite polarities, the contribution of the extracellular gradient is almost the same for both phases; consequently, it may not be possible to estimate which polarity affects the ANFs mainly.

In agreement with the presented results, several studies reported that symmetric biphasic pulses did not provide much evidence for polarity sensitivity (Undurraga et al., 2013; Guérit et al., 2018; Hughes et al., 2018; Xu et al., 2020). In addition, Spritzer groups found opposite results of polarity, which was in consistent with (Macherey et al., 2006), and also, they could not find polarity sensitivity for peak electrode locations (Spitzer and Hughes, 2017; Spitzer et al., 2019). They suggested that using symmetric biphasic pulse is not an excellent choice to study polarity sensitivity (Spitzer, Choi and Hughes, 2019). In line with findings by Undurraga, who reported the same ANO and CAT threshold detection using biphasic pulse (Undurraga *et al.*, 2013), it was found ANO/CAT ratios mostly close to one in perimodiolar array when a biphasic pulse was applied to the active electrodes.

In contrast to symmetric pulses, several studies demonstrated promising results in polarity investigations by using asymmetric pulse shapes, e.g., pseudo-monophasic and triphasic (Macherey et al., 2006, 2008, 2017; Undurraga et al., 2013; Carlyon et al., 2013, 2018; Bahmer et al., 2017; Mesnildrey et al., 2017; Jahn and Arenberg, 2019b). However, some of these studies could not provide direct evidence to prove the role of the polarity effect in estimating neural health, which might result from various factors such as stimulation strategy and CI systems.

Despite using triphasic pulse, Carlyon and Jahn groups (Carlyon et al., 2018; Jahn and Arenberg, 2019b) reported that up to 70% of investigated electrodes showed ANO sensitivity and could not prove polarity behavior as an indicator for estimating neural survival. Similar to their results, it was found more ANO sensitivity using asymmetric pulses, such as pseudo-monophasic and triphasic pulses, in the perimodiolar array. However, this ANO sensitivity occurred not only in degenerated cases but also in intact case; because the perimodiolar array is mostly close to the modiolus axis, anodic pulses may exhibit more efficiency since they

Die approbierte gedruckte Originalversion dieser Dissertation ist an der TU Wien Bibliothek verfügbar.
The approved original version of this doctoral thesis is available in print at TU Wien Bibliothek.
TU Bibliothek Your knowledge hub WIEN

active central parts of ANFs (Figure 3.25-28). On the other hand, it was found a reduction trend in polarity ratios from about 1 in intact to about 0.5 in the most degenerated case. As ANO sensitivity is observed more frequently regardless of neural health status, it was suggest that considering the ANO/CAT ratios and comparing them across the array might shed light on estimating neural health in future investigations.

4.2.2 Effect of cochlear implant stimulation strategy

Several clinical investigations demonstrated that MP strategy induces uniform thresholds across the CI and develops outcomes with poor tonotopic representation due to a broad electric field (Bierer and Middlebrooks, 2002; Bierer et al., 2015a), yet MP stimulation strategy is widely used as a standard strategy in commercial CI systems. In contrast, multipolar strategies such as BP, TP, and PTP produce sharper electric fields compared to the MP strategy (Kral et al., 1998; Bierer and Middlebrooks, 2002; Snyder et al., 2004; Nelson et al., 2008; Bierer and Faulkner, 2010; Landsberger et al., 2012; Srinivasan et al., 2013; Long et al., 2014). Evidence from numerous psychophysical and physiological studies suggests that multipolar strategies increase selectivity, reduce channel interaction, cause larger variation of detection thresholds between electrodes across CI array, and it is beneficial for diagnostic purposes, particularly for investigating the electrode neuron interface (Pfingst and Xu, 2004; Bierer, 2007; Bierer and Faulkner, 2010; Landsberger et al., 2012; Srinivasan et al., 2013; Long et al., 2014; Bierer and Nye, 2014; Schvartz-Leyzac et al., 2020). Undurraga and Chatterjee's groups have reported that multipolar strategies cause changes in AP initiation sites leading to threshold variation (Undurraga et al., 2012; Chatterjee and Kulkarni, 2014). In agreement with the findings mentioned above, it was found the obtained threshold values were more concentrated and in the same range in MP stimulation, whereas by applying multipolar strategies, threshold values created clusters based on different degeneration levels as well as cochlear turns.

While degeneration of ANFs occurs mostly in peripheral part (Fayad and Linthicum, 2006), peripheral processes may remain partly intact. However, depending on hearing loss levels, reducing in diameter and myelination thickness happens (Spoendlin and Schrott, 1989; Heshmat et al., 2020). These findings suggest that variation in peripheral processes is imminent; thus, peripheral excitation results in behavioral differences based on degeneration status across the array.

Various clinical studies had suggested that polarity effects were observed more significantly when multipolar strategies were applied (Macherey and Carlyon, 2010; Macherey et al., 2011; Undurraga et al., 2012; Jahn and Arenberg, 2019b; Mesnildrey et al., 2020). Miller and

Die approbierte gedruckte Originalversion dieser Dissertation ist an der TU Wien Bibliothek verfügbar.
The approved original version of this doctoral thesis is available in print at TU Wien Bibliothek.
TU Bibliothek Your knowledge hub WIEN

Chatterjee have reported that multipolar strategies excite more peripheral processes of ANFs and demonstrate better local ANFs activation and degeneration patterns (Miller et al., 2003; Chatterjee and Kulkarni, 2014). In alignment with those studies, presented results showed that with changing the level of degenerations in the peripheral process, at least for one polarity, threshold values were changed based on peripheral degeneration levels when multipolar strategies were used. Consequently, in the perimodiolar CI, the polarity threshold ratios significantly differed and followed a declining trend for intact to progressive degenerated cases, whereas, by using MP stimulation, the declining trend was lost. In addition, in the lateral CI, the anodic vs. cathodic sensitivity occurred mainly in severe to progressive degenerated cases vs. intact to moderate cases by only applying multipolar strategies. However, according to the results, applying symmetric pulse shape regardless of stimulation strategy led to similar threshold ranges in polarity, i.e., polarity threshold ratios close to one (Figure 3.24), which agrees with clinical studies (Macherey et al., 2006, 2008; Undurraga et al., 2013). Furthermore, Macherey group reported that using the BP strategy with symmetric pulse could not provide enough evidence for polarity behavior, whereas with applying asymmetric pulse, polarity effects were observed (Macherey and Carlyon, 2010; Macherey et al., 2011).

4.2.3 Effect of cochlear implant array

Commercially available CI arrays are generally produced in two types: lateral and perimodiolar arrays. In a lateral CI system, electrodes are located farther from the modiolus wall than in a perimodiolar array. To investigate the impact of electrode modiolus wall distance, it was used both CI systems in a realistic model as reported in manufacturer data. Consistent with (Schvartz-Leyzac et al., 2020), who observed that thresholds are directly proportional to electrode modiolus axis distance, the presented results indicate that lateral array needed larger threshold values compared to perimodiolar array.

However, owing to the fact that in a lateral array, the distance between channels is larger than in a perimodiolar array, it was placed an additional electrode between two investigated existed electrodes. In addition, in perimodiolar system, it was used the multipolar strategies with one gape in between channels (BP+1, TP+1, and PTP+1) to have the channel distances as similar as possible in both CIs. Our result showed that reducing the channel distance in lateral CI only affected the threshold ranges and not the overall behavior of the thresholds. Consequently, it was observed a significant increase in the threshold values due to the current shunt effect. Subsequently, increasing the channel distances in the perimodiolar CI led to a significant decrease in threshold values. Interestingly, in perimodiolar array, the threshold variation between cochlear turns slightly decreased due to wider electric field by setting one electrode

Die approbierte gedruckte Originalversion dieser Dissertation ist an der TU Wien Bibliothek verfügbar.
The approved original version of this doctoral thesis is available in print at TU Wien Bibliothek.
TU Bibliothek Your knowledge hub WIEN

gap between channels, which is in line with previous studies that reported variation in thresholds across the CI strongly depends on the expanse of the electric field (Bierer, 2007; Bierer et al., 2011; Bierer and Nye, 2014). Therefore, the results suggest that while the distance between electrodes alters the threshold ranges, the modiolus wall distance strongly affects threshold variations and consequently polarity ratios, not only across the array but also between degeneration levels when multipolar strategies are applied, as some clinical studies reported that the distance between electrode to modiolus wall impacts detection thresholds in multipolar strategies (Long et al., 2014; Mesnildrey et al., 2020).

On the other hand, similar to Long group (Long et al., 2014), who reported no significant difference in threshold ranges across the array in MP strategy, it was also found analogous threshold ranges in both CIs, not only across the array but also between different degeneration levels when applying MP strategy. Consequently, it was could not find any effect of electrode modiolus distance on polarity behavior in MP strategy, as also seen in Jahn and Arenburg's study (Jahn and Arenberg, 2019b) that used MP strategy and reported that electrode modiolus wall distance does not affect polarity behavior.

4.2.4 Perceptual efficacy

Our study investigated the impact of pulse types, stimulation strategies, and electrode distance to modiolus on thresholds, spike initiation sites, and polarity sensitivity for normal and degenerated ANFs. However, the perceptual efficacy of the artificially generated spiking patterns depends essentially also on the population size of spiking ANFs per active channel. Frequency information transmitted by a small group of ANFs may be lost already during the first neural processing in the cochlear nucleus. Therefore, the focus on a stimulation strategy with sharp frequency selectivity is sometimes successfully replaced by sending the same (combined) input to two channels because of a poor ANF density in a specific frequency region of a patient or by using an implant with a low channel number (Saleh et al., 2013; Bierer and Litvak, 2016; Zhou, 2017). Electrically evoked compound action potentials (ECAPs) recorded by modern CIs are of help to estimate the population size for each channel and intensity (Cullington, 2002; Abbas et al., 2004; Nehmé et al., 2014; DeVries et al., 2016). In addition, the amplitudes of the electrically evoked auditory brainstem response (EABR) (Bierer and Faulkner, 2010; Bierer et al., 2011; Causon et al., 2019) reflect the frequency responses of each channel along the first processing centers. Both techniques can be applied to adapt the findings for individual patient data.

Die approbierte gedruckte Originalversion dieser Dissertation ist an der TU Wien Bibliothek verfügbar.
The approved original version of this doctoral thesis is available in print at TU Wien Bibliothek.
TU Bibliothek Your knowledge hub WIEN

4.2.5 Conclusion

Neural health investigation is of great concern for improving the functionality of the CIs which provides better perception for CI recipients. Polarity sensitivity is one technique for estimating neural health status; however, the clinical and computational outcomes based on polarity sensitivity have been contradictory over the past decades. We believe various parameters are crucial for studying polarity sensitivity associated with neural health. This study aims to investigate the effect of some of these parameters on polarity sensitivity. The findings suggested:

I. The asymmetric pulse shape is more suitable for studying polarity sensitivity when other parameters such as stimulation strategy, electrode distance to the modiolus wall, and cochlear turn are also considered.

II. MP as the default stimulation strategy in most CIs causes a broad electric field and uniform thresholds across the CI that negatively impact the polarity sensitivity and do not reveal helpful information on polarity behavior related to the ANF degeneration status.

III. In contrast, multipolar strategies demonstrated clear information associated with neural health when asymmetric pulse shape was considered. Therefore, a potential approach for estimating neural health is achieved by combining the asymmetric pulse shapes with multipolar strategies such as BP, TP, and PTP.

IV. Finally, the distance between electrodes of the CI arrays and electrode distance to the modiolus wall affect threshold variations (consequently pulse polarity) only when multipolar strategies are applied, and the effect is not observed by MP strategy.

Die approbierte gedruckte Originalversion dieser Dissertation ist an der TU Wien Bibliothek verfügbar.
The approved original version of this doctoral thesis is available in print at TU Wien Bibliothek.
TU Bibliothek Your knowledge hub WIEN

4.3 Scala tympani versus scala vestibuli implantations

Due to several reasons, such as ossification, obstruction, and infection of the ST, the CI insertion in ST is not feasible. In addition, concerning under some circumstances, e.g., CI array dislocation, device failure, electrode extrusion, and upgrade CI technology, reimplantation is needed. However, pulling out the CI from ST may be causing some damage to the modiolus wall, or intracochlear breakage happens; also, in some cases, perielectrode fibrosis exists in ST, which raises the complexity of inserting CI again in ST (Balkany et al., 1996; Rinia et al., 2006). Hence, it is better to consider SV insertion as a valuable alternative.

Some studies reported equivalent results between former ST and later SV implantation (Steenerson et al., 1990; Pijl and Noel, 1992). Moreover, several clinical studies reported comparable performance between SV and ST users. Also, some of them published even slightly better performance in SV users (Deguine et al., 1993; Balkany et al., 1996; Gulya and Steenerson, 1996; Bird et al., 1999; Kiefer et al., 2000; Bacciu et al., 2002; Leonor and Santiago Luis, 2004; Lin et al., 2006, 2009; Nichani et al., 2011; Suzuki et al., 2011; Lee et al., 2019; Stock et al., 2020). Many computational modeling studies are available to investigate CI electrode position in ST (Kalkman et al., 2014; Hanekom and Hanekom, 2016; Bai et al., 2019; Heshmat et al., 2020; Potrusil et al., 2020); however, up to now, not a single computational investigation was done for electrode position in SV. Therefore, this dissertation tried to study the excitation behavior of human auditory fibers depending on electrode position in ST and SV.

In this part of the investigation, six ANFs were selected from different cochlear turns (basal, middle, and apical turns). In addition, three ANF health states, intact, intermediate, and progressive cases, were used to analyze the threshold excitation and AP initiation site with ST and SV electrodes. Electrodes in ST and SV were placed at an equal distance to the terminal part of intact ANFs; however, for degenerated cases, in which the reduction and loss of peripheral axons happen, electrodes in SV have a larger ANF distance compared to ST electrodes.

The excitation thresholds of both ST and SV stimulating electrodes demonstrated CAT sensitivity in the intact case in all selected ANFs, and also, the AP initiation sites happen in the peripheral process regardless of the electrode position. In contrast, in the degenerated cases, the excitation behavior of ANFs changed, and AP initiation sites differ depending on polarity and electrode position. Therefore, to obtain a better understanding, it is needed to investigate in more detail to analyze the AP sites and ANF excitation behavior.

Die approbierte gedruckte Originalversion dieser Dissertation ist an der TU Wien Bibliothek verfügbar.
The approved original version of this doctoral thesis is available in print at TU Wien Bibliothek.
TU Bibliothek Your knowledge hub WIEN

Furthermore, the highest voltage value does not really indicate that the closest part of the fiber can initiate the AP. According to the voltage membrane equation, there are three forces to alter the transmembrane potential: Firstly, AF, which is proportional to the second derivative of the extracellular voltage in every compartment with two neighbors and inversely proportional to its intracellular resistance and capacitance (Rattay, 1986, 1999). Secondly, the axial force is the current flow of the neighbor compartments and is again inversely proportional to its intracellular resistance and capacitance. Thirdly, the ionic current force is acting due to the opening of channels.

AF is the most important driving force in extracellular stimulation, whose values estimate the candidate sites of AP initiation. However, depending on the AF values of the neighbor compartments, a node with the highest AF may not initiate the AP, especially for the intact fibers at the threshold stimulation since the voltage values are low. In these cases, investigating the second force may help explain and understand the initiation of AP even in non-expected sites. However, before the pulse onset, the cell is in the resting state, and for the AP initiation, the most critical time is the stimulus onset, when the ionic forces do not start to act yet. At this time, the axial force of each compartment is mainly affected by the AFs of other neighboring compartments.

Moreover, the three-dimensional ANF pathways profoundly impact the excitation threshold and AP initiation sites; since the peripheral axons have a more spiral and irregular shape, the AF alone is not enough to detect the AP initiation sites in the intact case. Hence, it is necessary to consider axial current and combine it with AF to calculate the net driving force for accurate AP site detection. The AF and axial forces in the intact cases of investigated ANFs demonstrate that the net driving force in the nodes with the highest value of AF is almost zero, whereas, in the nodes where real AP occurs, the net driving force is positive, notably at the first half of the stimulus time.

On the other hand, in the degenerated cases, by reducing the peripheral axon diameters or losing the peripheral parts, the AP initiation sites can ideally be described only by AF behavior due to high extracellular potentials required for the degenerated fiber excitation that accordingly causes high AF values. Because the central axon has less irregular and helical shape and is more smooth and thicker than the peripheral axon, it is easier to stimulate; therefore, AF is a good indicator for the AP initiation site.

Furthermore, in the intermediate case where the peripheral processes are thinner than the intact case (2 µm vs. 0.5 µm), the first AP started in the peripheral process, with a positive AF value. However, the AP cannot propagate either due to faster AP propagation in the central process

Die approbierte gedruckte Originalversion dieser Dissertation ist an der TU Wien Bibliothek verfügbar.
The approved original version of this doctoral thesis is available in print at TU Wien Bibliothek.
TU Bibliothek Your knowledge hub WIEN

resulting in collision block or is not strong enough to load the soma capacitance and pass the soma. Hence, the real AP with positive AF happens in the central process.

The peripheral axon diameter often diminishes during the degeneration process, causing increased thresholds and frequently shifting the primarily exciting region from the peripheral process to the central process (Heshmat et al., 2020). A total loss of peripheral axons occurs in many cochlear neurons of people with severe hearing deficits (Spoendlin and Schrott, 1988), resulting in a trend to higher sensitivity (lower thresholds) for anodic versus cathodic stimulation. However, the polarity sensitivity is related to several factors, such as pulse shapes, stimulation strategy, ANF pathways, and electrode position (Heshmat et al., 2021).

In severe and profound hearing level cases, most fibers have degenerated, and the number of intact fibers is poor, but according to (Heshmat et al., 2020) study, several intact fibers are still existing, although it is significantly less. So to activate these majority, degenerated ANFs, it may need to apply strong stimulation, which may lead to firing the AP from different ANF sites, resulting in large jitters and delays that can disturb the temporal fine structure. Furthermore, one important finding in the strong stimulation investigation that shows the ST stimulating electrodes cause AP in different positions of the ANFs depending on the level of degeneration. In contrast, interestingly, the SV stimulating electrodes excite the central process in all investigated fibers regardless of degeneration levels.

In the second part of the ST and SV implantation investigation, two types of CI arrays, a perimodiolar and a lateral system, were used to investigate the excitation behavior of ANFs based on ST and SV electrode array insertion. For a systematic comparison, four ANFs from different cochlear turns were selected, and three ANF health statuses, one intact and two degenerated cases based on the various morphometry of the peripheral axon (Table 2.11) were considered. In addition, one symmetric pulse (biphasic) and one asymmetric pulse (pseudo-monophasic) with both polarities, ANO and CAT, were applied.

SV array insertion is located in the highest scalae in the cochlea; in general, the ANF distance to the center of the stimulating electrode in SV is longer than the ST array; though, it depends on the array type and the cochlear turns. Based on investigated ANFs in this study, the SV distance to fibers is larger than the ST array after the soma region (central process) for both CI array systems. However, in some cases in the upper basal turn, the electrode distance from the terminal and peripheral parts up to the soma of ANFs are almost similar between ST and SV in the perimodiolar array. Overall, depending on the ANF location, the electrode distance to the investigated fibers can differ between ST and SV.

Die approbierte gedruckte Originalversion dieser Dissertation ist an der TU Wien Bibliothek verfügbar.
The approved original version of this doctoral thesis is available in print at TU Wien Bibliothek.
TU Bibliothek Your knowledge hub WIEN

By selecting ANF from the upper basal turn, the excitation current in SV becomes less than ST regardless of pulse shape, array type, and ANF health status. The ANF pathways play a critical role in excitation cause the SV array stimulates with a lower threshold than ST. Moreover, other selected ANF, which is located at the beginning of the middle turn, shows the almost similar behavior that SV needs less current than ST array for the intact case. In addition, the pulse shape impacts the excitation threshold since the asymmetric pulse decreases threshold intensity and reduces the threshold difference between ST and SV arrays. Finally, another ANF from the middle turn shows that the ST requires less excitation current than SV regardless of ANF health status, and also, the asymmetric pulse shape again causes reduce the threshold intensity in both arrays regardless of ANF status.

For polarity sensitivity investigation, the results imply that the SV array is always CAT sensitive regardless of pulse shape, CI array system, cochlear turn, and ANF health status. In contrast, the polarity sensitivity depends on the array types, pulse shape, and ANF health status for the ST array insertion. In addition, the polarity behavior is changed based on cochlear turns that show the above-mentioned parameters such as pulse shape and CI array system affect the polarity, which is consistent with the latest investigation (Heshmat et al., 2021).

Die approbierte gedruckte Originalversion dieser Dissertation ist an der TU Wien Bibliothek verfügbar.
The approved original version of this doctoral thesis is available in print at TU Wien Bibliothek.
TU Bibliothek Your knowledge hub WIEN

References

Abbas, P.J., Hughes, M.L., Brown, C.J., Miller, C.A., South, H., 2004. Channel interaction in cochlear implant users evaluated using the electrically evoked compound action potential. Audiol. Neurotol. 9, 203–213.

Adunka, O., Kiefer, J., Unkelbach, M.H., Radeloff, A., Gstoettner, W., 2005. Evaluating cochlear implant trauma to the scala vestibuli. Clin. Otolaryngol. doi:10.1111/j.1365-2273.2004.00935.x

Albu, S., Babighian, G., 1997. Predictive factors in cochlear implants. Acta Otorhinolaryngol. Belg. 51, 11.

Alexiades, G., Roland Jr, J.T., Fishman, A.J., Shapiro, W., Waltzman, S.B., Cohen, N.L., 2001. Cochlear reimplantation: surgical techniques and functional results. Laryngoscope 111, 1608–1613.

Anatomy & Physiology, Special Senses Chapter, Bio 264 Textbook, BYU-Idaho, Biology Department, 2015. https://content.byui.edu/file/a236934c-3c60-4fe9-90aa-d343b3e3a640/1/module12/readings/sense_hearing.html.

Arbuthnott, E.R., Boyd, I.A., Kalu, K.U., 1980. Ultrastructural dimensions of myelinated peripheral nerve fibres in the cat and their relation to conduction velocity. J. Physiol. doi:10.1113/jphysiol.1980.sp013465

Arnesen, A.R., Osen, K.K., 1978. The cochlear nerve in the cat: Topography, cochleotopy, and fiber spectrum. J. Comp. Neurol. doi:10.1002/cne.901780405

Arnold, W., 1987. Myelination of the human spiral ganglion. Acta Otolaryngol. 104, 76–84.

Ashmore, J., Avan, P., Brownell, W.E., Dallos, P., Dierkes, K., Fettiplace, R., Grosh, K., 2010. ua (2010).„. remarkable cochlear Amplif. “, Hear. Res 266, 1–17.

Bacciu, S., Bacciu, A., Pasanisi, E., Vincenti, V., Guida, M., Barbot, A., Berghenti, T., 2002. Nucleus multichannel cochlear implantation in partially ossified cochleas using the Steenerson procedure. Otol. Neurotol. doi:10.1097/00129492-200205000-00019

Bachmaier Richard, Encke Jörg, Obando-Leitón Miguel, Hemmert Werner, B.S., 2019. Comparison of Multi-Compartment Cable Models of Human Auditory Nerve Fibers. Front. Neurosci. 13, 1173. doi:10.3389/fnins.2019.01173

Bahmer, A., Adel, Y., Baumann, U., 2017. Preventing facial nerve stimulation by triphasic pulse stimulation in cochlear implant users: intraoperative recordings. Otol. Neurotol. 38, e438–e444.

Bahmer, A., Baumann, U., 2013. Effects of electrical pulse polarity shape on intra cochlear neural responses in humans: triphasic pulses with cathodic second phase. Hear. Res. 306, 123–130.

Bahmer, A., Baumann, U., 2012a. Application of triphasic pulses with adjustable phase amplitude ratio (PAR) for cochlear ECAP recording: I. Amplitude growth functions. J. Neurosci. Methods 205, 202–211.

Bahmer, A., Baumann, U., 2012b. Application of triphasic pulses with adjustable phase amplitude ratio (PAR) for cochlear ECAP recording: II. Recovery functions. J. Neurosci. Methods 205, 212–220. doi:https://doi.org/10.1016/j.jneumeth.2011.12.006

Die approbierte gedruckte Originalversion dieser Dissertation ist an der TU Wien Bibliothek verfügbar.
The approved original version of this doctoral thesis is available in print at TU Wien Bibliothek.
TU Bibliothek Your knowledge hub WIEN

Bahmer, A. and Baumann, U. (2016) 'The underlying mechanism of preventing facial nerve stimulation by triphasic pulse stimulation in cochlear implant users assessed with objective measure', Otology & Neurotology. LWW, 37(9), pp. 1231–1237. doi: 10.1097/MAO.0000000000001156.

Bai, S., Encke, J., Obando-Leiton, M., Weiß, R., Schäfer, F., Eberharter, J., Böhnke, F., and Hemmert, W. (2019). Electrical Stimulation in the Human Cochlea: A Computational Study Based on High-Resolution Micro-CT Scans. Front. Neurosci. 13, 1312. https://doi.org/ 10.3389/fnins.2019.01312

Bai, S., Croner, A., Encke, J., and Hemmert, W. (2020). Electrical stimulation in the cochlea: Influence of modiolar microstructures on the activation of auditory nerve fibres. In *2020 42nd Annual International Conference of the IEEE Engineering in Medicine & Biology Society (EMBC)* (pp. 2324–2327).

Balkany, T., Bird, P.A., Hodges, A. V, Luntz, M., Telischi, F.F., Buchman, C., 1998. Surgical technique for implantation of the totally ossified cochlea. Laryngoscope 108, 988–992.

Balkany, T., Dreisbach, J., Cohen, N., Martinez, S., Valvassori, G., 1987. Workshop: surgical anatomy and radiographic imaging of cochlear implant surgery. Otol. Neurotol. 8, 195–200.

Balkany, T., Gantz, B.J., Steenerson, R.L., Cohen, N.L., 1996. Systematic approach to electrode insertion in the ossified cochlea. Otolaryngol. Neck Surg. 114, 4–11.

Bast, T.H., 1942. XXXII Development of the otic capsule: VI. Histological changes and variations in the growing bony capsule of the vestibule and cochlea. Ann. Otol. Rhinol. Laryngol. 51, 343–357.

Battmer, R.-D., Linz, B., Lenarz, T., 2009. A review of device failure in more than 23 years of clinical experience of a cochlear implant program with more than 3,400 implantees. Otol. Neurotol. 30, 455–463.

Battmer, R., Pesch, J., Stöver, T., Lesinski-Schiedat, A., Lenarz, M., Lenarz, T., 2006. Elimination of facial nerve stimulation by reimplantation in cochlear implant subjects. Otol. Neurotol. 27, 918–922.

Berrettini, S., Forli, F., Neri, E., Segnini, G., Franceschini, S.S., 2002. Scala vestibuli cochlear implantation in patients with partially ossified cochleas. J. Laryngol. Otol. 116, 946.

Bierer, J.A., 2007. Threshold and channel interaction in cochlear implant users: evaluation of the tripolar electrode configuration. J. Acoust. Soc. Am. 121, 1642–1653.

Bierer, Julie A, Bierer, S. M., Kreft, H. A., and Oxenham, A. J. (2015a). A fast method for measuring psychophysical thresholds across the cochlear implant array. *Trends in Hearing*, *19*, 2331216515569792. https://doi.org/10.1177/2331216515569792

Bierer, Julie Arenberg, Deeks, J. M., Billig, A. J., and Carlyon, R. P. (2015b). Comparison of signal and gap-detection thresholds for focused and broad cochlear implant electrode configurations. *Journal of the Association for Research in Otolaryngology*, *16*(2), 273–284. https://doi.org/10.1007/s10162-015-0507-y

Bierer, Julie A., and Litvak, L. (2016). Reducing Channel Interaction Through Cochlear Implant Programming May Improve Speech Perception. In *Trends in Hearing*. https://doi.org/10.1177/2331216516653389

Bierer, J.A., Faulkner, K.F., 2010. Identifying cochlear implant channels with poor electrode-neuron interface: partial tripolar, single-channel thresholds and psychophysical tuning curves. Ear Hear. 31, 247.

Bierer, J.A., Faulkner, K.F., Tremblay, K.L., 2011. Identifying cochlear implant channels with poor electrode-neuron interface: Electrically-evoked auditory brainstem responses measured with the partial tripolar configuration. Ear Hear. 32, 436.

Bierer, Julie Arenberg, and Middlebrooks, J. C. (2002). Auditory cortical images of cochlear-implant stimuli: dependence on electrode configuration. *Journal of Neurophysiology*, *87*(1), 478–492. https://doi.org/10.1152/jn.00212.2001

Die approbierte gedruckte Originalversion dieser Dissertation ist an der TU Wien Bibliothek verfügbar.
The approved original version of this doctoral thesis is available in print at TU Wien Bibliothek.
TU Bibliothek Your knowledge hub WIEN

Bierer, Julie Arenberg, and Nye, A. D. (2014). Comparisons between detection threshold and loudness perception for individual cochlear implant channels. *Ear and Hearing*, *35*(6), 641. https://doi.org/10.1097/AUD.0000000000000058

Bird, P.A., Butts, S., Balkany, T.J., Gomez, O., Hodges, A. V, Lee, D., 1999. Using the CLARION® Cochlear Implant in cochlear ossification. Ann. Otol. Rhinol. Laryngol. 108, 31–34.

Blamey, P., Artieres, F., Başkent, D., Bergeron, F., Beynon, A., Burke, E., Dillier, N., Dowell, R., Fraysse, B., Gallégo, S., Govaerts, P.J., Green, K., Huber, A.M., Kleine-Punte, A., Maat, B., Marx, M., Mawman, D., Mosnier, I., O'Connor, A.F., O'Leary, S., Rousset, A., Schauwers, K., Skarzynski, H., Skarzynski, P.H., Sterkers, O., Terranti, A., Truy, E., Van De Heyning, P., Venail, F., Vincent, C., Lazard, D.S., 2012. Factors affecting auditory performance of postlinguistically deaf adults using cochlear implants: An update with 2251 patients. Audiol. Neurotol. doi:10.1159/000343189

Boisvert, I., Reis, M., Au, A., Cowan, R., Dowell, R.C., 2020. Cochlear implantation outcomes in adults: A scoping review. PLoS One 15, e0232421.

Brydone, P., 1757. XCIV. A further account of the effects of electricity in the cure of some diseases: in a letter from Mr. Patrick Brydone to Dr. Robert Whytt, Professor of Medicine in the University of Edinburgh, and FR S. Philos. Trans. R. Soc. London 695–699.

Caldwell, A., Nittrouer, S., 2013. Speech perception in noise by children with cochlear implants.

Carlyon, R. P., Cosentino, S., Deeks, J. M., Parkinson, W., and Arenberg, J. A. (2018). Effect of stimulus polarity on detection thresholds in cochlear implant users: relationships with average threshold, gap detection, and rate discrimination. *Journal of the Association for Research in Otolaryngology*, *19*(5), 559–567. https://doi.org/10.1101/297085

Carlyon, R. P., Deeks, J. M., and Macherey, O. (2013). Polarity effects on place pitch and loudness for three cochlear-implant designs and at different cochlear sites. *The Journal of the Acoustical Society of America*, *134*(1), 503–509. https://doi.org/10.1121/1.4807900

Carlyon, R. P., Van Wieringen, A., Deeks, J. M., Long, C. J., Lyzenga, J., and Wouters, J. (2005). Effect of inter-phase gap on the sensitivity of cochlear implant users to electrical stimulation. *Hearing Research*, *205*(1–2), 210–224. https://doi.org/10.1016/j.heares.2005.03.021

Causon, A., O'Driscoll, M., Stapleton, E., Lloyd, S., Freeman, S., Munro, K.J. (2019). Extracochlear stimulation of electrically evoked auditory brainstem responses (eABRs) remains the preferred pre-implant auditory nerve function test in an assessor-blinded comparison. Otol. Neurotol. 40, 47–55. https://doi.org/10.1097/mao.0000000000002055

Chatterjee, M., and Kulkarni, A. M. (2014). Sensitivity to pulse phase duration in cochlear implant listeners: Effects of stimulation mode. *The Journal of the Acoustical Society of America*, *136*(2), 829–840. https://doi.org/10.1121/1.4884773

Clark, G.M., 1978. Cochlear implant surgery for profound or total hearing loss.

Clark, G.M., Clark, J.C.M., Furness, J.B., 2013. The evolving science of cochlear implants. Jama 310, 1225–1226.

Cohen, L.T., Saunders, E., Clark, G.M., 2001. Psychophysics of a prototype peri-modiolar cochlear implant electrode array. Hear. Res. 155, 63–81.

Cohen, L. T., Saunders, E., Knight, M. R., and Cowan, R. S. C. (2006). Psychophysical measures in patients fitted with Contour™ and straight Nucleus electrode arrays. *Hearing Research*, *212*(1–2), 160–175. https://doi.org/10.1016/j.heares.2005.11.005

Die approbierte gedruckte Originalversion dieser Dissertation ist an der TU Wien Bibliothek verfügbar.
The approved original version of this doctoral thesis is available in print at TU Wien Bibliothek.
TU Bibliothek Your knowledge hub WIEN

Cohen, N.L., Waltzman, S.B., 1993. Partial insertion of the nucleus multichannel cochlear implant: technique and results. Otol. Neurotol. 14, 357–361.

Colombo, J., and Parkins, C. W. (1987). A model of electrical excitation of the mammalian auditory-nerve neuron. *Hearing Research*, *31*(3), 287–311. https://doi.org/10.1016/0378-5955(87)90197-3

Cosentino, S., Carlyon, R.P., Deeks, J.M., Parkinson, W., Bierer, J.A., 2016. Rate discrimination, gap detection and ranking of temporal pitch in cochlear implant users. J. Assoc. Res. Otolaryngol. 17, 371–382.

Croghan, N. B. H., Duran, S. I., and Smith, Z. M. (2017). Re-examining the relationship between number of cochlear implant channels and maximal speech intelligibility. *The Journal of the Acoustical Society of America*, *142*(6), EL537–EL543. https://doi.org/10.1121/1.5016044

Cullington, H.E. (2002). Cochlear implants: objective measures. Wiley-Blackwell

Cunningham, R.F., Glade, R., 2019. Cochlear Implants for Children Who Are Deaf or Hard of Hearing.

Dallos, P., 1992. The active cochlea. J. Neurosci. 12, 4575–4585.

Davis, R.L., Liu, Q., 2011. Complex primary afferents: what the distribution of electrophysiologically-relevant phenotypes within the spiral ganglion tells us about peripheral neural coding. Hear. Res. 276, 34–43.

Degrees of Hearing Loss | Happy Ears Hearing Center. URL https://www.happyearshearing.com/hearing-loss/degrees-of-hearing-loss/.

Deguine, O., Fraysse, B., Uziel, A., Mondain, M., 1993. Surgical technique and results of cochlear implant in normal or ossified cochlea. Rev. Laryngol. 114, 5–8.

DeVries, L., Arenberg, J.G., 2018. Current focusing to reduce channel interaction for distant electrodes in cochlear implant programs. Trends Hear. 22, 2331216518813811.

DeVries, L., Scheperle, R., Bierer, J.A., 2016. Assessing the electrode-neuron interface with the electrically evoked compound action potential, electrode position, and behavioral thresholds. J. Assoc. Res. Otolaryngol. 17, 237–252.

Dhanasingh, A., Jolly, C., 2017. An overview of cochlear implant electrode array designs. Hear. Res. 356, 93–103.

Djourno, A., Eyries, C., Vallancien, B., 1957. Electric excitation of the cochlear nerve in man by induction at a distance with the aid of micro-coil included in the fixture. C. R. Seances Soc. Biol. Fil. 151, 423–425.

Donaldson, G.S., Peters, M.D., Ellis, M.R., Friedman, B.J., Levine, S.C., Rimell, F.L., 2001. Effects of the Clarion Electrode Positioning System on auditory thresholds and comfortable loudness levels in pediatric patients with cochlear implants. Arch. Otolaryngol. Neck Surg. 127, 956–960.

Dunn, C.C., Noble, W., Tyler, R.S., Kordus, M., Gantz, B.J., Ji, H., 2010. Bilateral and unilateral cochlear implant users compared on speech perception in noise. Ear Hear. 31, 296.

Edge, A.S.B., Chen, Z.-Y., 2008. Hair cell regeneration. Curr. Opin. Neurobiol. 18, 377–382.

Erixon, E., Högstorp, H., Wadin, K., Rask-Andersen, H., 2009. Variational anatomy of the human cochlea: Implications for cochlear implantation. Otol. Neurotol. doi:10.1097/MAO.0b013e31818a08e8

EURO, C.I.U., 2020. What is the cochlear implant? Eur. Assoc. Cochlear Implant Users. http//eurociu. eu/what-is-the-ci-. Accessed 5.

Evans, E.F., Wilson, J.P., 1975. Cochlear tuning properties: concurrent basilar membrane and single nerve fiber measurements. Science (80-.). 190, 1218–1221.

Die approbierte gedruckte Originalversion dieser Dissertation ist an der TU Wien Bibliothek verfügbar.
The approved original version of this doctoral thesis is available in print at TU Wien Bibliothek.
TU Bibliothek Your knowledge hub WIEN

Fayad, J.N., Linthicum Jr, F.H., 2006. Multichannel cochlear implants: relation of histopathology to performance. Laryngoscope 116, 1310–1320.

Feghali, J.G., Lefebvre, P.P., Staecker, H., Kopke, R., Frenz, D.A., Malgrange, B., Liu, W., Moonen, G., Ruben, R.J., Van De Water, T.R., 1998. Mammalian auditory hair cell regeneration/repair and protection: a review and future directions. Ear, nose throat J. 77, 276–285.

Fettiplace, R., Kim, K.X., 2014. The physiology of mechanoelectrical transduction channels in hearing. Physiol. Rev. 94, 951–986.

Finley, C.C., Skinner, M.W., 2008. Role of electrode placement as a contributor to variability in cochlear implant outcomes. Otol. Neurotol. Off. Publ. Am. Otol. Soc. Am. Neurotol. Soc. [and] Eur. Acad. Otol. Neurotol. 29, 920.

Fishman, K.E., Shannon, R. V, Slattery, W.H., 1997. Speech recognition as a function of the number of electrodes used in the SPEAK cochlear implant speech processor. J. Speech, Lang. Hear. Res. 40, 1201–1215.

Friedland, D.R., Venick, H.S., Niparko, J.K., 2003. Choice of ear for cochlear implantation: the effect of history and residual hearing on predicted postoperative performance. Otol. Neurotol. 24, 582–589.

Friedland, David R., Christina Runge-Samuelson, Humera Baig, and Jamie Jensen., 2010. 'Case-control analysis of cochlear implant performance in elderly patients', Archives of Otolaryngology–Head & Neck Surgery. American Medical Association, 136(5), pp. 432–438. doi:10.1001/archoto.2010.57

Frisch, C.D., Carlson, M.L., Lane, J.I., Driscoll, C.L.W., 2015. Evaluation of a new mid-scala cochlear implant electrode using microcomputed tomography. Laryngoscope 125, 2778–2783.

Gacek, R.R., Rasmussen, G.L., 1961. Fiber analysis of the statoacoustic nerve of guinea pig, cat, and monkey. Anat. Rec. 139, 455–463.

Gantz, B.J., Abbas, P.J., Tyler, R.S., Woodworth, G.G., Knutson, J.F., 1993. Multivariate predictors of audiological success with multichannel cochlear implants. Ann. Otol. Rhinol. Laryngol. doi:10.1177/000348949310201201

Gantz, B.J., Mccabe, B.F., Tyler, R.S., 1988. Use of multichannel cochlear implants in obstructed and obliterated cochleas. Otolaryngol. Neck Surg. 98, 72–81.

Garadat, S.N., Zwolan, T.A., Pfingst, B.E., 2012. Across-site patterns of modulation detection: relation to speech recognition. J. Acoust. Soc. Am. 131, 4030–4041.

Geier, L.L., Norton, S.J., 1992. The effects of limiting the number of Nucleus 22 cochlear implant electrodes programmed on speech perception. Ear Hear. 13, 340–348.

Gfeller, K., Lansing, C.R., 1991. Melodic, rhythmic, and timbral perception of adult cochlear implant users. J. Speech, Lang. Hear. Res. 34, 916–920.

Gleich, O., Wilson, S., 1993. The diameters of guinea pig auditory nerve fibres: distribution and correlation with spontaneous rate. Hear. Res. 71, 69–79.

Gisselson, L., 1950. Evidence favouring a possible humoral transmission in the inner ear. Acta Otolaryngol 38, 9–23.

Glueckert, R., Pfaller, K., Kinnefors, A., Rask-Andersen, H., Schrott-Fischer, A., 2005. The human spiral ganglion: New insights into ultrastructure, survival rate and implications for cochlear implants. Audiol. Neurotol. doi:10.1159/000086000

Goehring, T., Archer-Boyd, A., Deeks, J.M., Arenberg, J.G., Carlyon, R.P., 2019. A site-selection strategy based on polarity sensitivity for cochlear implants: effects on spectro-temporal resolution and speech perception. J. Assoc. Res. Otolaryngol. 20, 431–448.

Die approbierte gedruckte Originalversion dieser Dissertation ist an der TU Wien Bibliothek verfügbar.
The approved original version of this doctoral thesis is available in print at TU Wien Bibliothek.
TU Bibliothek Your knowledge hub WIEN

Goehring, T., Bolner, F., Monaghan, J. J. M., Van Dijk, B., Zarowski, A., and Bleeck, S. (2017). Speech enhancement based on neural networks improves speech intelligibility in noise for cochlear implant users. *Hearing Research*, *344*, 183–194. https://doi.org/10.1016/j.heares.2016.11.012

Goldman, D.E., 1943. Potential, impedance, and rectification in membranes. J. Gen. Physiol. 27, 37–60.

Gomaa, N.A., Rubinstein, J.T., Lowder, M.W., Tyler, R.S., Gantz, B.J., 2003. Residual speech perception and cochlear implant performance in postlingually deafened adults. Ear Hear. 24, 539–544.

Graven, S.N., Browne, J. V, 2008. Auditory development in the fetus and infant. Newborn infant Nurs. Rev. 8, 187–193.

Grant, L., Yi, E., Glowatzki, E., 2010. Two modes of release shape the postsynaptic response at the inner hair cell ribbon synapse. J. Neurosci. 30, 4210–4220.

Green Jr, J.D., Marion, M.S., Hinojosa, R., 1991. Labyrinthitis ossificans: histopathologic consideration for cochlear implantation. Otolaryngol. Neck Surg. 104, 320–326.

Guérit, F., Marozeau, J., Deeks, J.M., Epp, B., Carlyon, R.P., 2018. Effects of the relative timing of opposite-polarity pulses on loudness for cochlear implant listeners. J. Acoust. Soc. Am. 144, 2751–2763.

Gulya, A.J., Steenerson, R.L., 1996. The scala vestibuli for cochlear implantation: An anatomic study. Arch. Otolaryngol. Neck Surg. 122, 130–132.

Hardie, N.A., Shepherd, R.K., 1999. Sensorineural hearing loss during development: morphological and physiological response of the cochlea and auditory brainstem. Hear. Res. 128, 147–165.

Hardy, M., 1938. The length of the organ of Corti in man. Am. J. Anat. doi:10.1002/aja.1000620204

Hartmann, R., Topp, G., Klinke, R., 1984. Discharge patterns of cat primary auditory fibers with electrical stimulation of the cochlea. Hear. Res. 13, 47–62.

He, S., Xu, L., Skidmore, J., Chao, X., Jeng, F.-C., Wang, R., Luo, J., Wang, H., 2020. The effect of interphase gap on neural response of the electrically-stimulated cochlear nerve in children with cochlear nerve deficiency and children with normal-sized cochlear nerves. Ear Hear. 41, 918.

Heshmat, A., Sajedi, S., Chacko, L.J., Fischer, N., Schrott-Fischer, A., Rattay, F., 2020. Dendritic Degeneration of Human Auditory Nerve Fibers and Its Impact on the Spiking Pattern Under Regular Conditions and During Cochlear Implant Stimulation. Frontiers in Neuroscience. 14. https://doi.org/10.3389/fnins.2020.599868

Heshmat A, Sajedi S, Schrott-Fischer A and Rattay F., 2021 .Polarity Sensitivity of Human Auditory Nerve Fibers Based on Pulse Shape and Cochlear Implant Stimulation Strategy and Array. Frontiers in Neuroscience. 15:751599. https://doi.org/10.3389/fnins.2021.751599

Hinojosa, R., Marion, M., 1983. HISTOPATHOLOGY OF PROFOUND SENSORINEURAL DEAFNESS a. Ann. N. Y. Acad. Sci. 405, 459–484.

Hinojosa, R., Nelson, E.G., Lerner, S.A., Redleaf, M.I., Schramm, D.R., 2001. Aminoglycoside ototoxicity: a human temporal bone study. Laryngoscope 111, 1797–1805.

Hochmair-Desoyer, I.J., Hochmair, E.S., Motz, H., Rattay, F., 1984. A model for the electrostimulation of the nervus acusticus. Neuroscience 13, 553–562.

Hodgkin, A L, Huxley, A.F., 1952a. A quantitative description of ion currents and its applications to conduction and excitation in nerve. J Physiol. doi:10.1113/jphysiol.1952.sp004764

Hodgkin, A.L., Huxley, A.F., 1952b. A quantitative description of membrane current and its application to conduction and excitation in nerve. J. Physiol. 117, 500–544.

Die approbierte gedruckte Originalversion dieser Dissertation ist an der TU Wien Bibliothek verfügbar.
The approved original version of this doctoral thesis is available in print at TU Wien Bibliothek.
TU Bibliothek Your knowledge hub WIEN

Hodgkin, A.L., Huxley, A.F., 1952c. Currents carried by sodium and potassium ions through the membrane of the giant axon of Loligo. J. Physiol. 116, 449–472.

Holden, L.K., Finley, C.C., Firszt, J.B., Holden, T.A., Brenner, C., Potts, L.G., Gotter, B.D., Vanderhoof, S.S., Mispagel, K., Heydebrand, G., 2013. Factors affecting open-set word recognition in adults with cochlear implants. Ear Hear. 34, 342.

Hossain, W.A., Antic, S.D., Yang, Y., Rasband, M.N., Morest, D.K., 2005. Where is the spike generator of the cochlear nerve? Voltage-gated sodium channels in the mouse cochlea. J. Neurosci. doi:10.1523/JNEUROSCI.0123-05.2005

House, L.R., 1987. Cochlear implant: the beginning. Laryngoscope 97, 996–997.

Hughes, M.L., Abbas, P.J., 2006. Electrophysiologic channel interaction, electrode pitch ranking, and behavioral threshold in straight versus perimodiolar cochlear implant electrode arrays. J. Acoust. Soc. Am. 119, 1538–1547.

Hughes, M.L., Choi, S., Glickman, E., 2018. What can stimulus polarity and interphase gap tell us about auditory nerve function in cochlear-implant recipients? Hear. Res. 359, 50–63.

Hughes, M.L., Goehring, J.L., Baudhuin, J.L., 2017. Effects of stimulus polarity and artifact reduction method on the electrically evoked compound action potential. Ear Hear. 38, 332.

Humes, L.E., Kewley-Port, D., Fogerty, D., Kinney, D., 2010. Measures of hearing threshold and temporal processing across the adult lifespan. Hear. Res. 264, 30–40.

Isaacson, B., Booth, T., Kutz Jr, J.W., Lee, K.H., Roland, P.S., 2009. Labyrinthitis ossificans: how accurate is MRI in predicting cochlear obstruction? Otolaryngol. Neck Surg. 140, 692–696.

Jackler, R.K., Luxford, W.M., Schindler, R.A., McKerrow, W.S., 1987. Cochlear patency problems in cochlear implantation. Laryngoscope 97, 801–805.

Jagger, D.J., Housley, G.D., 2003. Membrane properties of type II spiral ganglion neurones identified in a neonatal rat cochlear slice. J. Physiol. 552, 525–533.

Jahn, K. N., and Arenberg, J. G. (2019a). Polarity Sensitivity in Pediatric and Adult Cochlear Implant Listeners. *Trends in Hearing*. https://doi.org/10.1177/2331216519862987

Jahn, K. N., and Arenberg, J. G. (2019b). Evaluating psychophysical polarity sensitivity as an indirect estimate of neural status in cochlear implant listeners. *Journal of the Association for Research in Otolaryngology*, *20*(4), 415–430. https://doi.org/10.1007/s10162-019-00718-2

Johnsson, L.-G., 1974. Sequence of degeneration of Corti's organ and its first-order neurons. Ann. Otol. Rhinol. Laryngol. 83, 294–303.

Johnsson, L.-G., Hawkins Jr, J.E., 1976. Degeneration patterns in human ears exposed to noise. Ann. Otol. Rhinol. Laryngol. 85, 725–739.

Jolly, C.N., Spelman, F.A., Clopton, B.M., 1996. Quadrupolar stimulation for cochlear prostheses: modeling and experimental data. IEEE Trans. Biomed. Eng. 43, 857–865.

Jwair, S., Prins, A., Wegner, I., Stokroos, R.J., Versnel, H., Thomeer, H.G.X.M., 2021. Scalar Translocation Comparison Between Lateral Wall and Perimodiolar Cochlear Implant Arrays-A Meta-Analysis. Laryngoscope 131, 1358–1368.

Kalkman, R.K., Briaire, J.J., Dekker, D.M.T., Frijns, J.H.M., 2014. Place pitch versus electrode location in a realistic computational model of the implanted human cochlea. Hear. Res. doi:10.1016/j.heares.2014.06.003

Kamakura, T., Nadol Jr, J.B., 2016. Correlation between word recognition score and intracochlear new bone and fibrous tissue after cochlear implantation in the human. Hear. Res. 339, 132–141.

Die approbierte gedruckte Originalversion dieser Dissertation ist an der TU Wien Bibliothek verfügbar.
The approved original version of this doctoral thesis is available in print at TU Wien Bibliothek.
TU Bibliothek Your knowledge hub WIEN

Karg, S.A., Lackner, C., Hemmert, W., 2013. Temporal interaction in electrical hearing elucidates auditory nerve dynamics in humans. Hear. Res. 299, 10–18.

Kawano, A., Seldon, H.L., Clark, G.M., Ramsden, R.T., Raine, C.H., 1998. Intracochlear factors contributing to psychophysical percepts following cochlear implantation. Acta Otolaryngol. 118, 313–326.

Keithley, E.M., 2020. Pathology and mechanisms of cochlear aging. J. Neurosci. Res. 98, 1674–1684.

Klepfer, R.N., Johnson, C.R., Macleod, R.S., 1997. The effects of inhomogeneities and anisotropies on electrocardiographic fields: a 3-D finite-element study. IEEE Trans. Biomed. Eng. 44, 706–719.

Khan, A.M., Handzel, O., Burgess, B.J., Damian, D., Eddington, D.K., Nadol Jr, J.B., 2005. Is word recognition correlated with the number of surviving spiral ganglion cells and electrode insertion depth in human subjects with cochlear implants? Laryngoscope 115, 672–677.

Khanna, S.M., Leonard, D.G.B., 1982. Basilar membrane tuning in the cat cochlea. Science (80-.). 215, 305–306.

Kiefer, J, Von Ilberg, C., Rupprecht, V., Huber-Egener, J., Baumgartner, W., Gstoettner, W., Forgasi, K., Stephan, K., 2000. Optimized speech understanding with the CIS-speech coding strategy in cochlear implants: The effect of variations in stimulus rate and number of channels. Cochlear Implant. 339–340.

Kiefer, Jan, Weber, A., Pfennigdorff, T., Von Ilberg, C., 2000. Scala vestibuli insertion in cochlear implantation: A valuable alternative for cases with obstructed scala tympani. ORL. doi:10.1159/000027755

Kileny, P.R., Zimmerman-Phillips, S., Zwolan, T.A., Kemink, J.L., 1992. Effects of channel number and place of stimulation on performance with the Cochlear Corporation multichannel implant. Am. J. Otol. 13, 117–123.

Kitterick, P.T., Lucas, L., Smith, S.N., 2015. Improving health-related quality of life in single-sided deafness: a systematic review and meta-analysis. Audiol. Neurotol. 20, 79–86.

Kong, Y.-Y., Cruz, R., Jones, J.A., Zeng, F.-G., 2004. Music perception with temporal cues in acoustic and electric hearing. Ear Hear. 25, 173–185.

Kral, A., Hartmann, R., Mortazavi, D., and Klinke, R. (1998). Spatial resolution of cochlear implants: the electrical field and excitation of auditory afferents. *Hearing Research*, *121*(1–2), 11–28. https://doi.org/10.1016/s0378-5955(98)00061-6

Lahav, A., Skoe, E., 2014. An acoustic gap between the NICU and womb: a potential risk for compromised neuroplasticity of the auditory system in preterm infants. Front. Neurosci. 8, 381.

Landsberger, D.M., Srinivasan, A.G., 2009. Virtual channel discrimination is improved by current focusing in cochlear implant recipients. Hear. Res. 254, 34–41.

Landsberger, D. M., Padilla, M., and Srinivasan, A. G. (2012). Reducing current spread using current focusing in cochlear implant users. *Hearing Research*, *284*(1–2), 16–24. https://doi.org/10.1016/j.heares.2011.12.009

Laszig, R., Aschendorff, A., Stecker, M., Müller-Deile, J., Maune, S., Dillier, N., Weber, B., Hey, M., Begall, K., Lenarz, T., 2004. Benefits of bilateral electrical stimulation with the nucleus cochlear implant in adults: 6-month postoperative results. Otol. Neurotol. 25, 958–968.

Lazard, D.S., Vincent, C., Venail, F., Van de Heyning, P., Truy, E., Sterkers, O., Skarzynski, P.H., Skarzynski, H., Schauwers, K., O'Leary, S., 2012. Pre-, per-and postoperative factors affecting performance of postlinguistically deaf adults using cochlear implants: a new conceptual model over time. PLoS One 7, e48739.

Leake, P.A., Hradek, G.T., 1988. Cochlear pathology of long term neomycin induced deafness in cats. Hear. Res. 33, 11–33.

Leal, M.C., Shin, Y.J., Laborde, M., Calmels, M., Verges, S., Lugardon, S., Andrieu, S., Deguine, O., Fraysse, B., 2003. Music perception in adult cochlear implant recipients. Acta Otolaryngol. 123, 826–835.

Die approbierte gedruckte Originalversion dieser Dissertation ist an der TU Wien Bibliothek verfügbar.
The approved original version of this doctoral thesis is available in print at TU Wien Bibliothek.
TU Bibliothek Your knowledge hub WIEN

Learning, L., 2021. Hearing and Equilibrium | Anatomy and Physiology [WWW Document]. URL https://courses.lumenlearning.com/nemcc-ap/chapter/special-senses-hearing-audition-and-balance/ (accessed 11.15.21).

Lee, J., Nadol, J.B., Eddington, D.K., 2011. Factors associated with incomplete insertion of electrodes in cochlear implant surgery: A histopathologic study. Audiol. Neurotol. doi:10.1159/000316445

Lee, J.Y., Hong, S.H., Moon, I.J., Kim, E.Y., Baek, E., Seol, H.Y., Kang, S., 2019. Effect of Cochlear Implant Electrode Array Design on Electrophysiological and Psychophysical Measures: Lateral Wall versus Perimodiolar Types. J. Audiol. Otol. 23, 145.

Leob, G.E., McHardy, J., 1995. Neural Prostheses. Biocompatibility in clinical practice.

Leonor, A., Santiago Luis, A., 2004. Bilateral cochlear implant user with a right ear scala vestibuli insertion and left ear scala tympani insertion: Case report. Int. Congr. Ser. doi:10.1016/j.ics.2004.08.083

Liberman, M.C., 2020. Hidden hearing loss: Primary neural degeneration in the noise-damaged and aging cochlea. Acoust. Sci. Technol. 41, 59–62.

Liberman, M.C., 2017. Noise-induced and age-related hearing loss: new perspectives and potential therapies. F1000Research 6.

Liberman, M.C., Kiang, N.Y., 1978. Acoustic trauma in cats: cochlear pathology and auditory-nerve activity. Acta Otolaryngol.

Lindhult J. Som igenom electriciteten blisvit lindrade eller lyckeligen botade [in Swedish]. Vetenskapesakademiens Handlingar (Proceedings of the Royal Academy of Sciences) 1752;13:305–8.

Lin, K., Marrinan, M.S., Waltzman, S.B., Roland, J.T., 2006. Multichannel cochlear implantation in the scala vestibuli. Otol. Neurotol. doi:10.1097/01.mao.0000224095.63354.1a

Lin, Y.S., 2009. Clinical outcomes of scala vestibuli cochlear implantation in children with partial labyrinthine ossification. Acta Otolaryngol. doi:10.1080/00016480802032819

Litvak, L.M., Spahr, A.J., Emadi, G., 2007. Loudness growth observed under partially tripolar stimulation: model and data from cochlear implant listeners. J. Acoust. Soc. Am. 122, 967–981.

Liu, W., Edin, F., Atturo, F., Rieger, G., Löwenheim, H., Senn, P., Blumer, M., Schrott-Fischer, A., Rask-Andersen, H., Glueckert, R., 2015. The pre-and post-somatic segments of the human type I spiral ganglion neurons–structural and functional considerations related to cochlear implantation. Neuroscience 284, 470–482.

Locher, H., de Groot, J.C.M.J., van Iperen, L., Huisman, M.A., Frijns, J.H.M., Chuva de Sousa Lopes, S.M., 2014. Distribution and development of peripheral glial cells in the human fetal cochlea. PLoS One 9, e88066.

Long, C.J., Holden, T.A., McClelland, G.H., Parkinson, W.S., Shelton, C., Kelsall, D.C., Smith, Z.M., 2014. Examining the electro-neural interface of cochlear implant users using psychophysics, CT scans, and speech understanding. JARO - J. Assoc. Res. Otolaryngol. doi:10.1007/s10162-013-0437-5

Luo, J., Xu, L., Chao, X., Wang, R., Pellittieri, A., Bai, X., Fan, Z., Wang, H., He, S., 2020. The effects of GJB2 or SLC26A4 gene mutations on neural response of the electrically stimulated auditory nerve in children. Ear Hear. 41, 194–207.

Luo, X., Wu, C.-C., Pulling, K., 2020. Combining current focusing and steering in a cochlear implant processing strategy. Int. J. Audiol. 1–6. doi:10.1080/14992027.2020.1822551

Macherey, O., and Carlyon, R. P. (2010). Temporal pitch percepts elicited by dual-channel stimulation of a cochlear implant. *The Journal of the Acoustical Society of America*, *127*(1), 339–349. https://doi.org/10.1121/1.3269042

Die approbierte gedruckte Originalversion dieser Dissertation ist an der TU Wien Bibliothek verfügbar.
The approved original version of this doctoral thesis is available in print at TU Wien Bibliothek.
TU Bibliothek Your knowledge hub WIEN

Macherey, O., Deeks, J.M., Carlyon, R.P., 2011. Extending the limits of place and temporal pitch perception in cochlear implant users. J. Assoc. Res. Otolaryngol. 12, 233–251.

Macherey, O., Carlyon, R.P., Chatron, J., Roman, S., 2017. Effect of pulse polarity on thresholds and on non-monotonic loudness growth in cochlear implant users. J. Assoc. Res. Otolaryngol. 18, 513–527.

Macherey, O., Carlyon, R.P., Van Wieringen, A., Deeks, J.M., Wouters, J., 2008. Higher sensitivity of human auditory nerve fibers to positive electrical currents. JARO - J. Assoc. Res. Otolaryngol. doi:10.1007/s10162-008-0112-4

Macherey, O., Van Wieringen, A., Carlyon, R.P., Deeks, J.M., Wouters, J., 2006. Asymmetric pulses in cochlear implants: effects of pulse shape, polarity, and rate. J. Assoc. Res. Otolaryngol. 7, 253–266.

Makary, C.A., Shin, J., Kujawa, S.G., Liberman, M.C., Merchant, S.N., 2011. Age-related primary cochlear neuronal degeneration in human temporal bones. J. Assoc. Res. Otolaryngol. 12, 711–717.

Marchese-Ragona, R., Pendolino, A.L., Mudry, A., Martini, A., 2019. The father of the electrical stimulation of the ear. Otol. Neurotol. 40, 404–406.

Mark, H.E., Rattay, F., 1990. Frequency discrimination of single-, double-, and triple-cycle sinusoidal acoustic signals. J. Acoust. Soc. Am. 88, 560–563.

Marrs, G.S., Spirou, G.A., 2012. Embryonic assembly of auditory circuits: spiral ganglion and brainstem. J. Physiol. 590, 2391–2408.

McHanwell, S., Brenner, E., Chirculescu, A.R.M., Drukker, J., van Mameren, H., Mazzotti, G., Pais, D., Paulsen, F., Plaisant, O., Caillaud, M.M., Laforêt, E., Riedere, B.M., Sañudo, J.R., Bueno-López, J.L., Doñate-Oliver, F., Sprumont, P., Teofilovski-Parapid, G., Moxham, B.J., 2008. The legal and ethical framework governing Body Donation in Europe - A review of current practice and recommendations for good practice. Eur. J. Anat.

McDermott, H.J. (2004). Music perception with cochlear implants: a review. Trends Amplif. 8, 49–82. https://doi.org/10.1177/108471380400800203

Mesnildrey, Q., Macherey, O., Carlyon, R.P., Venail, F., 2017. Polarity sensitivity in cochlear implants: relation with neural survival, in: Conference on Implantable Auditory Prostheses.

Mesnildrey, Q., Macherey, O., Herzog, P., Venail, F., 2019. Impedance measures for a better understanding of the electrical stimulation of the inner ear. J. Neural Eng. 16, 16023.

Mesnildrey, Q., Venail, F., Carlyon, R.P., Macherey, O., 2020. Polarity sensitivity as a potential correlate of neural degeneration in Cochlear implant users. J. Assoc. Res. Otolaryngol. 21, 89–104.

Miller, C.A., Abbas, P.J., Robinson, B.K., Rubinstein, J.T., Matsuoka, A.J., 1999. Electrically evoked single-fiber action potentials from cat: responses to monopolar, monophasic stimulation. Hear. Res. 130, 197–218.

Miller, C.A., Abbas, P.J., Rubinstein, J.T., Robinson, B.K., Matsuoka, A.J., Woodworth, G., 1998. Electrically evoked compound action potentials of guinea pig and cat: responses to monopolar, monophasic stimulation. Hear. Res. 119, 142–154.

Miller, M.I., Sachs, M.B., 1983. Representation of stop consonants in the discharge patterns of auditory-nerve fibers. J. Acoust. Soc. Am. doi:10.1121/1.389816

Miller, C. A., Abbas, P. J., Robinson, B. K., Rubinstein, J. T., and Matsuoka, A. J. (1999). Electrically evoked single-fiber action potentials from cat: responses to monopolar, monophasic stimulation. *Hearing Research*, *130*(1–2), 197–218. https://doi.org/10.1016/s0378-5955(99)00012-x

Die approbierte gedruckte Originalversion dieser Dissertation ist an der TU Wien Bibliothek verfügbar.
The approved original version of this doctoral thesis is available in print at TU Wien Bibliothek.
TU Bibliothek WIEN Your knowledge hub

Miller, C. A., Abbas, P. J., Rubinstein, J. T., Robinson, B. K., Matsuoka, A. J., and Woodworth, G. (1998). Electrically evoked compound action potentials of guinea pig and cat: responses to monopolar, monophasic stimulation. *Hearing Research*, *119*(1–2), 142–154. https://doi.org/10.1016/s0378-5955(98)00046-x

Moore, B.C.J., 2007. Cochlear hearing loss: physiological, psychological and technical issues. John Wiley & Sons.

Motz, H., Rattay, F., 1986. A study of the application of the Hodgkin-Huxley and the Frankenhaeuser-Huxley model for electrostimulation of the acoustic nerve. Neuroscience. doi:10.1016/0306-4522(86)90064-3

Mudry, A., Mills, M., 2013. The early history of the cochlear implant: a retrospective. JAMA Otolaryngol. Neck Surg. 139, 446–453.

Nadol, J.B., Eddington, D.K., 2006. Histopathology of the inner ear relevant to cochlear implantation. Cochlear brainstem Implant. 64, 31–49.

Nadol Jr, J.B., 1990. Degeneration of cochlear neurons as seen in the spiral ganglion of man. Hear. Res. 49, 141–154.

Nadol Jr, J. B. (1997). Patterns of neural degeneration in the human cochlea and auditory nerve: implications for cochlear implantation. *Otolaryngology-Head and Neck Surgery*, *117*(3), 220–228. https://doi.org/10.1016/s0194-5998(97)70178-5

Nadol, J. B., and Eddington, D. K. (2006). Histopathology of the inner ear relevant to cochlear implantation. *Cochlear and Brainstem Implants*, *64*, 31–49. https://doi.org/10.1159/000094643

Nadol Jr, J.B., 1983. Serial section reconstruction of the neural poles of hair cells in the human organ of Corti. I. Inner hair cells. Laryngoscope 93, 599–614.

Nadol JR, J.B., 1977. Electron microscopic observations in a case of long-standing profound sensorineural deafness. Ann. Otol. Rhinol. Laryngol. 86, 507–517.

Nadol Jr, J.B., Young, Y.-S., Glynn, R.J., 1989. Survival of spiral ganglion cells in profound sensorineural hearing loss: implications for cochlear implantation. Ann. Otol. Rhinol. Laryngol. 98, 411–416.

Nehmé, A., El Zir, E., Moukarzel, N., Haidar, H., Vanpoucke, F., Arnold, L. (2014). Measures of the electrically evoked compound action potential threshold and slope in HiRes 90KTM users. Cochlear Implants Int. 15, 53–60. https://doi.org/10.1179/1754762813Y.0000000039

Negm, M.H., Bruce, I.C., 2014. The effects of HCN and KLT ion channels on adaptation and refractoriness in a stochastic auditory nerve model. IEEE Trans. Biomed. Eng. 61, 2749–2759.

Nelson, D. A., Donaldson, G. S., and Kreft, H. (2008). Forward-masked spatial tuning curves in cochlear implant users. *The Journal of the Acoustical Society of America*, *123*(3), 1522–1543. https://doi.org/10.1121/1.2836786

Nernst, W., 1888. Zur kinetik der in lösung befindlichen körper. Zeitschrift für Phys. Chemie 2, 613–637.

Nichani, J., Green, K., Hans, P., Bruce, I., Henderson, L., Ramsden, R., 2011. Cochlear implantation after bacterial meningitis in children: outcomes in ossified and nonossified cochleas. Otol. Neurotol. 32, 784–789.

Noble, J. H., Gifford, R. H., Hedley-Williams, A. J., Dawant, B. M., and Labadie, R. F. (2014). Clinical evaluation of an image-guided cochlear implant programming strategy. *Audiology and Neurotology*, *19*(6), 400–411. https://doi.org/10.1159/000365273

Noble, J. H., Labadie, R. F., Gifford, R. H., and Dawant, B. M. (2013). Image-guidance enables new methods for customizing cochlear implant stimulation strategies. *IEEE Transactions on Neural Systems and Rehabilitation Engineering*, *21*(5), 820–829. https://doi.org/10.1109/TNSRE.2013.2253333

Die approbierte gedruckte Originalversion dieser Dissertation ist an der TU Wien Bibliothek verfügbar.
The approved original version of this doctoral thesis is available in print at TU Wien Bibliothek.
TU Bibliothek Your knowledge hub WIEN

Nopp, P., Schleich, P., D'haese, P., 2004. Sound localization in bilateral users of MED-EL COMBI 40/40+ cochlear implants. Ear Hear. 25, 205–214.

Organization, W.H., 1991. Report of the informal working group on prevention of deafness and hearing impairment program planning, Geneva, 18-21 June 1991. World Health Organization

Ota, C.Y., Kimura, R.S., 1980. Ultrastructural study of the human spiral ganglion. Acta Otolaryngol. doi:10.3109/00016488009127108

Otte, J., Schuknecht, H.F., Kerr, A.G., 1978. Ganglion cell populations in normal and pathological human cochleae. Implications for cochlear implantation. Laryngoscope 88, 1231–1246.

Parkinson, A.J., Arcaroli, J., Staller, S.J., Arndt, P.L., Cosgriff, A., Ebinger, K., 2002. The Nucleus® 24 Contour™ cochlear implant system: adult clinical trial results. Ear Hear. 23, 41S-48S.

Pfingst, B.E., Hughes, A.P., Colesa, D.J., Watts, M.M., Strahl, S.B., Raphael, Y., 2015a. Insertion trauma and recovery of function after cochlear implantation: Evidence from objective functional measures. Hear. Res. 330, 98–105.

Pfingst, B.E., Xu, L., 2004. Across-site variation in detection thresholds and maximum comfortable loudness levels for cochlear implants. J. Assoc. Res. Otolaryngol. 5, 11–24.

Pfingst, B.E., Xu, L., Thompson, C.S., 2004. Across-site threshold variation in cochlear implants: Relation to speech recognition. Audiol. Neurotol. 9, 341–352.

Pfingst, B.E., Zhou, N., Colesa, D.J., Watts, M.M., Strahl, S.B., Garadat, S.N., Schvartz-Leyzac, K.C., Budenz, C.L., Raphael, Y., Zwolan, T.A., 2015b. Importance of cochlear health for implant function. Hear. Res. 322, 77–88.

Pijl, S., Noel, F., 1992. The Nucleus multichannel cochlear implant: Comparison of scala tympani vs. scala vestibuli electrode placement in a single patient. Otolaryngol. Neck Surg. 107, 472–474.

Punte, A.K., De Ridder, D., Van de Heyning, P., 2013. On the necessity of full length electrical cochlear stimulation to suppress severe tinnitus in single-sided deafness. Hear. Res. 295, 24–29.

Polak, M., Hodges, A. V, King, J.E., Balkany, T.J., 2004. Further prospective findings with compound action potentials from Nucleus 24 cochlear implants. Hear. Res. 188, 104–116.

Potrusil, T., Heshmat, A., Sajedi, S., Wenger, C., Chacko, L.J., Glueckert, R., Schrott-Fischer, A., Rattay, F., 2020. Finite Element Analysis and Three-Dimensional Reconstruction of Tonotopically Aligned Human Auditory Fiber Pathways: A Computational Environment for Modeling Electrical Stimulation by a Cochlear Implant based on micro-CT. Hear. Res. 108001. https://doi.org/10.1016/j.heares.2020.108001

Rahne, T., Plontke, S.K., 2016. Functional result after cochlear implantation in children and adults with single-sided deafness. Otol. Neurotol. 37, e332–e340.

Rask-Andersen, H., Liu, W., Erixon, E., Kinnefors, A., Pfaller, K., Schrott-Fischer, A., Glueckert, R., 2012. Human cochlea: anatomical characteristics and their relevance for cochlear implantation. Anat. Rec. Adv. Integr. Anat. Evol. Biol. 295, 1791–1811.

Ranck, J. B. (1975). Which elements are excited in electrical stimulation of mammalian central nervous system: A review. *Brain Research*. https://doi.org/10.1016/0006-8993(75)90364-9

Rattay, F., 1999. The basic mechanism for the electrical stimulation of the nervous system. Neuroscience. doi:10.1016/S0306-4522(98)00330-3

Rattay, F., 1990. Electrical Nerve Stimulation: Theory, Experiments, and Applications - Back Matter, in: Electrical Nerve Stimulation: Theory, Experiments, and Applications.

Die approbierte gedruckte Originalversion dieser Dissertation ist an der TU Wien Bibliothek verfügbar.
The approved original version of this doctoral thesis is available in print at TU Wien Bibliothek.
TU Bibliothek Your knowledge hub WIEN

Rattay, F., 1986. Analysis of Models for External Stimulation of Axons. IEEE Trans. Biomed. Eng. doi:10.1109/TBME.1986.325670

Rattay, F., Aberham, M., 1993. Modeling Axon Membranes for Functional Electrical Stimulation. IEEE Trans. Biomed. Eng. doi:10.1109/10.250575

Rattay, F., Motz, H., 1987. Simulation of the response of a multichannel nerve array to pulse shapes produced by single-channel electrostimulation. Perception 16, 769–776.

Rattay, F., Greenberg, R.J., Resatz, S., 2003. „Neuron Modeling “, in; Handbook of Neuroprosthetic Methods, eds. Finn WE, LoPresti PG.

Rattay, F., Gebeshuber, I.C., Gitter, A.H., 1998. The mammalian auditory hair cell: A simple electric circuit model. J. Acoust. Soc. Am. 103, 1558–1565.

Rattay, F., Leao, R.N., Felix, H., 2001a. A model of the electrically excited human cochlear neuron. II. Influence of the three-dimensional cochlear structure on neural excitability. Hear. Res. doi:10.1016/S0378-5955(00)00257-4

Rattay, F., Danner, S.M., 2014. Peak I of the human auditory brainstem response results from the somatic regions of type I spiral ganglion cells: evidence from computer modeling. Hear. Res. 315, 67–79.

Rattay, F., Lutter, P., 1997. Speech sound representation in the auditory nerve: Computer simulation studies on inner ear mechanisms. ZAMM Zeitschrift fur Angew. Math. und Mech. doi:10.1002/zamm.19970771212

Rattay, F., Paredes, L.P., Leao, R.N., 2012. Strength–duration relationship for intra-versus extracellular stimulation with microelectrodes. Neuroscience 214, 1–13.

Rattay, F., Potrusil, T., Wenger, C., Wise, A.K., Glueckert, R., Schrott-Fischer, A., 2013. Impact of morphometry, myelinization and synaptic current strength on spike conduction in human and cat spiral ganglion neurons. PLoS One. doi:10.1371/journal.pone.0079256

Rattay, F., Lutter, P., Felix, H., 2002. A model of the electrically excited human cochlear neuron. Hear. Res. doi:10.1016/s0378-5955(00)00256-2

Rattay, F., Lutter, P., Felix, H., 2001b. A model of the electrically excited human cochlear neuronI. Contribution of neural substructures to the generation and propagation of spikes. Hear. Res. doi:10.1016/S0378-5955(00)00256-2

Reiss, L.A.J., 2020. Cochlear implants and other inner ear prostheses: today and tomorrow. Curr. Opin. Physiol.

Resnick, J. M., O'Brien, G. E., and Rubinstein, J. T. (2018). Simulated auditory nerve axon demyelination alters sensitivity and response timing to extracellular stimulation. *Hearing Research*, *361*, 121–137. https://doi.org/10.1016/j.heares.2018.01.014

Rhode, W.S., 1971. Observations of the vibration of the basilar membrane in squirrel monkeys using the Mössbauer technique. J. Acoust. Soc. Am. 49, 1218–1231.

Riederer, B.M., Bolt, S., Brenner, E., Bueno-López, J.L., Circulescu, A.R.M., Davies, D.C., De Caro, R., Gerrits, P.O., McHanwell, S., Pais, D., Paulsen, F., Plaisant, O., Sendemir, E., Stabile, I., Moxham, B.J., 2012. The legal and ethical framework governing Body Donation in Europe - 1st update on current practice. Eur. J. Anat.

Rinia, A.B., Olphen, A.F., Dunnebier, E.A., 2006. Cochlear implantation in obstructed cochleas: The effect of the degree of obstruction on the number of activated electrodes and the amount of postoperative speech perception. Clin. Otolaryngol. doi:10.1111/j.1749-4486.2006.01257.x

Rosen, S., 1992. Temporal information in speech: acoustic, auditory and linguistic aspects. Philos. Trans. R. Soc. London. Ser. B Biol. Sci. 336, 367–373.

Die approbierte gedruckte Originalversion dieser Dissertation ist an der TU Wien Bibliothek verfügbar.
The approved original version of this doctoral thesis is available in print at TU Wien Bibliothek.
TU Bibliothek Your knowledge hub WIEN

Rubinstein, J.T., Parkinson, W.S., Tyler, R.S., Gantz, B.J., 1999. Residual speech recognition and cochlear implant performance: Effects of implantation criteria. Am. J. Otol.

Saberi, K., Perrott, D.R., 1999. Cognitive restoration of reversed speech. Nature 398, 760.

Santarelli, R., Cama, E., Scimemi, P., Dal Monte, E., Genovese, E., Arslan, E., 2008. Audiological and electrocochleography findings in hearing-impaired children with connexin 26 mutations and otoacoustic emissions. Eur. Arch. oto-rhino-laryngology 265, 43–51.

Saleh, S. M., Saeed, S. R., Meerton, L., Moore, D. R., and Vickers, D. A. (2013). Clinical use of electrode differentiation to enhance programming of cochlear implants. *Cochlear Implants International*, *14*(sup4), 16–18. https://doi.org/10.1179/1467010013Z.000000000125

Saunders, E., Cohen, L., Aschendorff, A., Shapiro, W., Knight, M., Stecker, M., Richter, B., Waltzman, S., Tykocinski, M., Roland, T., 2002. Threshold, comfortable level and impedance changes as a function of electrode-modiolar distance. Ear Hear. 23, 28S-40S.

Schuknecht, H.F., 1993. Pathology of the ear (2nd edn), Lea and Febiger. Philadelphia, USA 191–253.

Schvartz-Leyzac, K.C., Pfingst, B.E., 2018. Assessing the relationship between the electrically evoked compound action potential and speech recognition abilities in bilateral cochlear implant recipients. Ear Hear. 39, 344.

Schvartz-Leyzac, K. C., Holden, T. A., Zwolan, T. A., Arts, H. A., Firszt, J. B., Buswinka, C. J., and Pfingst, B. E. (2020). Effects of electrode location on estimates of neural health in humans with cochlear implants. *Journal of the Association for Research in Otolaryngology*, *21*(3), 259–275. https://doi.org/10.1007/s10162-020-00749-0

Schvartz-Leyzac, K.C., Pfingst, B.E., 2016. Across-site patterns of electrically evoked compound action potential amplitude-growth functions in multichannel cochlear implant recipients and the effects of the interphase gap. Hear. Res. 341, 50–65.

Schvartz-Leyzac, K. C., Zwolan, T. A., and Pfingst, B. E. (2017). Effects of electrode deactivation on speech recognition in multichannel cochlear implant recipients. *Cochlear Implants International*, *18*(6), 324–334. https://doi.org/10.1080/14670100.2017.1359457

Servais, J.J., Hörmann, K., Wallhäusser-Franke, E., 2017. Unilateral cochlear implantation reduces tinnitus loudness in bimodal hearing: a prospective study. Front. Neurol. 8, 60.

Shamma, S.A., 1985. Speech processing in the auditory system I: The representation of speech sounds in the responses of the auditory nerve. J. Acoust. Soc. Am. 78, 1612--1621.

Shearer, A.E., Tejani, V.D., Brown, C.J., Abbas, P.J., Hansen, M.R., Gantz, B.J., Smith, R.J.H., 2018. In vivo electrocochleography in hybrid cochlear implant users implicates TMPRSS3 in spiral ganglion function. Sci. Rep. 8, 1–9.

Shepherd, R.K., Hatsushika, S., Clark, G.M., 1993. Electrical stimulation of the auditory nerve: the effect of electrode position on neural excitation. Hear. Res. 66, 108–120.

Shepherd, R.K., Javel, E., 1997. Electrical stimulation of the auditory nerve. I. Correlation of physiological responses with cochlear status. Hear. Res. 108, 112–144.

Simmons, F.B., 1966. Electrical stimulation of the auditory nerve in man. Arch. Otolaryngol. 84, 2–54.

Skinner, M.W., Ketten, D.R., Holden, L.K., Harding, G.W., Smith, P.G., Gates, G.A., Neely, J.G., Kletzker, G.R., Brunsden, B., Blocker, B., 2002. CT-derived estimation of cochlear morphology and electrode array position in relation to word recognition in Nucleus-22 recipients. J. Assoc. Res. Otolaryngol. 3, 332–350.

Sladen, D.P., Frisch, C.D., Carlson, M.L., Driscoll, C.L.W., Torres, J.H., Zeitler, D.M., 2017. Cochlear implantation for single-sided deafness: A multicenter study. Laryngoscope 127, 223–228.

Die approbierte gedruckte Originalversion dieser Dissertation ist an der TU Wien Bibliothek verfügbar.
The approved original version of this doctoral thesis is available in print at TU Wien Bibliothek.
TU Bibliothek Your knowledge hub WIEN

Sly, D.J., Heffer, L.F., White, M.W., Shepherd, R.K., Birch, M.G.J., Minter, R.L., Nelson, N.E., Wise, A.K., O'Leary, S.J., 2007. Deafness alters auditory nerve fibre responses to cochlear implant stimulation. Eur. J. Neurosci. 26, 510–522.

Smit, J. E., Hanekom, T., and Hanekom, J. J. (2008). Predicting action potential characteristics of human auditory nerve fibres through modification of the Hodgkin-Huxley equations. *South African Journal of Science*, *104*(7), 284–292.

Smulders, Y.E., van Zon, A., Stegeman, I., Rinia, A.B., Van Zanten, G.A., Stokroos, R.J., Hendrice, N., Free, R.H., Maat, B., Frijns, J.H.M., 2016. Comparison of bilateral and unilateral cochlear implantation in adults: a randomized clinical trial. JAMA Otolaryngol. neck Surg. 142, 249–256.

Smullen, J.L., Balkany, T.J., 2005. Implantation of the ossified cochlea. Oper. Tech. Otolaryngol. Neck Surg. 16, 117–120.

Snel-Bongers, J., Briaire, J.J., van der Veen, E.H., Kalkman, R.K., Frijns, J.H.M., 2013. Threshold levels of dual electrode stimulation in cochlear implants. J. Assoc. Res. Otolaryngol. 14, 781–790.

Snyder, R. L., Bierer, J. A., and Middlebrooks, J. C. (2004). Topographic spread of inferior colliculus activation in response to acoustic and intracochlear electric stimulation. *Journal of the Association for Research in Otolaryngology*, *5*(3), 305–322. https://doi.org/10.1007/s10162-004-4026-5

Spitzer, E. R., Choi, S., and Hughes, M. L. (2019). The effect of stimulus polarity on the relation between pitch ranking and ECAP spread of excitation in cochlear implant users. *Journal of the Association for Research in Otolaryngology*, *20*(3), 279–290. https://doi.org/10.1007/s10162-018-00712-0

Spitzer, E. R., and Hughes, M. L. (2017). Effect of stimulus polarity on physiological spread of excitation in cochlear implants. *Journal of the American Academy of Audiology*, *28*(09), 786–798. https://doi.org/10.3766/jaaa.16144

Spoendlin, H., 1985. Anatomy of Cochlear Innervation. Am. J. Otolaryngol. 6, 453–467. doi:https://doi.org/10.1016/S0196-0709(85)80026-0

Spoendlin, H., 1984. Factors inducing retrograde degeneration of the cochlear nerve. Ann. Otol. Rhinol. Laryngol. 93, 76–82.

Spoendlin, H., Schrott, A., 1987. The block surface method for evaluation of human inner ears. Acta Otolaryngol. 104, 25–36. doi:10.3109/00016488709124973

Spoendlin, H., 1972. Innervation densities of the cochlea. Acta Otolaryngol. doi:10.3109/00016487209138937

Spoendlin, H., Schrott, A., 1990. Quantitative evaluation of the human cochlear nerve. Acta Otolaryngol. 109, 61–70.

Spoendlin, H., Schrott, A., 1989. Analysis of the human auditory nerve. Hear. Res. doi:10.1016/0378-5955(89)90056-7

Spoendlin, H., Schrott, A., 1988. The spiral ganglion and the innervation of the human organ of corti. Acta Otolaryngol. doi:10.3109/00016488809119493

Steenerson, R.L., Gary, L.B., Wynens, M.S., 1990. Scala vestibuli cochlear implantation for labyrinthine ossification. Am. J. Otol. 11, 360–363.

Srinivasan, A. G., Padilla, M., Shannon, R. V, and Landsberger, D. M. (2013). Improving speech perception in noise with current focusing in cochlear implant users. *Hearing Research*, *299*, 29–36. https://doi.org/10.1016/j.heares.2013.02.004

Die approbierte gedruckte Originalversion dieser Dissertation ist an der TU Wien Bibliothek verfügbar.
The approved original version of this doctoral thesis is available in print at TU Wien Bibliothek.
TU Bibliothek Your knowledge hub WIEN

Stickney, G.S., Zeng, F.-G., Litovsky, R., Assmann, P., 2004. Cochlear implant speech recognition with speech maskers. J. Acoust. Soc. Am. 116, 1081–1091.

Stock, A., Bozzato, V., Kloska, S.P., Bozzato, A., Hoppe, U., Hornung, J., Dörfler, A., Struffert, T., 2020. Evaluation After Cochlear Implant Surgery. Clin. Neuroradiol. doi:10.1007/s00062-020-00922-1

Summerfield, A.Q., Marshall, D.H., 1995. Preoperative predictors of outcomes from cochlear implantation in adults: performance and quality of life. Ann. Otol. Rhinol. Laryngol. Suppl. 166, 105.

Suzuki, M., Goto, T., Kashio, A., Yasui, T., Sakamoto, T., Ito, K., Yamasoba, T., 2011. Preservation of vestibular function after scala vestibuli cochlear implantation. Auris Nasus Larynx. doi:10.1016/j.anl.2011.01.014

Tang, Q., Benítez, R., Zeng, F.G., 2011. Spatial channel interactions in cochlear implants, in: Journal of Neural Engineering. doi:10.1088/1741-2560/8/4/046029

Távora-Vieira, D., Marino, R., Acharya, A., Rajan, G.P., 2015. The impact of cochlear implantation on speech understanding, subjective hearing performance, and tinnitus perception in patients with unilateral severe to profound hearing loss. Otol. Neurotol. 36, 430–436.

Thomsen, E., 1967. The Ultrastructuhe of the Spiral Ganglion in the Guinea Pig. Acta Otolaryngol. 63, 442–448. doi:10.3109/00016486709123621

Tian, Q., Linthicum Jr, F.H., Fayad, J.N., 2006. Human cochleae with three turns: an unreported malformation. Laryngoscope 116, 800–803.

Trudel, M., Côté, M., Philippon, D., Simonyan, D., Villemure-Poliquin, N., Bussières, R., 2018. Comparative impacts of scala vestibuli versus scala tympani cochlear implantation on auditory performances and programming parameters in partially ossified cochleae. Otol. Neurotol. 39, 700–706.

Turner, C.W., Gantz, B.J., Vidal, C., Behrens, A., Henry, B.A., 2004. Speech recognition in noise for cochlear implant listeners: benefits of residual acoustic hearing. J. Acoust. Soc. Am. 115, 1729–1735.

Tykocinski, M., Saunders, E., Cohen, L.T., Treaba, C., Briggs, R.J.S., Gibson, P., Clark, G.M., Cowan, R.S.C., 2001. The contour electrode array: safety study and initial patient trials of a new perimodiolar design. Otol. Neurotol. 22, 33–41.

Undurraga, J.A., Carlyon, R.P., Wouters, J., Van Wieringen, A., 2013. The polarity sensitivity of the electrically stimulated human auditory nerve measured at the level of the brainstem. JARO - J. Assoc. Res. Otolaryngol. doi:10.1007/s10162-013-0377-0

Undurraga, J.A., Van Wieringen, A., Carlyon, R.P., Macherey, O., Wouters, J., 2010. Polarity effects on neural responses of the electrically stimulated auditory nerve at different cochlear sites. Hear. Res. 269, 146–161.

Undurraga, J. A., Carlyon, R. P., Macherey, O., Wouters, J., and Van Wieringen, A. (2012). Spread of excitation varies for different electrical pulse shapes and stimulation modes in cochlear implants. *Hearing Research*, *290*(1–2), 21–36. https://doi.org/10.1016/j.heares.2012.05.003

Van de Heyning, P., Vermeire, K., Diebl, M., Nopp, P., Anderson, I., De Ridder, D., 2008. Incapacitating unilateral tinnitus in single-sided deafness treated by cochlear implantation. Ann. Otol. Rhinol. Laryngol. 117, 645–652.

van den Honert, C., Kelsall, D.C., 2007. Focused intracochlear electric stimulation with phased array channels. J. Acoust. Soc. Am. 121, 3703–3716.

Van Der Marel, K. S., Briaire, J. J., Verbist, B. M., Muurling, T. J., and Frijns, J. H. M. (2015). The influence of cochlear implant electrode position on performance. *Audiology and Neurotology*, *20*(3), 202–211. https://doi.org/10.1159/000377616

Die approbierte gedruckte Originalversion dieser Dissertation ist an der TU Wien Bibliothek verfügbar.
The approved original version of this doctoral thesis is available in print at TU Wien Bibliothek.
TU Bibliothek Your knowledge hub WIEN

Van Wieringen, A., Carlyon, R.P., Laneau, J., Wouters, J., 2005. Effects of waveform shape on human sensitivity to electrical stimulation of the inner ear. Hear. Res. 200, 73–86.

Van Wieringen, A., Macherey, O., Carlyon, R.P., Deeks, J.M., Wouters, J., 2008. Alternative pulse shapes in electrical hearing. Hear. Res. 242, 154–163.

Versnel, H., Agterberg, M.J.H., de Groot, J.C.M.J., Smoorenburg, G.F., Klis, S.F.L., 2007. Time course of cochlear electrophysiology and morphology after combined administration of kanamycin and furosemide. Hear. Res. 231, 1–12.

Venail, F., and Mathiolon, C. (2015). Menjot De Champfleur S, Piron JP, Sicard M, Villemus F, Vessigaud MA, Sterkers-Artieres F, Mondain M, Uziel A. *Effects of Electrode Array Length on Frequency-Place Mismatch and Speech Perception with Cochlear Implants. Audiol Neurotol*, *20*, 102–111. https://doi.org/10.1159/000369333

Viana, L.M., O'Malley, J.T., Burgess, B.J., Jones, D.D., Oliveira, C.A.C.P., Santos, F., Merchant, S.N., Liberman, L.D., Liberman, M.C., 2015. Cochlear neuropathy in human presbycusis: Confocal analysis of hidden hearing loss in post-mortem tissue. Hear. Res. 327, 78–88.

Vickers, D., Degun, A., Canas, A., Stainsby, T., and Vanpoucke, F. (2016). Deactivating cochlear implant electrodes based on pitch information for users of the ACE strategy. In *Physiology, psychoacoustics and cognition in normal and impaired hearing* (pp. 115–123). Springer, Cham. https://doi.org/10.1007/978-3-319-25474-6_13

Vlastarakos, P. V, Nazos, K., Tavoulari, E.-F., Nikolopoulos, T.P., 2014. Cochlear implantation for single-sided deafness: the outcomes. An evidence-based approach. Eur. Arch. Oto-rhino-laryngology 271, 2119–2126.

Volta, A., 1800. XVII. On the electricity excited by the mere contact of conducting substances of different kinds. In a letter from Mr. Alexander Volta, FRS Professor of Natural Philosophy in the University of Pavia, to the Rt. Hon. Sir Joseph Banks, Bart. KBPR S. Philos. Trans. R. Soc. London 403–431.

Von Békésy, G., Wever, E.G., 1960. Experiments in hearing. McGraw-Hill New York.

VONDRÁŠEK, M., Sovka, P., TICHÝ, T., 2008. ACE Strategy with Virtual Channels. Radioengineering 17.

Waltzman, S., Cohen, N., Shapiro, W., 1995. Effects of cochlear implantation on the young deaf child, in: Cochlear Implants in Children. Karger Publishers, pp. 125–128.

Wangemann, P., 2006. Supporting sensory transduction: cochlear fluid homeostasis and the endocochlear potential. J. Physiol. 576, 11–21.

Wangemann, P., Schacht, J., 1996. Homeostatic mechanisms in the cochlea, in: The Cochlea. Springer, pp. 130–185.

WHO, 2020. Deafness and hearing loss. World Heal. Organ. URL https://www.who.int/news-room/fact-sheets/detail/deafness-and-hearing-loss#:~:text=Over 5%25 of the world%27s,will have disabling hearing loss.

Wikimedia Commons, 2020. File:Hawksbees Electrical Machine by Jean-Antoine Nollet.jpg.

Wikimedia Commons, 2021. File:Basis of Membrane Potential2.png. URL: https://commons.wikimedia.org/w/index.php?title=File:Basis_of_Membrane_Potential2.png&oldid=524748331

Wilson, B.S., Zerbi, M., Lawson, D.T., 1993. Identification of virtual channel conditions on the basis of pitch. Third Q. Prog. Rep.

Wilson B. A Treatise on Electricity. London: C. Davis and R. Dodsley; 1752.

Wright, A., 1984. Dimensions of the cochlear stereocilia in man and the guinea pig. Hear. Res. 13, 89–98.

Wu, P.Z., Liberman, L.D., Bennett, K., De Gruttola, V., O'Malley, J.T., Liberman, M.C., 2019. Primary neural degeneration in the human cochlea: evidence for hidden hearing loss in the aging ear. Neuroscience 407, 8–20.

Die approbierte gedruckte Originalversion dieser Dissertation ist an der TU Wien Bibliothek verfügbar.
The approved original version of this doctoral thesis is available in print at TU Wien Bibliothek.
TU Bibliothek WIEN Your knowledge hub

Xing, Yazhi, Devadoss J. Samuvel, Shawn M. Stevens, Judy R. Dubno, Bradley A. Schulte, and H.L., 2012. Age-related changes of myelin basic protein in mouse and human auditory nerve. PLoS One 7, e34500. doi:https://doi.org/10.1371/journal.pone.0034500

Xu, L., Skidmore, J., Luo, J., Chao, X., Wang, R., Wang, H., He, S., 2020. The effect of pulse polarity on neural response of the electrically-stimulated cochlear nerve in children with cochlear nerve deficiency and children with normal-sized cochlear nerves. Ear Hear. 41, 1306.

Yukawa, K., Cohen, L., Blamey, P., Pyman, B., Tungvachirakul, V., O'Leary, S., 2004. Effects of insertion depth of cochlear implant electrodes upon speech perception. Audiol. Neurotol. 9, 163–172.

Zaghis, A., Todini, L., Capaccio, P., Berta, L.G. della, Pignataro, L., 2003. Ossified versus patent cochlea: objective and subjective results of partial drill-out of the basal turn. J. Otolaryngol. 32.

Zaimi, A., Duval, T., Gasecka, A., Côté, D., Stikov, N., Cohen-Adad, J., 2016. AxonSeg: Open Source Software for Axon and Myelin Segmentation and Morphometric Analysis . Front. Neuroinformatics.

Zeitler, D.M., Lalwani, A.K., Roland Jr, J.T., Habib, M.G., Gudis, D., Waltzman, S.B., 2009. The effects of cochlear implant electrode deactivation on speech perception and in predicting device failure. Otol. Neurotol. 30, 7–13.

Zhou, N., 2016. Monopolar detection thresholds predict spatial selectivity of neural excitation in cochlear implants: Implications for speech recognition. PLoS One 11, e0165476.

Zhou, N. (2017). Deactivating stimulation sites based on low-rate thresholds improves spectral ripple and speech reception thresholds in cochlear implant users. *The Journal of the Acoustical Society of America*, *141*(3), EL243–EL248. https://doi.org/10.1121/1.4977235

Zirn, S., Polterauer, D., Keller, S., Hemmert, W. (2016). The effect of fluctuating maskers on speech understanding of high-performing cochlear implant users. Int. J. Audiol. 55, 295–304. https://doi.org/10.3109/14992027.2015.1128124

Zwislocki, J., Feldman, R.S., 1956. Just noticeable differences in dichotic phase. J. Acoust. Soc. Am. 28, 860–864.

Die approbierte gedruckte Originalversion dieser Dissertation ist an der TU Wien Bibliothek verfügbar.
The approved original version of this doctoral thesis is available in print at TU Wien Bibliothek.
TU Bibliothek Your knowledge hub WIEN

Die approbierte gedruckte Originalversion dieser Dissertation ist an der TU Wien Bibliothek verfügbar.
The approved original version of this doctoral thesis is available in print at TU Wien Bibliothek.

Curriculum Vitae

Profile

Amirreza Heshmat

Innsbrucker Strasse 1/13a
6060 Hall in Tirol, Austria

Email: amirreza.heshmat@i-med.ac.at

Date of Birth: 06.05.1987

Education

Since 04/19	Doctoral student (Dr. techn., PhD) - *Engineering Sciences* Vienna University of Technology
10/15 – 11/18	Master's degree (Dipl.-Ing., MSc) - *Biomedical Engineering* Vienna University of Technology
07/12 – 07/15	Pre-Master - *German language* and *Biomedical Engineering* Vienna University of Technology
10/05 – 10/10	Bachelor's degree (BA) - *Industrial Engineering* Islamic Azad University

Work Experience

Since 04/19	Project Assistant (Austrian Science Fund). Medical University of Innsbruck, Laboratory for Inner Ear Biology, Department of Otorhinolaryngology
Since 04/19	Research Assistant. Vienna University of Technology, Institute for Analysis and Scientific Computing

International Experience

Since 04/19	Cooperation with Department of Electrical and Computer Engineering Munich School of Bioengineering, Technical University of Munich, Germany

Papers in Peer-reviewed Journals

2021 **Heshmat A**, Sajedi S, Schrott-Fischer A and Rattay F., (2021) *Polarity Sensitivity of Human Auditory Nerve Fibers Based on Pulse Shape and Cochlear Implant Stimulation Strategy and Array*. Frontiers in Neuroscience. 15:751599. https://doi.org/10.3389/fnins.2021.751599

2020 **Heshmat, A**., Sajedi, S., Chacko, L. J., Fischer, N., Schrott-Fischer, A., and Rattay, F., (2020). *Dendritic Degeneration of Human Auditory Nerve Fibers and Its Impact on the Spiking Pattern Under Regular Conditions and During Cochlear Implant Stimulation.* Frontiers in Neuroscience, 14. https://doi.org/10.3389/fnins.2020.599868

2020 Potrusil, T., **Heshmat, A.,** Sajedi, S., Wenger, C., Chacko, L. J., Glueckert, R., Schrott-Fischer, A., and Rattay, F., (2020). *Finite element analysis and three-dimensional reconstruction of tonotopically aligned human auditory fiber pathways: a computational environment for modeling electrical*

Die approbierte gedruckte Originalversion dieser Dissertation ist an der TU Wien Bibliothek verfügbar.
The approved original version of this doctoral thesis is available in print at TU Wien Bibliothek.
TU Bibliothek Your knowledge hub WIEN

stimulation by a cochlear implant based on micro-CT. Hearing Research, 393, 108001. https://doi.org/10.1016/j.heares.2020.108001

2019 Fischer, N., Chacko, L. J., **Heshmat, A**., Eberharter, T., Riechelmann, H., Schmutzhard, J., Glueckert, R., and Schrott-Fischer, A., (2019). Changes in Na, K-ATPase alpha 3 in aging mouse spiral ganglion and organ of corti. B-ENT, 15(4), 273-279

Papers in Conference Contributions / Poster Presentations

2021 **Heshmat, A**., Sajedi, S., Schrott-Fischer, A., and Rattay, F., (2021). *Impact of peripheral degeneration of human cochlear nerve fibers on the spiking pattern and cochlear implant performance*. Conference on Implantable Auditory Prostheses (CIAP) USA.

2021 Croner, A., **Heshmat, A**., Chacko, L. J., Schrott-Fischer, A., Hemmert, W., and Bai, S., (2021). *Simulation of Electrical Excitation Patterns with Degenerating Auditory Nerve Fibers*. Conference on Implantable Auditory Prostheses (CIAP) USA.

2021 Tanzer, T., Sajedi, S., **Heshmat, A**., and Rattay, F., (2021). *Impact of auditory nerve fiber's diameter on the dynamic range during stimulation with a cochlear implant*. Conference on Implantable Auditory Prostheses (CIAP) USA.

2021 Croner, A., **Heshmat, A.,** Chacko, L. J., Glueckert, R., Schrott-Fischer, A., Hemmert, W., and Bai, S., (2021). *Simulation of Electrical Excitation Patterns With Degenerated Auditory Nerve Fibers*. Association for Research in Otolaryngology (ARO) - 44rd Annual Midwinter Meeting Conference USA.

2021 Bai, S., **Heshmat, A.,** Chacko, L. J., Croner, A., Gutierrez, JPC., Schrott-Fischer, A., and Hemmert, W., (2021). *Neuronal Excitation Patterns in two Cochlea Models Based on High-Resolution Micro-CT Scans*. Conference on Implantable Auditory Prostheses (CIAP) USA.

Die approbierte gedruckte Originalversion dieser Dissertation ist an der TU Wien Bibliothek verfügbar.
The approved original version of this doctoral thesis is available in print at TU Wien Bibliothek.
TU Bibliothek Your knowledge hub WIEN

2020 **Heshmat, A.**, Sajedi, S., Schrott-Fischer, A., and Rattay, F., (2020). *Dendritic degeneration of human cochlear ganglion neurons type I and its impact on the spiking pattern*. Bernstein Conference 2020. https://doi.org/10.12751/nncn.bc2020.0087

2020 Sajedi, S., **Heshmat, A.**, Schrott-Fischer, A., and Rattay, F., (2020). *Effects of dendritic degeneration of human cochlear ganglion neurons type I on cochlear implant performance*. Bernstein Conference 2020. https://doi.org/10.12751/nncn.bc2020.0214

2020 **Heshmat, A.**, Sajedi, S., Schrott-Fischer, A., and Rattay, F., (2020). *Comparison of extracellular voltage distribution in cochlear implant systems with and without carrier: a computational study based on micro-CT images of a human cochlea*. 2nd Annual Computational Data Neuroscience Symposium, Harvard University.

2020 Potrusil, T., **Heshmat, A.**, Sajedi, S., Wenger, C., Chacko, L.J., Glueckert, R., Schrott-Fischer, A. and Rattay, F., (2020). *Simulated nerve responses to cochlear implant stimulation based on three-dimensional micro-CT reconstruction of human auditory nerve.* Association for Research in Otolaryngology (ARO) - 43rd Annual Midwinter Meeting Conference.

2020 **Heshmat, A.**, Sajedi, S., Schrott-Fischer, A., and Rattay, F., (2020). *Polarity sensitivity from electrical stimulation of degenerated human cochlear neurons*. The Federation of European Neuroscience Societies (FENS) Conference.

2019 Sajedi, S., **Heshmat, A.**, Schrott-Fischer, A. and Rattay, F., (2019). *Cochlear implants for cat and man & what we learn from a modeling study*. Vienna young Scientists Symposium (VSS) Conference.

Die approbierte gedruckte Originalversion dieser Dissertation ist an der TU Wien Bibliothek verfügbar.
The approved original version of this doctoral thesis is available in print at TU Wien Bibliothek.
TU Bibliothek Your knowledge hub WIEN